The effect of water on partial melting in the upper mantle

A DISSERTATION
SUBMITTED TO THE FACULTY OF THE GRADUATE SCHOOL
OF THE UNIVERSITY OF MINNESOTA
BY

Travis Jay Tenner

IN PARTIAL FULFILLMENT OF THE REQUIREMENTS
FOR THE DEGREE OF
DOCTOR OF PHILOSOPHY

Advisor: Marc M. Hirschmann

June, 2010

Chapter II (pages 8 to 59) is reproduced from
Chemical Geology volume 227, pages 42-56, © 2009
Tenner, T.J., Hirschmann, M.M., Withers, A.C. & Hervig, R.L.
"Hydrogen partitioning between nominally anhydrous upper mantle minerals and melt between 3 and 5 GPa and applications to hydrous peridotite partial melting."
with kind permission of Elsevier B.V.

Acknowledgements

I would like to acknowledge the people who have helped me on my way to getting my PhD. Without their support I simply would not have gotten to this point in my career. First and foremost I would like to thank Marc Hirschmann. In both a literal and figurative sense Marc has been more than just my graduate student advisor. When I began taking geology classes in 2001, Marc taught my undergraduate mineralogy and petrology classes, and it was almost instantaneous that I recognized that this was *the* area of geology for me. In the summer of 2002, I went back home and worked a low paying summer job, just like I had since middle school. In hindsight, I had a world of potential but a lack of initiative to truly investigate what I would do with my life. So when Marc asked me to work in his experimental petrology lab as an undergraduate in the summer of 2002, he became a mentor to me and provided the challenge and stimulation that ultimately changed the course of my life. Working in the experimental petrology lab for two summers was my first real hands-on research. It also put me in an environment with graduate students and researchers who broadened my perspective in terms of what I would do beyond getting my bachelors degree. Marc encouraged me to go to graduate school, where I furthered my research skills by attaining a Masters degree at the University of Michigan. When I decided to continue on by getting my PhD at another university, Marc suggested that I come back to Minnesota. As an advisor, Marc has been ideal. He has been very involved, whether on campus or half a world away. Early on in the course of my PhD he set the bar high for what was expected of me. At times it was stressful and I wasn't sure if I could meet those expectations, but Marc never doubted in

my capabilities. Perhaps the best thing about Marc is that he put me in situations that allowed me to gain confidence in myself as a researcher. For example, I was pretty terrified when Marc suggested I become the electron microprobe research assistant early on in my PhD. However, being the RA allowed me to become a competent microprobe operator, and I had little doubt that I could go to Arizona State University and learn how to operate their secondary ion mass spectrometer, which was critical to my research. It was victories like these that allowed me to march up the steep learning curve that it took to get my PhD. Throughout the process of conducting and analyzing experiments, writing papers, and giving presentations Marc's demeanor as a critical, yet supportive evaluator has pushed me to perform at my highest level. Not only that, Marc has given me the freedom to pursue the things that excite me, such as attending SIMS workshops and microscopy society meetings. Marc, I can't thank you enough for all of your contributions.

I also owe a great deal of thanks to Tony Withers, who was instrumental to my research in several aspects. Tony helped me to master using various experimental apparati, hardware, and software, as well as cleverly engineering countless devices to make my job easier as a researcher. Tony has also been a fantastic academic peer, contributing as a co-author in my Chemical Geology publication (Chapter II), but also contributing with opinions and ideas that were critical to all aspects of my PhD research. Additionally, Tony was a great co-pilot on trips to Arizona State for marathon SIMS sessions, and I don't think I'll ever stop being amazed at what we were able to accomplish (when the SIMS was working smoothly) and/or overcome (when the SIMS

was not working so smoothly!) in our quest to acquire data for the good of the experimental petrology lab.

Ellery Frahm also deserves many thanks for his contributions in the electron microprobe lab. Ellery has provided knowledge and expertise in training me to use the electron microprobe and has been very patient and accommodating throughout my time as a research assistant in the lab. He has also given me a great deal of freedom and creativity when I collaborated with other researchers on projects, and also when I put together lab sessions while I was a TA for his electron microprobe theory and practice class. Ellery also suggested that I become a member of several microscopy societies, including the Minnesota microscopy society, which has given me to further insight into the world of EMPA and SEM analysis. I consider myself lucky to have been an RA in the electron microprobe lab over the course of my PhD because I discovered how much I enjoy the analytical aspect of my research from working in the probe lab and working with Ellery. Ellery is to be acknowledged in Chapters II and III of my dissertation for his advice on various EMPA analytical techniques pertaining to these projects.

I am also grateful to have worked with Rick Hervig in the SIMS lab at Arizona State University. Rick was instrumental in the initial setup of the SIMS for our analytical sessions, and helped us in the event that the SIMS misbehaved. Although Rick had a busy schedule of his own, he made sure that our visits to ASU were fruitful. Rick contributed as a co-author in my Chemical Geology publication (Chapter II), and will likely be a co-author when Chapter IV is published. Rick has also been very encouraging as far as my continued SIMS research, and is really the catalyst as far as my involvement

in the SIMS community. After my first trip to ASU, Rick suggested that I present my results at a SIMS conference at the University of Wisconsin, where I met several researchers in the SIMS community and learned about SIMS research outside of my area of expertise. Rick recommended that I apply (and eventually attend) a SIMS workshop at UCLA to further gain knowledge of this instrument, and then he invited me to demonstrate sample preparation techniques at his own SIMS workshop. As nerdy as it may be, I am proud to be a "friend of the ion", as Rick would say.

I thank Munir Humayun at Florida State University for analyzing my experimental run products by LA-ICP-MS, and providing timely feedback and contributions as part of Chapter III of this dissertation. His contributions greatly helped me in understanding critical parts of this project.

I would like to acknowledge Fred Davis, Ben Stanley, and Paola Ardia for their contributions both on an academic level, and on a personal level. You have all been fantastic peers in terms of providing ideas and offering opinions for work in the lab, wiring papers, and preparing for conferences. You have all provided a wonderful atmosphere in which to work in. Fred, it has been great bouncing ideas back and forth related to our own respective research projects because they're so intertwined. Ben, your intensity is like a triple shot of espresso in the lab and it has been exciting watching you become an expert at working with carbonated Martian glasses. Paola, you amaze me in how much you have accomplished in such a short time, with several projects simultaneously. It has also been a lot of fun getting to know all of you outside of the lab,

whether it's on the softball field, at your weddings, or at your parties. I look forward to keeping in touch and finding out what the future holds for you.

I would like to thank Dave Kohlstedt, Larry Edwards and Christy Haynes for being a part of my written and oral preliminary examination committees, despite their busy schedules. I would also like to thank Justin Revenaugh for chairing my final defense committee, and would like to thank David Kohlstedt and Tony Withers for being a part of my final defense committee. The support staff, and in particular, Sharon Kressler, Greg Gambeski, and Tonya Warren are to be commended for helping me with course registration, planning of exams, travel grants, paychecks, and reimbursements.

Erik Hauri and Paul Asimow are to be acknowledged for their helpful reviews pertaining to Chapter II, which has been published in the journal Chemical Geology. I would also like to acknowledge support from various grants that supported my research. The research for Chapter II was supported through NSF grants OCE0623550, EAR0456405, and EAR0757903, and the research for Chapter III was supported by NSF grants OCE0623550 and EAR0757903. Parts of my research were carried out in the Institute of Technology Characterization Facility at the University of Minnesota, which receives partial support from NSF through the NNIN program. SIMS analyses were obtained at the Arizona State University National SIMS facility, which is supported by NSF grant EAR0622775.

I owe a deep amount of gratitude to my family for providing support in a number of ways. To my parents, Steve and Judy, you did your absolute best to raise me, and you put me in a position to succeed. I am so proud that your unconditional love and support

has been an integral part of producing the first doctor in the Tenner family. You deserve special recognition for that. To my other family members: my brother Brandon, my Grandpa Dale and Grandma Jean, My Uncle David and Aunt Bonnie, My Uncle Bill and Aunt Annette, My Uncle Jeff and Aunt Kathy, my cousins Billee-Jo, Bobbie-Jo, Robyn, Ben, Toni, and Ally, and associated husbands, wives, and children, it has been wonderful having a family so tight knit to be able to spend time with, unwind, get advice from, laugh, and love over the course of my PhD. I would also like to acknowledge George, Cheryl, and Daniel Carranco. They have been very much a second family, and their enthusiasm pertaining to my research and my life in general has been refreshing.

Finally I would like to thank Nina Carranco. Nina, your presence throughout my PhD has meant everything to me. You have celebrated with me in my triumphs and you pushed me to keep going when I thought I couldn't continue. You have been unwavering in keeping me grounded throughout this process, balancing out all of my idiosyncrasies. Nina was an influential contributor to my final oral defense, providing critical feedback that allowed me to convey my research in an understandable way to a broad audience. Thank you for sticking by me in my quest to follow my dreams, even though it has changed plans of your own. I am indebted to you for forcing you to live in the bitter cold of the Midwest, and I surely owe you many days of warmth and sunshine! I love you, and I cannot thank you enough for your companionship.

Abstract

This thesis presents experimental constraints on incipient melting of mantle peridotite under hydrated conditions. High *P*-*T* experiments were performed at pressures of 3 to 13 GPa, and at temperatures of 1200-1450ºC. These experiments measure mineral/melt H_2O partitioning and storage capacity of peridotite components, as well as determine melting phase relations and the compositions of partial melts and residues of hydrated peridotite. Incipient melt H_2O concentrations are estimated by peridotite/melt H_2O partitioning ($D_{H_2O}^{peridotite/melt}$). To parameterize $D_{H_2O}^{peridotite/melt}$, mineral/melt H_2O partition coefficients were determined for all crystalline phases of the peridotite solidus assemblage (Chapter 2). Combining these $D_{H_2O}^{mineral/melt}$ values with corresponding modal abundances along the solidus yields a $D_{H_2O}^{peridotite/melt}$ of 0.005-0.010 from 1 to 5 GPa, which is dependent on pressure due to varying garnet and pyroxene modal abundances, and to variable pyroxene Al content. This $D_{H_2O}^{peridotite/melt}$ range predicts that incipient melts of MORB source (50-200 ppm H_2O_{bulk}) and OIB source (300-1000 ppm H_2O_{bulk}) upper mantle contain 0.5-3.8 wt.% and 3-20 wt.% dissolved H_2O, respectively. The amount of dissolved H_2O in incipient melt dictates hydrous solidus depression, ΔT, which ultimately controls the stability of hydrous melts at *P* and *T*. This ΔT-H_2O_{melt} relationship was investigated at 3.5 GPa by partially melting hydrated peridotite from 1200-1450ºC (Chapter 3). Mass balance of phases allows for determination of melt fractions (*F*) from experiments, as well as estimation of H_2O_{melt}. ΔT values are quantified as the difference in melting temperature between dry and wet peridotite at a particular *F*. Parameterization of ΔT as a function of

H_2O_{melt} predicts that solidus melts with 1.5, 5, 10, and 15 wt.% dissolved H_2O generate ΔT values of 50, 150, 250, and 300ºC, respectively. Combination of this paramterization with $D_{H_2O}^{peridotite/melt}$ (Chapter 2) insinuates that 500 ppm H_2O_{bulk} is necessary to stabilize melt across the observed seismic low velocity zone (LVZ) beneath oceanic lithosphere, which is significantly greater than the MORB source upper mantle H_2O_{bulk} of 50-200 ppm. This observation argues against suggestions that hydrous melting is solely responsible for the LVZ. At higher pressures the aforementioned parameterizations are difficult to constrain experimentally, but the onset of hydrous melting can be determined by the peridotite H_2O storage capacity, defined as the maximum H_2O concentration that peridotite can store without stabilizing a hydrous fluid or melt. A new method of determining a minerals H_2O storage capacity is employed, in which a hydrated monomineralic layer is equilibrated with a layer of hydrated peridotite and a small amount of melt (Chapter 4). Experiments were carried out at conditions near the 410 km transition zone (TZ) depth to investigate hydrous melting due to the H_2O storage capacity contrast between the TZ and upper mantle. Measured olivine and orthopyroxene H_2O storage capacities, combined with estimates of garnet H_2O storage capacity, and *P*-dependent lherzolite modes, yields a peridotite H_2O storage capacity of 700-1100 ppm directly above 410 km. This is not consistent with pervasive melting above 410 km, as this range is several times greater than MORB source upper mantle H_2O_{bulk}. However, regional melting in areas such as H_2O-rich OIB source, or areas of recent subduction may likely occur, leaving residues with ~1000 ppm H_2O_{bulk}.

Table of contents

List of Tables

List of Figures

Chapter I

Introduction

The distribution and behavior of H_2O with respect to peridotite has a significant effect on several upper mantle properties, which affect the global interior/exterior cycling of H_2O (Hirschmann, 2006). Measurements of H_2O dissolved in basaltic glasses from mid-ocean ridge (i.e. Michael, 1988; 1995; Jambon & Zimmermann, 1990) and oceanic island settings (i.e. Salters & Stracke 2004; Aubaud *et al.*, 2006), when combined with estimates of their extents of melting, suggest that bulk mantle H_2O concentrations range from 50-1000 ppm. Although these are relatively trace amounts, H_2O can have a significant influence on mantle properties because it behaves as an incompatible fluxing component, with a partitioning behavior similar to that of Ce (Michael, 1988; 1995; Jambon and Zimmermann, 1990). This behavior is perhaps most easily conceptualized in arc settings, where H_2O-rich fluids are released from the subducting slab and initiate fluxed melting at temperatures several hundreds of degrees lower than the dry peridotite solidus (Grove *et al*., 2006). In ridge and plume settings bulk H_2O contents are lower, but hydrous melting is still of critical importance, as the locus of melting is a key control on geochemical characteristics of basalt formation. The addition of H_2O to basalt source regions increases the axial depth of incipient melting, which in turn increases the depth interval in which incompatible-enriched, basalt forming melts are generated (Asimow & Langmuir, 2003). At even greater depths hydrous partial melting at the transition zone may act as a filter that traps incompatible elements, therefore depleting material that advects into the upper mantle (Bercovici & Karato, 2003).

Water also affects major element compositions of mantle melts, as low-pressure, spinel peridotite hydrous melts are SiO_2-rich (Kushiro, 1975; Hirose & Kawamoto, 1995; Gaetani & Grove, 1998) and may be the source of high-Mg andesites in shallow subduction zone settings (Kushiro *et al*., 1972, Hirose, 1997). In contrast, hydrous garnet peridotite melts are alkalic and nepheline normative (Green, 1973a; Kawamoto & Holloway, 1997). These contrasting results suggest that perhaps cation-OH^- association in peridotite melt varies as a function of pressure.

In terms of seismology several low velocity regions, ranging from the lithosphere/asthenosphere boundary (Yang *et al*., 2007; Kawakatsu *et al*., 2009) to the transition zone (Revenaugh & Sipkin, 1994; Courtier & Revenaugh, 2007), have been attributed to the presence of partial melt. If these studies are indeed detecting melt, it is most likely volatile fluxed melt, as the mantle adiabat in these regions is cooler than the dry peridotite solidus. Water is often attributed as the fluxing agent, but quantitative measurements of the effect of H_2O on partial melt stabilization at P and T are necessary to fully determine if hydrous melting is responsible for these seismic observations.

Although H_2O is a highly incompatible mantle component and affects the aforementioned melt characteristics, it plays an important role in the solid mantle as well. The incorporation of hydrogen into nominally anhydrous minerals strongly affects the mantles rheological properties (Mackwell et al. 1985; 1996; Mei & Kohlstedt, 2000a; 2000b), which means that the distribution of water in the upper mantle governs the convective behavior of the mantle. Water also enhances the electrical conductivity of mantle components (Karato, 1990; Dai & Karato, 2009), and information from

experimentally determined electrical conductivities can be compared to geophysically observed electrical conductivities to infer the bulk mantle H_2O content.

A key variable in determining the effect of H_2O on all of the aforementioned properties is the onset of hydrous mantle melting at *P* and *T*. Quantifying incipient melting is extremely valuable because it is intimately related to 3 things: 1) peridotite/melt H_2O partitioning; 2) the relationship between hydrous freezing point depression and the amount of dissolved H_2O in the melt; and 3) the peridotite H_2O storage capacity. A schematic diagram of incipient melting of peridotite is shown in Figure 1.1, which illustrates the inter-relationships of peridotite H_2O partitioning, freezing point depression, and H_2O storage capacity.

This thesis presents experimental investigations of the effect of water on incipient melting in the upper mantle. High pressure and temperature experiments were conducted in a multi-anvil apparatus at the Experimental Petrology Laboratory at the University of Minnesota. Experimental conditions ranged from 3-13 GPa, and 1200-1450ºC with starting materials that consist of a hydrated natural MORB (Chapter 2) or a hydrated fertile peridotite analog (Chapters 3 & 4). Examination of experimental run products involved electron microprobe analysis (EMPA) to determine phase compositions in all studies. EMPA was especially important in Chapter 3 for determining phase relations and estimating dissolved H_2O concentrations in heterogeneous quenched melts. Low-H background secondary ion mass spectrometry (SIMS) was employed to measure the H_2O concentrations in mineral phases (Chapters 2 & 4) and hydrous glasses (Chapter 2). Fourier transform infrared spectroscopy (FTIR) was also employed to measure water

contents (Chapters 2 & 3) and CO_2 contents (Chapter 3) in hydrous glass, as well as H_2O contents in some minerals (Chapter 2).

The following paragraphs outline the chapters of this thesis. Chapter 1 deals with experimentally determining peridotite/melt H_2O partitioning. Chapter 2 investigates the effect of hydrous peridotite solidus depression as a function of dissolved H_2O in the melt, and Chapter 3 focuses on quantifying peridotite H_2O storage capacity.

In Chapter 2 experimental determinations of mineral/melt H_2O partitioning ($D_{H_2O}^{mineral/melt}$) of olivine, orthopyroxene, and clinopyroxene are presented. These parameters are combined with corresponding modal abundances of mineral phases along the peridotite solidus, which allows for calculation of $D_{H_2O}^{peridotite/melt}$. It is estimated that $D_{H_2O}^{peridotite/melt}$ ranges from 0.005-0.010 from 1 to 5 GPa and varies as a function of pyroxene and garnet modal abundance, as well as Al_2O_3 concentration in pyroxenes. Incipient melt concentrations of MORB source and OIB source mantle are then calculated. This chapter has been published in the journal *Chemical Geology* (vol. 262, pages 42-56).

Chapter 3 focuses on hydrous peridotite partial melting at 3.5 GPa. The addition of H_2O to garnet peridotite produces melts that are alkalic and nepheline normative, and residual garnet is stabilized at greater extents of melting in the presence of H_2O. Over a range of observed melt fractions, hydrous peridotite melting occurs at significantly lower temperatures when compared to dry peridotite melting. This freezing point depression (denoted as ΔT) is directly related to the dissolved H_2O in the melt through mass balance (Fig 1.1) and is parameterized in order quantify peridotite hydrous solidus depression.

This chapter has been submitted to the journal *Journal of Petrology*. Combination of this parameterization with incipient upper mantle H_2O_{melt} concentrations based on $D_{H_2O}^{peridotite/melt}$ (Chapter 2) allows for determination of conditions necessary to stabilize hydrous melt along various mantle geotherms. In a co-authored publication, Hirschmann *et al.* (2009) used these models and calculated that a mantle concentration of 500 ppm H_2O_{bulk} is required to stabilize melt across the observed seismic low velocity zone (LVZ) beneath 50 Ma oceanic lithosphere. This value suggests that hydrous peridotite melting cannot be the sole cause of the LVZ (Mierdel *et al.*, 2007), as MORB source H_2O_{bulk} concentrations (50-200 ppm) are too low.

Finally, Chapter 4 investigates peridotite H_2O storage capacity above the 410 km transition zone. A new experimental method is employed, in which a monomineralic layer of hydrated olivine is equilibrated with a layer of hydrated peridotite and a small amount of melt. This places the olivine at realistic H_2O storage capacity conditions, as hydrous melt stability and H_2O activity are accurately constrained by the presence of multiply saturated peridotite. Peridotite H_2O storage capacity is determined from measured olivine and pyroxene H_2O storage capacities, estimates of high pressure garnet H_2O storage capacity, and corresponding modal abundances along a high pressure ridge adiabat. Based on the peridotite H_2O storage capacity directly above the transition zone, it is argued that it is unlikely that a global layer of hydrous melt exists atop this region. However, fluxed melting may occur locally above the transition zone, both from advecting OIB source mantle and from recent subduction zone related hydrous melting.

If hydrous melting occurs at 410 km, it will leave residues at their H_2O storage capacity. This chapter will be submitted to the journal *Contributions to Mineralogy and Petrology*.

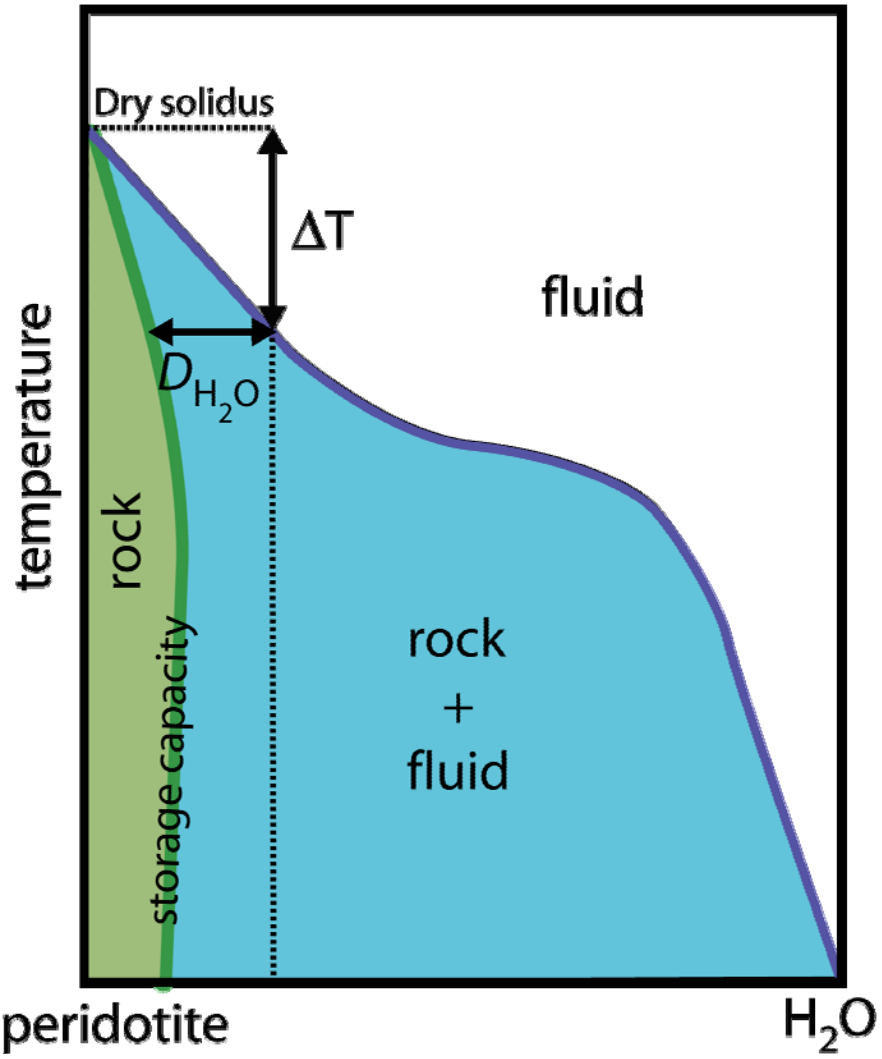

Figure 1.1. Schematic high pressure peridotite *T-X* diagram. Peridotite H_2O storage capacity is represented as the thick green line, and must trend to "0" at the dry peridotite solidus. In this diagram peridotite/melt H_2O partitioning (D_{H2O}) is represented as the ratio of the peridotite water storage capacity and incipient melt dissolved H_2O. Hydrous peridotite solidus depression is denoted as ΔT, and is directly related to the amount of

H_2O dissolved in the incipient melt. Peridotite/melt H_2O partitioning is investigated in Chapter 2. The relationship between hydrous peridotite solidus depression and dissolved H_2O in the melt is investigated in Chapter 3. The H_2O storage capacity of peridotite is investigated in Chapter 4.

Chapter II

Hydrogen partitioning between nominally anhydrous upper mantle minerals and melt between 3 and 5 GPa and applications to hydrous peridotite partial melting.

To extend our knowledge of partitioning of hydrogen between nominally anhydrous mantle minerals and basaltic melts to higher pressures, we conducted 8 experiments at 3-5 GPa and 1350–1440˚C on a modified mid-ocean ridge basalt (MORB) + 2 wt.% H_2O. H contents in olivine, orthopyroxene, clinopyroxene, and garnet were measured by counting $^{16}O^{1}H$ ions with low-blank SIMS, and total H_2O concentrations in coexisting glasses were measured by FTIR, SIMS, and electron microprobe. The glasses have water contents ranging from 4.1 to 8.9 wt. %. Eleven measured pyroxenes have H_2O concentrations ranging from 430 to 1430 ppm, two garnets have concentrations of 73 and 260 ppm, and one olivine has a concentration of 29 ppm. Mineral/melt hydrogen partition coefficients are as follows: $D_H^{cpx/melt}$ ranges from 0.014–0.021, $D_H^{opx/melt}$ ranges from 0.009–0.019, $D_H^{gt/melt}$ ranges from 0.001–0.0033, and $D_H^{ol/melt}$ has a value of 0.0006. Mineral/mineral hydrogen partitioning data are as follows: $D_H^{cpx/opx}$ ranges from 1.2–2, $D_H^{cpx/gt}$ has values of 5.5 and 14, and a single $D_H^{cpx/ol}$ has a value of 27. $D_H^{pyx/melt}$ correlates with the concentration of Al_2O_3 in pyroxene and with the concentration of Al on tetrahedral sites. Combining the mineral/melt hydrogen partitioning data from this study,

and estimates of mineral modes and compositions along the solidus, we estimate that $D_H^{perid/melt}$ increases from 0.006 at 1 GPa up to 0.01 near the garnet lherzolite/spinel lherzolite transition, owing to the maximum in Al_2O_3 concentration in pyroxenes. With increasing pressure $D_H^{perid/melt}$ for garnet lherzolite diminishes to 0.005 at 5 GPa, as pyroxenes become less aluminous and less abundant. As a result, incipient hydrous melts beneath oceanic ridges with bulk mantle H_2O contents of 50–200 ppm will have solidus partial melts with H_2O contents between 0.5 and 3.8 wt.%, while oceanic island mantle with 300–1000 ppm will have solidus partial melts with H_2O content between 3 and 20 wt.%.

Keywords: Hydrogen partitioning, experimental petrology, mantle melting

INTRODUCTION

It is well known that hydrous components can have a significant effect on key properties of the mantle. Compared to dry peridotite, mantle with modest amounts of H_2O has weaker rheology (Chopra & Paterson, 1984; Hirth & Kohlstedt, 1996; Wang *et al.*, 2004), enhanced electrical conductivity (Karato, 1990; Xu *et al.*, 1998; Huang *et al.*, 2005; Yoshino *et al.*, 2008), distinct seismological characteristics (Karato & Jung, 1998), and will initiate partial melting at lower temperatures (Green, 1973; Wyllie, 1979; Hirth & Kohlstedt, 1996). The partitioning of hydrogen between crystalline phases and melt has an important influence on all of these properties. This partitioning controls the concentration of H_2O in near-solidus melts, and thereby dictates the extent of hydrous

solidus depression (Hirschmann, 2006). Similarly, the partition coefficient controls the proportion of H_2O that is left in the residue, which in turn influences the relationship between partial melting and the physical properties of the mantle (Hirth & Kohlstedt, 1996).

The advent of low-blank secondary ion mass spectrometry (SIMS) analyses of H in nominally anhydrous minerals (Koga *et al.*, 2003) has facilitated direct determinations of mineral/melt hydrogen partitioning from coexisting mantle minerals and hydrous silicate melts (Koga *et al.*, 2003; Hauri *et al.*, 2006; Aubaud *et al.*, 2004, 2008). Combination of these data with typical modes for mantle lherzolite allows estimates of bulk mantle/melt partition coefficients for H, and these range from 0.007-0.009 (Aubaud *et al.*, 2004; Hauri *et al.*, 2006). However, mineral/melt hydrogen partition coefficients from these studies were determined chiefly at pressures of 3 GPa or lower. In theory, mantle/melt partitioning should vary with parameters such as pressure and water fugacity (Hirth & Kohlstedt, 1996; Asimow *et al.*, 2004). Additionally, major element compositions of minerals, and in particular, the Al_2O_3 contents of pyroxenes (Rauch & Keppler, 2002; Stalder & Skogby, 2002) likely influence the energetics of hydrogen storage in minerals and therefore mineral/melt partition coefficients (Aubaud *et al.*, 2004; Hauri *et al.*, 2006). Consequently, a full description of mineral/melt hydrogen partitioning near the peridotite solidus requires a fuller exploration of the influence of these parameters. The goal of this study is to investigate mineral/melt hydrogen partitioning at pressures beyond 3 GPa.

METHODS

Starting Materials and experimental procedures

Ideally, experimental studies of mineral/melt hydrogen partitioning applicable to peridotite would produce hydrous melt, pyroxenes, and garnet in equilibrium with olivine at high temperature and pressure, as the compositions of such phases are more likely to be directly relevant to mineral/melt partitioning during partial melting of typical mantle rocks. High pressure liquids in equilibrium with olivine are MgO-rich, and at the pressures of interest for this study (>3 GPa), such hydrous, low viscosity liquids do not readily quench to an analyzable glass, making partitioning studies difficult. Therefore, our starting materials are basalt-like in composition, as glasses produced from hydrous MORB crystallization experiments have previously been quenched to a glass from pressures as high as 3 GPa, even when containing up to ~12 wt.% H_2O (Aubaud *et al.*, 2008).

The initial starting material for this study consists of the same V25-RD1-T1C basalt employed previously by Aubaud *et al.* (2004, 2008). Water was added to the starting material with an oxide/hydroxide mixture having the composition of olivine ($Fo_{89.7}$) + 10 wt. % H_2O, which was synthesized using fully dried, reagent grade MgO and SiO_2 combined with $Mg(OH)_2$ and FeO powders. The mixture was hand-ground under acetone in an agate mortar and pestle for 2 hours. The resulting bulk composition contains 2 wt.% H_2O (Table 2.1).

A second batch of starting material was synthesized using the previously mentioned natural basalt and hydrous synthetic olivine, as well as Bamble orthopyroxene, synthetic wollastonite, and FeO powder (Table 2.1). This mixture is similar in

composition to the initial batch, but has a lower Al_2O_3 content, which allowed us to explore the effect of aluminum on pyroxene/melt hydrogen partitioning.

The starting material was packed into cleaned and annealed $Au_{75}Pd_{25}$ capsules (1.6 mm diameter, 0.2 mm thickness) using a drill blank and steel dye set, hand-squeezed in a vice. The ends of the capsule were shaped into cones with a bench top lathe, and were sealed by placing the capsules in a water-cooled vice and spot welding the tips of the cones with a graphite welder. This method has the advantage of limiting water loss by heating during welding. The final height of each capsule was ~2 mm.

Experiments were conducted in a 1000 ton Walker-type multi-anvil press, using cast $MgO–Al_2O_3–SiO_2–Cr_2O_3$ octahedra and integrated gasket fins. The WC anvils used in the multi-anvil assembly have 12 mm truncations, and straight-walled graphite furnaces were used for all experiments. Temperature was controlled using type D ($W_{97}Re_3/W_{75}$-Re_{25}) thermocouple, which was located directly above the capsule. The P–T uncertainties of experiments are believed to be ± 0.3 GPa and ± 15˚C, respectively, using the calibration described in Dasgupta *et al.* (2004). The pressures of the experiments range from 3 to 5 GPa, and temperatures range from 1350–1440˚C. To facilitate growth of crystals large enough to analyze by SIMS the experiments were initially held above the liquidus for a period of two hours, taking care not to exceed the melting point of the $Au_{75}Pd_{25}$ capsules, then slowly cooled (with a ramp rate of 0.3 or 0.1 degrees/minute) to the final run temperature, and held for a period of 24 hours. Individual run conditions for all experiments are given in Table 2.2.

Sample preparation

Each capsule was extracted from the quenched assembly and sectioned using a 50 μm diameter tungsten wire saw. Diamond lapping films (30 to 0.1 μm) were used to polish the exposed surfaces of the capsules, which were held in place on brass bullet mounts by Crystalbond™ 509 (Aremco Products). No epoxy impregnation was done to any of the samples, as this would interfere with the vacuum and hydrogen blank during SIMS analyses.

Additionally, the second halves of capsules were doubly polished for analysis of hydrous species in the glass by Fourier transform infrared spectroscopy (FTIR). Once both sides were polished, the samples were cleaned in multiple baths of acetone and ethyl alcohol to remove Crystalbond and other contaminants that could potentially contribute absorption in the infrared region. The thickness of each analyzed region was determined using a high-precision mechanical stage microscope, which is accurate to ± 2 μm.

Electron Microprobe Analysis

Major element contents of all minerals and glasses were analyzed by wavelength-dispersive spectroscopy using a JEOL JXA8900R electron microprobe (EMP). All analyses were performed by using a 15 kV accelerating voltage, with counting times of 10 seconds for the peak and 5 seconds for the background for all elements. Standards consisted of natural olivine, enstatite, diopside, omphacite, hornblende, pyrope, quartz, two basaltic glasses, chromite, Mn-hortonolite, and potassium-feldspar, used in various, but consistent, configurations to quantify the oxide contents in olivine, pyroxene, garnet, and glass (melt). Crystalline phases were analyzed with a 20 nA beam current and a fully focused (1–2 μm) beam. Hydrous glasses were analyzed with a 10 nA beam current and

a 30 μm spot size to limit beam damage and volatile loss from the glasses during analyses. The Na count rate was monitored on the glass at these conditions and no appreciable decrease in count rate was noticeable after the first 30 seconds of counting time. Regardless, Na and K were always counted first on their respective spectrometers to reduce the effect of any volatile loss.

To help characterization of the concentrations of hydrous components, the glasses were analyzed for oxygen following the methodology of Agee (2008). All elements were analyzed as metals, and oxygen was assigned to the other elements in the bulk composition, with the assumption that any excess oxygen is associated with hydrogen. To detect oxygen in standards and unknowns, we used a synthetic LDE1-6, multi-layered (W-Si), wavelength dispersive crystal, with a 2-d lattice spacing of 6.0 nm. Oxygen count rates were determined by integrating the area under the peak via wavelength scans to account for differences in peak shapes between the standard and the run products. The total integrated counting time for oxygen was 44 seconds, and was calibrated against an enstatite standard (McGuire *et al.*, 1992). H_2O contents derived by this method were incorporated into the ZAF data reduction algorithm to account for the matrix effects of the H and associated O on calculated major element concentrations.

Fourier transform infrared spectroscopy (FTIR)

The combined hydroxyl and molecular water contents in the glasses were quantified by unpolarized FTIR, using a Nicolet Series II Magna–IR spectrometer equipped with a Nic-Plan microscope, globar source, KBr beamsplitter, and a liquid nitrogen-cooled MCT-A detector. Concentrations were determined by following the technique of Ohlhorst *et al.*

(2001) for background subtractions and calibrations on the 4500 cm^{-1} (hydroxyl) and 5200 cm^{-1} (molecular water) combination bands of the FTIR spectra. Baselines extend from 4280 to 4680 cm^{-1} for the 4500 cm^{-1} combination band**,** and 4680 to 5400 cm^{-1} for the 5200 cm^{-1} combination band. Using the heights of the combination bands the concentration can be calculated using the Beer–Lambert law for both molecular water and hydroxyl:

$$c_{H_2O} = \frac{1802 * A_{H_2O}}{d\rho} * \frac{1}{\varepsilon_{H_2O}}, \quad (1)$$

$$c_{H_2O} = \frac{1802 * A_{OH}}{d\rho} * \frac{1}{\varepsilon_{OH}} \quad (2)$$

Where c_{H_2O} represents the respective molecular water and hydroxyl concentrations (expressed as wt.% H_2O) , A is the absorbance of the combination band (cm^{-1}), d is the sample thickness (cm), ρ is the density (g/l), and ε is the molar absorption coefficient (0.56 ± 0.05 l • mol^{-1} • cm^{-2} for both ε_{OH} and ε_{H_2O}, respectively). We initially assumed a density of 2819 g/l for equations (1) and (2) and iteratively solved the density using the relation for hydrous basalt from Ohlhorst *et al.* (2001):

$$\rho = (-20.8 \pm 6.6)c_{water} + (2819 \pm 13.5). \quad (3)$$

The combined concentrations from equations (1) and (2) represent the total H_2O content in the glasses.

Secondary Ion Mass Spectrometry (SIMS)

Mineral and glass standards from the SIMS calibration study of Aubaud *et al.* (2007) were carefully removed from their indium mounts, re-polished to a 1 μm surface, and

cleaned in 3 sequential acetone baths and 3 ethyl alcohol baths. Additionally, the halves of the experimental capsules characterized by EMP analysis were re-polished to a 1 μm surface to remove the carbon coat, and cleaned with the same sequence of acetone and ethyl alcohol. The standards and experimental run products were then pressed into indium mounts (Fig. 2.1), and the completed mounts were cleaned in successive baths of acetone and ethyl alcohol. We did not attempt to polish the surface of the completed mounts (as was done in Aubaud *et al.* (2007)), and this did not appear to affect the quality of SIMS measurements. Samples were sputter-coated with Au prior to SIMS measurements.

SIMS measurements were carried out on the Cameca 6f instrument at Arizona State University. Prior to analyses, the SIMS was baked out for 24 hours to minimize H_2O in the vacuum (total pressure was $\sim 5\times10^{-10}$ torr during the session). Using a Cs^+ primary ion source with a beam current of 5–10 nA and an impact energy of 19 KeV, the ion source was tuned in critical illumination mode to produce a uniform beam diameter of ~35 μm (vs. aperture or Köhler illumination, e.g., Clement & Compston, 1990). The primary ion beam was tuned with electromagnet steering plates to achieve co-linearity in x and y, which was critical in achieving well-resolved data (see section labeled Ion beam alignment, below). Prior to each analysis, the beam was rastered over a 40×40 μm area to sputter away the gold coating and any surface adsorbed contaminants. A potential of -9000V was applied to the sample, resulting in the acceleration of negative secondary ions produced by the primary ion impacts away from the sputtering site. A 100 μm diameter field aperture was placed in the pathway of the secondary beam to allow only those ions

sputtered from a ~10 μm diameter circular area in the center of the crater into the mass spectrometer. Secondary ions with excess kinetic energies of 0 ± 125 eV (energy bandpass centered and wide open) were allowed into the mass spectrometer, detected with an electron multiplier, and corrected for background and counting system deadtime.

Sample charging was controlled using the Cameca normal-incidence electron gun (Slodzian *et al.*, 1986). The filament voltage was matched to the sample potential so that electrons would only reach the sample if the crater charged up positively (via positive ion impact and negative secondary ion departure). The electron gun was tuned to maximize the signal for $^{18}O^-$. As a consequence of changing the secondary magnet (to detect other species), which influences the steering of the low-energy electron gun, it was not possible to obtain maximum secondary ion count rates for all species. However, this has little effect on $^{16}O^1H^-$ and $^{19}F^-$ and only decreases the $^{12}C^-$ and $^{30}Si^-$ intensity by ~10%. Regardless of this effect, we observed that the secondary ion ratios were reproducible throughout analysis sessions. Each analysis consisted of counting negative ion intensities for ^{12}C, $^{16}O^1H$, ^{18}O, ^{19}F, ^{30}Si, ^{32}S, and ^{35}Cl, with counting times of 10, 5, 5, 5, 2, 5, and 5 seconds, respectively. This cycle was repeated 6 times in each analysis. The intensities of the ^{12}C, ^{19}F, ^{32}S, and ^{35}Cl were not quantified; rather, they were monitored to detect overlap of the analyzed area on any foreign and possibly hydrous material in pits and/or cracks around the phases of interest.

Ion beam alignment

Commonly, a SIMS mount will not be oriented uniformly with the ion beam, either due to slight topography across the mount, or owing to a slight tilt in the sample holder itself.

This, in concert with the strong (~2V/μm) extraction field above the sample, will cause the primary ion beam to "wander" as the 1" diameter mount is moved to analyze different samples, even if the voltage on the steering plates is constant. As a result, the voltage on the primary beam steering plates must be adjusted when the sample is moved a few hundred microns or more so that the primary beam strikes the sample in the same place (relative to the secondary ion optic axis). If the secondary ions originate from the same point (again relative to the secondary optic axis), a high level of consistency can be achieved during analyses (Fig. 2.2). We define the secondary ion optic axis as the point where the secondary ion image pinches out as the field on the secondary magnet is increased and decreased. This point is visualized using the ion imaging system common to Cameca nf and 1270/1280 series instruments (Fig. 2.3). An ideal way to align the SIMS is to steer the primary beam directly onto the ion optical axis using the primary beam deflectors and center the secondary ion field aperture on that same crossover.

Locating and analyzing small (~40 μm) areas of interest

The Cameca 6f SIMS is equipped with an oblique reflected light optical microscope to aid in locating points of interest for analysis. In samples with multiple phases it may be difficult to impossible to find individual points of interest to analyze, especially if phases are 100 μm or less in size. One way to find small, individual phases for analysis is to combine backscattered images from an EMP/SEM with a reflected light image of the same area. In this case the JEOL JXA8900R electron microprobe at the University of Minnesota was used to collect backscattered images as well as reflected light images of various points of interest amongst samples. With a magnification of 650x, a

backscattered image was produced with a field of view approximately 160×160 μm (Fig. 2.4a). This corresponds to the field of view of the optical microscope on this particular electron microprobe (Fig. 2.4b). Features that are distinguishable on BSE and/or optical images from the microprobe, such as inclusions, pits, or grain interphase boundaries can also be found on the optical microscope on the SIMS, thus allowing for navigation and locating small areas of interest for analysis. The use of polishing materials that produce topography between phases also aids in navigation and location of small, analyzable features.

The analytical protocol described above removes the gold coat (and surface contaminants) from an area larger than that from which ions are accepted (resulting in low backgrounds from vacuum contaminants). However, this also results in variable results when attempts are made to analyze adjacent areas (now without a surrounding conducting Au-coat). As a result, it is difficult to obtain more than one analysis on phases smaller than ~80 μm in diameter (without removing the sample from the vacuum system and re-coating with gold). An approach we have found very useful to minimizing the removal of the gold coat is to align the primary beam impact site on the secondary ion optic axis using the nearest pool of indium mounting material. We can obtain an ion image of $^{19}F^-$ (no $^{18}O^-$ has been detected) in the indium, align the primary beam and mark the location of the impact site, and then proceed to the area of interest, confident that further correction of primary ion steering in the area will be minor at most.

RESULTS

Phase Compositions

Major element compositions of all experimental crystalline phases and glasses determined by electron microprobe analysis are reported in Tables 2.3 and 2.4. In an attempt to determine the phase proportions and to characterize Fe loss from the starting material over the course of the experiment, we performed mass balance calculations using the phase compositions. As apparent from the low Fe contents of all phases (Tables 2.3 and 2.4), mass balance calculations estimate significant Fe loss for each experiment (Table 2.2), ranging from 40% to 90% relative. Errors in all mass balance calculations are significant, with sums of squares ranging from 0.3 to 224. This is likely owing to weighing errors in the starting mixture, and/or inaccuracies in microprobe analyses of the hydrous glasses. Consequently, we do not report the modes of phases present in the run products of this study.

SIMS calibration

Using the measured H_2O and SiO_2 contents from Aubaud *et al.* (2007), and count rates of $^{16}O^{1}H$ and ^{30}Si from our SIMS analyses (Table 2.5), we establish linear calibration curves for basaltic and rhyolitic glasses, orthopyroxene, clinopyroxene, garnet, and olivine (Fig. 2.5). For olivine the calibration has a large uncertainty, owing to variations in measured water contents in olivine standard AC94 (see Table 2.5). The other calibration lines are well resolved, with r^2 values ranging from 0.96 to 0.99. Although each phase produces a calibration curve with a unique slope, compositional differences among standards of the same phase do not have a measurable effect on the calibration. For example, basaltic and rhyolitic glasses produce nearly identical calibration curves. Similarly, the slopes of the orthopyroxene and clinopyroxene calibrations are nearly indistinguishable. Also, garnets

with diverse Ca/Mg/Fe ratios (Aubaud *et al.*, 2007; Bell *et al.*, 1995, 2004) plot along the same trend**.**

Hydrogen background during SIMS measurements

Using $^{16}O^{1}H$ intensities from the dry olivine (Fo_{100}) blank from our SIMS session and the calibration curve for olivine, we can estimate the background hydrogen concentration during analyses. Over the course of the SIMS measurements on the mineral standards mount (Fig. 2.1a) the average of 10 dry blank measurements equates to a background of 10 ppm (Table 2.6). In performing a sample change to the mount which contained the hydrous glass standards and experimental run products (Fig. 2.1b) the $^{16}O^{1}H$ background steadily decreased from an estimated 66 ppm down to 30 ppm over the course of analyzing all phases from the experimental run products, which took place over a ~24 hour period.

H contents of minerals by SIMS

The analyzed mineral grains in the experiments range from 50 to 500 microns in diameter, and nearly all of them are crack-free. The lack of significant cracks is owing to the gradual and uniform decompression of the multi-anvil apparatus, as compared to the more rapid, uniaxial decompression of piston cylinder experiments. Also, all of the phases are homogenous within the resolution of microprobe WDS and backscatter detection, with the exception of the analyzed orthopyroxene in experiment M374 (Fig. 2.6a), which has a rim with a slight aluminum enrichment. For this experiment, SEM/BSE imaging of the charge following SIMS analyses shows that the SIMS pits are located in the Al-poor cores of the two analyzed orthopyroxene grains (Fig. 2.6b)**.**

The results of the SIMS analyses of all phases are reported in Table 2.7. To filter out analyses suffering from surface contamination, we used the clinopyroxene grains in experiments M355 and M374 as a benchmark, because SIMS analyses showed ^{12}C, ^{32}S, and ^{35}Cl intensities comparable to those measured on the mineral standards, which are nominally C-, S-, and Cl- free. For M355 and M374 clinopyroxene measurements the absolute standard deviation among their respective calculated H_2O concentrations (in wt. %) is 0.007, which we assigned to be the maximum standard deviation for the other data sets. Any measurements which caused the standard deviation among calculated concentrations to exceed 0.007 were deemed contaminated, and are not used in any quantifications of this study. Correspondingly, the contaminated data produce ^{12}C, ^{32}S, and ^{35}Cl count rates that are 1 to 3 orders of magnitude greater than those of the standard ^{12}C, ^{32}S, and ^{35}Cl count rates. Clinopyroxene H_2O concentrations range from 800 to 1530 ppm (n=17), orthopyroxenes yield concentrations ranging from 430 to 1030 ppm (n=8), garnets yield concentrations ranging from 69 to 277 ppm (n=4), and 4 measurements on a single olivine run product each yielded a blank-corrected concentration of 29 ppm.

H_2O contents in glasses from FTIR, EMP, and SIMS analyses

Five of the 8 experiments had areas of glass that were large enough to analyze by FTIR, and their spectra are shown in Fig. 2.7. Total H_2O contents in the glasses range from 4.83 to 7.25 wt. % (Table 2.8), and the ratio of H-bearing species (as OH/H_2O) in these glasses shows a positive correlation with total H_2O content, similar to the basaltic glasses studied by Ohlhorst *et al.* (2001) (Fig. 2.8).

We also analyzed all of the glasses by electron microprobe. Despite our best efforts the totals for metals plus oxygen were poor, ranging between 96 and 98%, even though matching chemistry and good totals could be achieved on 2 basaltic glass standards and on a suite of 7 rhyolites with 0.1 to 6 wt. % H_2O. These low totals are not owing to unanalyzed elements, as full WDS scans (including the light element crystal) failed to reveal any foreign elements present in the experimental glasses and FTIR analyses indicated insignificant CO_2 and carbonate concentrations. Further, the use of different standards, different element spectrometer placements, high order peak overlap filtering in the vicinity of the oxygen peak, and varying the carbon coat thickness did not improve the totals. However, the analyses do allow estimation of the H_2O concentration in the glasses by calculating the difference between the analyzed oxygen and that oxygen required for charge neutrality with the analyzed metals. The excess oxygen is then assigned to H_2O and these range from 5.44 to 9.41 wt. % (Table 2.4).

The H_2O contents derived from FTIR correlate linearly with those estimated by EMP, although the slope is not unity (Fig. 2.9). We can use this correlation to estimate "FTIR equivalent" H_2O contents of 4.14, 4.57, and 6.11 wt. % for the glasses in experiments M373, M374, and M333, respectively.

SIMS measurements also quantified H_2O concentrations in all 8 glasses, and these range from 6.09 to 8.85 wt. % (Table 2.7). Although these are broadly similar to the concentrations derived by EMP analyses, the correlation between SIMS and EMP, as well as the correlation between SIMS and FTIR are poor (Fig. 2.9). We do not fully understand the discrepancy between FTIR and SIMS-derived H_2O contents, as both

methods were carefully calibrated. Fortunately, the discrepancies do not result in very large uncertainties in mineral/melt partition coefficients and consequently, we will consider H_2O concentrations derived from both SIMS and FTIR in the following sections.

Hydrogen partition coefficients between minerals and melt

By combining the average of the H_2O contents of mineral phases from each experiment and the corresponding H_2O contents of the glasses, 14 mineral/melt and 7 mineral/mineral hydrogen partition coefficients can be determined from 3 to 5 GPa (Table 2.9). Observed values of $D_H^{cpx/melt}$, $D_H^{opx/melt}$, $D_H^{gt/melt}$, and $D_H^{ol/melt}$ range from 0.012–0.024 (n=7), 0.007–0.021, (n=4), 0.0008–0.0036 (n=2), and 0.0004–0.0007 (n=1), respectively. Observed mineral/mineral coefficients include values for $D_H^{cpx/opx}$, $D_H^{cpx/gt}$, and $D_H^{cpx/ol}$, which range from 1.2–2 (n=4), 5.5 to 14 (n=2), and 27 (n=1), respectively.

DISCUSSION

Comparison to previous results: $D_H^{gt/melt}$, and $D_H^{ol/melt}$

The values of $D_H^{gt/melt}$ are similar in magnitude to those determined previously by Hauri *et al.* (2006) and Aubaud *et al.* (2008). Aubaud *et al.* (2008) noted a linear correlation between $D_H^{gt/melt}$ and TiO_2 concentration for garnets grown from basaltic melts, but found that $D_H^{gt/melt}$ for garnet/melt pairs coexisting with peridotitic assemblages plotted above that trend. The smaller $D_H^{gt/melt}$ determined in this study agrees with the TiO_2 correlation identified by Aubaud *et al.* (2008), but the larger one is more similar to the peridotite-applicable values of $D_H^{gt/melt}$.

The lone $D_H^{ol/melt}$ determined in this study is a factor of 2-4 lower than previous determinations from lower pressure experiments (Aubaud *et al.* 2004; Hauri *et al.* 2006). This may indicate that $D_H^{ol/melt}$ diminishes with pressure. On the other hand, *increases* with pressure have been predicted from thermodynamic analysis (Asimow *et al.* 2004), and data from 0.5-2 GPa (Aubaud *et al.* 2004; Hauri *et al.* 2006) do not reveal any pressure dependence. Therefore, better standards and more data are needed before a pressure dependence for $D_H^{ol/melt}$ can be established, particularly because our olivine calibration is not well-constrained, and because our single olivine analysis is near the limit of detection and therefore likely has high uncertainty.

The effect of Al on $D_H^{pyx/melt}$ and H incorporation mechanisms in pyroxene.

Previous studies have shown that $D_H^{pyx/melt}$ correlates with the Al_2O_3 content of pyroxenes, C_{Al2O3}^{pyx}, (Aubaud *et al.*, 2004, 2008; Hauri *et al.*, 2006; Grant *et al.*, 2007) and more specifically with the concentration of Al in tetrahedral sites (Al_{pyx}^{IV}). As shown in Figure 2.10, the partition coefficients determined in this study are consistent with these previously identified correlations, though the new values for cpx and two of the opx plot slightly above the correlation between $D_H^{pyx/melt}$ and Al_{pyx}^{IV}. This could potentially suggest that there is a modest pressure dependence to the relationship between $D_H^{pyx/melt}$ and Al_{pyx}^{IV} or that alternative aluminous substitutions involving octahedral Al aid stabilization of hydrogen in pyroxene at high pressures. However, the deviation from the trend of the lower pressure data is modest and could simply reflect analytical uncertainties. Empirically the correlations can be represented by simple linear regressions:

$$D_{\mathrm{H}}^{\mathrm{pyx}} = 0.0015 C_{\mathrm{Al2O3}}^{\mathrm{pyx}} + 0.0082;\ r^2 = 0.39 \quad (4)$$

and

$$D_{\mathrm{H}}^{\mathrm{pyx}} = 0.0983 Al_{\mathrm{pyx}}^{\mathrm{IV}} + 0.0062;\ r^2 = 0.61 \quad (5)$$

The scatter in the data from both trends could well be owing to analytical uncertainties, and neither regression is unambiguously statistically superior. In our view, empirical estimation of $D_{\mathrm{H}}^{\mathrm{pyx/melt}}$ at magmatic conditions up to 5 GPa is at present equally valid from either $C_{\mathrm{Al2O3}}^{\mathrm{pyx}}$ or $\mathrm{Al}_{\mathrm{pyx}}^{\mathrm{IV}}$.

Looking a little further into the mechanism of H substitution in aluminous pyroxene, the charge-coupled substitution with $\mathrm{Al}_{\mathrm{pyx}}^{\mathrm{IV}}$ can be illustrated by reactions written in several different fashions. For instance, the equilibrium between the Tschermaks-type Al substitution in pyroxene and a defect associate in which H is charge balanced by tetrahedral Al may be represented by:

$$\mathrm{MgAl^{VI}Al^{IV}SiO_6 + H_2O + 2Mg_2SiO_4 => 2Mg_2Al^{IV}HSiO_6 + MgSiO_3} \quad (6)$$

(Kohn *et al.*, 2005). Alternatively, the same equilibrium between aluminous defect complexes can be represented using the notation of Kröger & Vink (1956), in which subscripts identify crystallographic sites and superscripts represent local charge deficits ($'$), surfeits ($^{\bullet}$) and neutrality ($^{\times}$):

$$\left\{\mathrm{Al}_{\mathrm{Mg}}^{\bullet} - \mathrm{Al}_{\mathrm{Si}}'\right\}^{\times} + \mathrm{Si}_{\mathrm{Si}}^{\times} + 2\mathrm{O}_{\mathrm{O}}^{\times} + \mathrm{H_2O} + 2\mathrm{Mg_2SiO_4} = 2\left\{\mathrm{Al}_{\mathrm{Si}}' - \mathrm{OH}_{\mathrm{O}}^{\bullet}\right\}^{\times} + \mathrm{Mg}_{\mathrm{Mg}}^{\times} + 3\mathrm{MgSiO_3} \quad (7)$$

The above equilibrium is valid for aluminous pyroxene coexisting with forsterite. A more general expression for formation of $\left\{\mathrm{Al}_{\mathrm{Si}}' - \mathrm{OH}_{\mathrm{O}}^{\bullet}\right\}^{\times}$ defect complexes is:

$$2\mathrm{Si}_{\mathrm{Si}}^{\times} + 2\mathrm{O}_{\mathrm{O}}^{\times} + \mathrm{Al_2O_3} + \mathrm{H_2O} = 2\left\{\mathrm{Al}_{\mathrm{Si}}' - \mathrm{OH}_{\mathrm{O}}^{\bullet}\right\}^{\times} + 2\mathrm{SiO_2} \quad (8)$$

where Al_2O_3, H_2O and SiO_2 represent oxide components in coexisting melt or mineral phases. The substitution mechanism represented by Equation (8) is promoted by conditions of high a_{Al2O3}, high f_{H2O} and low a_{SiO2}.

As noted above, there is some possibility that the pyroxenes in this study also have some component of H charge coupled to octahedral Al, as this could be a potential explanation for the somewhat high values of $D_H^{pyx/melt}$ for the amount of tetrahedral aluminum present (Fig. 2.10b). An equivalent equilibrium between a hydrous defect complex involving octahedral Al and melt components is:

$$4Mg_{Mg}^{\times} + 2O_O^{\times} + Al_2O_3 + H_2O = 2\left\{Al_{Mg}^{\bullet} - V_{Mg}'' - OH_O^{\bullet}\right\}^{\times} + 4MgO \qquad (9)$$

where V_{Mg}'' represents an M site vacancy. Thus, the formation of the $\left\{Al_{Mg}^{\bullet} - V_{Mg}'' - OH_O^{\bullet}\right\}^{\times}$ defect complex is promoted by high a_{Al2O3}, high f_{H2O} and low a_{MgO}. The relative stability of the two hydrous defect complexes might then be expected to depend upon the ratio of SiO_2 and MgO activities:

$$\left\{Al_{Si}' - OH_O^{\bullet}\right\}^{\times} + 2Mg_{Mg}^{\times} + SiO_2 = \left\{Al_{Mg}^{\bullet} - V_{Mg}'' - OH_O^{\bullet}\right\}^{\times} + Si_{Si}^{\times} + 2MgO \qquad (10)$$

so that $\left[\left\{Al_{Si}' - OH_O^{\bullet}\right\}^{\times}\right] / \left[\left\{Al_{Mg}^{\bullet} - V_{Mg}'' - OH_O^{\bullet}\right\}^{\times}\right] \propto \frac{a_{MgO}^2}{a_{SiO_2}}$.

Scant evidence for pairing of H and octahedral Al in pyroxene has been found previously (Rauch & Keppler, 2002; Kohn *et al.* 2005). The notable exceptions are Ca-eskolaite-rich pyroxenes with significant octahedral vacancies, (Smyth *et al.*, 1991; Katayama & Nakashima, 2003), but we consider that such substitutions could potentially be favored at the higher pressures of our experiments. To investigate the possible

incorporation mechanism(s) in these pyroxenes, we performed unpolarized FTIR on unoriented pyroxene crystals in experiments M355 and M357. The spectra of each crystal produce broad peaks from 2500–3800 cm^{-1} (Fig. 2.11). The lack of narrow well-resolved peaks in these spectra makes it difficult to assign the O-H stretching vibrations to particular crystallographic locations. However, the spectra are similar to those of Ca-eskolaite-rich pyroxenes found by Smyth *et al.* (1991) and Katayama & Nakashima (2003). In particular, the peak location of the M357 cpx spectra (~3450 cm^{-1}) has been interpreted in these previous studies as a wavenumber region where hydrogen is associated with M2 vacancies in the pyroxene structure.

However, our pyroxene spectra also resemble those from previous studies (Rauch & Keppler, 2002; Aubaud *et al.*, 2007) where H_2O is not associated with the pyroxene structure, but is instead attributed to a foreign phase contribution, such as fluid inclusions and/or planar defects. If this scenario were true, we would argue that any foreign phase contribution is homogenous in our pyroxenes, as several spatially distributed measurements yield nearly identical spectra. Additionally, the H_2O contents of the pyroxenes, derived from the areas of the FTIR spectra and using the calibration of Paterson (1982)**,** yield concentrations comparable to the corresponding SIMS-derived concentrations of the pyroxenes (970 ppm for M355 opx and 760 ppm for M357 cpx from FTIR vs. 1000 ppm and 1040 ppm by SIMS, respectively). As no hydrous phase is stable at the run conditions of this study, a likely explanation would be that H_2O structurally bound in pyroxene at pressure and temperature exsolved upon quench to form a homogenously distributed, submicroscopic hydrous phase. However, the key point is

that the broad absorptions in the 3000-3600 cm^{-1} region in the analyzed pyroxenes do not easily lend themselves to clear evidence regarding coupling to tetrahedral or octahedral Al.

Calculated peridotite/melt hydrogen partitioning and the H_2O contents of near-solidus partial melts.

Determining the locus of small-degree dehydration melting of peridotite requires an estimate of the concentration of H_2O in the incipient partial melt, as this determines the stability of that melt relative to its dry counterpart at equivalent pressures (Aubaud *et al.*, 2004). The concentration of H_2O in the incipient melt can in turn be calculated from an appropriate set of partition coefficients by application of the batch melting equation at a melt fraction of zero (F=0), provided one knows the applicable mineral/melt partition coefficients and the modes of peridotite minerals, X^{i}, as a function of pressure:

$$D_{\mathrm{H}}^{\mathrm{perid/melt}} = X^{\mathrm{ol}} D_{\mathrm{H}}^{\mathrm{ol/melt}} + X^{\mathrm{opx}} D_{\mathrm{H}}^{\mathrm{opx/melt}} + X^{\mathrm{cpx}} D_{\mathrm{H}}^{\mathrm{cpx/melt}} + X^{\mathrm{gt}} D_{\mathrm{H}}^{\mathrm{gt/melt}} + X^{\mathrm{spinel}} D_{\mathrm{H}}^{\mathrm{spinel/melt}} \qquad (11)$$

We derive the proportions of minerals near the solidus of peridotite by extrapolation of mineral mode/melt fraction trends from the 1 GPa experiments of Baker & Stolper (1994) and Baker *et al.* (1995), and the 3-7 GPa experiments of Walter (1998). We assume that the mode of olivine remains constant at 53% throughout this interval and that the spinel mode is 2% up to the initial stability of garnet at 2.8 GPa. The modes of cpx and opx are fit to the experimental data to give

$$C^{\mathrm{cpx}} = -1.024P^2 + 11.09P + 3.267 \qquad (12)$$

$$C^{\mathrm{opx}} = -1.983P^2 + 1.784P + 30.20, \qquad (13)$$

Above 2.8 GPa garnet becomes the stable aluminous phase, and the mode of garnet varies in response to changes in cpx and opx mode (Fig. 2.12). We assume that $D_H^{ol/melt}$ and $D_H^{gt/melt}$ have constant values of 0.0018 and 0.003, respectively (Aubaud *et al.* 2008), and that $D_H^{spinel} = 0$. For reasons noted above, we use the value for olivine from lower pressure experiments, rather than the lower value from the single datum of this study. Pyroxene/melt partition coefficients are taken from the correlation with Al_2O_3 in pyroxene (Fig. 2.10a, Eqn. 4) and the concentration of Al_2O_3 in pyroxene along the peridotite solidus is inferred from a compilation of near-solidus peridotite experiments (Fig. 2.13). There is considerable scatter regarding the Al concentrations in these pyroxenes, presumably owing to experimental difficulties in producing homogeneous aluminous pyroxenes. We adopt a parameterization of C_{Al2O3}^{pyx} (see Figure caption for details) that skirts the minimum values observed experimentally (Fig. 2.13). Because partition coefficients in pyroxene are larger than for olivine and garnet, they exert significant control on $D_H^{perid/melt}$ and so using a low estimate for C_{Al2O3}^{pyx} produces calculated values of $D_H^{perid/melt}$ that are likely minima.

The resulting predicted values of $D_H^{perid/melt}$ (Fig. 2.14) vary with pressure, increasing from 0.006 at 1 GPa to 0.01 near 3 GPa, where the pyroxenes are the most aluminous. Following the onset of garnet stability, C_{Al2O3}^{pyx} diminishes, causing $D_H^{perid/melt}$ to also decrease down to 0.005 at 5 GPa

With $D_H^{perid/melt}$ values ranging from 0.005 to 0.01, the calculated H_2O concentration of incipient partial melts of peridotite beneath oceanic ridges can be

estimated. For bulk concentrations of 50–200 ppm bulk H (Michael, 1988, 1995; Danyushevsky *et al.*, 2000; Dixon *et al.*, 2002; Saal *et al.*, 2002; Simons *et al.*, 2002) solidus (zero melt fraction) partial melts beneath ridges have H_2O contents ranging from 0.5–3.8 wt.% from 1 to 5 GPa. Note however, that these estimates are for the true incipient melt fraction (F=0). For a small finite melt fraction of 0.1%, which might plausibly be interconnected and perhaps geophysically detectable, the maximum concentrations falls to 3.2 wt.%. Estimates of solidus depression for such modest H_2O concentrations (Aubaud *et al.*, 2004; Medard & Grove, 2008) are no more than 100°C, which corresponds to a deepening of melting along a sub-ridge adiabat of no more than 30 km.

For ocean island settings with bulk mantle hydrogen contents ranging from 300–1000 ppm (Dixon *et al.*, 1997, 2002; Jamtveit *et al.*, 2001; Hauri, 2002; Nichols *et al.*, 2002; Wallace *et al.*, 2002; Seaman *et al.*, 2004), peridotite/melt partition coefficients from 3–5 GPa suggest incipient partial melts could have H_2O contents ranging from 3-20 wt.%. Such hydrous partial melts would clearly be stable at depths much greater than the intersection with the dry solidus. Precise estimation of the depths of initial melting would therefore require experimental data on partition coefficients above 5 GPa. Clearly though, hydrous melting beneath oceanic island source regions likely extends to considerable depths.

Table 2.1. Starting materials for this study.

Oxide	Batch 1 (wt. %)*	Batch 2 (wt. %)*
SiO_2	47.72	50.56
TiO_2	1.27	0.87
Al_2O_3	12.77	8.84
Cr_2O_3	0.02	0.04
FeO	9.42	11.17
MnO	0.12	0.09
MgO	15.55	16.11
CaO	8.35	8.43
Na_2O	2.59	1.76
K_2O	0.20	0.14
H_2O	2.00	2.00
Total	100.00	100.00

* The bulk composition is estimated by calculating appropriate ratios of natural mineral and oxide powders to produce the compositions shown. All of the components were then scaled to produce a 200 mg batch.

Table 2.2. Experimental run conditions from this study.

Exp #	Batch	T(i)	T(f)	Cooling Rate (deg/min)	P (GPa)	Phases*	Relative Fe loss (%)**
M371	2	1450	1350	0.3	3	Cpx, **Opx, Glass**	66
M373	2	1450	1380	0.1	3	**Ol, Cpx,** Opx, **Glass**	61
M357	2	1480	1405	0.3	4	Gt, **Cpx, Opx, Glass**	71
M355	1	1505	1405	0.3	4	**Cpx, Opx, Glass**	73
M366	2	1505	1405	0.3	4	**Opx, Cpx, Glass**	63
M374	2	1505	1435	0.1	4	**Opx, Cpx, Glass**	74
M333	1	1500	1440	0.3	5	**Gt, Cpx, Glass**	88
M372	2	1540	1440	0.3	5	**Gt, Cpx, Glass**	38

***** Phases in bold indicate those that have had hydrogen/total water contents quantified.

** Relative Fe loss from the bulk composition is estimated by mass balance, which uses phase compositions determined by EMP analyses.

Table 2.3. Results of electron microprobe analyses of crystalline phases, reported in wt. %.
Reported results are the average of 10 analyses per crystal.

Run	Phase	SiO_2	TiO_2	Al_2O_3	Cr_2O_3	FeO	MnO	MgO	CaO	Na_2O	K_2O	Total (wt.%)
M371	cpx	55.39	0.12	3.42	0.10	3.41	0.09	21.48	15.29	1.00	0.02	100.32
	opx	57.25	0.06	2.03	0.06	5.27	0.07	33.74	1.78	0.20	0.02	100.48
M373	cpx	52.48	0.26	6.76	0.10	0.80	0.04	18.84	19.04	1.22	0.03	99.57
	opx	57.87	0.07	2.19	0.05	3.41	0.07	34.03	1.62	0.19	0.02	99.53
	ol	42.53	0.01	0.12	0.02	2.49	0.05	55.33	0.21	0.03	0.02	100.79
M357	cpx	54.92	0.19	6.26	0.04	2.55	0.11	20.13	12.62	2.10	0.04	98.95
	opx	56.03	0.08	4.19	0.07	3.77	0.10	32.64	1.90	0.44	0.02	99.24
	gt	41.98	0.34	24.70	0.09	4.94	0.19	22.61	4.53	0.06	0.03	99.46
M355	cpx	55.17	0.14	6.99	0.14	2.08	0.12	23.00	10.60	1.70	0.03	99.96
	opx	55.46	0.10	6.25	0.11	2.67	0.11	33.38	1.56	0.40	0.03	100.04
M366	cpx	55.93	0.11	5.14	0.08	4.23	0.10	21.57	12.16	1.41	0.03	100.76
	opx	57.29	0.05	3.01	0.04	5.41	0.09	32.91	1.84	0.32	0.03	101.00
M374	cpx	54.10	0.16	6.33	0.05	1.71	0.05	22.17	14.21	1.42	0.02	100.22
	opx core	57.09	0.04	2.38	0.05	4.87	0.06	34.36	1.75	0.28	0.03	100.91
M333	cpx	56.70	0.19	7.35	0.05	1.47	0.11	21.43	10.65	2.46	0.02	100.43
	gt	43.61	0.29	24.91	0.13	2.84	0.17	23.66	3.83	0.06	0.02	99.52
M372	cpx	55.63	0.13	5.55	0.03	6.48	0.08	20.06	9.82	2.13	0.03	99.93
	gt	42.21	0.17	23.90	0.09	9.98	0.15	19.61	3.66	0.10	0.04	99.89

Table 2.4. Results of electron microprobe analyses of glasses. Reported results are the average of 21 analyses per glass. met = metal (wt.%), ox = oxide (wt.%).

Run	Type	$Si(O_2)$	$Ti(O_2)$	$Al(_2O_3)$	$Cr(_2O_3)$	Fe(O)	Mn(O)	Mg(O)	Ca(O)	$Na(_2O)$	$K(_2O)$	O	Total	H_2O inf.* (+/-)
M371	met	24.03	0.66	5.81	0.02	3.17	0.07	6.12	7.18	1.55	0.16	49.15	97.91	
	ox	51.41	1.11	10.99	0.02	4.08	0.09	10.15	10.04	2.08	0.19		90.16	7.75 (1.07)
M373	met	17.96	0.82	7.78	0.01	0.99	0.06	9.84	10.41	3.37	0.23	45.38	96.86	
	ox	38.43	1.37	14.71	0.02	1.27	0.07	16.31	14.56	4.54	0.28		91.57	5.29 (0.79)
M357	met	23.14	0.96	6.03	0.01	2.38	0.07	6.92	6.43	2.32	0.26	48.62	97.16	
	ox	49.51	1.61	11.40	0.01	3.06	0.09	11.47	9.00	3.13	0.32		89.60	7.56 (1.14)
M355	met	22.63	0.84	7.57	0.02	2.07	0.08	7.52	6.61	2.03	0.21	48.49	98.06	
	ox	48.42	1.40	14.30	0.03	2.66	0.10	12.46	9.25	2.73	0.25		91.60	6.45 (0.90)
M366	met	24.08	0.69	5.89	0.01	3.66	0.07	6.18	6.81	1.52	0.17	48.67	97.73	
	ox	51.51	1.14	11.13	0.01	4.71	0.09	10.24	9.53	2.06	0.20		90.61	7.12 (1.38)
M374	met	19.66	0.85	6.50	0.01	2.52	0.07	11.38	7.18	2.20	0.23	46.45	97.05	
	ox	42.06	1.41	12.28	0.01	3.24	0.09	18.88	10.05	2.96	0.28		91.27	5.78 (1.22)
M333	met	23.85	0.84	5.86	0.01	0.89	0.05	7.40	6.53	2.10	0.22	49.04	96.79	
	ox	51.02	1.40	11.07	0.02	1.14	0.07	12.27	9.14	2.83	0.26		89.23	7.56 (1.03)
M372	met	23.66	0.90	3.76	0.01	5.45	0.07	5.97	6.07	1.27	0.22	48.55	95.94	
	ox	50.62	1.50	7.11	0.02	7.02	0.09	9.90	8.49	1.72	0.27		86.72	9.21 (1.13)

*The H_2O content is inferred by subtracting oxide totals from the corresponding metals total.

Table 2.5. Infrared and SIMS data for the standards.

Sample	SiO_2 (wt.%)	H_2O (wt.%)	H_20/SiO_2 ref.£	$^{16}O^1H$(cps)	^{30}Si (cps)	$^{16}O^1H/^{30}Si$	$^{16}O^1H/^{30}Si$ (blank corr.)*	^{12}C (cps)	^{19}F (cps)	^{32}S (cps)	^{35}Cl (cps)
Basaltic Glass											
JdFD10	50.11	0.348	2	2.69E+03	6.13E+03	4.41E-01		6.33E+01	3.36E+03	1.30E+04	1.97E+03
KN54Sta52	50.81	0.495	2	1.06E+04	8.25E+03	1.28E+00		1.47E+02	5.76E+03	1.18E+04	1.06E+03
KN54Sta51	50.68	0.647	2	8.69E+03	7.32E+03	1.19E+00		1.62E+02	1.03E+04	1.56E+04	4.93E+02
AC49	49.57	1.98	2	1.02E+04	3.49E+03	2.92E+00		5.91E+02	2.34E+03	2.46E+02	5.63E+02
AC46	48.66	3.91	2	1.40E+04	2.71E+03	5.15E+00		4.24E+02	1.79E+03	4.64E+02	4.43E+02
AC47	47.40	6.03	2	1.86E+04	2.60E+03	7.16E+00		3.06E+02	1.69E+03	8.62E+02	4.26E+02
AC50	47.32	7.65	2	2.73E+04	3.05E+03	8.99E+00		3.55E+02	2.15E+03	1.22E+03	5.56E+02
Rhyolitic Glass											
EDF Natural	77.04	0.23	2	7.48E+02	2.84E+03	2.62E-01		8.99E-01	3.50E+03	8.03E+00	1.08E+03
NSLG	75.32	0.13	1	7.65E+02	3.70E+03	2.06E-01		8.33E-01	1.40E+04	1.47E+02	7.78E+03
NSL1	74.81	1.16	1	3.74E+03	2.89E+03	1.29E+00		1.88E+01	1.01E+04	9.52E+01	5.89E+03
EDF2.4	74.79	2.74	3	5.38E+03	2.18E+03	2.46E+00		1.12E+01	2.57E+03	8.50E+00	8.17E+02
N3	73.03	3.30	1	7.89E+03	2.73E+03	2.88E+00		1.13E+01	9.56E+03	7.79E+01	5.72E+03
N3.35	73.00	3.51	1	1.04E+04	3.28E+03	3.16E+00		1.17E+01	1.24E+04	9.60E+01	6.95E+03
N4b	72.50	4.11	1	1.16E+04	3.32E+03	3.49E+00		1.59E+01	1.22E+04	1.01E+02	6.78E+03
EDF4b	73.67	4.20	3	7.35E+03	2.63E+03	2.78E+00		1.12E+01	3.39E+03	1.05E+01	1.07E+03
N5	71.83	5.06	1	1.03E+04	2.74E+03	3.72E+00		1.13E+01	9.85E+03	7.21E+01	4.96E+03
N6	71.06	6.09	1	1.32E+04	3.10E+03	4.26E+00		1.18E+01	1.14E+04	8.52E+01	5.97E+03

Table 2.5. Infrared and SIMS data for the standards (cont.).

Sample	SiO_2 (wt.%)	H_2O (wt.%)	H_20/SiO_2 ref.£	$^{16}O^1H$(cps)	^{30}Si (cps)	$^{16}O^1H/^{30}Si$	$^{16}O^1H/^{30}Si$ (blank corr.)*	^{12}C (cps)	^{19}F (cps)	^{32}S (cps)	^{35}Cl (cps)
Olivine											
ROM177	38.87	0.0125	4	4.39E+01	2.58E+03	1.70E-02	1.22E-02	3.18E+00	4.41E+02	1.50E+00	8.33E-01
ROM250 OL2	39.16	0.0183	4	2.05E+02	5.76E+03	3.55E-02	3.34E-02	7.53E+00	3.56E+02	1.07E+00	1.97E+00
ROM250 OL13	38.61	0.0243	4	2.77E+02	6.29E+03	4.40E-02	4.20E-02	2.88E+00	1.68E+03	5.33E-01	2.10E+00
AC90 Core†	42.03	0.0079	2	1.81E+02	5.97E+03	3.02E-02	2.82E-02	6.00E+00	1.39E+01	3.70E+00	4.63E+00
AC86	41.07	0.0073	2	3.45E+02	6.08E+03	5.66E-02	5.49E-02	2.00E+00	2.39E+01	1.10E+00	2.53E+00
Fo100	42.70	0	2	1.32E+01	4.26E+03	3.09E-03	0.00E+00	2.63E+00	3.30E+00	8.33E-01	1.27E+00
Damaping OL	40.77	0.0001	5	1.95E+01	6.25E+03	3.12E-03	1.37E-03	2.43E+00	1.07E+01	4.66E-01	1.53E+00
Ant Hill OL	40.54	0.0009	2	1.94E+01	3.73E+03	5.17E-03	2.25E-03	6.33E-01	9.13E+00	3.33E-01	1.80E+00
San Carlos OL	41.37	0.0001	2	1.42E+01	4.41E+03	3.23E-03	7.41E-04	1.27E+00	7.23E+00	9.33E-01	2.13E+00
AC56	39.98	0.0064	2	6.48E+01	4.71E+03	1.37E-02	1.14E-02	1.57E+00	8.10E+00	7.00E-01	1.60E+00
AC58	40.22	0.0048	2	6.73E+01	5.07E+03	1.33E-02	1.11E-02	2.13E+00	1.04E+01	9.66E-01	2.10E+00
AC84 Core†	41.21	0.0052	2	3.39E+01	3.70E+03	9.06E-03	5.77E-03	9.99E-01	6.63E+00	4.33E-01	2.00E-01
AC87	40.57	0.0478	2	1.02E+03	5.30E+03	1.92E-01	1.90E-01	4.36E+00	1.19E+01	1.07E+00	2.83E+00
AC94 Rim‡	42.36	0.1488±0.06	1,2	2.13E+03	4.77E+03	4.47E-01	4.45E-01	3.08E+00	1.21E+01	1.23E+00	1.57E+00
Orthopyroxene											
Bamble Dry	56.03	0	2	9.83E+00	3.75E+03	2.61E-03	0.00E+00	1.10E+00	1.17E+02	3.33E-01	6.33E-01
Damaping OPX	55.44	0.0078	2	9.65E+01	6.64E+03	1.45E-02	1.25E-02	1.48E+00	1.02E+02	2.67E-01	2.07E+00
India	54.52	0.0141	2	2.02E+02	7.62E+03	2.65E-02	2.47E-02	8.16E-01	3.82E+01	3.66E-01	6.00E-01
Kenya	57.24	0.0147	2	1.72E+02	6.35E+03	2.70E-02	2.50E-02	3.16E-01	8.96E+00	4.33E-01	7.00E-01
KBH-1	54.68	0.0217	6	1.90E+02	4.96E+03	3.81E-02	3.56E-02	8.00E-01	1.42E+02	5.33E-01	2.33E+00
ROM273-OG2	57.37	0.0263	4	3.05E+02	6.93E+03	4.40E-02	4.21E-02	4.80E+00	5.77E+02	1.33E-01	1.47E+00

Table 2.5. Infrared and SIMS data for the standards (cont.).

Sample	SiO_2 (wt.%)	H_2O (wt.%)	H_20/SiO_2 ref.£	$^{16}O^1H$(cps)	^{30}Si (cps)	$^{16}O^1H/^{30}Si$	$^{16}O^1H/^{30}Si$ (blank corr.)*	^{12}C (cps)	^{19}F (cps)	^{32}S (cps)	^{35}Cl (cps)
Clinopyroxene											
Dish Hill	47.90	0	2	1.77E+01	8.72E+03	2.03E-03	6.00E-04	3.16E+00	2.60E+03	1.07E+00	3.90E+00
Tunguska	55.27	0.0106	2	1.51E+02	7.24E+03	2.08E-02	1.91E-02	1.92E+00	3.78E+02	1.27E+00	2.13E+00
ROM271 DI10	55.32	0.0195	4	1.68E+02	7.45E+03	2.26E-02	2.09E-02	2.18E+00	6.11E+02	6.66E-01	2.57E+00
PMR53	54.78	0.0268	6	3.29E+02	7.25E+03	4.53E-02	4.36E-02	1.31E+01	1.06E+03	1.17E+00	3.70E+00
ROM271 DI16	55.82	0.0439	4	4.03E+02	6.82E+03	5.90E-02	5.72E-02	1.06E+01	8.68E+02	1.17E+00	1.73E+00
ROM271DI21	55.09	0.0490	4	4.98E+02	7.22E+03	6.90E-02	6.72E-02	5.13E+00	1.02E+03	3.00E-01	3.43E+00
Garnet											
Ant Hill Dry	40.93	0	2	1.93E+01	8.02E+03	2.40E-03	6.61E-04	1.80E+00	7.38E+01	9.33E-01	4.23E+00
ROM263 GT52	41.97	0.0015	4	3.16E+01	8.23E+03	3.83E-03	2.14E-03	5.16E+00	1.34E+02	1.90E+00	4.50E+00
ROM263 GT25	41.85	0.0032	4	5.18E+01	5.81E+03	8.90E-03	4.44E-03	5.55E+00	1.24E+02	6.00E-01	3.60E+00
ROM263 GT 09	41.53	0.0040	4	4.74E+01	7.91E+03	6.00E-03	4.23E-03	3.53E+00	1.95E+02	1.30E+00	3.46E+00
Dora Maira	43.52	0.0043	2	3.58E+01	4.98E+03	7.20E-03	4.39E-03	1.35E+00	1.07E+03	9.66E-01	1.40E+00
MON9GT	42.20	0.0056	6	5.74E+01	7.06E+03	8.12E-03	6.15E-03	5.41E+00	1.81E+02	8.33E-01	2.83E+00
Ant Hill Clear	39.45	0.0060	2	8.36E+01	7.88E+03	1.06E-02	8.83E-03	1.73E+00	1.97E+02	7.66E-01	3.66E+00
Ant Hill Dark	41.15	0.0189	2	1.25E+02	6.54E+03	1.91E-02	1.79E-02	1.92E+00	5.27E+01	5.33E-01	1.77E+00

* Blank corrected $^{16}O^1H/^{30}Si$ ratios were calculated by subtracting the $^{16}O^1H$ count rate of the blank from that of the sample, and dividing the result by the ^{30}Si count rate of the sample.

† For samples AC84 and AC90, the reported H_2O concentrations are determined from unpolarized FTIR measurements on randomly oriented grains, and using the calibration method from Paterson (1982). An orientation factor of 1/3 has been used, and the resulting concentrations have been multiplied by 3.5 to remain consistent with the other measurements, which use the calibration of Bell *et al.* (2003).

‡ For sample AC94, the H_2O content is the average of concentrations measured in three fragments of the single crystal standard used in this study, together with the measurement from the rim of the crystal from Aubaud *et al.* (2007). Fragments used as standards in this study were analyzed using unpolarized FTIR. Integrated absorptions in the OH stretching region were corrected for sample thickness and orientation (determined by EBSD), based on the Absorption indicatrix of AC87 from Aubaud *et al.* (2007). The stated uncertainty (±0.06 wt.% H_2O) represents the range of H_2O concentrations measured in AC94.

£ References: 1. This study; 2. Aubaud *et al.* (2007); 3. Withers & Behrens (1999); 4. Bell *et al.* (2004); 5. Koga *et al.* (2003); 6. Bell *et al.* (1995).

Table 2.6. Estimated $^{16}O^{1}H$ background (in ppm) of the SIMS, based on the olivine calibration (fig. 2.5) and intermittent measurements taken on the Fo_{100} (dry blank) standard over the course of all measurements. 42.7 = 42.7% SiO_2 in Fo_{100}.

Fo^{100}	$^{16}O^{1}H/^{30}Si$	$(^{16}O^{1}H/^{30}Si)*42.7$	Bkg. (ppm)
1	3.43E-03	0.146	11.5
2	4.00E-03	0.171	13.5
3	2.59E-03	0.111	8.8
4	3.29E-03	0.141	11.1
5	2.30E-03	0.098	7.7
6	3.09E-03	0.132	10.4
7	2.95E-03	0.126	10.0
8	3.25E-03	0.139	11.0
9	2.86E-03	0.122	9.6
10	2.69E-03	0.115	9.1
		Average	10.3
Sample Change			
1	1.96E-02	0.838	66.2
2	1.54E-02	0.659	52.1
3	1.44E-02	0.616	48.7
4	1.24E-02	0.529	41.8
5	1.26E-02	0.539	42.6
6	1.16E-02	0.494	39.0
7	9.34E-03	0.399	31.5
8	9.02E-03	0.385	30.4
9	9.03E-03	0.386	30.5

Table 2.7. SIMS data of mineral and glass experimental run products from this study. Data shaded in dark gray exceed the range of values of SIMS measurements considered to be uncontaminated.

Sample	P,T (GPa, °C)	$(OH/Si)_{(SIMS)}*SiO_{2(EMP)}$	H_2O content by SIMS(wt. %)	^{12}C (cps)	^{19}F (cps)	^{32}S (cps)	^{35}Cl (cps)
Cpx							
M373, 1	3, 1380	6.06	0.0794	1.30E+00	8.67E+01	5.66E-01	8.66E-01
M373, 2	3, 1380	8.14	0.1066	3.41E+01	1.40E+02	2.40E+00	1.43E+00
M373 Avg.		6.06	0.794				
M355, 1	4, 1405	8.12	0.1063	1.97E+00	7.18E+01	9.99E-02	5.00E-01
M355, 2	4, 1405	8.86	0.1161	1.60E+00	8.45E+01	3.00E-01	7.33E-01
M355, 3	4, 1405	9.37	0.1228	2.25E+00	9.72E+01	9.99E-02	8.33E-01
M355, 4	4, 1405	8.98	0.1177	6.53E+00	9.08E+01	7.00E-01	1.93E+00
M355 Avg.		8.83	0.1157				
M357, 1	4, 1405	7.79	0.1021	1.38E+02	9.23E+01	5.30E+00	2.17E+01
M357, 2	4, 1405	8.19	0.1073	2.82E+00	9.64E+01	2.00E-01	8.99E-01
M357, 3	4, 1405	9.26	0.1213	2.53E+02	1.02E+02	5.70E+00	3.09E+01
M357, 4	4, 1405	7.71	0.1010	2.22E+00	8.96E+01	1.23E+00	2.50E+00
M357 Avg.		7.90	0.1041				
M366, 1	4, 1405	7.79	0.1020	5.78E+01	8.74E+01	5.46E+00	1.75E+01
M366, 2	4, 1405	7.53	0.0987	3.16E+00	8.21E+01	5.33E-01	7.66E-01
M366, 3	4, 1405	9.19	0.1203	6.51E+02	8.26E+01	3.36E+01	5.86E+01
M366 Avg.		7.66	0.1003				
M374, 1	4, 1435	6.30	0.0825	2.32E+00	5.13E+01	3.33E-02	6.66E-01
M374, 2	4, 1435	6.16	0.0806	2.27E+01	5.89E+01	3.30E+00	2.20E+00
M374, 3	4, 1435	7.08	0.0927	7.85E+00	7.70E+01	5.66E-01	1.60E+00
M374 Avg.		6.51	0.0853				
M333, 1	5, 1440	8.11	0.1062	1.58E+01	6.03E+01	5.06E+00	1.49E+01
M333, 2	5, 1440	7.64	0.1000	6.65E+01	4.85E+01	1.09E+01	3.31E+01
M333 Avg.		7.87	0.1031				
M372, 1	5, 1440	10.09	0.1322	4.64E+02	5.03E+01	2.03E+01	1.20E+01
M372, 2	5, 1440	11.68	0.1530	2.11E+02	5.29E+01	2.46E+01	1.95E+01
M372 Avg.		10.89	0.1426				

Table 2.7 (cont). SIMS data of mineral and glass experimental run products from this study. Data shaded in gray exceed the range of values of SIMS measurements considered to be uncontaminated.

Sample	P,T (GPa, °C)	$(OH/Si)_{(SIMS)}*SiO_{2(EMP)}$	H_2O content by SIMS (wt. %)	^{12}C (cps)	^{19}F (cps)	^{32}S (cps)	^{35}Cl (cps)
Opx							
M371, 1	3, 1350	5.65	0.0610	2.45E+01	3.69E+01	2.53E+00	1.29E+01
M371, 2	3, 1350	6.26	0.0676	1.13E+02	4.44E+01	1.44E+01	2.35E+02
M371, 3	3, 1350	13.30	0.1436	7.80E+02	1.20E+02	1.62E+02	3.24E+02
M371, 4	3, 1350	7.58	0.0819	1.28E+03	5.13E+01	3.89E+01	4.67E+01
M371 Avg.		5.95	0.0643				
M355, 1	4, 1405	9.50	0.1026	4.52E+01	6.75E+01	1.77E+00	3.70E+00
M355, 2	4, 1405	11.20	0.1210	2.31E+02	7.67E+01	1.07E+01	2.09E+01
M355, 3	4, 1405	9.42	0.1017	2.72E+00	7.84E+01	1.50E+00	1.67E+00
M355, 4	4, 1405	8.74	0.0944	7.08E+00	5.52E+01	9.33E-01	4.13E+00
M355 Avg.		9.22	0.0996				
M366, 1	4, 1405	8.97	0.0968	2.41E+02	7.33E+01	6.06E+00	2.55E+01
M366, 2	4, 1405	7.59	0.0819	5.30E+00	5.47E+01	7.66E-01	9.99E+00
M366 Avg.		7.59	0.0819				
M374, 1	4, 1435	4.00	0.0432	4.56E+00	2.13E+01	8.33E-01	2.33E-01
M374, 2	4, 1435	4.06	0.0439	3.21E+00	1.78E+01	1.00E-02	9.99E-01
M374 Avg.		4.03	0.0435				
Garnet							
M333, 1	5, 1440	0.33	0.0078	2.06E+01	9.53E+00	1.70E+00	4.93E+00
M333, 2	5, 1440	0.30	0.0069	3.15E+00	7.90E+00	1.30E+00	5.80E+00
M333 Avg.		0.32	0.0074				
M372, 1	5, 1440	1.02	0.0239	2.90E+01	6.10E+00	1.56E+01	1.28E+01
M372, 2	5, 1440	1.19	0.0277	4.41E+01	1.62E+01	1.66E+01	3.08E+01
M372 Avg.		1.10	0.0258				

Table 2.7 (cont.). SIMS data of mineral and glass experimental run products from this study.

Sample	P,T (GPa, °C)	$(OH/Si)_{(SIMS)}$*$SiO_{2(EMP)}$	H_2O content by SIMS (wt. %)	^{12}C (cps)	^{19}F (cps)	^{32}S (cps)	^{35}Cl (cps)
Olivine							
M373, 1	3, 1380	0.39	0.0031	9.33E-01	6.86E+00	3.33E-01	1.33E-01
M373, 2	3, 1380	0.36	0.0028	8.00E-01	6.66E+00	4.33E-01	2.33E-01
M373, 3	3, 1380	0.38	0.0030	9.66E-01	7.73E+00	6.66E-01	6.00E-01
M373, 4	3, 1380	0.37	0.0029	1.03E+00	5.33E+00	7.00E-01	5.00E-01
M373 Avg.		0.37	0.0029				
Glass*							
M371	3, 1350	353	6.11 ± 0.37	1.14E+03	1.07E+03	2.02E+01	4.85E+02
M373	3, 1380	399	6.90 ± 0.41	1.40E+03	2.24E+03	1.08E+02	1.53E+03
M357	4, 1405	421	7.28 ± 0.44	2.41E+03	2.70E+03	3.52E+01	1.22E+03
M355	4, 1405	352	6.09 ± 0.37	1.68E+03	1.76E+03	2.78E+01	8.20E+02
M366	4, 1405	405	7.01 ± 0.42	3.16E+03	2.60E+03	2.04E+01	1.26E+03
M374	4, 1435	371	6.42 ± 0.39	8.19E+02	1.41E+03	3.24E+01	6.21E+02
M333	5, 1440	512	8.85 ± 0.53	2.41E+03	2.45E+03	7.63E+00	1.39E+03
M372	5, 1440	494	8.55 ± 0.51	2.99E+03	2.21E+03	1.62E+01	9.95E+02

* Errors in glass H_2O concentrations were estimated by assuming a 6% error, based on crystal measurements.

Table 2.8. Hydrogen speciation and total water contents in glass run products from FTIR spectroscopy. A_{OH} and A_{H_2O} denote absorbance, while A^*_{OH} and $A^*_{H_2O}$ denote the integrated intensity.

Sample	Thickness (cm)	Density (g/l)	A_{OH}	A_{H_2O}	A^*_{OH}	$A^*_{H_2O}$	c_{OH} (wt. %)	c_{H_2O} (wt.%)	c_{water},(+/-) (wt.%)
M371-1	0.0236	2680	0.046	0.085	7.8	19.2	2.36	4.33	6.69 (0.86)
M371-2	0.0236	2680	0.046	0.085	7.7	19.2	2.36	4.33	6.69 (0.86)
M357	0.0191	2587	0.035	0.066	5.7	15.0	2.20	4.17	6.37 (0.82)
M355	0.0297	2717	0.053	0.068	8.6	16.5	2.13	2.70	4.83 (0.61)
M366-1	0.0103	2704	0.018	0.030	3.0	6.7	2.11	3.42	5.53 (0.72)
M366-2	0.0103	2699	0.019	0.030	3.2	7.2	2.23	3.52	5.75 (0.75)
M372-1	0.0095	2669	0.017	0.040	2.7	11.0	2.20	5.02	7.22 (0.94)
M372-2	0.0095	2668	0.017	0.040	2.8	11.2	2.20	5.07	7.27 (0.95)

Table 2.9. Mineral/melt hydrogen partition coefficients, including the Al content of pyroxenes (atomic proportions on a six O basis).

Sample	P,T (GPa,°C)	Al_2O_3 (wt.%)	Al(IV)	Al(VI)	$D_{H\ (SIMS/FTIR)}^{min/melt}$	$D_{H(SIMS/SIMS)}^{min/melt}$	$D_{H}^{min/melt}$ avg.
Cpx							
M373	3, 1380	6.76	0.123	0.154	0.019(3)*	0.012(1)	0.015(2)
M357	4, 1405	6.26	0.050	0.202	0.016(2)	0.014(1)	0.015(2)
M355	4, 1405	6.99	0.077	0.199	0.024(3)	0.019(2)	0.021(3)
M366	4, 1405	5.14	0.042	0.162	0.018(2)	0.014(1)	0.016(2)
M374	4, 1435	6.33	0.099	0.155	0.019(3)*	0.013(1)	0.016(2)
M333	5, 1440	7.35	0.043	0.247	0.017(2)*	0.012(1)	0.014(2)
M372	5, 1440	5.55	0.028	0.191	0.020(3)	0.017(2)	0.018(3)
Opx							
M371	3, 1350	2.03	0.038	0.044	0.010(1)	0.010(1)	0.010(1)
M355	4, 1405	6.25	0.113	0.137	0.021(3)	0.016(1)	0.019(2)
M366	4, 1405	3.01	0.046	0.074	0.015(2)	0.012(1)	0.014(2)
M374	4, 1435	2.38	0.053	0.042	0.010(1)*	0.007(0)	0.009(1)
Gt							
M333	5, 1440				0.0012(2)*	0.00083(7)	0.0010(1)
M372	5, 1440				0.0036(5)	0.0030(3)	0.0033(4)
Ol							
M373	3, 1380				0.0007(3)*	0.0004(2)	0.0006(3)

Partition coefficients are calculated from mineral and melt H_2O averages.

$D_{H\ (SIMS/FTIR)}^{pyx/melt}$ uses glass H_2O contents derived by FTIR, except for *, which use EMP data to estimate "FTIR equivalent" H_2O concentrations (see text).

$D_{H(SIMS/SIMS)}^{pyx/melt}$ uses glass H_2O contents by SIMS.

Error in the last decimal place is given in parentheses.

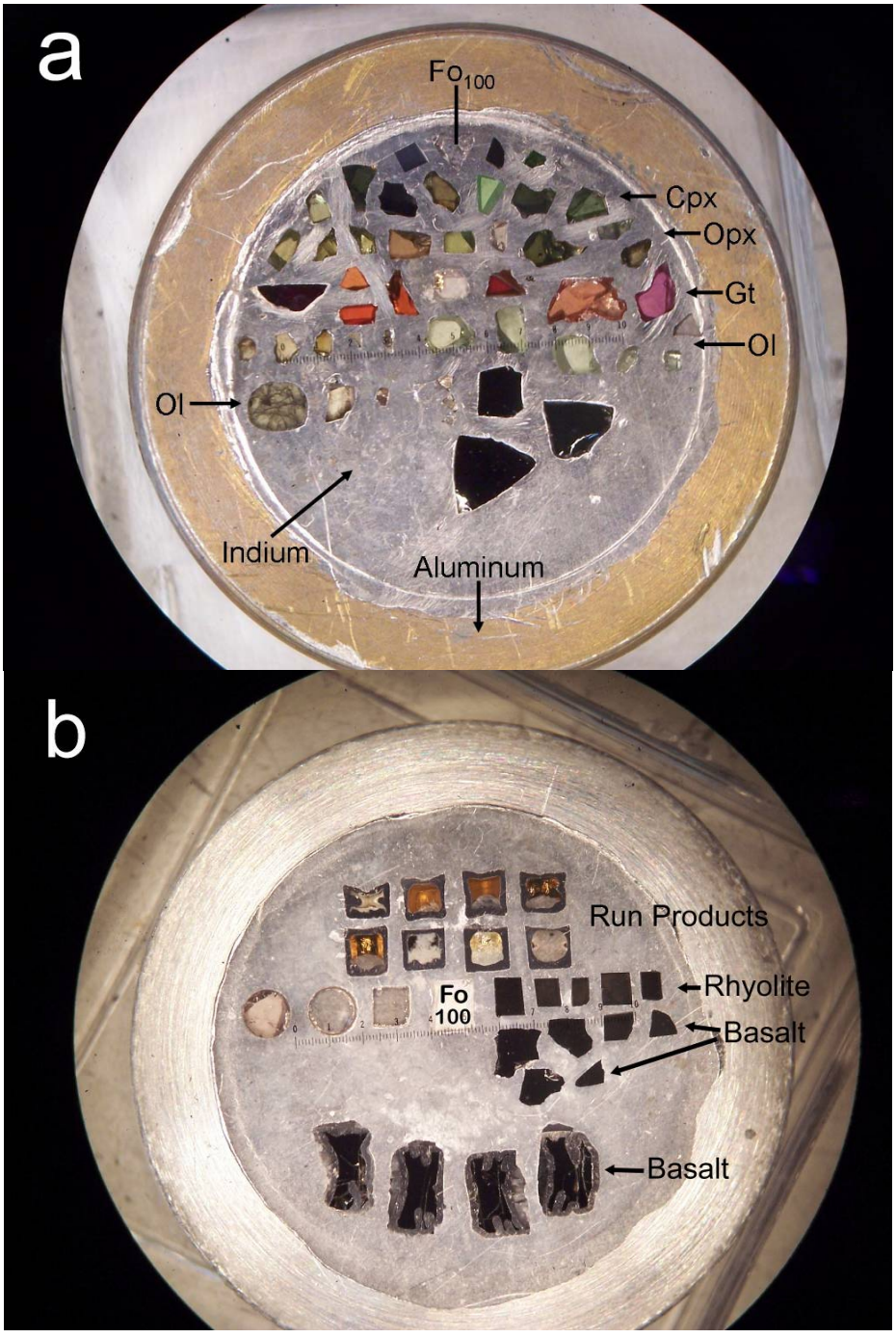

Figure 2.1. SIMS mounts of (a) mineral standards and (b) glass standards and experimental run products. Standards and unknowns are mounted in indium metal and pressed into an aluminum ring. The outer diameter of the ring is approximately 2.5 cm.

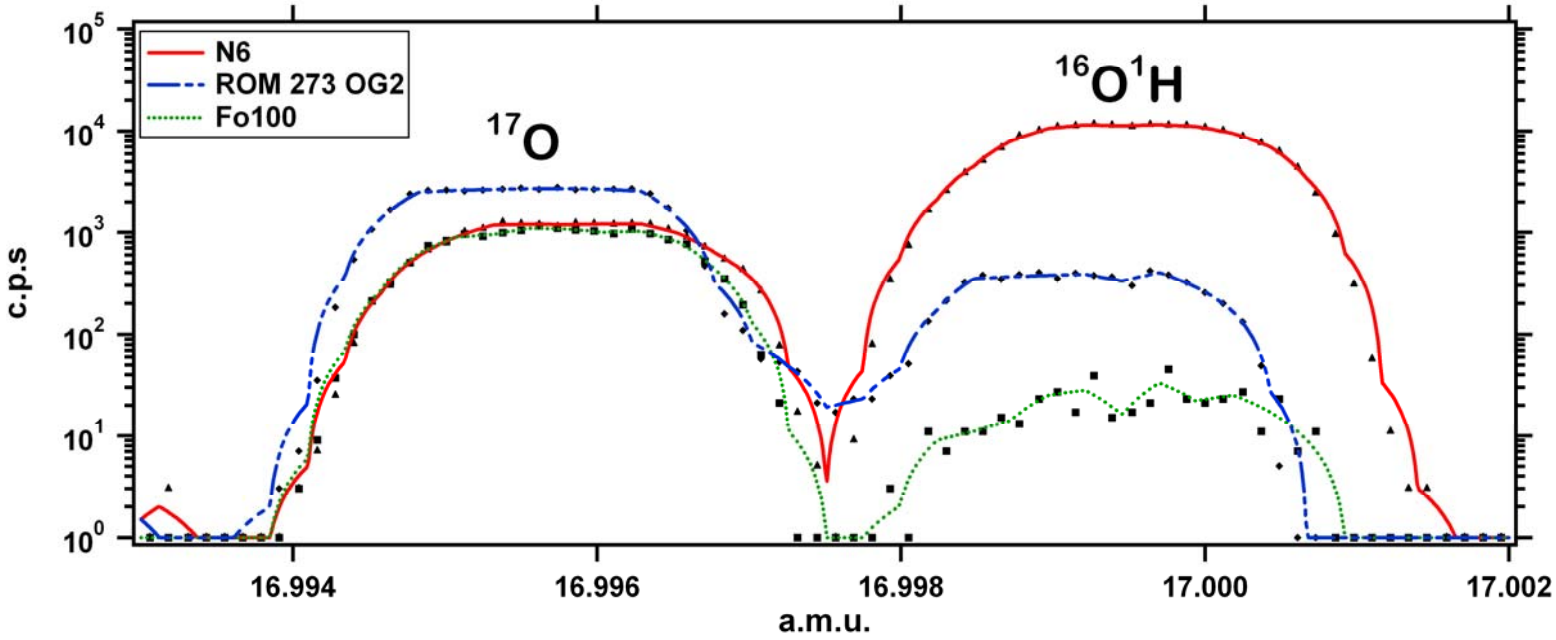

Figure 2.2. High resolution ^{17}O and $^{16}O^{1}H$ count rates for rhyolitic glass (N6), orthopyroxene (ROM 273 OG2), and dry blank (Fo_{100}) standards. ^{17}O and $^{16}O^{1}H$ differ in mass by 0.0037 a.m.u, yet count rates for each isotope are well separated with a broad plateau across a mass range. This resolution owes to a properly aligned beam, and results in precise and accurate measurements. Similar count rate "plateaus" were achieved on all other isotopes measured in this study.

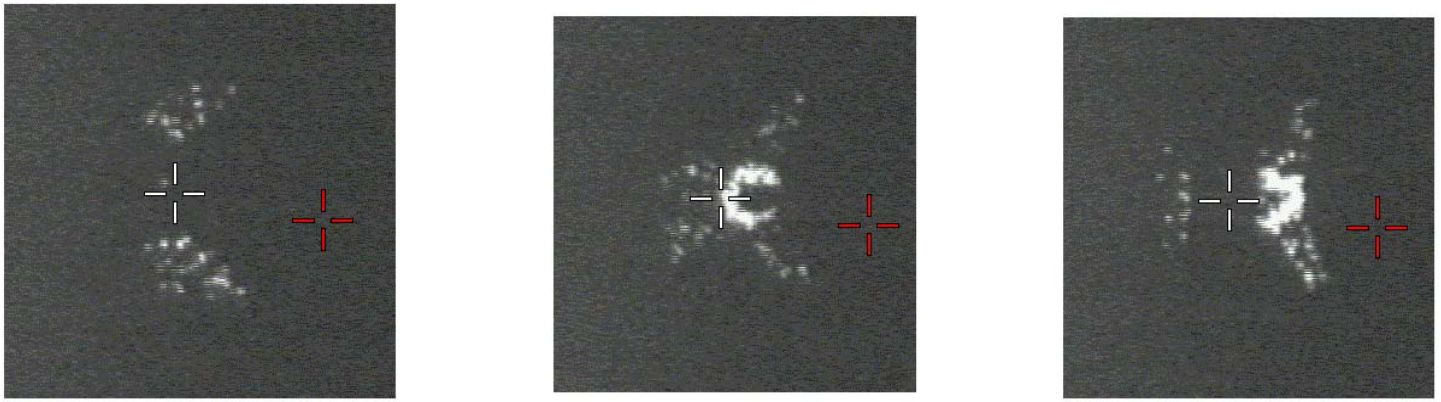

Figure 2.3. $^{19}F^-$ secondary ion image on indium, which illustrates the secondary ion optic axis (located with the white reticle). The center image has the mass adjusted by the secondary magnets to maximize the count rate. The left image is that of when the secondary magnets are adjusted to a decreased mass (vertically pinching out), while the right image is that of when the secondary magnets are adjusted to an increased mass (horizontally pinching out). It can be seen in the center image that the primary ion beam is generating secondary ions slightly to the right of the secondary ion axis. Steering of the primary magnets can re-align the primary ion beam to produce secondary ions with the greatest count rate when the secondary magnets are aligned directly over the secondary ion axis.

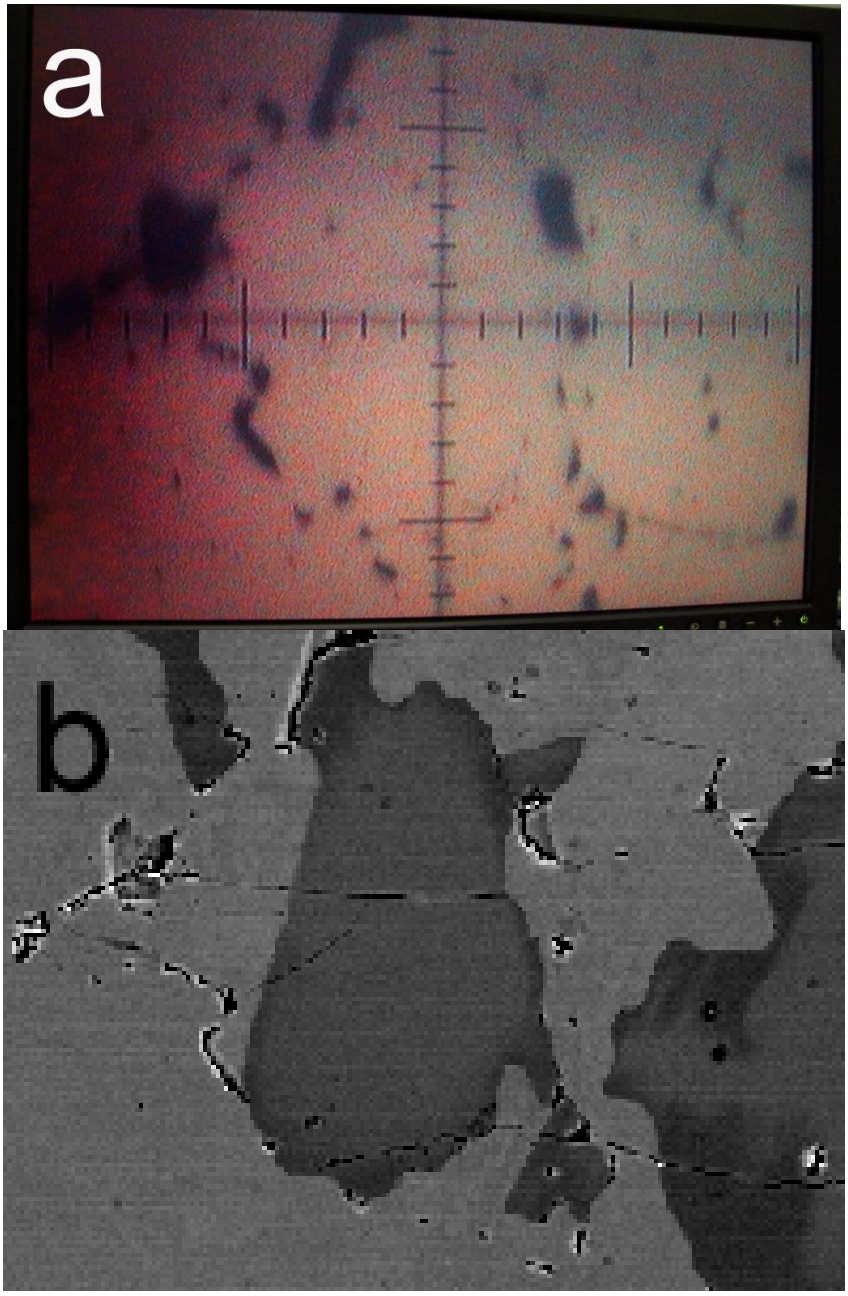

Figure 2.4. Corresponding optical (reflected light) and backscattered electron images of a 50×100 micron orthopyroxene grain in run product M374. Comparison between these images and the optical image observed during SIMS analyses are used to locate points for SIMS measurements.

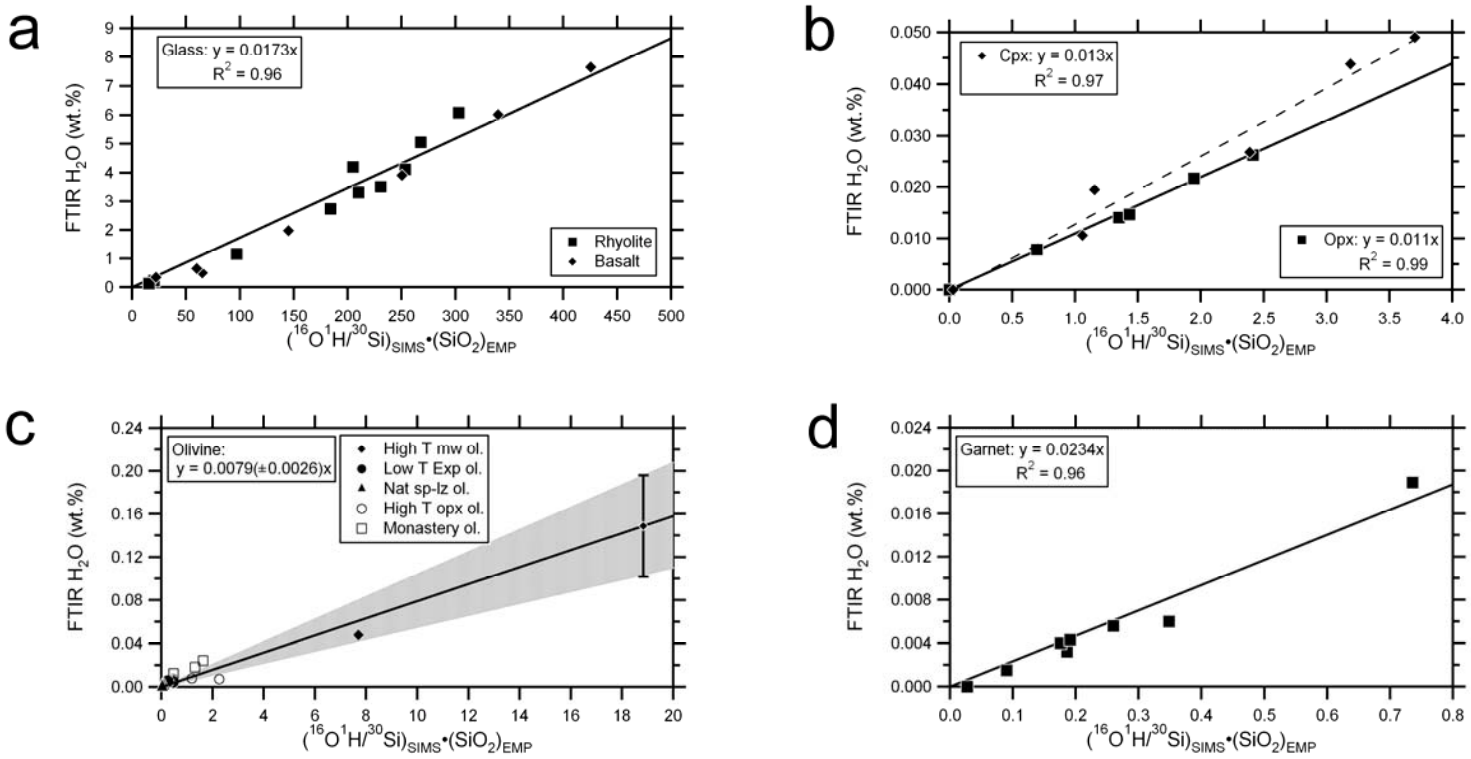

Figure 2.5. FTIR–SIMS calibration curves. The ratio of $^{16}O^{1}H$ /^{30}Si counts observed by SIMS are multiplied by the SiO_2 content of the phase observed by EMP and compared to the H_2O concentration in the standard from FTIR analyses. (a) basaltic and rhyolitic glass, (b) orthopyroxene and clinopyroxene, (c) olivine, and (d) garnet. For olivine the shaded region indicates the uncertainty in the working curve owing to compositional heterogeneity in the most H_2O-rich olivine standard (see Table 2.5).

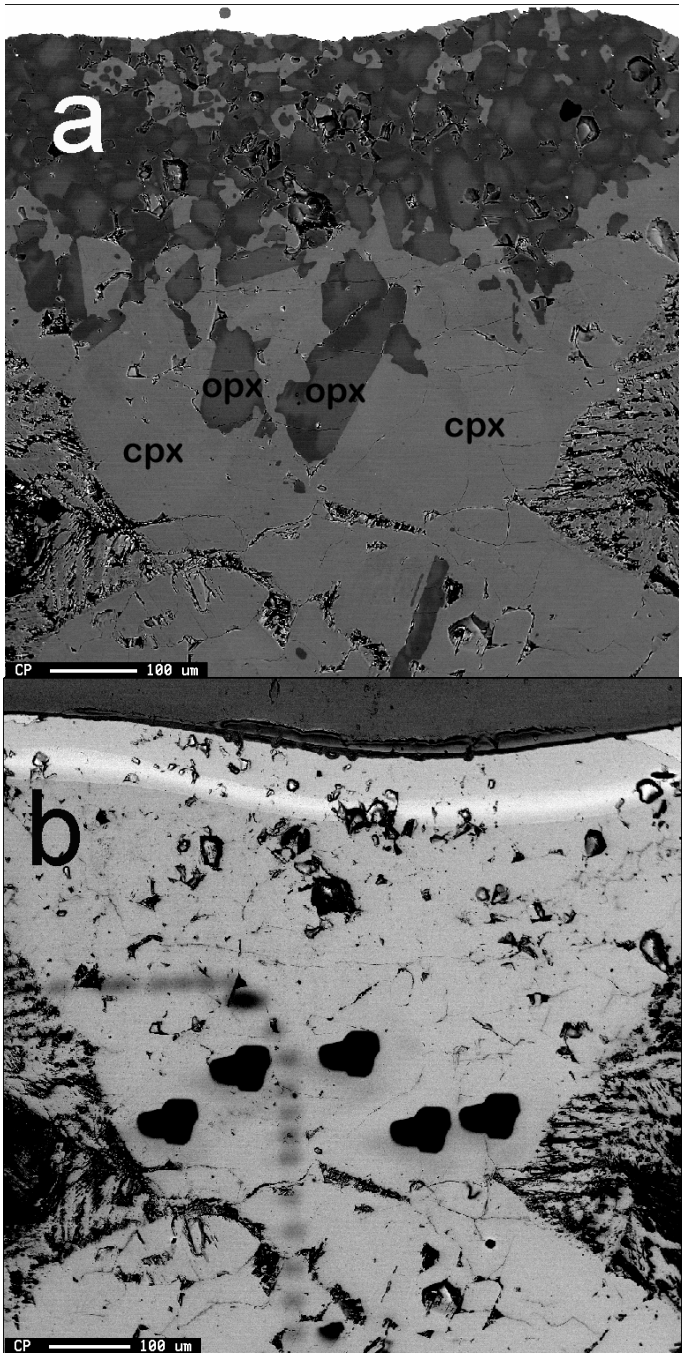

Figure 2.6. The location of SIMS cpx and opx measurements in experiment M374. (a) Backscattered image prior to SIMS analysis. (b) backscattered image of the same experiment (gold coated), after SIMS analysis.

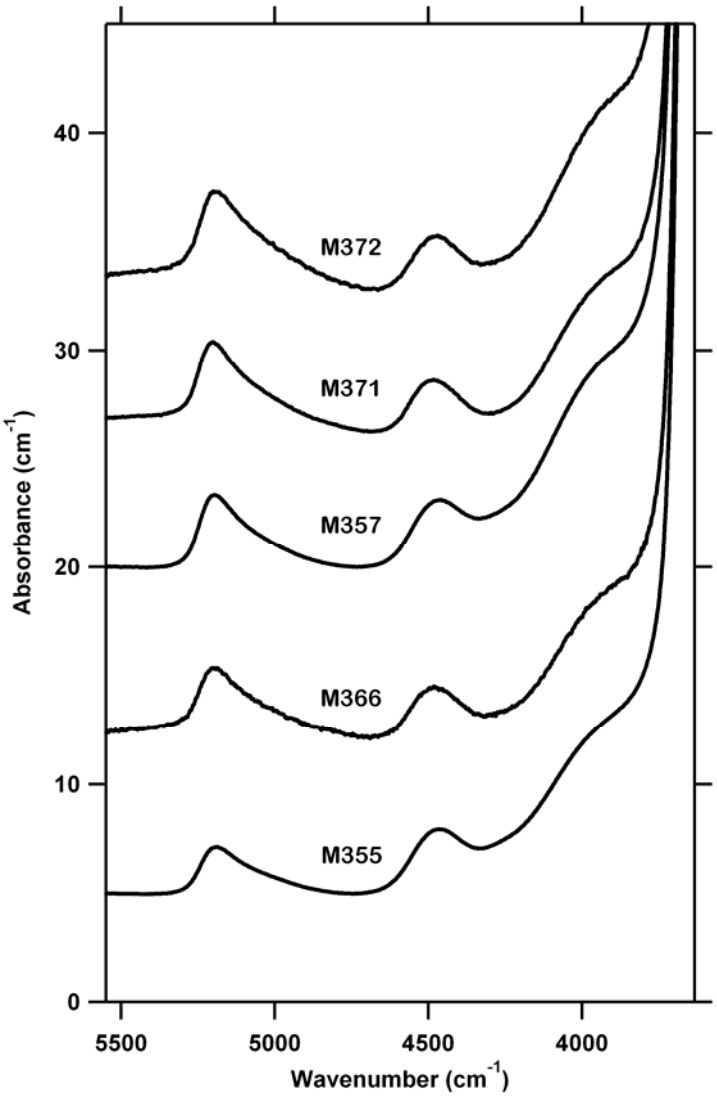

Figure 2.7. FTIR spectra of glasses in the near infrared showing peaks at 4500 cm^{-1} (OH) and 5200 cm^{-1} (H_2O). All spectra are normalized to a thickness of 1 cm. A straight line baseline correction following the method of Ohlhorst *et al.* (2001) was applied to the spectra, which is the same method employed by Aubaud *et al.* (2007) on FTIR measurements of all hydrous glass standards in Table 2.5. Total water contents range from 4.83 wt.% (M355) to 7.25 wt% (M372).

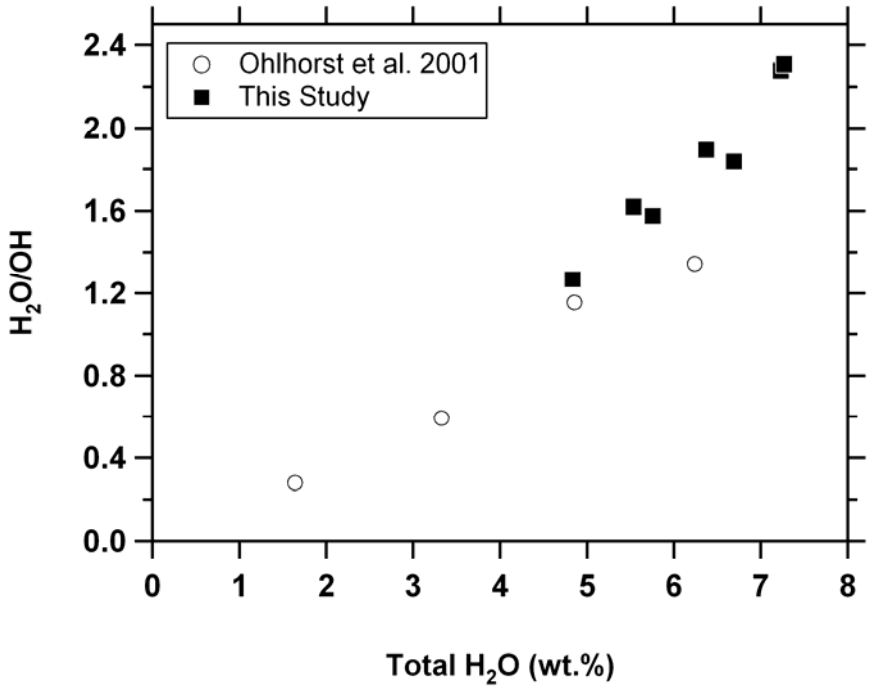

Figure 2.8. Ratio of hydrous species concentrations as a function of total H_2O content measured in glasses from this study and in basaltic glasses from Ohlhorst *et al.* (2001). The agreement between these trends suggests that the background removal in this study produces quantitative results consistent with that of Ohlhorst *et al.* (2001).

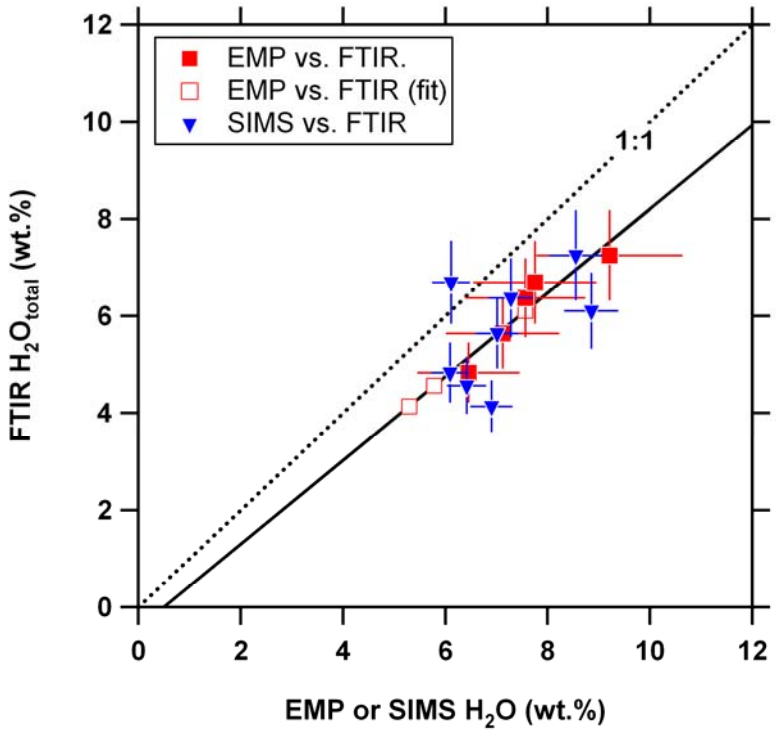

Figure 2.9. EMP and SIMS derived water contents versus FTIR derived total H_2O contents in hydrous glasses from this study. FTIR and EMP derived H_2O contents (red closed symbols) yield a linear trend (r^2 = 0.88) with the following equation: $FTIR_{H2O}$ = (0.8642*EMP_{H2O}) –0.4271. Using EMP measurements, "FTIR equivalent" water contents of 4.14, 4.57, and 6.11 wt.% (open symbols) are derived for the glasses in experiments M373, M374, and M333, respectively. Neither trend is at unity (dotted line), as EMP and SIMS derived H_2O contents are, on average, 20% greater than corresponding H_2O measurements by FTIR.

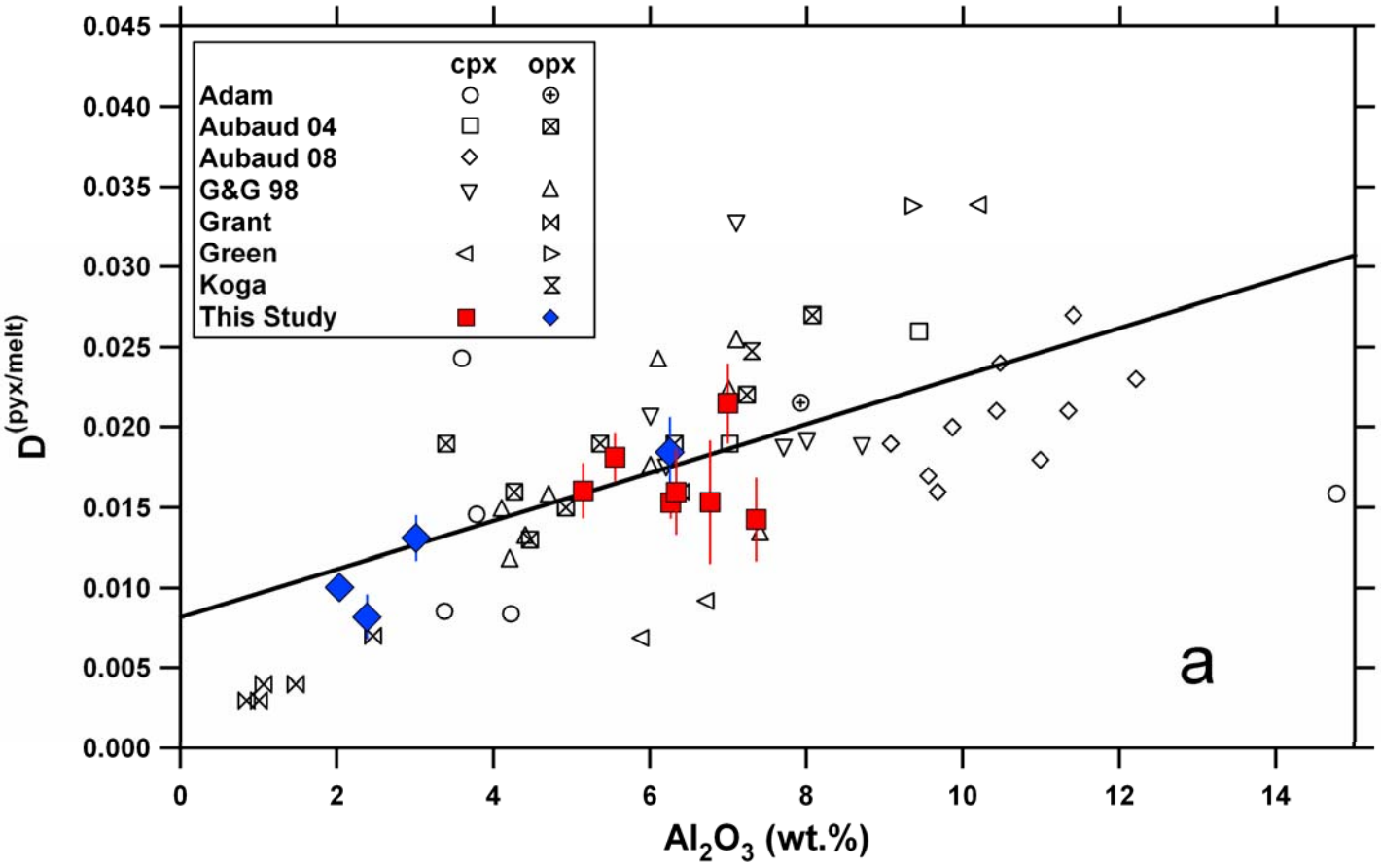
cpx
opx
Adam
Aubaud 04
Aubaud 08
G&G 98
Grant
Green
Koga
This Study
a
D(pyx/melt)
Al2O3 (wt.%)
0.045
0.040
0.035
0.030
0.025
0.020
0.015
0.010
0.005
0.000
0
2
4
6
8
10
12
14

Fig 2.10a.

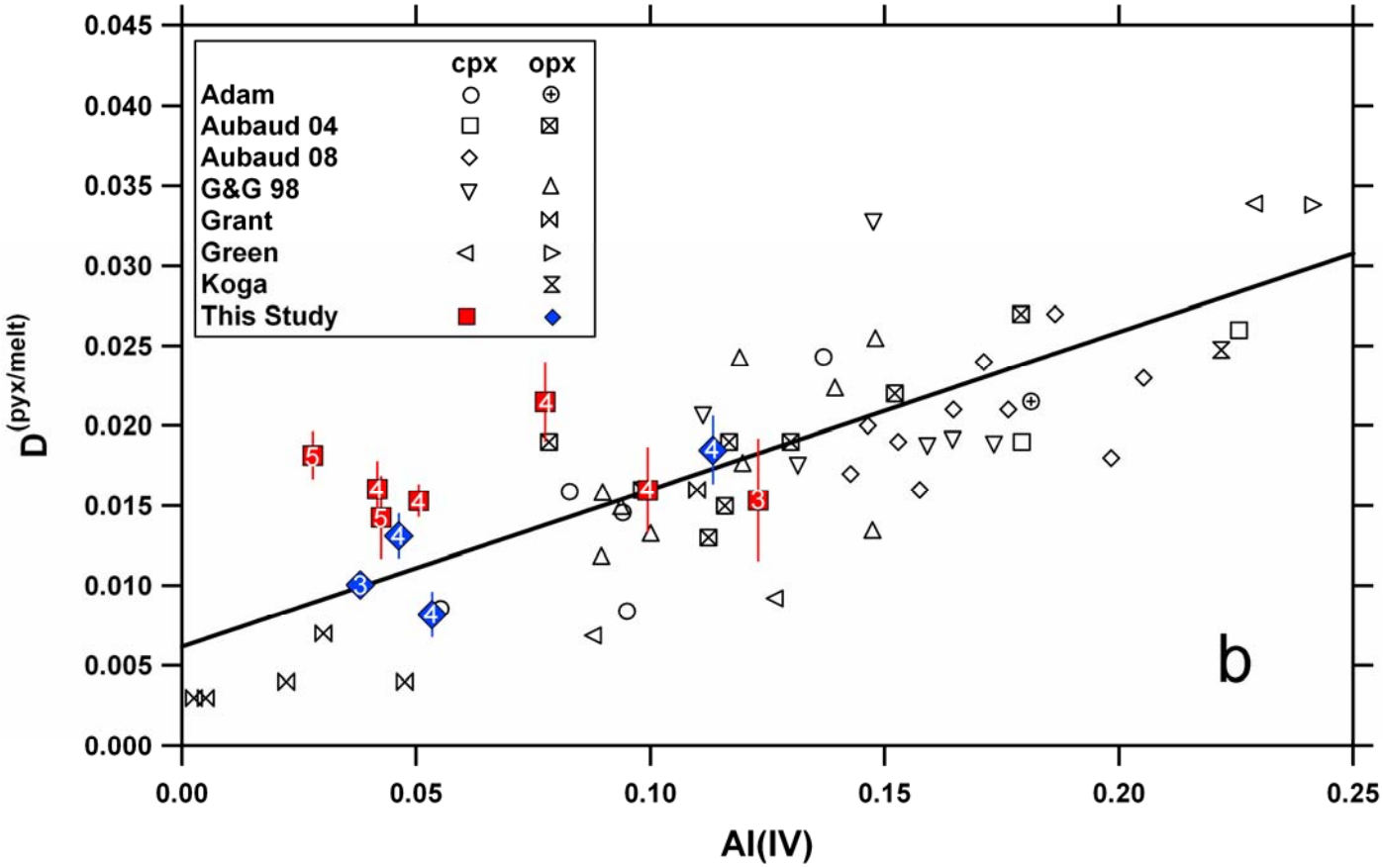
cpx
opx
Adam
Aubaud 04
Aubaud 08
G&G 98
Grant
Green
Koga
This Study
D(pyx/melt)
Al(IV)
b
0.045
0.040
0.035
0.030
0.025
0.020
0.015
0.010
0.005
0.000
0.00
0.05
0.10
0.15
0.20
0.25

Fig 2.10b.

Figure 2.10. a) Al_2O_3 in pyroxenes versus $D_H^{pyx/melt}$. **b)** Pyroxene tetrahedral aluminum component versus $D_H^{pyx/melt}$. Data from this study includes pressure (GPa). Error bars in data from this study represent the difference in $D_H^{pyx/melt}$ when using H_2O contents in glasses derived from FTIR and SIMS. Equations of best fit lines can be found in the text. Data from previous studies include those of Koga *et al.* (2003), Aubaud *et al.* (2004), (2008), Grant *et al.* (2007), Hauri *et al.* (2006). Hauri *et al.* $D_H^{pyx/melt}$ data are derived from measurements on experiments from Gaetani & Grove (1998), Green *et al.* (2000), Adam & Green (2003), Adam (unpub.).

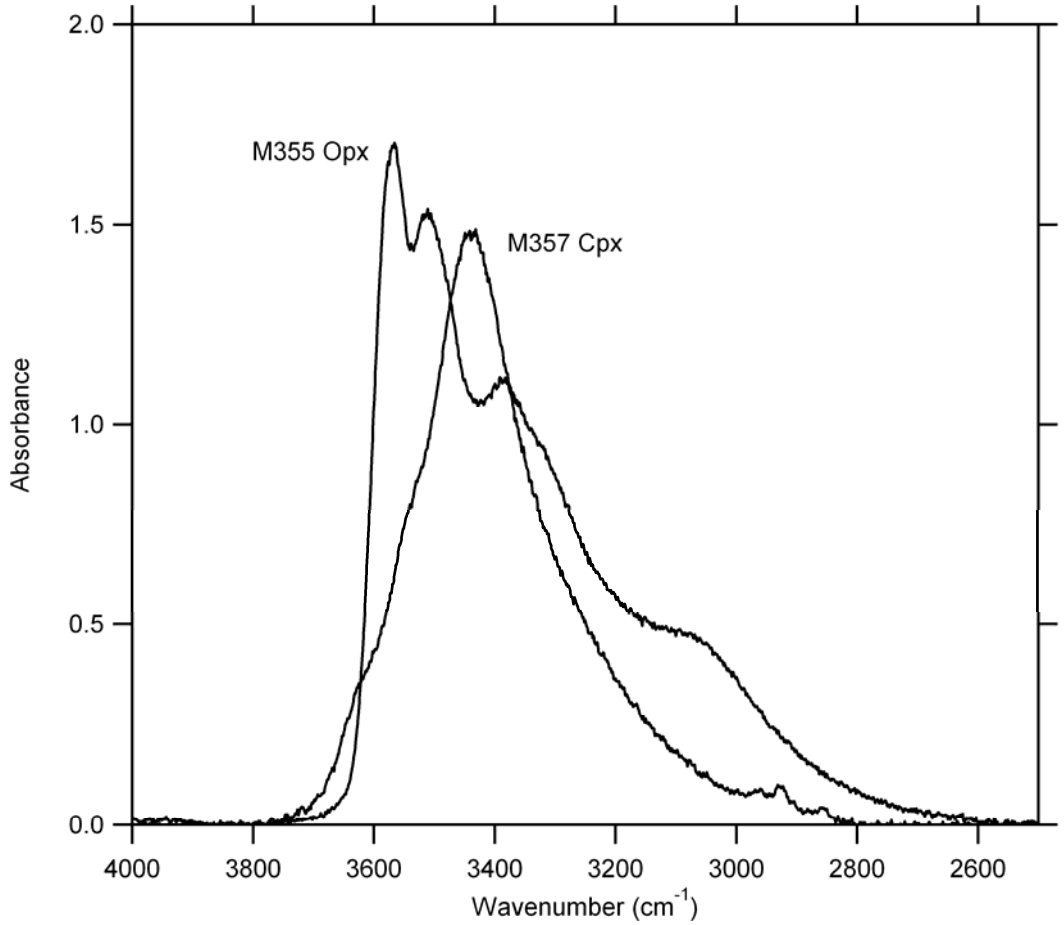

Figure 2.11. Unpolarized FTIR spectra of unoriented orthopyroxene from experiment M355 and clinopyroxene from M357. Spectra are normalized to 1 mm thickness. Peak areas yield concentrations of 970 and 760 ppm for M355 opx and M357 cpx, respectively, using the calibration of Paterson (1982), and are similar to SIMS-derived concentrations (1000 ppm and 1040 ppm, respectively).

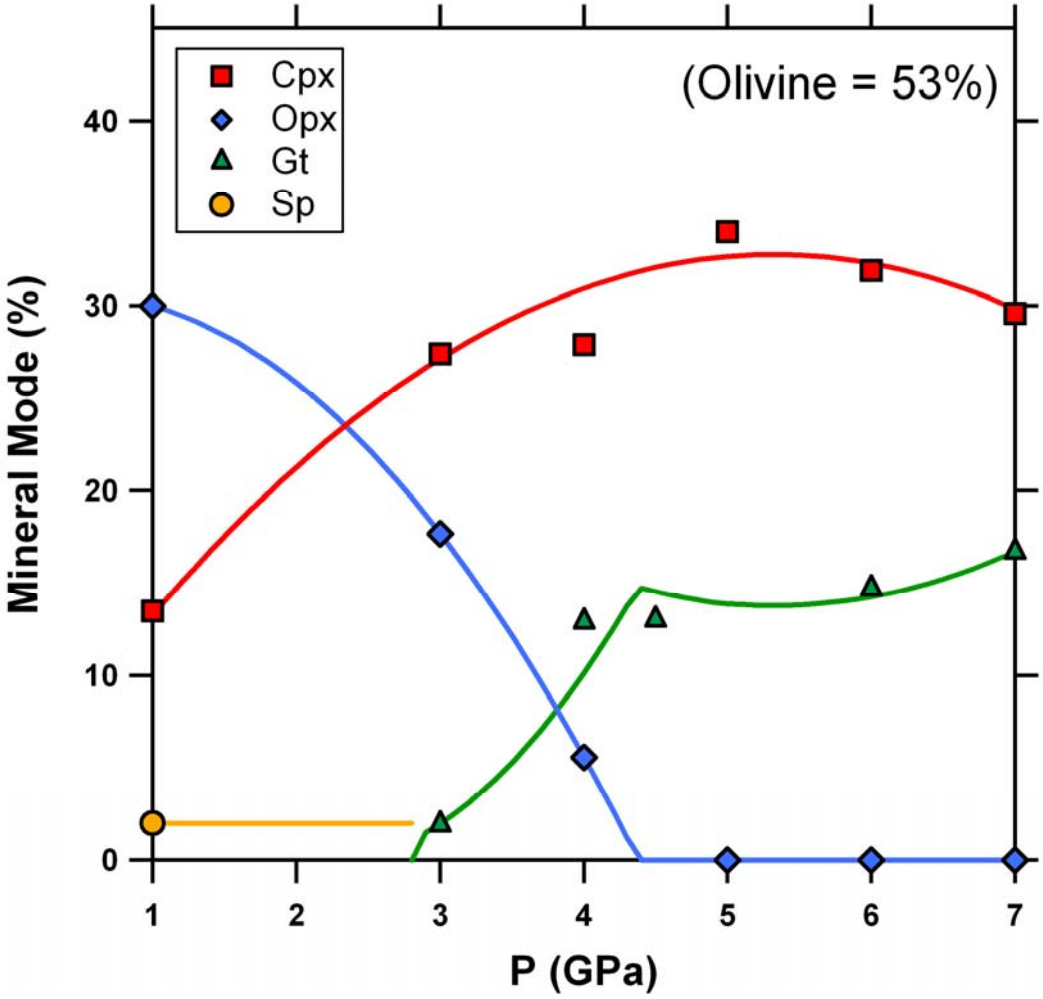

Figure 2.12. Mineral modes along the peridotite solidus from 1 to 7 GPa based on extrapolations to the solidus of the 1 GPa data of Baker & Stolper (1994) and Baker *et al.* (1995) and the 3-7 GPa data of Walter (1998). The mode of cpx and opx are given by

$C^{cpx} = -1.024P^2 + 11.09P + 3.267$, and $C^{opx} = -1.983P^2 + 1.784P + 30.20$. Olivine is constant at 53%, spinel is 2% from 1 to 2.8 GPa, and garnet is the difference calculated by closure from olivine and pyroxene modes. In the spinel facies, the mode differs from unity by up to 2%, but this has negligible influence on the calculated mode.

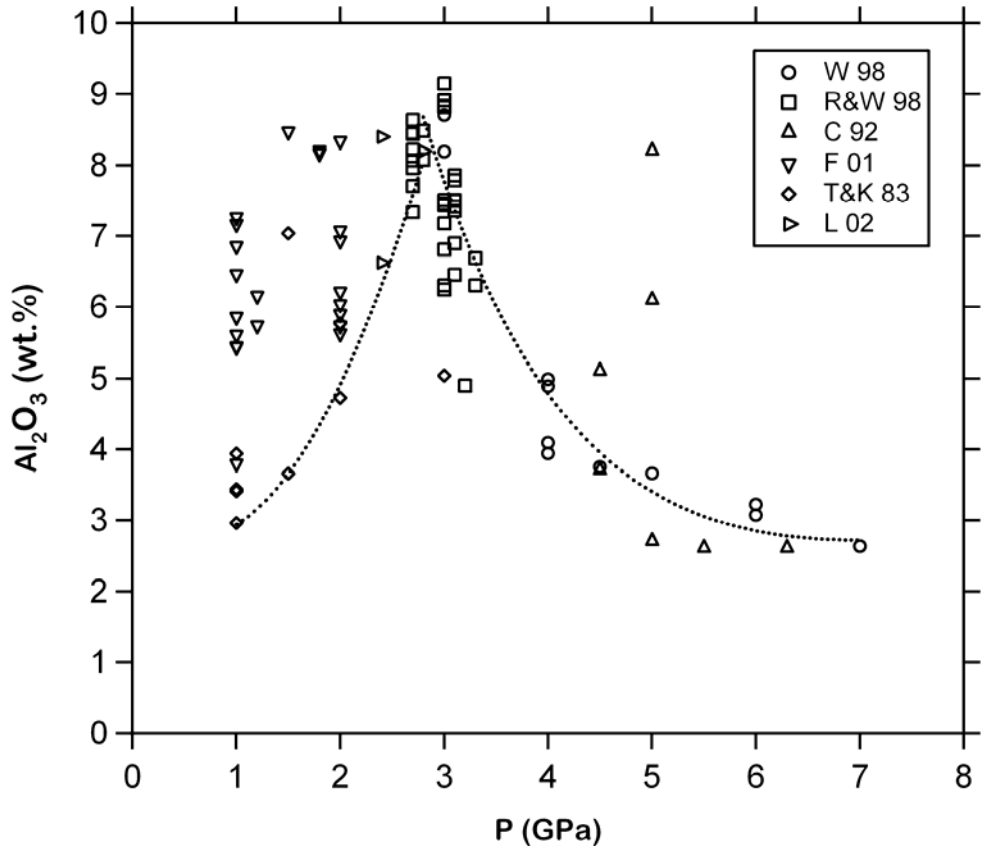

Figure 2.13. Al_2O_3 concentration in pyroxenes from experiments on natural and near-natural materials near the peridotite solidus. Data from Takahashi & Kushiro (1983), Canil (1992), Baker & Stolper (1994), Robinson & Wood (1998), Walter (1998), Falloon *et al.* (2001), Longhi (2002). The scatter in Al_2O_3 at a given pressure may reflect experimental uncertainties as well as the variations in composition, melt fraction, and

phase assemblage in the experiments. We adopt a parameterization of these data that tends to skirt the minimum Al concentrations, which has the effect of making H_2O less compatible in peridotite than it might be. In the spinel peridotite region (up to 2.8 GPa), the paramterization is given by C_{Al2O3}^{pyx} =1.0874*P^2-1.28852P+3.138, where P is in GPa. In the garnet peridotite region (above 2.8 GPa), the parameterization is C_{Al2O3}^{pyx} =34.409exp(-0.66435*(P-0.5619))+0.3200P.

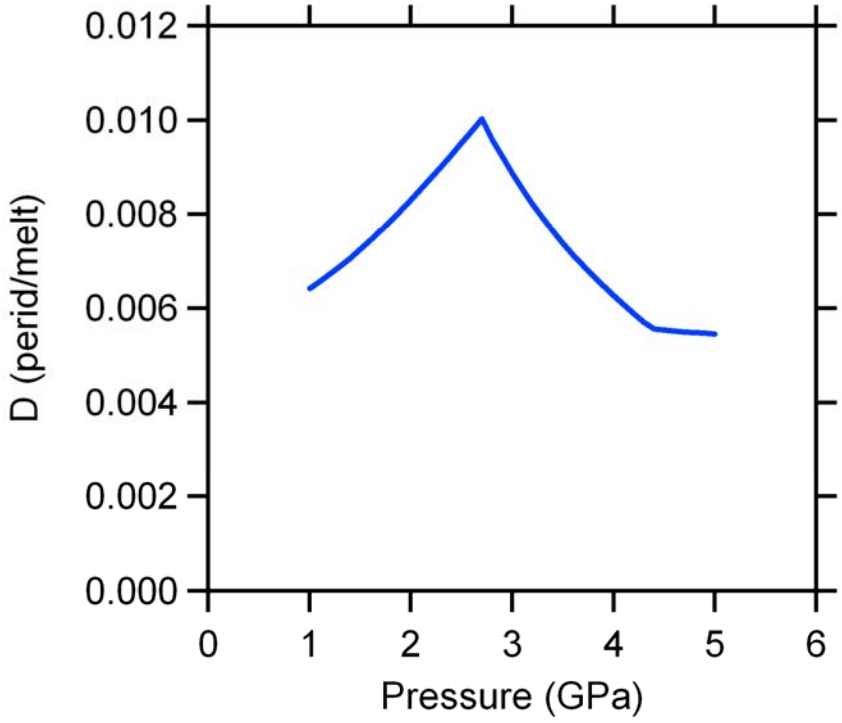

Figure 2.14. $D_H^{perid/melt}$ from 1 to 5 GPa, derived from mineral modes along the solidus, as well as mineral/melt hydrogen partitioning from previous studies as well as this study. From 1–3 GPa $D_H^{perid/melt}$ increases with pressure (to a maximum at 3 GPa) as a result of increasing pyroxene Al content (and therefore increasing $D_H^{pyx/melt}$) along the solidus from 1–3 GPa. The onset of garnet stability beyond 3 GPa diminishes Al content in the

pyroxenes (and therefore decreasing $D_{\mathrm{H}}^{\mathrm{pyx/melt}}$) , which contributes to a $D_{\mathrm{H}}^{\mathrm{perid/melt}}$ decrease from 3 to 5 GPa. The $D_{\mathrm{H}}^{\mathrm{perid/melt}}$ is likely a minima, owing to the use of pyroxene solidus compositions with the least Al, and therefore H_2O contents in partial melts derived from our $D_{\mathrm{H}}^{\mathrm{perid/melt}}$ represent a maxima.

Chapter III

The effect of H_2O on partial melting of garnet peridotite at 3.5 GPa

We present experimental determinations of the influence of H_2O on partial meting of garnet peridotite at 3.5 GPa. We employ a synthetic analogue of fertile peridotite similar to KLB-1 with bulk H_2O contents of 1.5, 2.5, and 5 wt. %. Experiments were performed at temperatures ranging from 1200-1450°C, and produce complex polyphase regions of quenched melt. Detailed analysis of these quenched regions by EMPA and LA-ICP-MS allow reconstruction of partial melt compositions. Mass balance indicates that melt fractions (*F*) range from 0.17-0.33 and dissolved water contents range from 4.5 to 23.5 wt. %. One exceptional experiment produced quenched glass that allowed independent verification of major element and H_2O content of partial melts by FTIR. Partial melts are highly magnesian (19-27 wt.% MgO), low in SiO_2 (41-49 wt.%), with high CaO (8-14 wt.%) and CaO/Al_2O_3 (0.9-1.3). Although ultramafic, the partial melts are distinct from komatiites as they are alkalic rather than tholeiitic. The high CaO and CaO/Al_2O_3 suggest similarities to ankaramites from island arcs, though the latter are much less magnesian. Compared to dry partial melts, hydrous partial melts of garnet peridotite are depleted in SiO_2 and Al_2O_3 and enriched in MgO, FeO*, and CaO; these effects are opposite to that of water on spinel peridotite melt compositions. The alkalic character of the melts may be owing in part to association of OH^- with network modifying cations in high pressure, depolymerized melts and in part to low-temperature stabilization of garnet, which

enhances CaO/Al_2O_3. The influence of H_2O on enhanced melting of garnet peridotite can be quantified by the difference in temperature required to achieve a given melt fraction under dry and wet conditions, ΔT, which is controlled by the concentration of H_2O dissolved in the melt. For melts that contain 1.5, 5, 10, and 15 wt. % H_2O, respectively, the experiments indicate values of ΔT of 50, 150, 250, and 300 °C. At modest H_2O contents (<10 wt.%), these results are consistent with previous models used to parameterize dehydration melting in the deeper parts of oceanic basalt source regions. At higher H_2O contents, the results diverge to lower values of ΔT, perhaps owing to increasing concentrations of H_2O species in silicate liquids.

Key words: experimental petrology; freezing point depression; hydrous garnet peridotite; melt fraction; partial melting

INTRODUCTION

H_2O has a key influence on the production and the composition of partial melts in the mantle. This is most evident in subduction zone environments, where partial melts can contain large amounts of H_2O (e.g., Wallace, 2005), but is also true beneath ridges and oceanic islands, where small amounts of H_2O may have a significant effect on the locus of partial melting and the composition of aggregated melts (Asimow & Langmuir, 2003). It may also be true in deeper parts of the mantle, where hydrous melting is implicated in observed geophysical anomalies (Bercovici & Karato, 2003; Hirschmann, 2006). In the last 40 years, there have been many studies of hydrous melting of mantle peridotite (e.g., Lambert & Wyllie, 1968; Kushiro, 1972; Green, 1973a; Mysen & Boettcher, 1975;

Hirose & Kawamoto, 1995; Gaetani & Grove, 1998; Kawamoto & Holloway, 1997; Grove *et al.*, 2006), yet there remain important aspects that are poorly known. In particular, the quantitative influence of H_2O on the proportion and composition of partial melts of garnet peridotite are not well-constrained and more generally, comparatively little data are available regarding the influence of pressure on hydrous melting. Hydrous melting of garnet peridotite may occur beneath ridges and oceanic islands (Hirth & Kohlstedt, 1996; Asimow & Langmuir, 2003; Ito *et al.*, 2003; Hirschmann, 2006; Hirschmann *et al.*, 2009), and the effect of pressure on melt production may be of importance to understanding melting above subduction zones.

The most obvious effects of H_2O on partial melting of peridotite are a dramatic lowering of the solidus (Kushiro *et al*., 1968; Green, 1973b; Mysen & Boettcher, 1975; Kawamoto & Holloway, 1997; Grove *et al.*, 2006) and enhanced production of partial melt (Stolper & Newman, 1994; Gaetani & Grove, 1998; Hirschmann *et al.*, 1999; Asimow & Langmuir, 2003). Experimental quantification of the influence of H_2O on melt production from spinel peridotite includes the studies of Hirose and Kawamoto (1995), Hirose (1997), Gaetani and Grove (1998), and Hall (1999). Studies of hydrous melt production from garnet peridotite include experiments from Kawamoto and Holloway (1997) and Hall (1999), and at very high pressure (10-24 GPa), Litasov and Ohtani (2002) and Kawamoto (2004). Hirschmann *et al.* (2009) found that all of these could be parameterized with a single relatively simple cryoscopic parameterization, though the collective scatter in the data is large and more high-quality data are needed to better parameterize the influence of H_2O on melt production in the mantle.

The compositions of partial melts of peridotite are also affected by H_2O. Hydrous partial melts of spinel peridotite, renormalized on an anhydrous basis, tend to be more silicic and aluminous and have less FeO* and MgO than their dry counterparts (Hirose & Kawamoto, 1995; Hirose, 1997; Gaetani & Grove, 1998). In contrast, inverse experiments long ago showed that hydrous alkaline partial melts, with low SiO_2 and low Al_2O_3 and high FeO and MgO, can be in equilibrium with garnet peridotite residua (Bultitude & Green, 1967-1968; Green, 1973a), suggesting that hydrous partial melts of garnet peridotite are alkalic. Similarly, Kawamoto and Holloway (1997) found that H_2O-rich partial melts of garnet peridotite at 5-11 GPa are very low in SiO_2 and Al_2O_3 and resemble highly alkalic partial melts such as kimberlite. Thus, the compositions of hydrous partial melts of garnet peridotite seem to be quite distinct from those derived from hydrous spinel peridotite.

Experimental investigations of hydrous partial melting of peridotite at high pressure present severe experimental challenges. Above 3 GPa, partial melts of dry peridotite rarely quench to glass (e.g., Walter, 1998), and the problem is exacerbated for hydrous melts. The heterogeneous products produced during quenching hinder accurate analysis of melt compositions and, critically, prevent direct analysis of the dissolved H_2O content. Accurate determination of the compositions of heterogeneous quenched melts requires large regions free from pre-existing crystals, which in turn prohibits quantitative examination of experiments with small fractions of melt. This is most unfortunate, because H_2O-induced partial melting produces small melt fractions in many natural environments, such as beneath ridges and oceanic islands (e.g., Asimow & Langmuir,

2003). Also, the high temperatures prevailing near the dry solidus of garnet peridotite (>1450 °C) cause additional experimental problems – at these temperatures, H_2O tends to be lost through experimental capsules by diffusion and Fe from experimental charges alloys with containers (Hirose & Kawamoto, 1994; Gaetani & Grove, 1998; Hall *et al.*, 2004).

One approach to overcoming these difficulties is to perform experiments that quantitatively parameterize the effect of H_2O on partial melting, thereby allowing extrapolation to the conditions of hydrous melting in the mantle. For example, hydrous peridotite partial melting experiments can be performed with greater bulk water contents than those estimated in the upper mantle. This reduces the experimental temperatures required to generate appreciable, analyzable, melt fractions and should also minimize open system effects such as diffusive loss of H_2O and Fe alloying with capsule material. Unfortunately, adding more H_2O to peridotite further inhibits production of homogenous glass, so determining the equilibrium composition of hydrous melts must be overcome by other means. Here we present experiments documenting hydrous partial melting of garnet peridotite at 3.5 GPa with variable amounts of added H_2O. Our experiments produced large melt pools that allow many individual determinations of the melt composition by electron microprobe analysis (EMPA). By filtering the EMPA data by an equilibrium criterion, we extract the compositions of melts unaffected by quench modification. These melt pools were also analyzed by LA-ICP-MS. The LA-ICP-MS data provide better volume-averages of the heterogeneous quench products than individual EMPA points. Mass balance calculations then allow us to deduce temperature-H_2O-melt fraction

relationships and hence the influence of H_2O on the production of partial melts of garnet peridotite.

METHODS

Starting materials and experimental procedures

Experimental conditions and run products are compiled in Table 3.1. The starting materials for the experiments consisted of a peridotite base composition combined in various proportions with a hydrous component having the composition of either olivine + 10 wt.% H_2O or olivine + 18 wt. % H_2O. The base composition was synthesized from reagent grade oxides and carbonates. An Fe-free mixture was first decarbonated at 1000 °C, followed by addition of FeO. The bulk composition was constructed to match the composition of Kilbourne Hole fertile spinel peridotite (KLB-1), which was verified by microprobe analyses of a glass bead made by containerless vitrification, as described by Davis *et al.* (2009) (Table 3.2). Two hydrous olivine compositions were also synthesized from a mixture of oxides and hydroxides and have the composition of $Fo_{89.7}$ + 10 and $Fo_{89.7}$ + 18 wt. % H_2O. The peridotite and the hydrous olivine compositions were combined to produce 3 separate, KLB-1-like, hydrous starting materials, with bulk water contents of 1.5, 2.5, and 5 wt. % H_2O (Table 3.2).

Experimental charges were contained in $Au_{75}Pd_{25}$ alloy capsules, which are reasonably effective at reducing H_2O loss from capsules (Kawamoto & Hirose, 1994; Gaetani & Grove, 1998; Hall *et al.*, 2004). To limit H_2O vaporization on welding, capsules were sealed by first using a lathe to shape their tops to a cone and then spot-welding. They were then reshaped into approximately 2×2 mm capped cylinders.

Additionally, some capsules were Fe-presaturated to further limit Fe loss during experiments. Presaturation was accomplished by melting a mid-ocean ridge basalt in the capsule in a gas mixing furnace at 1250°C and with a CO/CO_2 gas stream set at an oxygen fugacity of ~QFM – 2.5 for 24 hours. The glass was then dissolved with HF.

Experiments were performed with a 1000-ton Walker-type multi-anvil apparatus. The multi-anvil was chosen for these experiments, rather than a piston-cylinder device, for several reasons. First, it has an hourglass-shaped thermal profile, with the hottest temperatures located along the sides of the capsule, which segregates melts into pools large enough to facilitate analysis by an electron microprobe. Second, there is a faster quench rate in the multi-anvil device, owing to the smaller furnace, and this improves the likelihood of quenching glass. Third, the very slow and controlled decompression of multi-anvil experiments limits the formation of decompression cracks in run products, which aids in preservation of sample textures during polishing.

The multi-anvil assemblies consisted of cast octahedra (MgO-Al_2O_3-SiO_2-Cr_2O_3) with integrated gasket fins. All experiments were carried out with straight-walled graphite furnaces, and the WC cubes in the multi-anvil assembly have 12 mm truncations. Type D ($W_{97}Re_3/W_{75}Re_{25}$) thermocouples were employed to control the temperature of experiments and were located directly above the capsule in the assembly. A temperature uncertainty of ± 15°C was determined for the multi-anvil from the calibration described in Dasgupta *et al.* (2004).

All experiments were performed at a force of 170 tons, which is equivalent to a pressure of 3.7 GPa based on the pressure calibration in Dasgupta *et al.* (2004). However,

this region of pressure space was calibrated with the quartz-coesite phase transition, which takes place several hundred degrees below the temperatures of the experiments of this study. To more accurately determine the pressure at our run conditions we performed a calibration based on the Al_2O_3 concentration of enstatite equilibrated with pyrope in the MAS system (Perkins *et al.*, 1981). Starting materials consisted of reagent grade MgO, Al_2O_3, and SiO_2, in proportions that produce an enstatite/pyrope ratio of 1.5:1. Oxalic acid was added as a flux, and constituted ~10 wt. % of the starting material. The mixture was homogenized under acetone in a mortar and pestle for 2 hours. The multi-anvil assembly for the pressure calibration is identical to the hydrous peridotite melting experiments, with the exception of the starting materials. Two experiments were carried out at temperatures of 1300 and 1400°C, respectively, with a force of 170 tons. Run products were sectioned and polished, and Al_2O_3 contents of enstatites were quantified by electron microprobe analysis (see Analytical Techniques for details). Using the model derived by Perkins et al. (1981), both the 1300 and 1400°C calibrations predict a pressure of 3.5 GPa (Fig. 3.1).

Analytical Techniques

Sample preparation

Following quench, each experimental capsule was extracted and sectioned with a 50 μm diameter tungsten wire saw. The grit from the wire saw was carefully removed from the exposed run product surface with a stream of acetone, and this surface was vacuum impregnated with Petropoxy 154 (Burnham Petrographics products) to help retain quench textures during polishing. Diamond lapping films of 3 and 1 μm grit were used to polish

the surfaces. Although a high-quality polish could be achieved on crystalline phases, the melt phase commonly formed a delicate, heterogeneous mat consisting of quench crystals, pores formerly occupied by hydrous fluid exsolved during quench, and, in some cases, quench-modified glass. These quench materials rarely polished to a uniform flat surface because the small interstitial phases were easily plucked. Typically, the quenched melt formed an uneven, recessed surface (Fig. 3.2). In one exceptional experiment, which we describe further below, the melt quenched to a large pool of homogeneous glass (Fig. 3.3).

Electron microprobe analysis

Major element concentrations of all phases from run products were determined by wavelength-dispersive spectroscopy using a JEOL JXA8900R electron microprobe (Tables 3.3, 3.5-3.8). A 15 kV accelerating voltage was used for all analyses along with a 10 nA beam current and a fully focused beam, with peak counting times of 10 seconds and background count times of 5 seconds for all elements. Standards consisted of olivine, enstatite, diopside, pyrope, hornblende, two basaltic glasses, Mn-hortonolite, omphacite, chromite, and K-feldspar, used in various, but consistent configurations to measure element oxide concentrations in olivine + orthopyroxene + quenched melt ± garnet ± clinopyroxene. Volatile migration under the electron beam was monitored by measuring Na count rates on both basaltic glass standards as well as quenched melt run products, and no reduction of the count rate was observed for counting times beyond 30 seconds. Regardless, Na and K were always measured first on their respective spectrometers.

Analysis of quenched melts by LA-ICP-MS

As an independent check on the composition of the melts from this study, 10 of the 19 samples were analyzed by laser ablation-inductively coupled plasma-mass spectrometry (LA-ICP-MS) to determine the composition of quenched melt regions (Table 3.4). Measurements were performed with a UP 193FX ArF (193 nm) excimer laser ablation system (New Wave^{TM} Research, Fremont, CA, USA) coupled to an Element XR sector-field ICP-MS (Thermo Electron GMBH, Bremen, Germany) at the Plasma Analytical Facility in the National High Magnetic Field Laboratory. Samples are placed in the UP 193FX ablation cell, and ablation-produced aerosols were swept into the mass spectrometer by a stream of ultra-high purity He gas, at a rate of 800 ml/min. To optimize the signal on the ICP-MS a stream of Ar gas (~900-1400 ml/min) was added downstream. Spot sizes for the samples of this study were 20, 35, or 50 μm in diameter, depending on the size of the quenched melt region. These spot sizes correspond to a sample volume of ~600 μm^3 (20 μm spot) to 3800-5000 μm^3 (50 μm spot) per analysis. Samples were ablated in line scan mode, with step sizes of 10 μm/s for 50 μm pits, and step sizes of 5 μm/s for 20 and 35 μm pits. The number of analyses for each glass is given in Table 3.4. The total volume of quenched melt analyzed by LA-ICP-MS for each average composition reported in Table 3.4 ranged from 1.3-5.0 x 10^5 μm^3. All analyses were performed with a repetition rate of 20 Hz and 100% power output (2.5 GW/cm^2, 12 J/cm^2). The peaks ^{23}Na, ^{25}Mg, ^{27}Al, ^{29}Si, ^{31}P, ^{39}K, ^{44}Ca, ^{47}Ti, ^{53}Cr, ^{55}Mn, and ^{57}Fe, were acquired by peak jumping in low mass resolution ($M/\Delta M = 400$), with a 10% mass window and an acquisition time of 50 ms for each peak top. Data were acquired exclusively with the Analog mode of the electron multiplier to avoid detector cross-over

issues (Humayun et al., submitted). A gas blank was subtracted to remove contributions to the measured intensities from molecular isobaric interferences and blanks stemming from the plasma. Measured intensities were converted to concentrations in oxide weight % using relative sensitivity factors (Humayun *et al.*, 2007; Gaboardi and Humayun, 2009) obtained on silicate glass standards, with all oxides determined normalized to 100%. Standards consisted of the MPI-DING glasses GOR128-G, ML3B-G, KL2-G, T1-G, StHs6/80-G, and ATHO-G (Jochum *et al.*, 2006). USGS glass standards BHVO-2G and BCR-2G were run as independent controls to validate standardization. Further details of the LA-ICP-MS technique, including substantiation of its accuracy and precision for major element analysis of complex quenched textures, can be found in Humayun *et al.* (submitted).

FTIR analysis of glassy quenched melt

One of the run products, experiment M418 (Fig. 3.3), produced a quenched melt with a glassy region large enough to perform Fourier transform infrared spectroscopy (FTIR). In addition to providing an opportunity for more precise microprobe analysis (see below), this allowed FTIR determination of dissolved H_2O and therefore enabled evaluation of the assumption that H_2O was conserved during experiments. FTIR analysis of this glass also allowed determination of the concentration of CO_2 that unavoidably infiltrated into the capsules from the multianvil assembly. We sectioned part of the capsule into a wafer with the tungsten wire saw, and parallel-polished each face of the wafer to a 1 μm surface. The thickness of the analyzed region was determined with a Zeiss Axio Imager™ microscope, which has a precision of 1 micron. Unpolarized FTIR analysis of

the glass was performed with a Nicolet Series II Magna-IR spectrometer fitted with a Nic-Plan microscope, using a white light source for far-IR OH-H_2O measurements and an infrared source for mid-IR CO_2 measurements. A KBr beamsplitter, and a liquid nitrogen-cooled MCT-A detector were employed for all measurements. Care was taken to measure glassy regions that were free of cracks, quench crystals or inclusions.

Concentrations of OH and H_2O, were determined from the combination bands in the 4500 cm^{-1} (hydroxyl) and 5200 cm^{-1} (molecular water) regions of the FTIR spectra (Fig. 3.12), using background subtraction methods and calibrations on hydrous glasses from Ohlhorst *et al.* (2001) (Fig. 3.12). The concentration of hydroxyl and molecular water was derived using the Beer-Lambert law:

$$c_i = \frac{M_i * A_i^*}{d\rho\varepsilon_i^*} \quad (1)$$

where c_i is the concentration, M_i is the molar mass, A_i^* is the integrated intensity (cm^{-1}), d is the sample thickness (cm), ρ is the density (g/l), and ε_i^* is the integrated molar absorption coefficient (143 and 154 $l \bullet mol^{-1} \bullet cm^{-2}$ for ε_{H2O}^* and ε_{OH}^*, respectively). Using an initial density of 2819 g/l, we iteratively solved for ρ (Eqn. 2) using the parameterization for hydrous basaltic glass from Ohlhorst *et al.* (2001):

$$\rho = (-20.8 \pm 6.6)c_{water} + (2819 \pm 13.5) \quad (2)$$

Combining c_{H_2O} and c_{OH} (Eqn. 1) represents the total H_2O content in the glass.

Additional FTIR analysis of the glass of experiment M418 allowed determination of CO_2 content that diffused into the starting materials during the experiment. This was done using the pair of IR active bands at ~1440 and ~1520 cm^{-1} resulting from the

antisymmetric stretch of CO_3^{2-} (Fig. 3.13), using a straight-line background correction. We use an integrated molar absorption coefficient of 69,500 l•mol^{-1}•cm^{-2}, based on the calibration of carbonated basaltic glass from Fine & Stolper (1986), and the iterated density determined for the hydrous glass FTIR measurement (Eqn. 2). These parameters, combined with the FTIR spectra predict that the glass contains 1.6 wt. % CO_2. This result is not surprising, as Gaetani & Grove (1998) report CO_2 contents of ~1.25 wt. % for glasses of similar composition with ~5 wt. % H_2O at 1.2 and 2 GPa, using AuPd capsules and a similar assembly design.

Estimating equilibrium melt compositions from EMPA and LA-ICP-MS analysis

Owing to the tendency of the experimentally-formed melts to crystallize during quench, the composition of the melt phase is heterogeneous and quench-modified. Therefore, to extract representative compositions of the equilibrium melt phase, we performed a large number of EMPA and LA-ICP-MS point analyses on each experiment, amounting to 75-250, and 44-213 individual spots, respectively, depending on the exposed cross-sectional area of the quenched partial melt regions. Experience suggested to us that selecting points manually always resulted in a biased set of analyses, as the user unavoidably oversamples regions with better polish, which are characteristically composed of particular minerals (chiefly clinopyroxene) quenched from the melt. Consequently, the analyses were performed over a systematic grid over the entire exposed regions of quenched melt. As melt fraction (F) becomes small, accurate determination of the melt composition is increasingly challenging. First, melt compositions under low F conditions cannot be precisely and accurately determined by LA-ICP-MS because the spot size approaches the

size of the melt pools, and thus limits the number of analyses that can be taken. For this reason, only 10 of the 19 experiments presented in this study were analyzed by LA-ICP-MS. Second, under low *F* conditions averages of EMPA analyses may not be wholly representative of equilibrium melt compositions, as regions of melt likely become quench-modified by the surrounding residue (owing to decreases in the volume/surface area ratio). Therefore, to eliminate EMPA analyses of spots that may have been affected by quench modification, we filtered the analyses based on the calculated value of the olivine/melt Fe/Mg exchange coefficient:

$$K_D = \frac{[X_{Fe}^{ol}][X_{Mg}^{melt}]}{[X_{Fe}^{melt}][X_{Mg}^{ol}]} \quad (3)$$

calculated between each melt analysis and the average olivine composition from the experiment. Only those melt analyses that produced values of K_D within a specified range were accepted as possibly representative of the equilibrium melt composition. The majority of EMPA and LA-ICP-MS analyses from experiments with 1.5 and 2.5 wt. % bulk H_2O show a nearly overlapping K_D range in the interval of 0.27-0.39, but the EMPA data include a spectrum of analyses that spread to lower K_D values. We interpret these lower values as quench-modified and therefore assume that the interval between 0.27-0.39 represents analyses that are close to equilibrium (Fig. 3.4, top panels). This range is very similar to results from previous studies (Ulmer, 1989; Gaetani & Grove, 1998; Falloon & Danyushevsky, 2000) applicable to anhydrous and hydrous peridotite partial melting systems for temperatures and pressures spanning 1000–1600ºC and 1 to 3 GPa.

For experiments with 1.5 and 2.5 wt. % bulk H_2O that have only been analyzed by EMPA the equilibrium melt compositions are therefore taken as the average of analyses with a K_D range of 0.27-0.39. Experiments with 5 wt. % bulk H_2O are treated similarly, except that the span of K_D values found from experiments analyzed both by EMPA and LA-ICP-MS are in the range between 0.27 and 0.50 (Fig. 3.4, middle panels). This upward shift in the K_D range may be due to the very high H_2O contents of these melts, as suggested by Toplis (2005). For experiments with 5 wt. % bulk H_2O, analyzed only by EMPA (i.e. Fig. 3.4, bottom panels), we employ this wider K_D range to filter melt analyses.

Comparison between LA-ICP-MS and EMPA analysis of melts, and estimation of equilibrium melt compositions.

Average compositions of filtered EMPA and LA-ICP-MS melt compositions are similar within statistical uncertainty except for Al_2O_3 and Na_2O (Table 3.4). For Na_2O, melt analyses by LA-ICP-MS yield concentrations that are –30% to +70% (with an average of +16%) relative of predictions based on Na mass balance between melt and residue. Measurements of the glassy region of melt in experiment M418 by EMPA and LA-ICP-MS yield broadly similar results of 0.7 and 0.9 wt. % Na_2O, respectively, while Na mass balance of M418 predicts a melt Na_2O content of 0.7 wt. %. However, for all other experiments EMPA analyses of Na_2O in the melts are anomalously low, ranging from –16% to –83% (with an average of –54%) of estimation by Na mass balance. We hypothesize that Na_2O concentrations in the quenched regions are highly heterogeneous, owing to the effects of quench and the possible redistribution of alkalis by fluids exsolved

during quench. Consequently, whereas the mean LA-ICP-MS analyses are quite close to those expected based on mass balance, individual uncertainties are large and that the microprobe analyses of Na_2O, sampling only the near-surface areas that are most affected by redistribution (or loss) of quench-produced fluids, are not reliable. It should be noted that regardless of the Na_2O melt content employed in the mass balance (LA-ICP-MS, EMPA, theoretical) there is no effect on the predicted *F* values and mineral modes of this study, and the only effect is variation in the residual sum of squares in the mass balance.

In the case of Al_2O_3, LA-ICP-MS analyses of the melt (Table 3.4) are, on average, 13% lower than corresponding analyses by EMPA. We do not believe that EMPA analysis is the source of error, as measurements of secondary glass standards with a range of Al_2O_3 contents were well-resolved in our analytical sessions– all Al_2O_3 analyses of secondary basaltic glass standards taken during EMPA sessions for each experiment agree to within 2% relative of accepted values. We suspect that the discrepancy is owing to a mis-calibration for Al_2O_3 during LA-ICP-MS analysis. Regardless, the use of Al_2O_3 contents determined by LA-ICP-MS has a minimal effect on the mass balance, with no effect on olivine mode, an average of a 3% relative error on *F*, and an average of a 5% relative error on opx mode, when compared to a mass balance using Al_2O_3 melt contents derived by EMPA.

Although there is general agreement between EMPA and LA-ICP-MS melt analyses (except for Al_2O_3 and Na_2O) we must consider which analytical technique provides the best data in determining the overall melt composition. In determining preferred melt compositions where both EMPA and LA-ICP-MS data exist for an

experiment (i.e. M387, M382, M418, M399, M412, M395, M411, M417, M426, M434) we base our recommendations on two considerations: 1) uncertainties for different oxides by each analytical technique, and 2) if appropriate, that the use of EMPA data will allow for a consistent comparison to experiments that have only been analyzed by EMPA (i.e. M384, M388, M396, M402, M423, M422). For minor elements MnO, Cr_2O_3, and TiO_2, LA-ICP-MS data sets have standard deviations that are, on average, ~4 times less than corresponding EMPA data (Tables 3.3 & 3.4). Therefore, we use LA-ICP-MS derived concentrations for these elements when data are available. For major elements SiO_2, FeO*, MgO, and CaO, the LA-ICP-MS data also have a lower standard deviation when compared to EMPA, but the difference is smaller and the mean concentrations are similar and so we use EMPA data for these elements. For reasons previously mentioned, we use EMPA data for Al_2O_3, and LA-ICP-MS data for alkalis when they are available. In Tables 3.3 and 3.4, preferred melt compositions are listed in bold. For purposes of mass balance and plots of comparisons of melt compositions found later in this paper, experiments with preferred melt compositions that combine EMPA and LA-ICP-MS data are normalized to 100 percent totals by holding LA-ICP-MS-derived element concentrations constant.

Mass balance, melt fractions, modal abundances, and corrections for olivine addition

Using the compositions of the bulk starting materials (Table 3.2) and those of the analyzed phases (Tables 3.3-3.8), the proportions of phases present in each experiment were calculated by mass balance using an unweighted least squares scheme (Table 3.9).

Fe was included as a separate phase in the mass balance to investigate the degree to which Fe was lost from the sample owing to alloying with the AuPd capsule. Residual sums of squares range from 0.004 to 0.104 and the median value is 0.035. This compares favorably to similar studies in both dry and volatile-fluxed systems (Walter, 1998; Gaetani & Grove, 1998; Dasgupta *et al.*, 2007b). Experiments yield relative Fe-losses in the range of 0 to 30%.

The addition of H_2O to starting materials as hydrous olivine increases the mode of olivine in the bulk assemblage and so makes the bulk composition more refractory than typical fertile peridotite. Therefore melt fractions generated from experiments using each of the hydrous batches of this study would be greater under the same conditions if the system were similar to a typical fertile peridotite such as KLB-1. Jaques & Green (1980) used this relationship, albeit in an opposite sense, to generate dry melts of pyrolite and lherzolite to investigate the generation of mantle derived primary magmas. In their study, starting materials consisted of pyrolite or lherzolite minus 40% olivine in order to facilitate large melt pools in equilibrium with peridotititic mineral assemblages. To determine pyrolite equivalent melt fractions, Jaques and Green (1980) simply multiplied nominal *F* values by the percentage of pyrolite in the system (60%). One consideration of this approach, however, is that it introduces a modest error to the effective Mg# (=100*Mg/(Mg+Fe)) of the starting material and hence to the resulting phase assemblage, because the olivine added does not have the same Mg# as olivine in equilibrium at the *P–T* conditions of the experiments. However, as discussed further below, the Mg# of olivine in our experiments is likely more influenced by the modest

amounts of Fe-loss to the AuPd capsules. Overall, the influence of shifts in olivine or bulk Mg# can be thought as causing the experimental charge to become more or less refractory and therefore as influencing the relationship between melt fraction and temperature. As detailed below, we chose to treat this by correcting the effective temperature of each experiment, and so the influence of olivine addition on the Mg# of equilibrium phases need not be considered when correcting melt fractions to typical bulk peridotite compositions. Therefore, we used an approach similar to Jaques and Green (1980) to estimate "olivine corrected" melt fractions of KLB-1 peridotite. The hydrous batches in this study with 1.5, 2.5 and 5 wt. % H_2O can be thought of as KLB-1 peridotite plus 13, 21.5, and 22.8% olivine, respectively (Table 3.2). We therefore divide the nominal melt fractions (F) of experiments using these hydrous batches by 0.87, 0.785, and 0.772, respectively, to produce values of F appropriate for typical fertile peridotite. Residual mineral modes are also normalized to account for this correction (Table 3.9).

RESULTS

Run product textures

For a given bulk water content, the highest temperature experiments produce the largest quenched melt regions, with harzburgitic residues. Garnet is present only below 1375 and 1300°C for starting materials with 1.5% and 2.5% bulk H_2O, respectively, and is not present in experiments with 5% bulk H_2O, even at temperatures as low as 1200°C. Cpx is present only in experiments ≤1350°C for the bulk composition with 1.5 wt. % H_2O. Quenched melt regions decrease in area with increasing temperature (Fig. 3.2). The thermal profile of the multi-anvil not only segregates melts to the outer edges of the

capsule, but it segregates mineral phases as well. A mineral assemblage dominated by olivine crystals grows adjacent to the melt pools, while orthopyroxene ± garnet ± clinopyroxene tend to concentrate at the top and bottom of the capsules (Fig. 3.2). Even though the majority of the partial melt phase is located at the outer edges of the capsule, interstitial melt remains throughout the majority of the capsule, allowing communication among all the phases.

Olivines form euhedral crystals, which grow up to 50 microns in diameter. Orthopyroxenes form sub-euhedral crystals that are 10-20 microns in diameter, and garnet and clinopyroxene, when present, form crystals less than 10 microns in diameter. Backscattered electron images of all run products suggest that crystalline phases are homogeneous. In many cases olivine EMP analyses were collected as a traverse of points across a single crystal in contact with melt, and these analyses reveal no zoning. For orthopyroxene, garnet, and clinopyroxene, crystals were too small to carry out a traverse of analyses to test for zoning, and instead single analyses of several crystals determined the averaged composition of these phases. However, the standard deviation among analyses of these phases suggests homogeneity between each crystal (Tables 3.6-3.8). It is possible that a thin quench rim (<10 microns) formed around olivine crystals in contact with melt, so as a result, care was taken to measure their interior regions.

Phase relations and compositions.

Melting relations

Irrespective of the bulk water content, trends in modes of residual minerals versus corrected melt fraction yield systematic trends for each of the bulk compositions (Fig.

3.5). The olivine modes suggest that greater bulk H_2O reduces the amount of residual olivine at a given melt fraction, though there is considerable scatter, which is likely owing to uncertainties in the measured SiO_2 contents of the melts (Table 3.3), and the effect these have on the mass balance. The orthopyroxene mode increases from 0.24 to 0.31 as melt fraction increases from 0.20 to 0.27, and then decreases to 0.1 as *F* increases to 0.39. This indicates that orthopyroxene is in reaction relation until after the exhaustion of cpx and garnet, as has also been found for partial melting of anhydrous garnet peridotite (Walter, 1998). Garnet remains as a residual phase until *F* reaches a value of ~0.25 and clinopyroxene is only present in the lowest melt fraction (<0.24) experiments with 1.5% bulk H_2O.

Melt

Partial melts (Fig. 3.6) are MgO-rich (19-27 wt.%) and SiO_2-poor (41-49 wt.%) and are enriched in CaO (8-14%) but have modest Al_2O_3 concentrations (9.5-10.5 wt.%) and FeO* contents that range between 7 and 11 wt.%. Under the classification scheme of Le Bas (2000) these compositions are komatiitic. Liquid compositions are nepheline normative, except for experiments M388 and M418. If projected to lower MgO contents, for example, by olivine fractionation, they are basanitic to nephelinitic according to the classification of Le Bas (1989). With decreasing melt fraction, the most prominent changes are that MgO and SiO_2 diminish and CaO becomes enriched (Fig. 3.7). Al_2O_3 also becomes enriched, but the changes are small in magnitude. CaO/Al_2O_3 ratios range from 0.9 to 1.3, and increase with decreasing *F*. CaO concentrations are likely close to a maximum at the lowest melt fractions, where cpx becomes saturated. The scatter in the

FeO* trend is likely related to varying degrees of Fe-loss per experiment. The Mg#s of partial melts range from 78.5 to 86, and in general increase with increasing *F*. Owing to Fe-loss, the FeO concentrations at a given melt fraction or MgO concentration are lower than would be expected from hydrous partial melting of unmodified peridotite at 3.5 GPa. TiO_2 contents double (0.4–0.8 wt. %) as *F* decreases within the bounds of this study, and Cr_2O_3 (0.25–0.37 wt. %) and MnO (~0.17 wt. %) contents are constant at *F*. Na_2O contents are scattered, but appear to trend with the anhydrous peridotites of Walter (1998). The low bulk K_2O content (~0.02 wt. %) of our starting materials produces correspondingly low melt values, and scatter in these data likely reflect the limit of detection of EMPA. Only one experiment had a melt region that quenched to a glass and thereby allowed direct determination of its H_2O content directly. Inferred H_2O contents by difference from 100% totals from electron microprobe analysis yields unrealistic concentrations, likely due to the effect of plucked, uneven quench surfaces on microprobe analyses. Concentrations of H_2O in the remaining experiments were estimated based on mass balance (see below: Estimated versus measured H_2O the melt).

Anomalous analyses of low F melts

Experiments M386, M392, and M400 were the lowest temperature experiments of their respective bulk compositions (Table 3.1), and qualitatively the melt fractions in these experiments are the lowest of this study. However, this proved to be problematic because the melt pools were so small that it was difficult to achieve any analyses that were representative of the equilibrium composition. Of the analyses taken, the filtered microprobe data of these melt pools lead to an average composition that is more silica

rich and significantly more calcic than the other melts of this study would suggest when trending to low *F*. The disparity between the composition of these low *F* melt regions and the other, higher *F* regions is apparent when plotted in the Le Bas classification scheme (Fig. 3.7). The likely explanation for this disparity is that the filtered, low *F* analyses are not those of equilibrium melt, but are instead of cpx that formed from the melt upon quench. Consequently, we cannot use the melt compositions from these experiments, although the mineral assemblages and compositions remain of interest.

Mineral Compositions

The Mg#s of olivine and opx range from 92 to 94 and have considerable scatter when plotted as a function of *F*, owing to varying degrees of Fe-loss (Fig. 3.8a, 3.8b). However, the trend of olivine and opx Mg# versus melt fraction, when separated by Mg# of the charge, show trends that parallel that of dry 3 GPa Walter (1998) data, demonstrating that mineral Mg#s increase with increasing *F*.

For a given bulk H_2O content CaO and Al_2O_3 of opx vary little, but with increasing bulk H_2O, both CaO and Al_2O_3 concentrations are reduced (Fig. 3.9). With increasing melt fraction, clinopyroxenes increase in Al_2O_3 (2.5 to 3.2 wt. %) and Mg# (91.7 to 92.4), and decrease in CaO (19.5 to 17.6 wt. %), TiO_2 (0.10 to 0.06 wt. %), and Na_2O (0.7 to 0.6 wt. %) (Fig. 3.10). Clinopyroxenes quenched from melt are distinct from equilibrium pyroxenes, most notably in that they are highly enriched in Al_2O_3, TiO_2, and FeO* (Table 3.3). With increasing melt fraction, garnets increase in Cr_2O_3 (1.5 to 2.5 wt. %) and Mg# (83 to 87) and decrease in TiO_2 (0.18 to 0.08 wt. %), Al_2O_3 (22.7 to 22 wt. %), MnO (0.22 to 0.17 wt. %), and CaO (6.2 to 5.4 wt. %) (Fig. 3.11).

Estimated versus measured H_2O in the melt.

If H_2O has not been lost over the course of an experiment, one can estimate the partial melt H_2O concentration by batch melting (Shaw, 1970):

$$c_{\text{melt}}^{H_2O} = c_{\text{bulk}}^{H_2O}\left[\frac{1}{\left(D_{H_2O}^{\text{residue/melt}} + F(1 - D_{H_2O}^{\text{residue/melt}})\right)}\right] \quad (4)$$

where $c_{\text{bulk}}^{H_2O}$ is the bulk H_2O content and $D_{H_2O}^{\text{residue/melt}}$ is calculated from the mineral modes (from mass balance) along with their corresponding $D_{H_2O}^{\text{mineral/melt}}$ values (Tenner *et al.*, 2009; Table 3.9). Resulting H_2O contents based on mass balance range from 4.5 wt. % for the highest *F*, lowest bulk H_2O experiment to 23.5 wt. % for the lowest temperature, highest bulk H_2O content experiment (Table 3.9).

To investigate the H_2O retention of our experimental assembly, we compare the estimated H_2O melt content of experiment M418 (Eqn. 4) to the measured total H_2O content of the quenched glass that we quantified by FTIR. Using the $c_{\text{bulk}}^{H_2O}$ (1.5 wt. %), *F* (0.33), and $D_{H_2O}^{\text{residue/melt}}$ (0.0026), batch melting predicts a $c_{\text{melt}}^{H_2O}$ value of 4.5 wt. %. Using the data acquired by FTIR, the sum of the OH^- and H_2O concentrations of the 4500 and 5200 cm^{-1} combination bands (Fig. 3.12) produces a total water content of 4.31 wt. % in the quenched glass of M418 (Fig. 3.3). As the mass balance and FTIR measurements produce very similar results, we conclude that H_2O loss is minimal in our experimental assembly, especially considering that experiment M418 is at the upper-end of the temperature range of this study (1450ºC), where one would predict the greatest H_2O loss. Thus, the FTIR-derived H_2O content of experiment M418 validates estimates of the melt H_2O contents from the other experiments. This inference contrasts with that of

Kawamoto and Hirose (1994) and Hall et al. (2004), who found modest but systematic H_2O losses from AuPd capsules during experiments at similar durations and temperatures in piston cylinder experiments. We speculate that the hygroscopic MgO castable ceramic octahedra produced a comparatively hydrous environment in the multianvil assembly. However, we recognize that our assumed H_2O contents for experiments other than M418 are subject to fairly large uncertainties.

DISCUSSION

Hydrous partial melts of garnet peridotite are alkalic

A key characteristic of the melt compositions documented in this study is that they are alkalic. As mentioned in the Introduction, inferences that hydrous partial melts of garnet peridotite are alkalic go back many years (Bultitude & Green, 1967-1968; Green, 1973) and previous direct partial melting experiments on hydrous garnet peridotite have also found alkalic liquid compositions (Hall, 1999; Kawamoto and Holloway, 1997). It is generally thought that the addition of H_2O to peridotite enhances SiO_2 concentrations of partial melts (Kushiro, 1975) and that hydrous partial melting of peridotite produces silica-oversaturated liquids (e.g., Hirose & Kawamoto, 1995; Gaetani & Grove, 1998), but as elaborated below, this applies to spinel peridotite and not to garnet peridotite.

Comparison to other experimental studies of hydrous garnet peridotite

Our study represents an intermediate set of conditions between those of Hall (1999), who performed hydrous peridotite partial melting experiments at 3 GPa with comparatively small bulk H_2O contents (0.5-0.75 wt. %), and the higher pressure (5-11 GPa), higher bulk H_2O content (14 wt.%) experiments of Kawamoto and Holloway (1997).

Unsurprisingly, the melt compositions in our experiments are intermediate between those of the two studies. Hall (1999) performed experiments using a sandwich technique (Stolper, 1980). Bulk H_2O contents in the experiments ranged from 0.5 to 0.75 wt. %. Partial melt compositions of Hall (1999) are similar to those from the present study (Fig. 3.15), given the slightly different total H_2O contents and pressures (3 vs. 3.5 GPa). The principal differences are that the liquids from Hall (1999) have lower CaO concentrations and CaO/Al_2O_3 ratios (0.4-0.9) than for our partial melts. The former difference occurs partly because many of the experiments of Hall (1999) are cpx saturated, but also liquids that are not cpx-saturated are systematically lower in CaO than corresponding liquids from this study. This may be owing to difference in H_2O content, although the CaO contents of our melts do not show systematic changes as a function of bulk H_2O. Differences in CaO/Al_2O_3 derive in part from differences in CaO, but are also in part owing to differences in pressure (3.5 vs. 3 GPa).

The partial melting experiments of Kawamoto and Holloway (1997) were performed with a similar starting material to this study (KLB-1 peridotite), but with much greater H_2O contents and at higher pressures (5-11 GPa). Compared to the present results, partial melt compositions are less silicic and aluminous, more FeO* and MgO-rich at a given melt fraction (Fig. 3.15) and CaO/Al_2O_3 ratios of high pressure hydrous melts are drastically higher (1.1-5.4). These shifts are similar in direction as expected for partial melting of dry garnet peridotite (Walter, 1998), but greater in magnitude. For example, variations in SiO_2 content are much greater for hydrous partial melts. Kawamoto and Holloway hypothesized that H_2O-undersaturated peridotite could be a source for

komatiites, and our melts have compositions that suggest that hydrous melting of fertile garnet peridotite at 3.5 GPa produces liquids with some similarities to komatiite magmas (Fig. 3.14). However, because the experimental partial melts are alkalic, komatiites cannot be derived from hydrous partial melts of fertile garnet peridotite. If komatiites are derived from hydrous partial melts of peridotite, they must derive from lower pressures and/or more depleted peridotite bulk compositions (e.g., Grove *et al.*, 1999).

Hydrous vs. nominally anhydrous partial melts of garnet peridotite

Compared to partial melting experiments of garnet peridotite at comparable pressures (Hirose & Kushiro, 1993; Walter, 1998), the hydrous partial melts have lower SiO_2 and Al_2O_3 and higher FeO*, MgO, and CaO (Fig. 3.15). These effects are similar to those of pressure itself. However, compositional shifts for the hydrous partial melts are more extreme, most notably for SiO_2 and CaO, meaning that the hydrous partial melts of garnet peridotite have lower SiO_2 and higher CaO than dry melts at any comparable pressure.

The effect of H_2O on partial melts of spinel versus garnet peridotite

As mentioned above, H_2O has a completely different influence on the compositions of partial melts of garnet peridotite than it has on partial melts of spinel peridotite (Hirose and Kawamoto, 1995; Hirose, 1997; Gaetani & Grove, 1998). In particular, hydrous spinel peridotite melts are more silicic and aluminous, and have lower FeO*, MgO, and CaO/Al_2O_3 than their anhydrous counterparts (Fig. 3.15). Therefore, the behavior of network modifying cations (Mg, Fe, Ca) and network forming cations (Si and Al) are affected in opposite manners for partial melts of garnet vs. spinel peridotite. Thus, whereas high Mg andesites might plausibly derive from hydrous partial melting of spinel

peridotite (Hirose, 1997), hydrous partial melts of garnet lherzolite are silica-depleted and alkalic.

Why are the effects of H_2O so different for partial melts of peridotite in the spinel and garnet stability fields? We suspect that two factors contribute to the difference. The first is owing to differences in the structures of high pressure and low pressure partial melts of peridotite, and the second is owing to the expansion of garnet stability at temperatures below the dry peridotite solidus.

With increasing pressure, the SiO_2 concentrations of all partial melts of peridotite are reduced (e.g., Hirose and Kushiro, 1993; Walter, 1998) and consequently the silicate network becomes increasingly depolymerized. As a consequence, the role of network modifying species can change. For example, Hirschmann *et al.* (1998) showed that alkalis increase the SiO_2 content of partial melts of peridotite at 1 GPa, but that the effect diminishes to negligible at 3 GPa. They argued that the influence of alkalis on silica activity arises chiefly by interactions with highly polymerized (Q^4) silica species (e.g., Hess, 1995) which are not abundant in the low-silica liquids that are generated at high pressure. The shift in influence of H_2O (or more specifically, OH^-) may be analogous to this. However, whereas alkalis greatly increase the SiO_2 of partial melts at low pressure and are approximately neutral at high pressure, hydrous melting at high pressure markedly diminishes SiO_2 in the melts. Thus, the explanation offered by Hirschmann *et al.* (1998) for alkalis provides only a partial explanation for the influence of H_2O at high pressure. Possibly, OH^- associates with network modifying cations (Mg^{2+}, Fe^{2+}, Ca^{2+}) in

high pressure melts, reducing the activity coefficients of MgO, FeO, and CaO in the melt and increasing their concentrations when buffered by peridotite minerals.

Another factor influencing melt compositions is expansion of the stability field of garnet. Garnet stability is enhanced at lower temperature, so by lowering the solidus temperature H_2O allows partial melts to be saturated with garnet to higher melt fractions. Thus, at 3.5 GPa under hydrous conditions, garnet persists up to a melt fraction of 0.25, whereas interpolation of the data of Walter (1998) suggests that it should be expended at about 0.15 for dry melting. Increased stability of garnet results in lower Al_2O_3 concentrations at garnet saturation and consequently, in higher CaO/Al_2O_3 ratios, which in turn, contribute to the alkalic character of the melts.

The formation of highly calcic alkalic liquids by partial melting of hydrous garnet peridotite raises the question as to whether deep partial melting above subduction zones may produce analogous magmas and whether any such magmas may be represented in arc-related lavas. Indeed, hydrous fluids are released by subducting slabs to pressures in excess of 4 GPa (Hacker, 2008), and so there is bound to be hydrous partial melting in the mantle wedge at depths where garnet is stable. Of course, the majority of hydrous arc-related magmas are much more silicic, but nepheline-normative ultra-calcic ankaramites, which are volumetrically minor but widespread in many arcs worldwide (e.g., Carr & Rose, 1984; Sisson & Bronto, 1998; Schiano *et al.*, 2000) have several important similarities to the partial melts produced in this study, including low SiO_2 (43-49 wt. %) and high CaO/Al_2O_3 (>1.1). On the other hand, these ultracalcic arc magmas are generally much lower in MgO (4-14%), are more enriched both in CaO (13-19%) and

Al2O3 (10-19%), and lack distinctive trace element signatures of garnet in their source (Schiano et al. 2000). Clearly, such lavas could not be generated directly from conditions similar to those of our experiments without significant modification, including fractionation and likely other processes in the mantle or crust, but our results do establish that liquids with similarities to arc ankaramites can be generated by deep hydrous melting of peridotite.

Arc-related ankaramites have not previously been considered to be plausibly derived from partial melting of peridotite. Schiano et al. (2000) argued that arc-related ankaramites are derived from pyroxenitic lithologies, in part because they believed that hydrous partial melts of peridotite must be silicic. Schmidt *et al*. (2004) found that hypersthene-normative ultracalcic magmas could be generated by partial melting of depleted peridotite in the presence of a mixed H_2O-CO_2 fluid at 1.5-2 GPa, but argued that nepheline-normative equivalents could not be generated in the presence of orthopyroxene, again owing to the low SiO_2 content of the lavas. Our experimental results contradict both of these conclusions and show that liquids with strong affinities to undersaturated ankaramites in arcs can indeed be generated by partial melting of hydrous garnet peridotite in the deepest parts of mantle wedges. Admittedly, more work would be required to make the link between these enigmatic rocks and deep melts of garnet peridotite, perhaps including consideration of the effects of source depletion of garnet and enhancement of alkalis either by lower degrees of partial melting or metasomatic slab addition.

Influence of H_2O on melt production from garnet peridotite

One of the principal goals of this study is to determine experimentally the influence of H_2O on the extent of melting of peridotite. This is a key parameter in determining the role of dehydration of nominally anhydrous minerals on the locus and extent of melting beneath ridges and oceanic islands, in the low velocity zone, and in the deep upper mantle atop the 410 km discontinuity (Katz *et al.*, 2003; Hirschmann *et al.*, 2009; Hirschmann, 2010). Following Katz *et al.* (2003), the influence of water on partial melting can be illustrated by comparing the melt fraction produced from peridotite as a function of temperature under hydrous and nominally anhydrous conditions (Fig. 3.16a). With decreasing melt fraction, the temperature-melt fraction trend of a peridotite with a given bulk H_2O content deviates to progressively lower temperatures relative to the nominally anhydrous trend. This is owing to the increasing concentration of H_2O in the partial melt (Katz *et al.*, 2003). The deviation of the hydrous trend from the nominally anhydrous (or for convenience, "dry") trend at a given F is defined as ΔT:

$$\Delta T = T^{\text{dry}} - T^{\text{hydrous}} \tag{5}$$

ΔT is directly related to the dissolved H_2O in the melt owing to its cryoscopic influence (Hirschmann *et al.*, 1999; 2009; Katz *et al.*, 2003; Aubaud *et al.*, 2004). An analogous relationship has been considered for the influence of CO_2 by Dasgupta *et al.* (2007). The H_2O concentration, $c_{\text{melt}}^{H_2O}$, in a partial melt of peridotite with a given bulk composition, $c_{\text{bulk}}^{H_2O}$, at a particular melt fraction can be calculated from the batch melting relationship (Eqn. 4), provided that $D_{H_2O}^{\text{perid/melt}}$, the bulk peridotite/melt partition coefficient for H_2O, is known (e.g., Aubaud *et al.*, 2004; 2008; Hauri *et al.*, 2006; Tenner *et al.*, 2009). Thus, given a relationship between ΔT and dissolved H_2O in the melt (Fig. 3.16b), the trend of

melt fraction versus temperature can be calculated for a peridotite with a given bulk H_2O concentration (Fig. 3.16a). The experiments of the present study can help refine this relationship for partial melting of garnet peridotite.

The first step towards calculating ΔT versus dissolved H_2O in the melt from the present experiments is to estimate the relationship between temperature and melt fraction for dry melting of peridotite at 3.5 GPa. As there are few relevant data at precisely this pressure, we take the intercept of zero percent melting of dry fertile peridotite at 3.5 GPa from the solidus parameterization of Hirschmann (2000) and interpolate between the 3 and 4 GPa temperature-melt fraction trends determined by Walter (1998) (Fig. 3.17a) to yield:

$$T^{dry}\ (^{o}C) = 242.5F + 1523 \quad (6)$$

However, before we can examine the influence of dissolved H_2O on ΔT from our experimental determinations, we must account for experimental artifacts that influence their melt-fraction-temperature relationship. We have already discussed the influence of olivine mode on the melt fraction (see Methods section, above), but now we must address the effects of Fe-loss and CO_2 infiltration during the experiments.

Correcting ΔT for Fe-loss of the starting material

Previous studies (Kawamoto and Hirose, 1994; Gaetani & Grove, 1998; Hall, 1999; Hall *et al.*, 2004; Aubaud *et al.*, 2008) showed that AuPd capsules retain the majority of Fe in starting materials, but that some Fe-loss is common, even in cases where capsules are Fe-presaturated. With increasing bulk Mg#, peridotite becomes more refractory. To account for this, we consider the analysis of Hirschmann (2000), who demonstrated that the

lherzolite solidus at 3 GPa increases by 13.3°C/Mg# (Fig. 3.17b). If we assume that Mg# affects only the solidus temperature, meaning that the effect of Mg# on the temperature-melt fraction slope can be neglected, then the correction to the melting temperature of peridotite of any Mg# can be compared to that of normal fertile peridotite, which we take to be 89.6, that of KLB-1 (Davis *et al.*, 2009). This correction, given by:

$$T_{\text{Fe-loss}}^{\text{correction}} = 13.3 \bullet (\text{Bulk Mg\#}_{\text{post experiment}} - 89.6) \quad (7)$$

is added to the calculation of ΔT (Eqn. 5), thereby increasing ΔT in cases where there is Fe-loss and decreasing ΔT when there is Fe-gain (Fig 3.17c).

Correcting ΔT due to infiltration of CO_2 into the system

Like H_2O, CO_2 enhances the extent of partial melting of peridotite and the magnitude of this enhancement at 3 GPa was determined empirically by Dasgupta *et al.* (2007a):

$$\Delta T(^{\circ}\text{C}) = 27.04 \times C_{\text{CO}_2}^{\text{L}} + 1490.75 \times \ln[(100 - 1.18 \times C_{\text{CO}_2}^{\text{L}})/100] \quad (8)$$

where $C_{\text{CO}_2}^{\text{L}}$ is the dissolved concentration of CO_2 in weight percent. We assume that this relationship is not appreciably different at 3.5 GPa. Thus, using the CO_2 content derived from FTIR measurements on the quenched glass of experiment M418, we back-correct to a CO_2-free system, and this has the effect of diminishing the values of ΔT for each experiment (Fig. 3.17c). We assume that all the partial melts have the same concentration as the measured CO_2 in the melt (glass) of M418 (1.6 wt.%), which corresponds to a temperature subtraction of 14.8 degrees from ΔT. Together with the original relation for ΔT (Eqn. 5), the relationship taken for dry melting of peridotite at 3.5 GPa (Eqn. 6), and the correction for Fe-loss (Eqn. 7), this allows calculation of ΔT from temperatures of our 3.5 GPa experiments for which the melt fraction is known:

$$\Delta T = 242.5F + 1523 - T^{\text{hydrous}} + 13.3 \bullet (\text{Bulk Mg\#}_{\text{post experiment}} - 89.6) - 14.8 \quad (9)$$

Influence of dissolved H_2O in the melt on ΔT

Calculated values of ΔT from our experiments, together with those calculated in a similar fashion from previously published experiments from 1-3 GPa are shown in Figure 3.18. Our experimental data at 3.5 GPa suggests that 5, 10, and 15 wt.% dissolved H_2O result in lowering the temperature of melting, ΔT, of approximately 150, 250, and 300 °C, respectively. This trend is in general agreement with previous determinations, although the collective older data show much more scatter.

Trends in ΔT versus dissolved H_2O (in units of weight percent, C_{H2O}) can be modeled by several approaches. Katz *et al.*, (2003) adopted an empirical parameterization of the form:

$$\Delta T = \mathrm{K} C_{\mathrm{H2O}}^{\gamma} \quad (10)$$

As shown in Figure 3.18, the 3.5 GPa data can be fit to this function with K=70.9 and γ=0.552. The next simplest approach is a parameterization based on the cryoscopic equation:

$$T = \frac{T(F)_{\text{peridotite}}}{\left(1 - \frac{\mathrm{R}}{\Delta \hat{S}^{\text{fusion}}_{\text{peridotite}}} \ln\left(1\text{-}X^{\text{melt}}_{\text{OH}^-}\right)\right)} \quad (11)$$

(Hirschmann *et al.*, 1999, 2009; Aubaud *et al.*, 2004), where R is the gas constant, $T(F)_{\text{peridotite}}$ is the temperature of melting of dry peridotite at a melt fraction of (F), $\Delta \hat{S}^{\text{fusion}}_{\text{peridotite}}$ is the molar entropy of fusion of peridotite, and $X^{\text{melt}}_{\text{OH}^-}$ is the mole fraction of dissolved OH^- in the melt. Here it is presumed that all H_2O is dissolved as OH^- (e.g.,

Hirschmann *et al.*, 2009) and a key variable is the assumed molar unit of silicate melts, such as an oxide or 8-oxygen unit (Hirschmann *et al.*, 2009). Values of $\Delta\hat{S}^{\text{fusion}}_{\text{peridotite}}$ can then be calculated from calorimetric determinations of the entropy of fusion per unit mass (Kojitani & Akaogi, 1997) and estimates of the molecular weight per mole. Fits to this form for oxide molar units (Hirschmann *et al.*, 2009) are displayed in Figure 3.18.

Finally, a more advanced thermodynamic approach is to account for the likely speciation of dissolved H_2O as OH^- and H_2O species according to the reaction:

$$H_2O + O^{2-} = 2\ OH^- \tag{12}$$

To do this, we adopt the non-ideal speciation model of Stolper (1989) and Silver *et al.*, (1990). We can apply this model to a cryoscopic calculation by equating the activity of the oxygen ion with that of the silicate component of the melt (e.g., Silver & Stolper, 1985; Stolper, 1989), which gives:

$$T = \frac{T(F)_{\text{peridotite}}}{\left(1 - \frac{\text{R}}{\Delta\hat{S}^{\text{fusion}}_{\text{peridotite}}} \ln\left(a^{\text{melt}}_{O^{2-}}\right)\right)} \tag{13}$$

where $a^{\text{melt}}_{O^{2-}}$ is activity of oxygen in the silicate melt and is calculated from the non-ideal speciation model of Silver *et al.*, (1990). This too is shown in Figure 3.18.

Among the different calculated trends of ΔT versus dissolved H_2O content, none is ideal. Naturally, the empirical fit to the experimental data in the form of Katz *et al.*, (2003) provides the closest match to the actual experiments. It also matches well the 3 GPa data of Hall (1999). However, the fit produces unrealistically large increases in ΔT at very small H_2O contents, where data are lacking; e.g, providing 90 °C of freezing point

depression for just 1.5 wt. % dissolved H_2O. This would have the effect of greatly enhancing the influence of small amounts of H_2O during dehydration partial melting of peridotite compared to previously adopted thermodynamically-based models (Hirschmann *et al.*, 2009). Recent direct experimental constraints on dehydration melting of peridotite at similar pressures suggests that these models are accurate (Ardia *et al.*, in prep), and that therefore we do not favor application of the empirical parameterization.

The thermodynamically-based calculations do not have a similarly strong influence on ΔT at low concentrations of dissolved H_2O, but are only partially successful at reproducing the experimental data at high H_2O concentrations. For low melt H_2O concentrations the relatively simple cryoscopic model with an oxide mole fraction for silicate and all H_2O as hydroxyl provides a good match to the experimental data up to ~10 wt. % H_2O. Between 8 and 10 wt. % melt H_2O the data exhibit some scatter in ΔT (~40°), with simple cryoscopy providing a better fit to data at the upper ΔT values, while the speciation model fits the lower ΔT data over this interval. Beyond 10 wt. % dissolved H_2O in the melt the simple cryoscopic model overestimates freezing point depression, whilst the speciation model with a single oxygen mole fraction of silicate provides a better fit to the experiments with more H_2O-rich melts. We presume that a more satisfying fit to the data across a wider range of H_2O concentrations would be attained with a thermodynamic model that incorporated larger silicate molar units and a rigorous speciation model between H_2O and OH-, but such a formulation is beyond the scope of the present work. For conditions where the melt has <10 wt. % H_2O, such as are expected by dehydration partial melting beneath ridges and oceanic islands (Hirschmann *et al.*,

2009), and for all but the most extreme conditions beneath island arcs (Grove *et al.*, 2003; Wallace, 2005), the simpler formulation adequately represents the experimental data. For more extreme conditions with highly hydrous partial melts, as might apply during the initiation of partial melting near the hydrous peridotite solidus (Grove *et al.*, 2006) or owing to dehydration partial melting above the 410 km discontinuity (Hirschmann *et al.*, 2006), larger H_2O concentrations may prevail and a more-advanced speciation model may be required. We note, however, that such processes are, respectively, either at much lower temperature or much higher pressure than the present experiments.

CONCLUSIONS

• Hydrous peridotite partial melts at 3.5 GPa are highly magnesian, low in SiO_2, have high CaO/Al_2O_3, and are alkalic. Although technically classified as komatiites according to the scheme of Le Bas (2000), they have similarities to ankaramites found in arc settings, owing to their low SiO_2 and high CaO/Al_2O_3 .

• Addition of water to garnet lherzolite has an influence on partial melt that is the opposite of its influence on spinel lherzolite. Compared to their anhydrous equivalents, hydrous partial melts of garnet peridotite are *depleted in* SiO_2 and Al_2O_3, and *enriched* in MgO, FeO*, and CaO, whereas hydrous partial melts of spinel peridotite are enriched in SiO_2 and Al_2O_3, and depleted in MgO, FeO*, and CaO. Thus, the influence of water on the structure and energetics in equilibrium with peridotite at high pressure is different from its effect at low pressure; at high pressure, H_2O may associate with network forming cations (Mg, Fe, Ca), rather than network modifying cations (Si and Al).

• The addition of H_2O to garnet peridotite enhances the extent of partial melting at 3.5 GPa, such that liquids with 5, 10, and 15 wt. % H_2O, respectively achieve a given melt fraction at 150, 250, and 300° C below that required to achieve the same melt fraction from dry peridotite. The effect is non-linear, becoming less potent per increment of H_2O addition at higher H_2O concentrations. Parameterization of these freezing point depressions by simple cryoscopic approximation is successful to ~10 wt.% H_2O. At higher H_2O concentrations, cryoscopy overpredicts the extent of freezing point depression, likely owing at least in part to speciation of dissolved H_2O as OH^- and H_2O.

Table 3.1. Experimental conditions and run products.

Exp. #	Bulk H_2O (wt.%)	T (°C)	t(h)	Phase assemblage
M392	1.5	1275	24	melt+ol+opx+gt+cpx
M386	1.5	1325	24	melt+ol+opx+gt+cpx
M384	1.5	1350	24	melt+ol+opx+gt+cpx
M388	1.5	1375	24	melt+ol+opx+gt
M387	1.5	1425	24	melt+ol+opx
M382	1.5	1450	24	melt+ol+opx
M418*	1.5	1450	12	melt+ol+opx
M400	2.5	1250	24	melt+ol+opx+gt
M399	2.5	1275	24	melt+ol+opx+gt
M396	2.5	1300	24	melt+ol+opx+gt
M402	2.5	1325	24	melt+ol+opx
M412*	2.5	1325	24	melt+ol+opx
M395	2.5	1350	24	melt+ol+opx
M411*	2.5	1350	24	melt+ol+opx
M417*	2.5	1350	12	melt+ol+opx
M423	5	1200	12	melt+ol+opx
M422	5	1225	12	melt+ol+opx
M426	5	1250	12	melt+ol+opx
M434*	5	1275	12	melt+ol+opx

* indicates experiments where capsules have been Fe-presaturated.

Table 3.2. Starting material compositions

	Nat. KLB-1[1]	KLB-1 ox.[2]	Hyd. Ol ox. mix 1*	Hyd. Ol ox mix 2*	**Batch 1***	**Batch 2***	**Batch 3***
SiO_2	44.84	44.92	36.60	33.50	43.59	42.81	41.64
TiO_2	0.11	0.16	--	--	0.14	0.12	0.12
Al_2O_3	3.51	3.92	--	--	3.34	2.97	2.82
Cr_2O_3	0.32	0.28	--	--	0.24	0.21	0.20
FeO*	8.20	8.09	8.98	8.22	8.20	8.28	8.11
MnO	0.12	0.12	--	--	0.10	0.09	0.09
MgO	39.52	38.76	44.02	40.30	39.42	39.93	39.10
CaO	3.07	3.79	--	--	3.23	2.87	2.73
Na_2O	0.30	0.25	--	--	0.21	0.19	0.18
K_2O	0.02	0.03	--	--	0.03	0.02	0.02
H_2O	0.00	0.00	10.40	17.98	1.51	2.50	5.00
Total	100.01	100.32	100	100	100	100	100
Mg#	89.6	89.5	89.7	89.7	89.6	89.6	89.6
% dry Ol**					13	21.5	22.8

[1] Measured value of glass sphere from Davis *et al.* (2009)
[2] Measured value of glass sphere using the methodology of Davis *et al.* (2009)
* Compositions are based on mass of oxides added to the mixture. For batches 1&2, the mixture consists of KLB-1 oxide + hydrous olivine oxide mix 1, while batch 3 consists of KLB-1 oxide + hydrous olivine mix 2.
** Percentage of dry olivine, from the hydrous olivine mix, added to KLB-1 ox. to produce the specified batch.

Table 3.3. Composition of partial melt (in weight percent, recalculated anhydrous) analyzed by EMPA.

Exp. #	M392	M386	M384	M388	M387	M382	M418	M400	M399	M396
T (ºC)	1275	1325	1350	1375	1425	1450	1450	1250	1275	1300
H_2O_{bulk} (wt. %)	1.5	1.5	1.5	1.5	1.5	1.5	1.5	2.5	2.5	2.5
n	24	10	11	33	79	121	181	16	119	43
SiO_2	45.83(0.16)	48.71(0.23)	**42.11(1.45)**	**48.52(0.54)**	**46.03(2.10)**	**45.17(1.11)**	**46.12(0.69)**	46.81(0.22)	**42.87(1.89)**	**43.35(0.60)**
TiO_2	1.37(0.04)	0.71(0.05)	**0.81(0.10)**	**0.66(0.16)**	0.56(0.14)	0.52(0.05)	0.48(0.12)	1.04(0.22)	0.73(0.22)	**0.63(0.17)**
Al_2O_3	10.08(0.12)	9.82(0.31)	**10.42(1.71)**	**10.33(0.61)**	**9.66(1.10)**	**9.37(0.49)**	**8.79(0.43)**	10.90(0.19)	**10.70(1.24)**	**9.83(0.27)**
Cr_2O_3	0.34(0.02)	0.46(0.04)	**0.29(0.10)**	**0.33(0.09)**	0.33(0.08)	0.37(0.06)	0.34(0.07)	0.35(0.03)	0.26(0.08)	**0.29(0.09)**
FeO*	6.64(0.05)	6.55(0.15)	**10.32(1.08)**	**7.32(0.38)**	**8.63(0.64)**	**9.50(0.67)**	**9.29(0.31)**	6.36(0.06)	**10.20(1.02)**	**10.60(0.36)**
MnO	0.12(0.01)	0.14(0.02)	**0.20(0.06)**	**0.16(0.05)**	0.16(0.04)	0.18(0.05)	0.16(0.05)	0.10(0.01)	0.16(0.06)	**0.16(0.05)**
MgO	12.72(0.10)	15.11(0.30)	**22.30(1.73)**	**18.88(0.70)**	**22.39(3.77)**	**24.33(1.78)**	**24.57(1.53)**	13.22(0.14)	**20.94(2.79)**	**22.40(0.74)**
CaO	18.72(0.13)	18.54(0.29)	**12.31(1.36)**	**13.04(0.99)**	**11.50(1.63)**	**9.91(1.17)**	**9.47(0.70)**	19.60(0.13)	**13.82(2.87)**	**12.38(1.25)**
Na_2O	0.81(0.01)	0.64(0.02)	**0.77(0.45)**	**0.69(0.36)**	0.66(0.22)	0.55(0.18)	0.69(0.08)	0.67(0.02)	0.23(0.08)	**0.19(0.08)**
K_2O	0.02(0.00)	0.02(0.00)	**0.47(0.16)**	**0.07(0.05)**	0.07(0.04)	0.11(0.06)	0.09(0.02)	0.02(0.01)	0.08(0.04)	**0.18(0.05)**
Total	96.66	100.72	100	100	100	100	100	99.08	100	100
Mg#	77.4	80.4	79.4	82.1	82.2	82.0	82.5	78.7	78.5	79.0
Fe/Mg $K_D^{ol/melt}$	--	--	0.31(0.02)	0.32(0.02)	0.31(0.04)	0.29(0.02)	0.34(0.01)	--	0.33(0.06)	0.34(0.01)
Exp. #	M402	M412	M395	M411	M417	M423	M422	M426	M434	
T (ºC)	1325	1325	1350	1350	1350	1200	1225	1250	1275	
H_2O_{bulk} (wt. %)	2.5	2.5	2.5	2.5	2.5	5	5	5	5	
n	40	136	77	219	55	117	104	175	167	
SiO_2	**44.39(3.61)**	**44.42(0.69)**	**43.37(1.32)**	**44.80(0.66)**	**45.49(1.63)**	**42.28(1.84)**	**41.57(2.81)**	**43.41(1.68)**	**44.53(1.64)**	
TiO_2	**0.52(0.07)**	0.54(0.12)	0.55(0.16)	0.53(0.13)	0.44(0.15)	**0.58(0.18)**	**0.57(0.24)**	0.50(0.17)	0.48(0.17)	
Al_2O_3	**9.18(1.02)**	**9.80(0.25)**	**9.72(0.52)**	**9.35(0.21)**	**9.38(0.54)**	**10.64(0.62)**	**9.57(0.85)**	**9.82(0.59)**	**9.40(0.51)**	
Cr_2O_3	**0.36(0.07)**	0.33(0.08)	0.36(0.09)	0.36(0.09)	0.34(0.10)	**0.28(0.09)**	**0.36(0.17)**	0.36(0.10)	0.38(0.12)	
FeO*	**8.92(0.74)**	**9.54(0.42)**	**10.41(0.77)**	**8.13(0.33)**	**10.77(0.84)**	**8.22(0.54)**	**9.02(0.96)**	**7.62(0.59)**	**9.14(0.66)**	
MnO	**0.15(0.04)**	0.17(0.04)	0.17(0.05)	0.15(0.05)	0.15(0.05)	**0.16(0.05)**	**0.15(0.08)**	0.16(0.05)	0.16(0.07)	
MgO	**24.43(2.67)**	**24.10(0.71)**	**24.73(1.45)**	**26.12(0.70)**	**24.49(2.00)**	**24.08(1.37)**	**27.35(2.24)**	**26.01(1.49)**	**26.41(1.50)**	
CaO	**11.63(2.12)**	**10.93(0.64)**	**10.53(1.24)**	**10.49(0.42)**	**8.31(1.02)**	**13.38(3.00)**	**11.24(2.90)**	**11.84(1.94)**	**9.13(1.70)**	
Na_2O	**0.37(0.23)**	0.14(0.06)	0.12(0.05)	0.12(0.06)	0.40(0.13)	**0.17(0.06)**	**0.07(0.05)**	0.18(0.10)	0.20(0.06)	
K_2O	**0.05(0.04)**	0.06(0.03)	0.06(0.03)	0.09(0.03)	0.24(0.08)	**0.22(0.06)**	**0.11(0.04)**	0.10(0.03)	0.16(0.05)	
Total	100	100	100	100	100	100	100	100	100	
Mg#	83.0	81.8	80.9	85.1	80.2	83.9	84.4	85.9	83.7	
Fe/Mg $K_D^{ol/melt}$	0.34(0.03)	0.39(0.02)	0.34(0.04)	0.39(0.02)	0.36(0.05)	0.40(0.03)	0.38(0.05)	0.40(0.04)	0.38(0.04)	

*Errors in parentheses are 1σ of the mean. Data in bold are preferred melt compositions (see also, Table 3.4).

*Data shaded in dark grey indicate analyses of low *F* melt pools, in which quench modification has left no equilibrium melt texture. The reported compositions are of the quenched cpx within the melt regions.

Table 3.4. Composition of partial melt (in weight percent) analyzed by LA-ICP-MS.

Exp. #	M387	M382	M418	M399	M412	M395	M411	M417	M426	M434
T (ºC)	1425	1450	1450	1275	1325	1350	1350	1350	1250	1275
Bulk H_2O(wt. %)	1.5	1.5	1.5	2.5	2.5	2.5	2.5	2.5	5	5
Spot Size (µm)	50	50	50	20	35	50	50	50/20	50	50
Step Size (µm/s)	10	10	10	5	5	10	10	10/5	10	10
Spot vol. (μm^3)	3800	3800	3800	600	1800	3800	3800	3800/600	5000	5000
Vol. avg'd(μm^3)	$3.9x10^5$	$4.5x10^5$	$4.1x10^5$	$1.3x10^5$	$1.5x10^5$	$1.7x10^5$	$5.8x10^5$	$3.3x10^5$	$3.9x10^5$	$5.0x10^5$
n	102	119	107	213	81	44	153	159	77	100
SiO_2	46.09(0.95)	44.56(0.61)	45.31(0.52)	43.86(1.13)	45.03(0.85)	44.55(0.68)	44.61(0.76)	44.92(1.29)	44.10(1.64)	45.64(1.71)
	+0.1	*-1*	*-2*	*+2*	*+1*	*+3*	*-0.4*	*-1*	*+2*	*+2*
TiO_2	**0.55(0.04)**	**0.55(0.02)**	**0.50(0.02)**	**0.70(0.05)**	**0.52(0.03)**	**0.52(0.02)**	**0.50(0.03)**	**0.51(0.03)**	**0.49(0.04)**	**0.47(0.05)**
	-2	***+6***	***+5***	***-3***	***-2***	***-4***	***-5***	***+17***	***-0.8***	***-4***
Al_2O_3	7.82(0.28)	8.15(0.22)	7.79(0.25)	8.90(0.63)	8.58(0.37)	8.25(0.23)	8.13(0.22)	8.51(0.54)	9.01(0.51)	8.57(0.55)
	-19	*-13*	*-11*	*-17*	*-13*	*-15*	*-12*	*-9*	*-7*	*-9*
Cr_2O_3	**0.37(0.03)**	**0.37(0.02)**	**0.36(0.01)**	**0.25(0.02)**	**0.36(0.02)**	**0.34(0.01)**	**0.36(0.02)**	**0.35(0.02)**	**0.35(0.03)**	**0.37(0.04)**
	+11	***-0.2***	***+7***	***-6***	***+7***	***-4***	***-3***	***+6***	***-1***	***-4***
FeO*	9.43(0.82)	8.82(0.49)	9.40(0.17)	9.81(0.62)	9.69(0.56)	9.97(0.50)	8.25(0.54)	10.57(0.61)	7.24(0.65)	8.83(1.04)
	+9	*-7*	*+1*	*-4*	*+2*	*-4*	*+2*	*-2*	*-5*	*-3*
MnO	**0.19(0.01)**	**0.18(0.01)**	**0.18(0.00)**	**0.17(0.01)**	**0.18(0.01)**	**0.17(0.01)**	**0.18(0.01)**	**0.17(0.01)**	**0.17(0.02)**	**0.18(0.02)**
	+19	***+3***	***+13***	***+9***	***+10***	***+5***	***+20***	***+14***	***+8***	***+12***
MgO	24.38(1.05)	25.79(0.86)	25.91(1.01)	20.84(1.77)	24.02(1.07)	25.24(0.63)	26.96(0.74)	24.10(2.01)	26.37(1.06)	25.90(1.38)
	+9	*+6*	*+5*	*-0.5*	*-0.3*	*+2*	*+3*	*-2*	*+1*	*-2*
CaO	10.22(0.56)	10.26(0.51)	9.56(0.32)	14.07(1.21)	10.49(0.67)	10.34(0.22)	10.28(0.47)	9.87(0.74)	11.48(0.88)	9.29(0.91)
	-11	*+4*	*+1*	*+2*	*-4*	*-2*	*-2*	*+19*	*-3*	*+2*
Na_2O	**0.84(0.13)**	**1.20(0.13)**	**0.90(0.05)**	**1.32(0.28)**	**1.00(0.17)**	**0.51(0.08)**	**0.63(0.11)**	**0.82(0.17)**	**0.59(0.06)**	**0.69(0.1)**
	+27	***+120***	***+30***	***+480***	***+630***	***+320***	***+440***	***+100***	***+220***	***+250***
K_2O	**0.08(0.02)**	**0.10(0.03)**	**0.08(0.01)**	**0.06(0.02)**	**0.10(0.06)**	**0.06(0.01)**	**0.08(0.03)**	**0.15(0.04)**	**0.08(0.01)**	**0.04(0.01)**
	-8	***-8***	***-7***	***-26***	***+77***	***+11***	***-13***	***-36***	***-20***	***-77***
Total	100.00	100.00	100.00	100.00	100.00	100.00	100.00	100.00	100.00	100.00
Mg#	82.2	83.9	83.1	79.1	81.6	81.9	85.3	80.3	86.7	83.9
Fe/Mg $K_D^{ol/melt}$	0.31(0.04)	0.34(0.03)	0.34(0.02)	0.34(0.04)	0.39(0.03)	0.34(0.02)	0.40(0.03)	0.35(0.03)	0.43(0.05)	0.38(0.05)

*Errors in parentheses are 1σ of the mean. Data in bold are preferred melt compositions (see also, Table 3.3).

*Numbers in italics are the relative difference (in percent) of the LA-ICP-MS oxide concentrations with respect to the melt oxide concentrations measured by EMPA.

Table 3.5. Composition (in weight percent) of olivine

Exp. #	M392	M386	M384	M388	M400	M399	M396	M400	M399	M396
T (ºC)	1275	1325	1350	1375	1250	1275	1300	1250	1275	1300
Bulk H_2O (wt. %)	1.5	1.5	1.5	1.5	2.5	2.5	2.5	2.5	2.5	2.5
n	10	10	12	10	10	10	10	18	10	10
SiO_2	40.59(0.13)	41.01(0.18)	41.20(0.20)	40.37(0.35)	41.14(0.31)	41.40(0.11)	41.36(0.22)	41.36(0.18)	41.00(0.13)	40.91(0.19)
TiO_2	-0.01(0.05)	0.02(0.06)	0.04(0.07)	0.00(0.05)	0.01(0.08)	0.01(0.01)	0.01(0.09)	0.00(0.06)	0.01(0.07)	0.01(0.05)
Al_2O_3	0.04(0.02)	0.07(0.02)	0.06(0.02)	0.08(0.01)	0.09(0.02)	0.10(0.01)	0.09(0.02)	0.06(0.03)	0.03(0.01)	0.04(0.02)
Cr_2O_3	0.07(0.03)	0.07(0.05)	0.05(0.03)	0.06(0.03)	0.09(0.04)	0.10(0.02)	0.10(0.07)	0.05(0.05)	0.05(0.03)	0.05(0.05)
FeO*	8.45(0.07)	7.31(0.15)	7.13(0.12)	6.52(0.07)	6.24(0.13)	6.03(0.06)	6.63(0.09)	8.01(0.14)	7.88(0.12)	8.15(0.14)
MnO	0.10(0.02)	0.10(0.02)	0.10(0.04)	0.10(0.03)	0.08(0.03)	0.09(0.03)	0.10(0.03)	0.09(0.02)	0.10(0.03)	0.09(0.04)
MgO	50.16(0.16)	50.96(0.24)	50.70(0.25)	53.02(0.22)	51.86(0.20)	52.40(0.51)	51.56(0.43)	50.29(0.39)	50.12(0.19)	50.74(0.28)
CaO	0.09(0.02)	0.14(0.02)	0.13(0.02)	0.14(0.02)	0.13(0.02)	0.12(0.02)	0.13(0.03)	0.10(0.02)	0.09(0.02)	0.09(0.01)
Na_2O	0.00(0.01)	0.02(0.02)	0.00(0.01)	0.01(0.01)	0.00(0.02)	0.01(0.01)	0.01(0.02)	0.01(0.02)	0.00(0.01)	0.00(0.01)
K_2O	0.02(0.01)	0.02(0.01)	0.02(0.02)	0.02(0.01)	0.02(0.01)	0.01(0.01)	0.02(0.02)	0.03(0.01)	0.02(0.01)	0.02(0.01)
Total	99.52	99.72	99.43	100.31	99.66	100.25	99.99	100.01	99.29	100.12
Mg#	91.4	92.6	92.7	93.5	93.7	93.9	93.3	91.8	91.9	91.7
Exp. #	M402	M412	M395	M411	M417	M423	M422	M426	M434	
T (ºC)	1325	1325	1350	1350	1350	1200	1225	1250	1275	
Bulk H_2O (wt. %)	2.5	2.2	2.5	2.5	2.5	5	5	5	5	
n	10	10	10	10	10	10	10	10	10	
SiO_2	40.92(0.31)	40.95(0.13)	40.91(0.17)	41.51(0.13)	41.64(0.30)	41.63(0.19)	41.38(0.28)	41.97(0.34)	41.20(0.33)	
TiO_2	0.07(0.10)	0.00(0.08)	0.01(0.03)	-0.02(0.07)	0.02(0.05)	-0.03(0.06)	0.02(0.05)	0.01(0.08)	0.02(0.07)	
Al_2O_3	0.06(0.03)	0.04(0.01)	0.06(0.01)	0.05(0.02)	0.06(0.02)	0.02(0.01)	0.04(0.03)	0.04(0.03)	0.04(0.02)	
Cr_2O_3	0.06(0.03)	0.06(0.05)	0.06(0.04)	0.07(0.06)	0.08(0.06)	0.08(0.04)	0.06(0.06)	0.07(0.07)	0.04(0.06)	
FeO*	6.48(0.17)	7.70(0.11)	7.20(0.10)	6.22(0.10)	7.77(0.25)	7.05(0.34)	6.35(0.33)	6.13(0.20)	6.74(0.12)	
MnO	0.08(0.04)	0.09(0.03)	0.08(0.02)	0.09(0.06)	0.06(0.04)	0.07(0.04)	0.08(0.04)	0.06(0.04)	0.08(0.03)	
MgO	51.69(0.28)	50.47(0.18)	50.92(0.37)	51.64(0.31)	49.99(0.24)	51.96(0.22)	51.47(0.54)	52.37(0.30)	51.75(0.49)	
CaO	0.11(0.03)	0.11(0.03)	0.12(0.10)	0.08(0.01)	0.09(0.03)	0.07(0.03)	0.09(0.03)	0.05(0.03)	0.08(0.03)	
Na_2O	0.01(0.02)	0.00(0.01)	0.01(0.01)	0.00(0.02)	0.01(0.02)	0.00(0.01)	0.00(0.01)	0.00(0.01)	0.01(0.02)	
K_2O	0.02(0.02)	0.02(0.02)	0.01(0.01)	0.02(0.01)	0.03(0.02)	0.03(0.02)	0.02(0.01)	0.02(0.02)	0.02(0.03)	
Total	99.51	99.44	99.38	99.66	99.76	100.88	99.50	100.72	99.97	
Mg#	93.4	92.1	92.6	93.7	92.0	92.9	93.5	93.8	93.2	

*Errors in parentheses are 1σ of the mean.

Table 3.6. Composition (in weight percent) of orthopyroxene

Exp. #	M392	M386	M384	M388	M387	M382	M418	M400	M399	M396
T (ºC)	1275	1325	1350	1375	1425	1450	1450	1250	1275	1300
Bulk H_2O (wt. %)	1.5	1.5	1.5	1.5	1.5	1.5	1.5	2.5	2.5	2.5
n	10	10	11	10	10	10	11	10	11	9
SiO_2	55.51(0.35)	55.95(0.14)	55.11(0.73)	55.04(0.38)	56.08(0.23)	56.17(0.30)	55.41(0.31)	56.29(0.28)	55.43(0.51)	54.98(0.42)
TiO_2	0.04(0.04)	0.03(0.06)	0.03(0.07)	0.04(0.05)	-0.01(0.05)	0.01(0.01)	0.01(0.06)	0.03(0.05)	0.04(0.05)	0.03(0.05)
Al_2O_3	2.18(0.03)	2.84(0.07)	2.85(0.27)	2.98(0.16)	3.10(0.14)	3.08(0.20)	2.89(0.09)	2.06(0.09)	2.17(0.05)	2.43(0.15)
Cr_2O_3	0.37(0.04)	0.50(0.05)	0.46(0.07)	0.60(0.07)	0.63(0.04)	0.61(0.07)	0.68(0.10)	0.34(0.04)	0.40(0.07)	0.43(0.05)
FeO*	5.47(0.15)	4.74(0.10)	4.52(0.15)	4.31(0.18)	4.13(0.08)	4.13(0.27)	4.34(0.20)	5.13(0.16)	5.15(0.16)	5.42(0.21)
MnO	0.09(0.02)	0.11(0.12)	0.09(0.03)	0.10(0.03)	0.08(0.03)	0.08(0.02)	0.08(0.04)	0.08(0.03)	0.08(0.02)	0.08(0.03)
MgO	34.87(0.23)	34.76(0.36)	34.84(0.3)	34.86(0.31)	34.98(0.48)	34.89(0.44)	35.27(0.22)	35.42(0.31)	35.00(0.21)	35.13(0.30)
CaO	1.18(0.06)	1.51(0.08)	1.59(0.10)	1.48(0.06)	1.32(0.06)	1.18(0.07)	1.13(0.07)	1.16(0.04)	1.13(0.06)	1.08(0.08)
Na_2O	0.08(0.01)	0.08(0.02)	0.08(0.02)	0.07(0.02)	0.07(0.02)	0.07(0.02)	0.05(0.03)	0.05(0.01)	0.04(0.02)	0.04(0.02)
K_2O	0.03(0.01)	0.02(0.01)	0.02(0.01)	0.02(0.01)	0.02(0.01)	0.02(0.01)	0.02(0.02)	0.02(0.01)	0.02(0.01)	0.01(0.01)
Total	99.82	100.54	99.58	99.50	100.41	100.23	99.89	100.58	99.46	99.63
Mg#	91.9	92.9	93.2	93.5	93.8	93.8	93.5	92.5	92.4	92.0

Exp. #	M402	M412	M395	M411	M417	M423	M422	M426	M434
T (ºC)	1325	1325	1350	1350	1350	1200	1225	1250	1275
Bulk H_2O (wt. %)	2.5	2.2	2.5	2.5	2.5	5	5	5	5
n	13	10	10	10	10	10	10	11	10
SiO_2	55.73(0.62)	55.81(0.39)	55.82(0.17)	56.17(0.23)	55.47(0.33)	55.02(0.33)	55.91(0.35)	56.39(0.38)	55.29(0.51)
TiO_2	-0.02(0.07)	0.02(0.07)	0.01(0.04)	0.02(0.06)	0.04(0.11)	0.04(0.08)	0.03(0.07)	0.03(0.07)	0.08(0.07)
Al_2O_3	2.57(0.15)	2.51(0.23)	2.54(0.20)	2.28(0.18)	2.59(0.08)	2.49(0.08)	1.79(0.16)	2.06(0.28)	1.77(0.17)
Cr_2O_3	0.58(0.10)	0.63(0.07)	0.58(0.08)	0.60(0.11)	0.65(0.1)	0.66(0.09)	0.59(0.06)	0.57(0.15)	0.52(0.06)
FeO*	4.41(0.21)	4.89(0.11)	4.83(0.22)	4.10(0.20)	4.93(0.10)	4.29(0.10)	4.27(0.22)	4.31(0.33)	4.44(0.12)
MnO	0.09(0.04)	0.06(0.03)	0.07(0.03)	0.08(0.03)	0.09(0.04)	0.09(0.04)	0.09(0.03)	0.06(0.04)	0.06(0.03)
MgO	35.67(0.64)	35.00(0.30)	35.47(0.24)	36.07(0.30)	35.32(0.21)	36.91(0.31)	36.57(0.25)	36.45(0.37)	36.43(0.26)
CaO	0.97(0.09)	0.87(0.08)	0.88(0.05)	0.75(0.04)	0.84(0.04)	0.66(0.03)	0.62(0.07)	0.65(0.13)	0.62(0.05)
Na_2O	0.04(0.03)	0.04(0.02)	0.05(0.02)	0.03(0.01)	0.04(0.03)	0.03(0.02)	0.01(0.01)	0.02(0.02)	0.04(0.02)
K_2O	0.02(0.02)	0.02(0.02)	0.03(0.01)	0.02(0.02)	0.02(0.01)	0.03(0.02)	0.02(0.02)	0.02(0.01)	0.02(0.01)
Total	100.05	99.85	100.27	100.11	99.99	100.22	99.91	100.56	99.26
Mg#	93.5	92.7	92.9	94.0	92.4	93.9	93.9	93.8	93.6

*Errors in parentheses are 1σ of the mean.

Table 3.7. Composition (in weight percent) of garnet

Exp. #	M392	M386	M384	M388	M400	M399	M396
T (ºC)	1275	1325	1350	1375	1250	1275	1300
Bulk H_2O (wt. %)	1.5	1.5	1.5	1.5	2.5	2.5	2.5
n	10	10	5	10	10	10	9
SiO_2	41.68(0.19)	42.22(0.12)	42.13(0.28)	42.04(0.26)	42.17(0.27)	41.62(0.17)	42.39(0.25)
TiO_2	0.18(0.08)	0.13(0.09)	0.11(0.06)	0.10(0.06)	0.10(0.07)	0.09(0.03)	0.08(0.04)
Al_2O_3	22.57(0.21)	22.32(0.23)	21.90(0.14)	21.87(0.30)	22.70(0.19)	22.20(0.13)	22.36(0.11)
Cr_2O_3	1.68(0.20)	2.54(0.21)	2.59(0.13)	2.61(0.35)	2.04(0.19)	2.22(0.11)	2.43(0.17)
FeO*	7.29(0.12)	6.16(0.17)	6.06(0.30)	5.73(0.36)	7.03(0.19)	6.78(0.18)	6.66(0.14)
MnO	0.22(0.04)	0.21(0.04)	0.17(0.02)	0.19(0.03)	0.20(0.04)	0.21(0.03)	0.20(0.03)
MgO	19.96(0.28)	20.69(0.25)	20.67(0.22)	20.78(0.42)	20.36(0.33)	20.04(0.15)	20.80(0.17)
CaO	6.02(0.21)	6.21(0.18)	5.78(0.18)	5.88(0.33)	6.12(0.22)	6.15(0.20)	5.43(0.24)
Na_2O	0.01(0.01)	0.01(0.02)	0.01(0.02)	0.00(0.01)	0.00(0.01)	0.00(0.01)	0.00(0.01)
K_2O	0.02(0.01)	0.02(0.01)	0.02(0.01)	0.02(0.01)	0.01(0.01)	0.01(0.01)	0.02(0.01)
Total	99.63	100.50	99.43	99.22	100.73	99.33	100.38
Mg#	83.0	85.7	85.9	86.6	83.8	84.0	84.8

*Errors in parentheses are 1σ of the mean.

Table 3.8. Composition (in wt. %) of clinopyroxene

Exp. #	M392	M386	M384
T (ºC)	1275	1325	1350
Bulk H_2O (wt. %)	1.5	1.5	1.5
n	8	8	7
SiO_2	53.16(0.38)	53.60(0.24)	52.95(1.10)
TiO_2	0.10(0.04)	0.12(0.05)	0.00(0.05)
Al_2O_3	2.41(0.09)	3.04(0.09)	3.05(0.24)
Cr_2O_3	0.57(0.09)	0.71(0.07)	0.60(0.07)
FeO*	3.13(0.09)	3.07(0.13)	3.04(0.10)
MnO	0.08(0.04)	0.08(0.02)	0.06(0.02)
MgO	19.39(0.15)	20.38(0.24)	20.70(0.24)
CaO	19.25(0.14)	18.02(0.33)	17.37(0.17)
Na_2O	0.68(0.03)	0.56(0.05)	0.58(0.07)
K_2O	0.02(0.00)	0.02(0.01)	0.02(0.02)
Total	98.79	99.61	98.49
Mg#	91.7	92.2	92.4

*Errors in parentheses are 1σ of the mean.

Table 3.9. Data acquired by mass balance

Exp. #	T (C)	ΔT[1] (uncorr,corr)	F[2] (uncorr, corr)	Ol Mode[2] (uncorr, corr)	Opx Mode[2] (uncorr, corr)	Gt Mode[2] (uncorr, corr)	Cpx Mode[2] (uncorr, corr)	Mass Bal. Sum of Squares	Rel.Fe loss (%)[3]	Post Exp. Bulk Mg#	$D_{(res/melt)}$[4]	H_2O in Melt (wt.%)[5]
1.5% H_2O_{bulk}												
M384	1350	214, 219	0.17, 0.20	0.55, 0.48	0.21, 0.24	0.04, 0.05	0.03, 0.03	0.015	17	91.1	0.0041	8.7
M388	1375	201, 221	0.22, 0.25	0.55, 0.48	0.21, 0.24	0.02, 0.02	0	0.006	27	92.2	0.0037	6.7
M387	1425	166, 180	0.28, 0.32	0.55, 0.48	0.18, 0.21	0	0	0.019	23	91.8	0.0033	5.3
M382	1450	146, 156	0.30, 0.34	0.52, 0.45	0.18, 0.21	0	0	0.041	20	91.5	0.0032	5.0
M418	1450	153, 156	0.33, 0.38	0.54, 0.47	0.13, 0.15	0	0	0.025	14	90.9	0.0026	4.5
2.5% H_2O_{bulk}												
M399	1275	292, 287	0.18, 0.23	0.60, 0.49	0.19, 0.24	0.03, 0.04	0	0.005	9	90.4	0.0033	13.7
M396	1300	274, 266	0.21, 0.27	0.58, 0.46	0.19, 0.24	0.02, 0.03	0	0.024	5	90.1	0.0034	11.8
M402	1325	259, 273	0.25, 0.32	0.55, 0.43	0.20, 0.25	0	0	0.104	23	91.8	0.0034	9.9
M412	1325	261, 258	0.26, 0.33	0.58, 0.46	0.16, 0.20	0	0	0.024	9	90.5	0.0030	9.5
M395	1350	236, 235	0.26, 0.33	0.56, 0.44	0.18, 0.23	0	0	0.004	11	90.6	0.0032	9.5
M411	1350	241, 259	0.28, 0.36	0.55, 0.43	0.17, 0.22	0	0	0.017	26	92.1	0.0030	8.9
M417	1350	248, 232	0.31, 0.39	0.61, 0.50	0.07, 0.09	0	0	0.073	1(gain)	89.5	0.0019	8.0
5% H_2O_{bulk}												
M423	1200	374, 390	0.21, 0.27	0.54, 0.40	0.24, 0.31	0	0	0.061	25	91.9	0.0038	23.5
M422	1225	361, 377	0.26, 0.34	0.52, 0.38	0.22, 0.28	0	0	0.076	25	91.9	0.0033	19.1
M426	1250	334, 357	0.25, 0.32	0.55, 0.42	0.21, 0.27	0	0	0.052	31	92.5	0.0034	19.8
M434	1275	321, 329	0.30, 0.39	0.54, 0.40	0.16, 0.21	0	0	0.014	18	91.3	0.0027	16.6

1. ΔT values are quantified using uncorrected F values. Uncorrected ΔT is calculated from Eqns. 5 and 6. Corrected ΔT accounts for Fe-loss and CO_2 infiltration (Eqn. 9)
2. F and modes are corrected for olivine addition to the starting material. Initial F, and opx, cpx, and garnet modes have been divided by the percentage of KLB-1 oxide in the starting material (0.87, 0.785, and 0.772, respectively) for 1.5, 2.5, and 5% bulk H_2O batches. Olivine modes were corrected by the following: (Ol $Mode_{uncorr}$ – (1 – %KLB-1 $oxide_{bulk}$))/%KLB-1 $oxide_{bulk}$.
3. Relative Fe-loss is estimated from the mass balance, using uncorrected F and residual modes.
4. Residue/melt H_2O partitioning is determined using the uncorrected residual modes, and the following mineral/melt H_2O partition coefficients from Tenner *et al.* (2009): olivine: 0.0018, pyroxene: (0.0015 • Al_2O_3(wt.%)) + 0.0082, garnet: 0.003.
5. H_2O in the melt is estimated by batch melting (Eqn. 4), using the reported $D_{res/melt}$, and using uncorrected F.

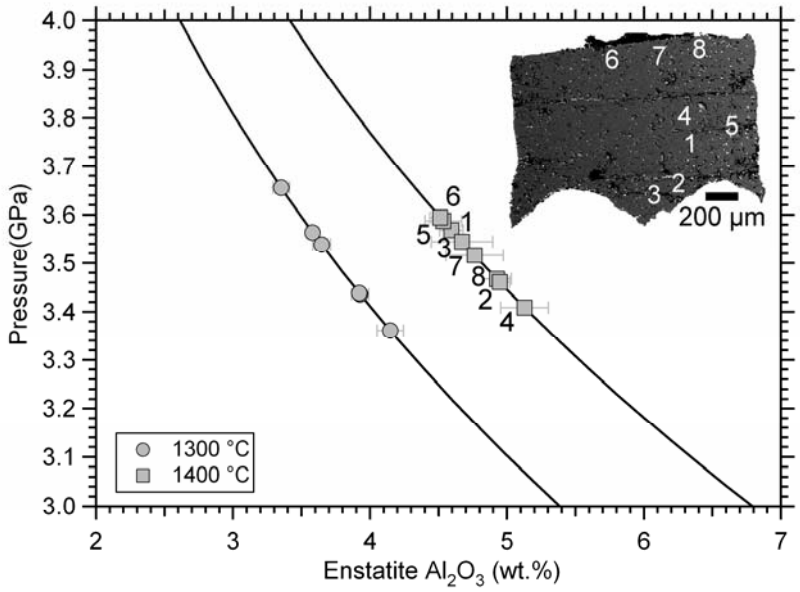

Figure 3.1. Measured Al_2O_3 contents of enstatite in equilibrium with pyrope used to calibrate the pressure of the multi-anvil assembly based on the experimental determinations and parameterization of Perkins *et al.* (1981). EMPA analyses were performed along transects across enstatite-pyrope grain boundaries, with 1 µm spacing between analyses. Each data point in the figure represents averaged analyses (n = 2–10) closest to the grain boundary while still within enstatite. The inset BSE image shows the locations of the 8 en-py grain boundaries (denoted with numbers) that were analyzed for the 1400ºC calibration. Data points for the 1400ºC calibration are correspondingly labeled, and the analyses suggest no systematic lateral or vertical variability due to the thermal profile in the capsule. The parameterization was constructed from the Al_2O_3 isopleths in Fig. 2 of Perkins *et al.* (1981) to yield the following relations: 1300°C: P = -1.3805ln($C^{En}_{Al_2O_3}$ (wt. %)) + 5.3249; 1400 °C: P = -1.4528ln($C^{En}_{Al_2O_3}$ (wt. %)) + 5.7837. Enstatite Al_2O_3 contents of the 1300 and 1400°C calibration experiments predict pressures of 3.49 ± 0.1 and 3.53 ± 0.07 GPa, respectively.

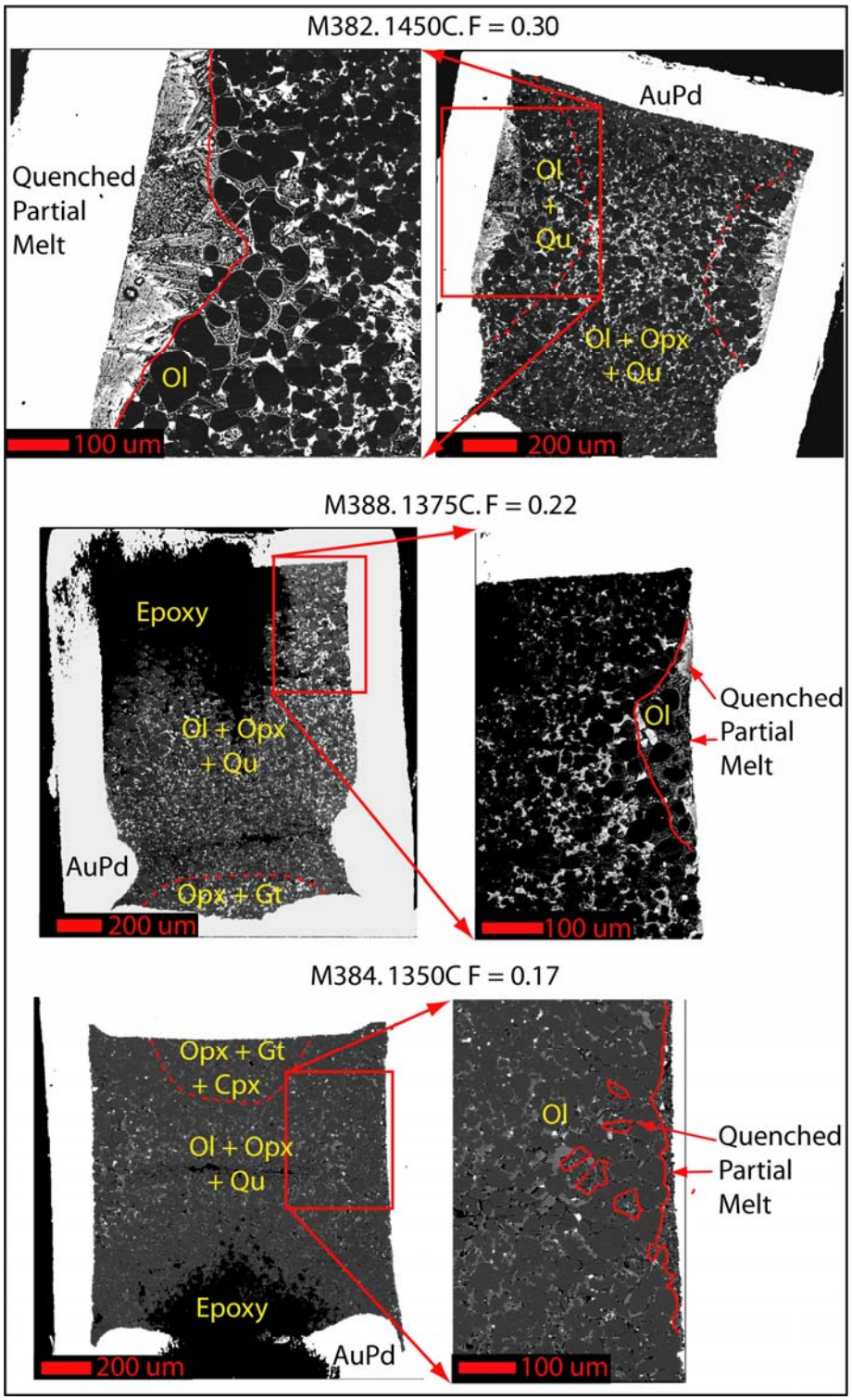

Figure 3.2. Backscattered electron images of 3 GPa, 1.5 wt. % bulk H_2O run products from 1450ºC down to 1350ºC. **M382** (1450 °C): Easily discernable melt pools form at the outer edges of the capsule, and illustrate the thermal profile through an experimental

charge. Partial melts quenched to a 400×100 μm-sized region and large (up to 50 μm) olivine crystals grow adjacent to the quenched melt regions. Orthopyroxene crystals are concentrated at the top and bottom of the charge, interspersed with olivine crystals. **M388** (1375 °C): The melt pool consists of a smaller (200×75 μm) region of quench crystals, with another region likely buried in epoxy on the left side of the charge. The quality of the polish diminishes with decreasing melt fraction, likely owing to a greater amount of exsolved H_2O on quench and therefore more problems with crystal plucking during polishing. However a tiny portion of well-polished quenched crystal material was retained near the top of the quench region. Garnet is present in the residue, forming at the bottom and the top of the capsule. **M384 (**1350 °C): Partial melts quench to ~30×30 μm poorly-polished pockets of quench crystals, owing to low *F* and high water content (8.5 wt. %) melt. Cpx and garnet are both present in the residue.

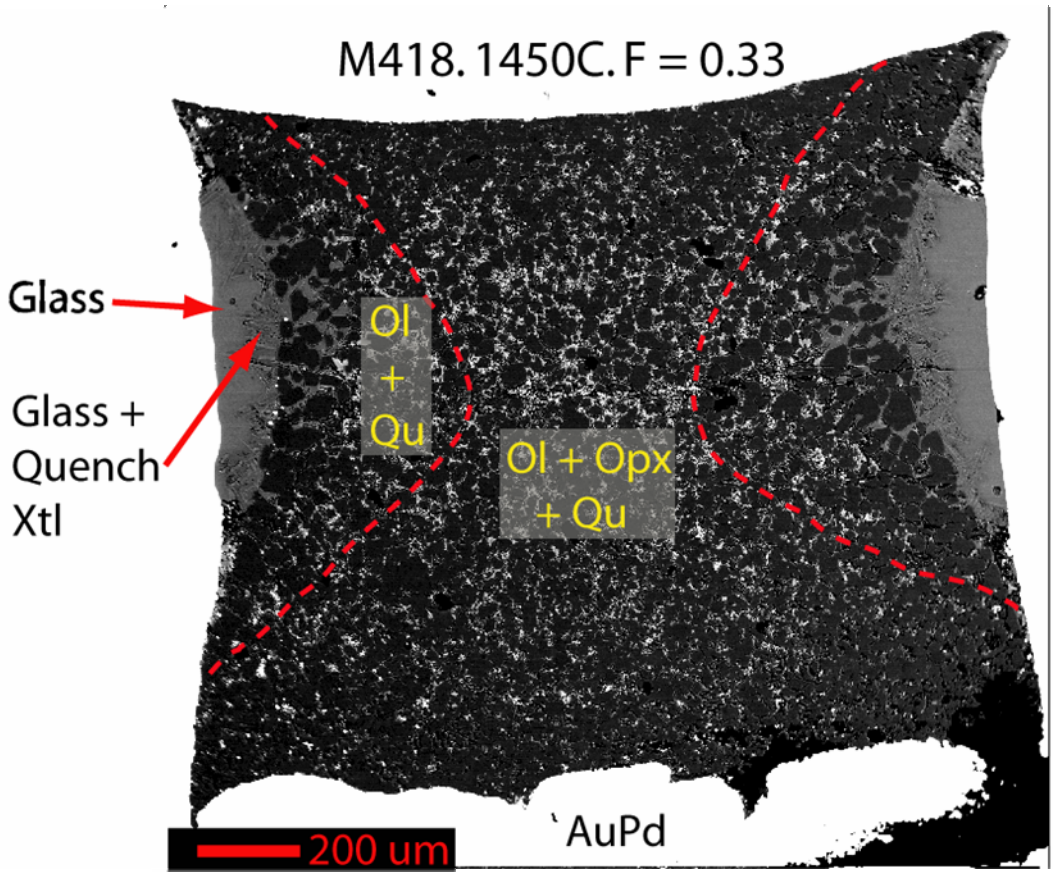

Figure 3.3. Backscattered electron image of experiment M418, in which the majority of melt quenched to a homogenous glass. Analysis of this glass allows comparison to melt compositions from experiments from which melts quenched to complex polyphase aggregates. For example, the experimental conditions for M418 are identical to experiment M382, with the exception that M418 employed an Fe-presaturated capsule. Mass balance predicts similar modal phase relations between M382 and M418 (Table 3.9), and melt compositions (Table 3.3, Table 3.4). Also, FTIR analysis of the glass allows direct determination of dissolved H_2O and CO_2 contents (see text).

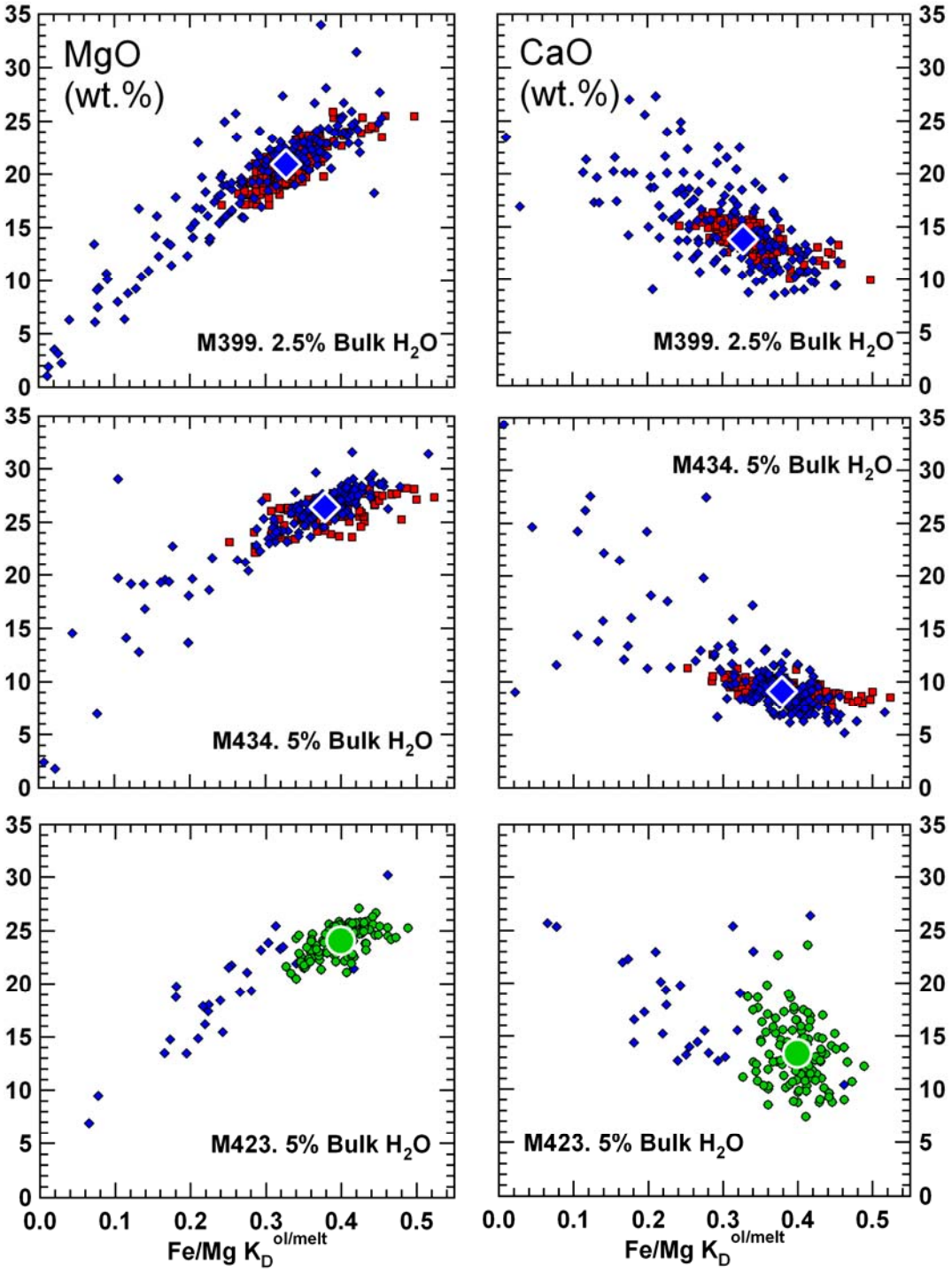

Figure 3.4. Variations in MgO and CaO in partial melts as a function of Fe/Mg K_D, used to illustrate our technique of filtering of melt analyses. Data points are recalculated anhydrous. Melts of experiments M399 and M434 were analyzed by both LA-ICP-MS (red solid squares) and EMPA (solid blue diamonds). The different techniques yield

compositions that overlap both in oxide concentration and K_D range. Low K_D (<0.27) EMPA analyses are believed to be of melts that have been quench modified, and are not included in averaging melt compositions in Table 3.3. Experiments with 1.5 and 2.5 wt. % bulk H_2O (ex: M399) that were analyzed by both techniques suggest that the majority of melt analyses have a K_D range of 0.27-0.39. Liquid compositions from experiments from these series for which LA-ICP-MS analyses are absent are therefore filtered using this range of values of K_D. Experiments with 5 wt. % bulk H_2O that were analyzed by both techniques (e.g., M434) produce data clouds where the majority of points have a K_D range of 0.27-0.5. Therefore, we use this larger K_D range to filter melt analyses for experiments analyzed only by EMPA for this more hydrous series. This is illustrated in the MgO and CaO vs. K_D plots of experiment M423 (5 wt. % bulk H_2O, melt analysis only by EMPA) where the equilibrium melt composition (green filled circles) is taken as the average of analyses in the K_D range of 0.27-0.5.

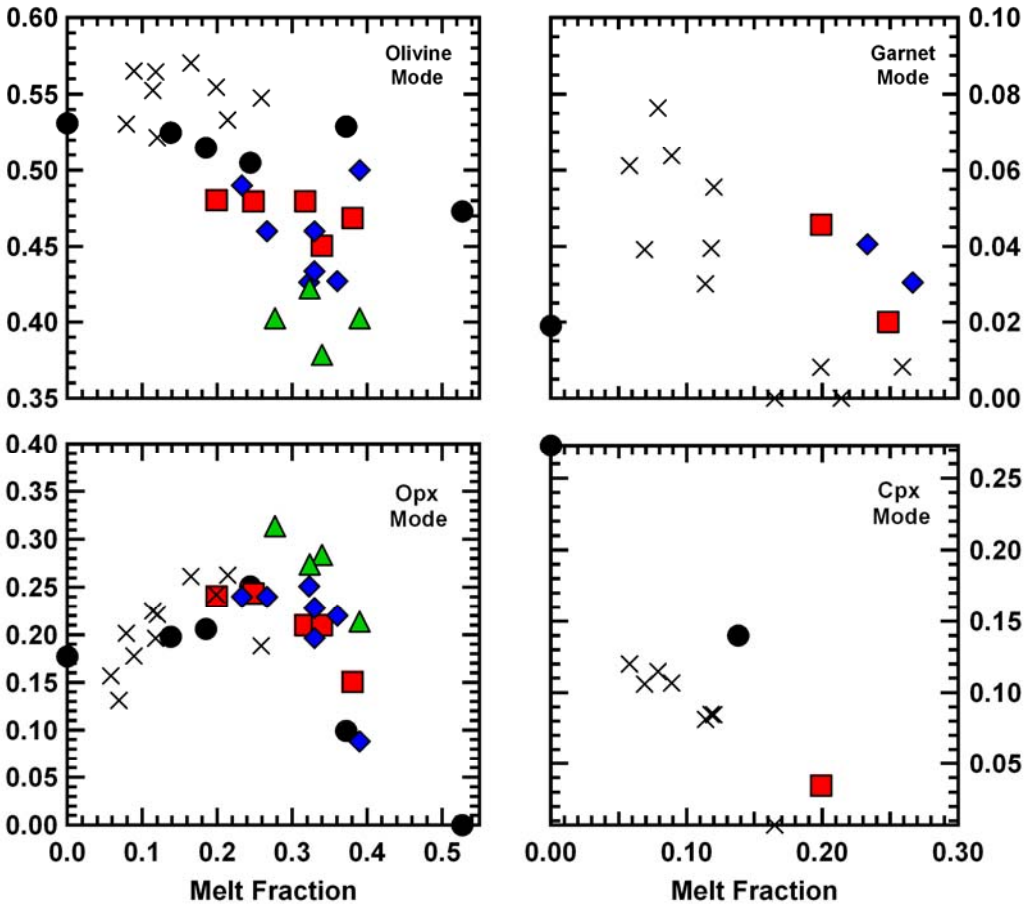

Figure 3.5. Residual mineral modes as a function of melt fraction. Red filled squares, blue filled diamonds, and green filled triangles represent data from experiments with 1.5, 2.5, and 5% bulk H_2O, respectively. Mineral modes have been corrected for the addition of olivine to the starting materials. Shown for comparison are the peridotite residual modes from partial melting experiments at 3 GPa for nominally anhydrous peridotite (Walter, 1998) (filled circles) and hydrous peridotite (Hall, 1999) (crosses). Compared to dry partial melting of peridotite, the addition of H_2O reduces the olivine mode and stabilizes garnet to higher melt fractions (above 0.2), but has no discernable effect on pyroxene modes.

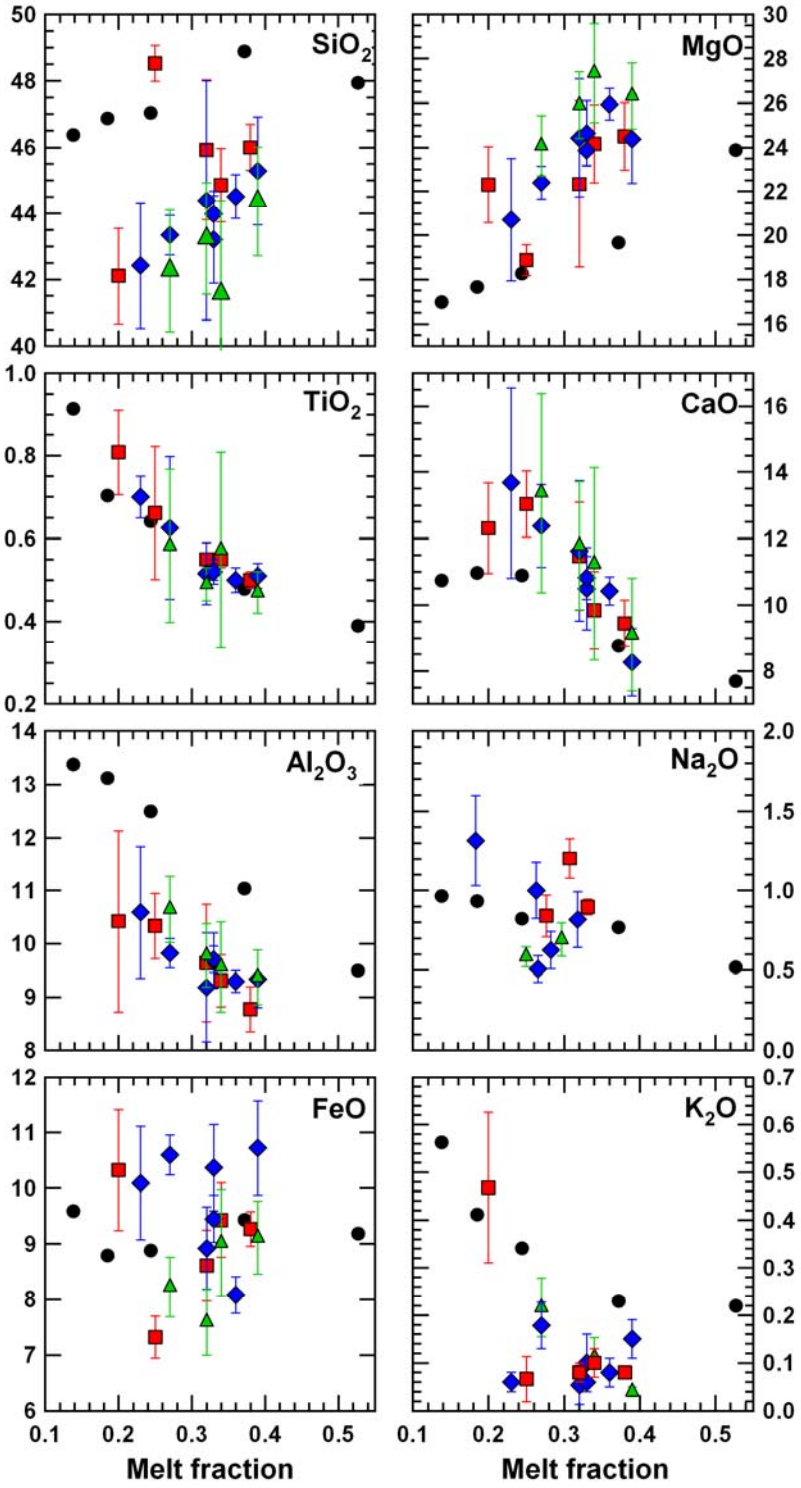

Figure 3.6. Concentration of oxides in partial melts as a function of melt fraction. Red filled squares, blue filled diamonds, and green filled triangles represent compositions from experiments with 1.5, 2.5, and 5% bulk H_2O, respectively. Shown for comparison

are melt compositions for nominally dry peridotite at 3 GPa (Walter, 1998) (filled black circles). Oxide contents are recalculated anhydrous, and *F* is corrected for the addition of olivine to starting materials. Large uncertainties are owing to the heterogeneity of quenched melts in nearly all of the experiments. Uncertainties are smaller (Table 3.3) for the melt composition of experiment M418, which produced quenched glass (Fig. 3.3). The scatter in FeO is likely owing to modest and variable amounts of Fe-loss. Partial melts become increasingly calcic with decreasing *F* when compared to dry peridotite melting. Partial melts of Walter (1998) are enriched in K_2O because the starting material (KR4003) has >3 times more K_2O than KLB-1. Illustrated Na_2O contents are those determined by LA-ICP-MS.

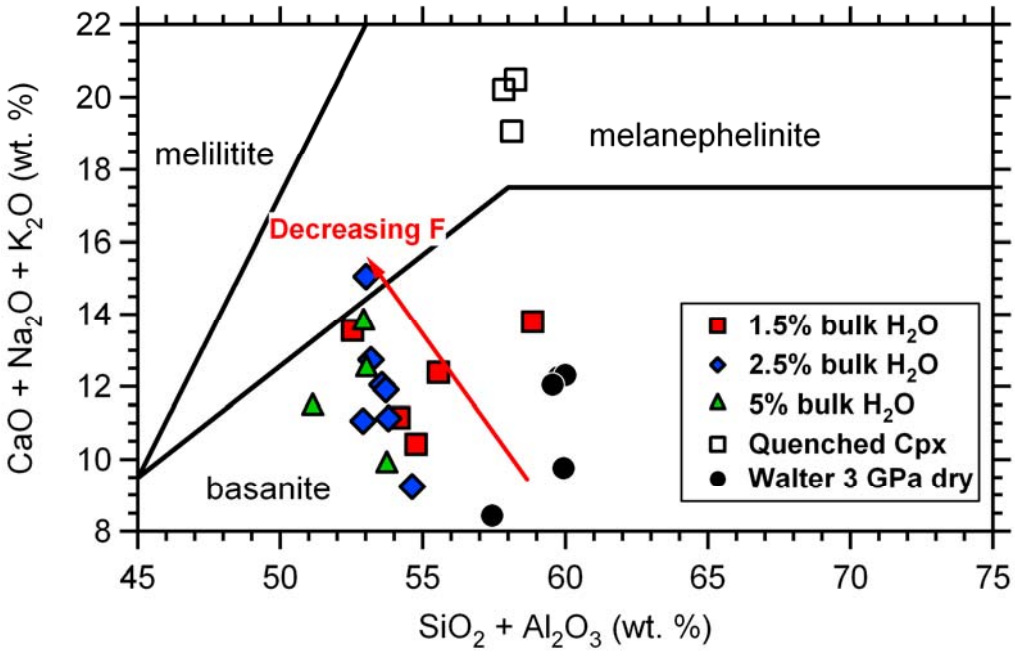

Figure 3.7. Normative melt compositions following the classification scheme of Le Bas (1989). Oxide contents are normalized to 100% totals. With decreasing *F* melts increase in alkali content, approaching the field of melanephelinites. Also plotted are qualitatively low *F* experiments (open squares) where melt pools have been compromised by

quenched cpx, as evidenced by much greater CaO+alkali contents in the measured compositions. The fact that the "melt" compositions for these experiments do not trend with those from other experiments contributes to our conclusion that they do not represent equilibrium melt compositions and so we do not include them in our discussions of melt compositions or melting relations.

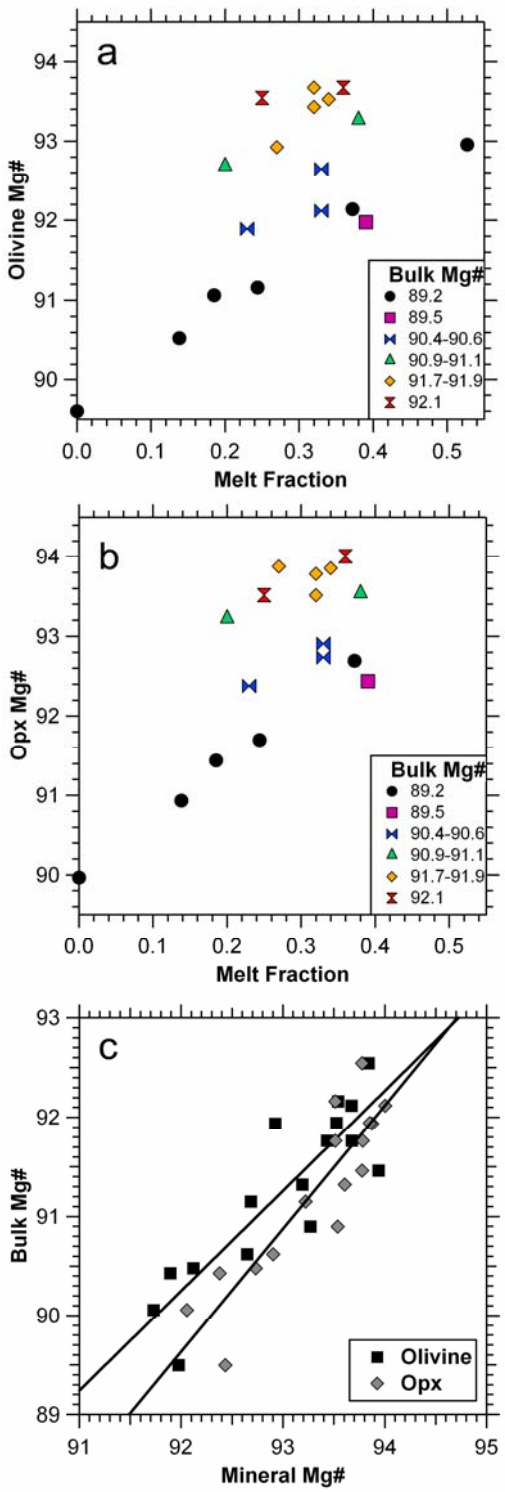

Figure 3.8. Relationship between Mg#s of olivine and opx to calculated bulk Mg# of experimental run products. **a)** and **b)** Mg# versus melt fraction for olivine and orthopyroxene, respectively. Black, filled circles are from partial melting of nominally

dry peridotite at 3 GPa (Walter, 1998). As expected, for a given bulk Mg#, olivine and opx Mg# increase with increasing *F*. **c)** Olivine and opx Mg# as a function of bulk Mg#. The trends can be represented by $Mg\#_{bulk} = (1.0084 \bullet Mg\#_{olivine}) - 2.5244$ ($R^2 = 0.76$), and $Mg\#_{bulk} = (1.2405 \bullet Mg\#_{opx}) - 24.491$ ($R^2 = 0.79$). These fits allow calculation of the bulk Mg# for experiments M386, M392, and M400, (where equilibrium melt analyses are not possible), which allows for estimation of their *F* values.

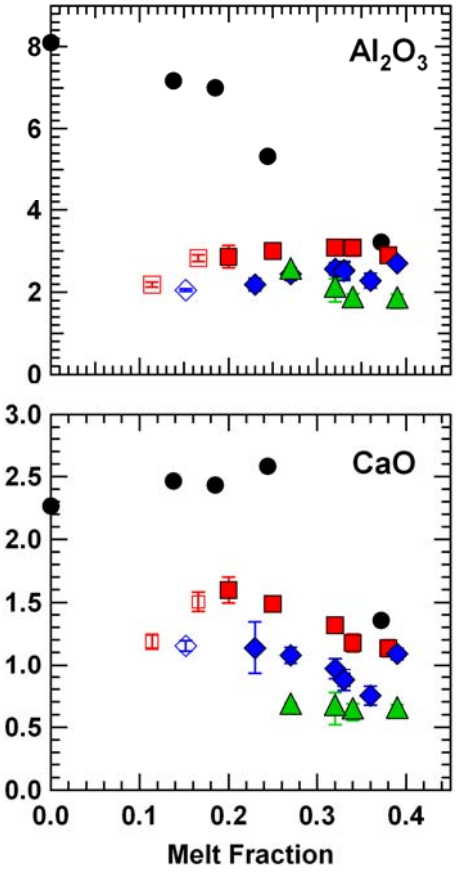

Figure 3.9. Orthopyroxene Al_2O_3 and CaO concentrations as a function of melt fraction. Solid symbols follow previous figures. For experiments with low melt fractions, values of *F* are estimates and are plotted as open symbols. In these cases, estimated values of *F* values are determined as follows: Using the olivine and opx Mg#'s from experiments M386, M392, and M400 (Tables 3.5 and 3.6), we use the fits from Fig. 3.8c to predict

their post experiment bulk Mg#'s (90.8, 89.6, and 90.1, respectively). We can then predict the effect of Fe-loss on ΔT (Eqn. 7) and use the CO_2 correction to calculate "corrected" run temperatures of these experiments (1326, 1260, and 1242ºC, respectively). Then using parameterization for ΔT versus H_2O in the melt (Eqn. 10) and Eqns. 4, 5, and 9 we can determine which value of F produces a ΔT where T^{hydrous} is equivalent to the "corrected" run temperature. For Eqn. 4 a $D_{H_2O}^{\text{residue/melt}}$ value of 0.0037 is used, which approximates $D_{H_2O}^{\text{residue/melt}}$ for other experiments in this study (Table 3.9). This yields F values of 0.17, 0.11, and 0.16 for M386, M392, and M400, respectively. Orthorpyroxene Al_2O_3 content is not affected by F, but CaO content decreases slightly as F increases. For both Al_2O_3 and CaO, increasing bulk H_2O diminishes concentrations for a given F.

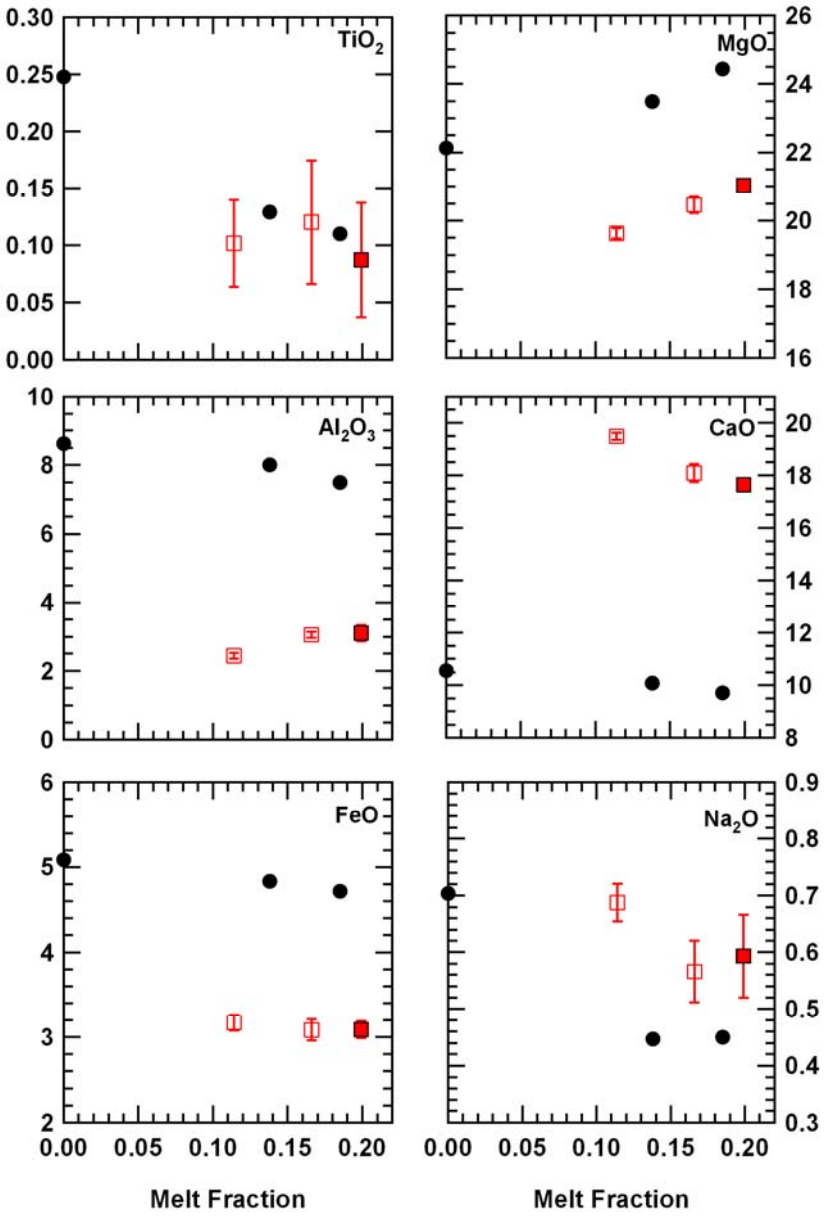

Figure 3.10. Clinopyroxene compositions as a function of melt fraction. Open symbols are oxide contents using *F* values based on the ΔT vs. H_2O in the melt parameterization (see Fig. 3.9 caption). Mg# increases, and CaO, and to a lesser extent, TiO_2 and Na_2O decrease with increasing *F*. MgO, FeO, and Al_2O_3 concentrations are lower than that of dry 3 GPa melting at *F*, while CaO contents increase with the addition of H_2O to peridotite.

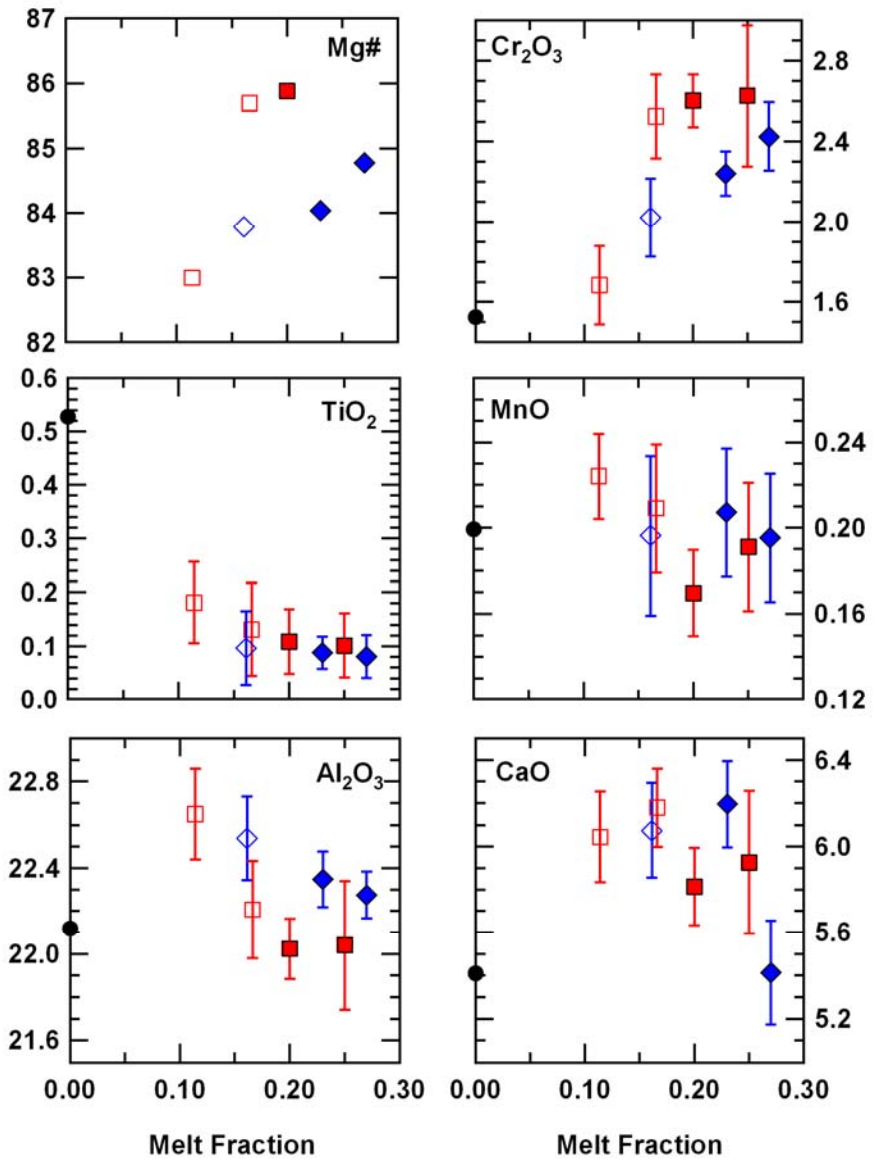

Figure 3.11. Garnet compositions as a function of melt fraction. Open symbols are oxide contents using F values based on the ΔT vs. H_2O in the melt parameterization (see Fig. 3.9 caption). Mg# and Cr_2O_3 increase, while TiO_2, MnO, and Al_2O_3 decrease as F increases. Increasing amounts of H_2O reduces Mg# and Cr_2O_3 content while increasing the Al_2O_3 content at a given melt fraction. The addition of H_2O stabilizes garnet to greater F when compared to anhydrous peridotite melting.

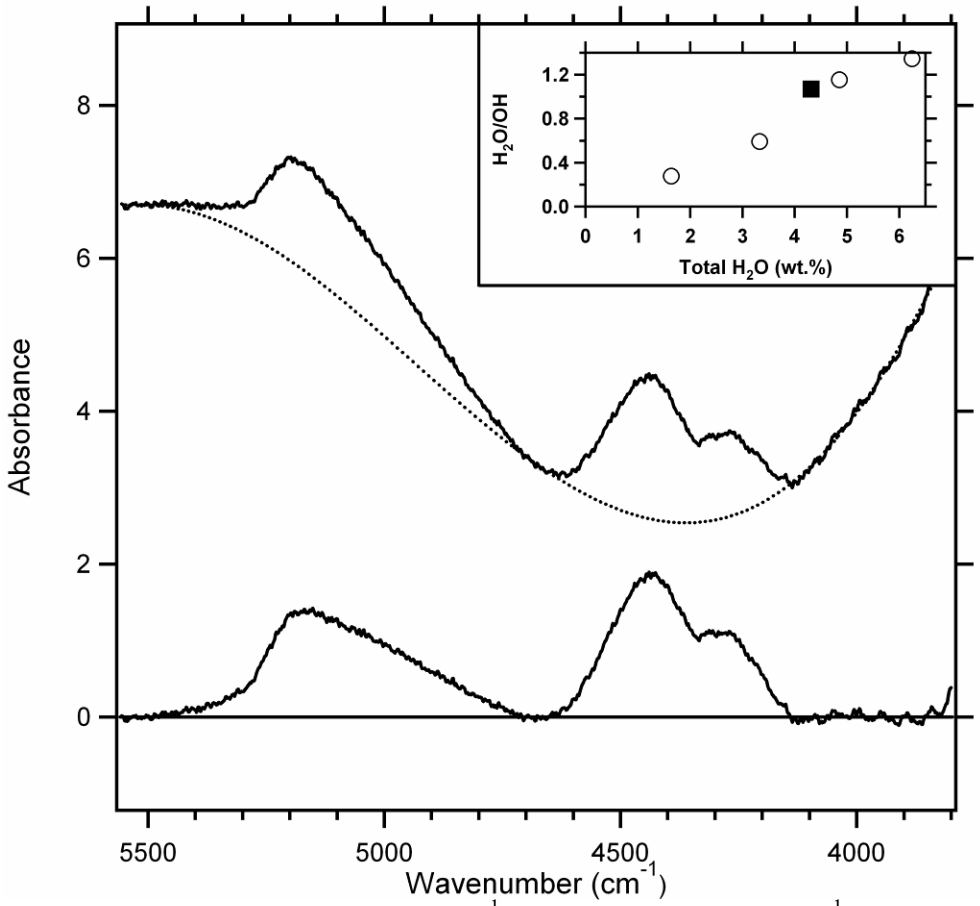

Figure 3.12. FTIR spectra of the 4500 cm^{-1} (hydroxyl) and 5200 cm^{-1} (molecular water) regions of the glass from experiment M418 (3 GPa, 1450ºC, 1.5 wt. % bulk H_2O). Spectra are normalized to a thickness of 1 cm. The top spectrum is the raw spectrum and illustrates the 2-gaussian fit to the background. The bottom spectrum is that resulting after background correction. Parameters in Eqn. 1 used to quantify the total water content in the glass are as follows: d = 0.0068 cm, ρ = 2729 g/l, $A^*_{H_2O}$ = 3.30 cm^{-1}, and A^*_{OH} = 3.31 cm^{-1} yielding values of c_{H_2O} and c_{OH} of 2.23 wt. % , and 2.08 wt. %, respectively, or a total water content of 4.31 wt. %. This is consistent with that inferred by mass balance (4.50 wt. %). **Inset:** Total H_2O content of glass as a function of the ratio of hydrous species concentrations. The datum from experiment M418 is represented by the closed symbol, while the open symbols are the measured basaltic glasses from the study

of Ohlhorst *et al.* (2001). Our datum match the trend produced by the Ohlhorst et al. basaltic glasses, which suggests that our background removal produces a result that is consistent with the Ohlhorst et al. technique.

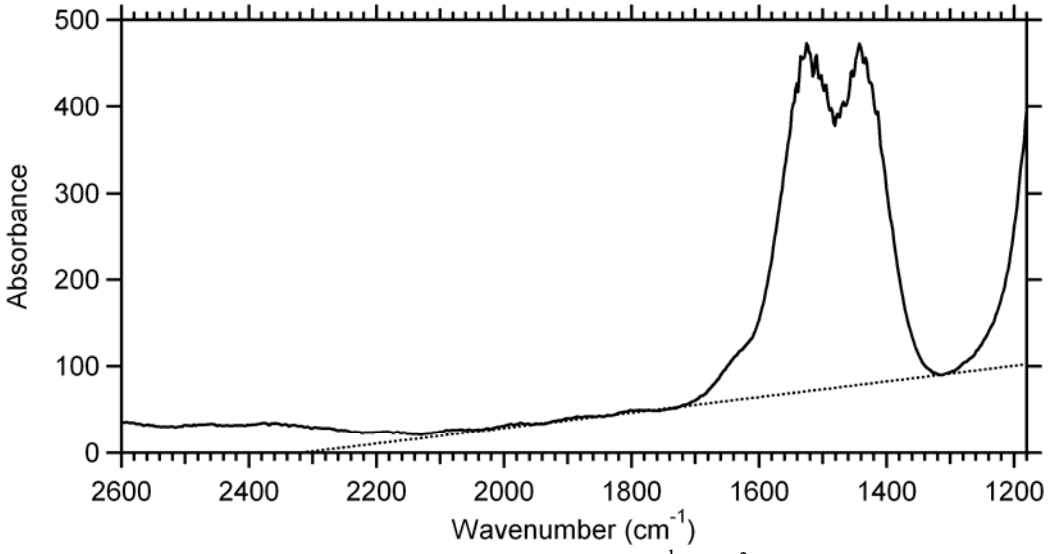

Figure 3.13. FTIR spectra of the 1440 and 1520 cm^{-1} CO_3^{2-} doublet from the quenched glass of experiment M418. The raw spectrum is normalized to a thickness of 1 cm, and a linear background correction is applied as illustrated. No CO_2 peak is observed at ~2350 cm^{-1}. Parameters in Eqn. 1 used to quantify the CO_2 content in the glass are as follows: d = .0045 cm, ρ = 2729 cm^{-1}, $A_{CO_3^{2-}}$ = 318 cm^{-1}, yielding a CO_2 content of 1.64 wt. %. Two additional FTIR measurements on the glass (not shown) yield concentrations of 1.61 and 1.54 wt. % CO_2.

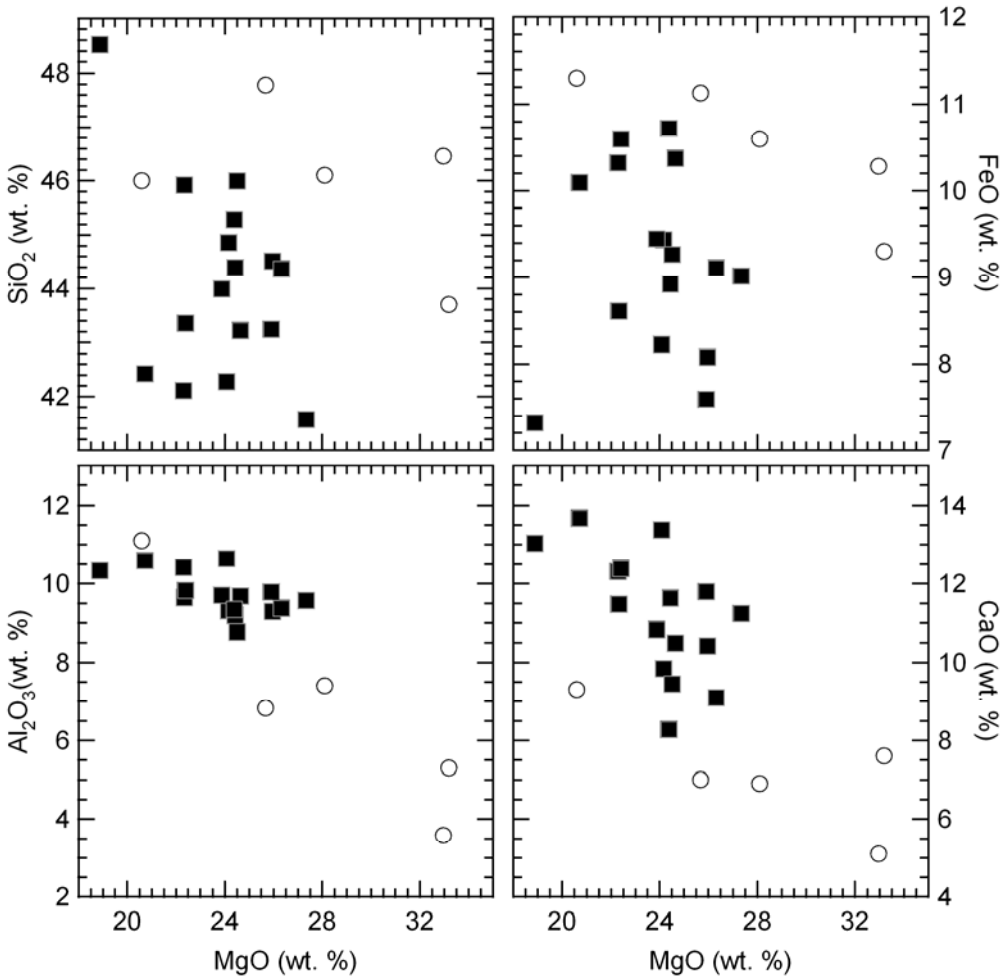

Figure 3.14. Comparison of melt compositions of this study (solid squares) to the estimated parental komatiite magma compositions (open circles) of Nisbet *et al.* (1993). Similar to the results of Kawamoto and Holloway (1997), our melts are more alkalic than komatiite parental magmas, which suggests that hydrous melting of fertile garnet peridotite is not the source of komatiites.

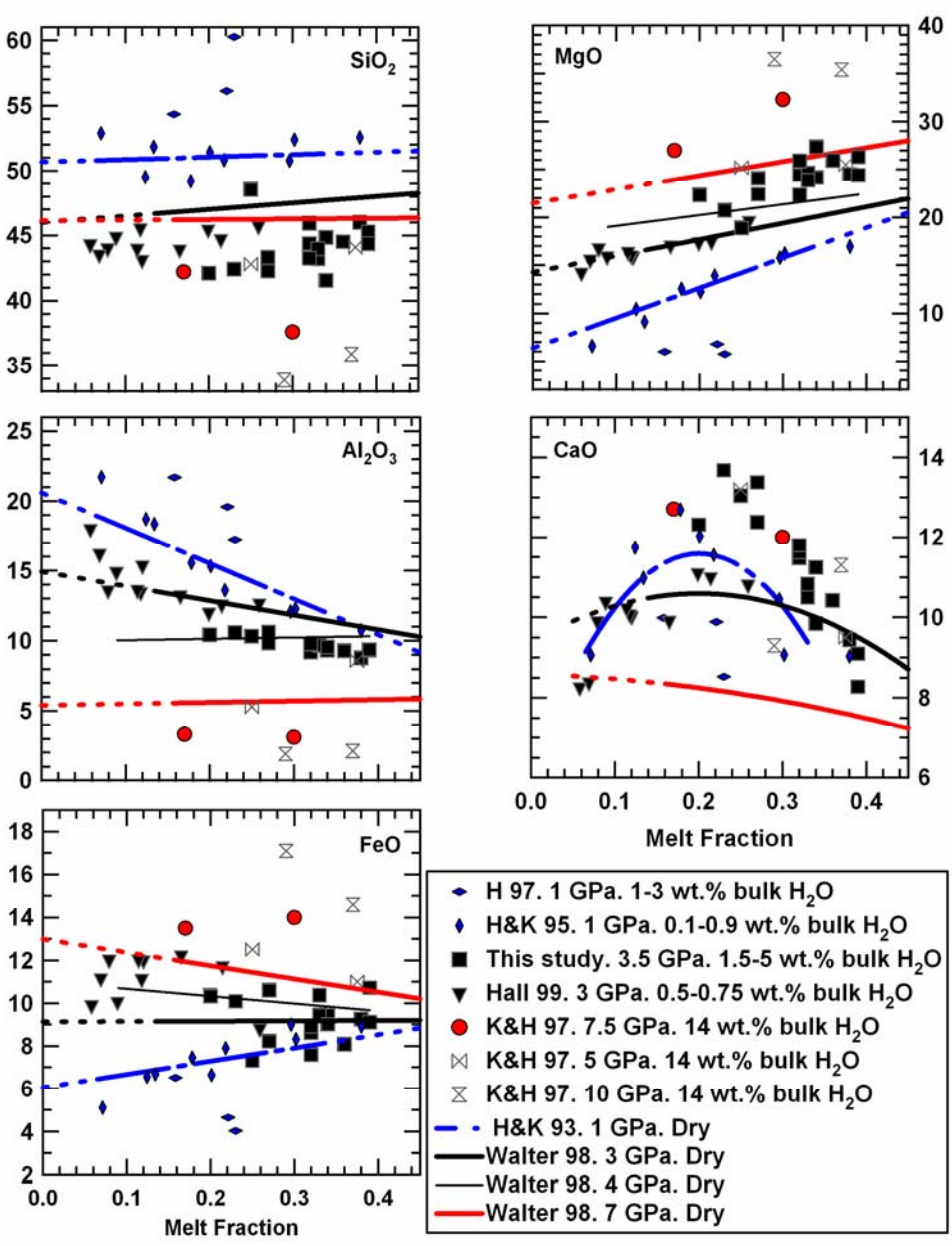

Figure 3.15. Comparison of partial melts of dry and hydrous spinel and garnet lherzolite. Hydrous partial melt compositions are recalculated anhydrous. Solid curves are fits to experimental data, and dashed lines are extrapolations. Anhydrous 4 GPa SiO_2 and CaO melt trends plot on top of 3 GPa data. In the spinel stability field (blue fit line, blue diamonds), hydrous melts are more silicic and aluminous, and are FeO*, MgO, and CaO depleted, when compared to anhydrous melt compositions. In contrast, hydrous melts in

the garnet stability field (red and black fit lines and data) are *less* silicic and aluminous, and *more* enhanced in FeO*, MgO, and CaO, when compared to anhydrous peridotite melting. Varying degrees of Fe-loss affect FeO* concentrations in partial melts of this study. Experimental data also include the following studies: Hirose (1997), Hirose & Kawamoto (1995), Hall (1999), Kawamoto & Holloway (1997), Hirose & Kushiro (1993), and Walter (1998).

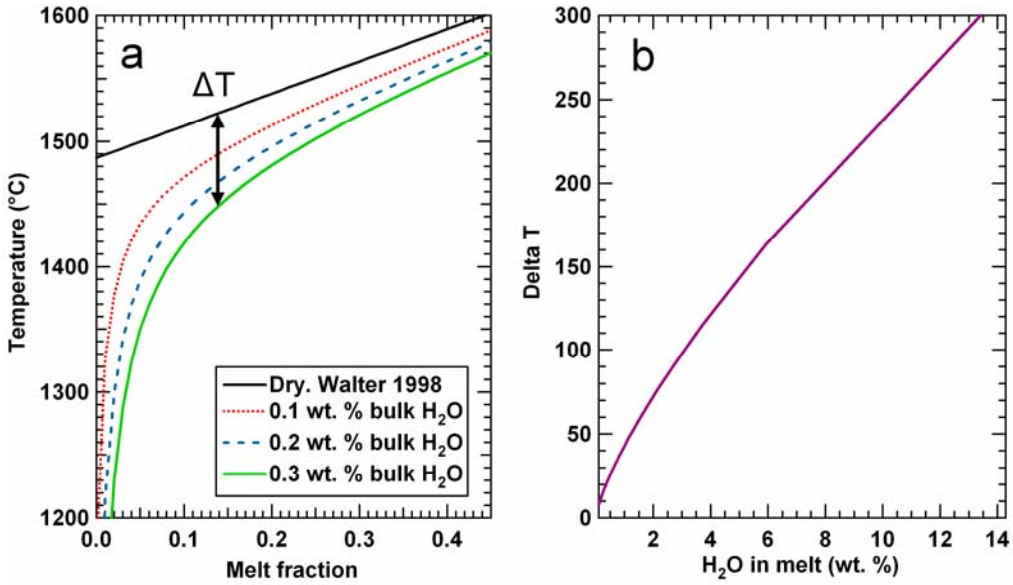

Figure 3.16. Schematic illustration of the effect of water on hydrous melting, based on the parameterization of Katz et al. (2003). **(a)** Comparative melting curves for both hydrous and dry systems. For a given bulk H_2O content there is a unique melting curve that deviates further from dry melting with decreasing F, due to the strong partitioning of water into partial melts. The temperature difference between the dry and wet melting curves, at a given F, is defined as ΔT (Eqn. 5), which is therefore a measure of the influence of dissolved H_2O on the extent of melting. **(b)** ΔT as a function of melt H_2O content. Determination of ΔT and melt H_2O content from experiments at various temperatures and values of F produces a simple monotonic relationship.

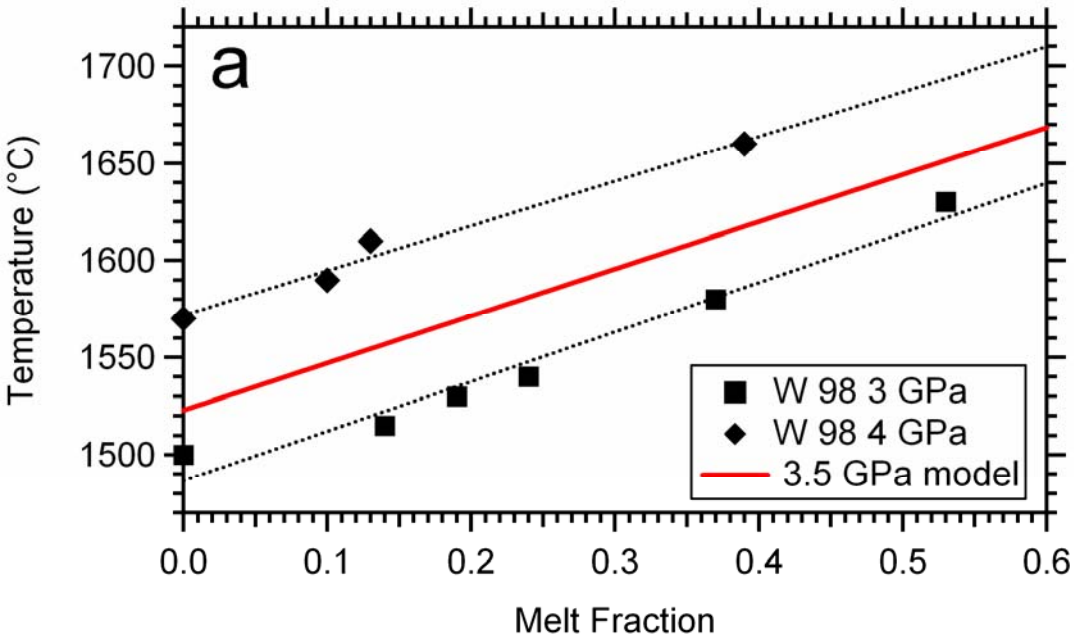

Figure 3.17a.

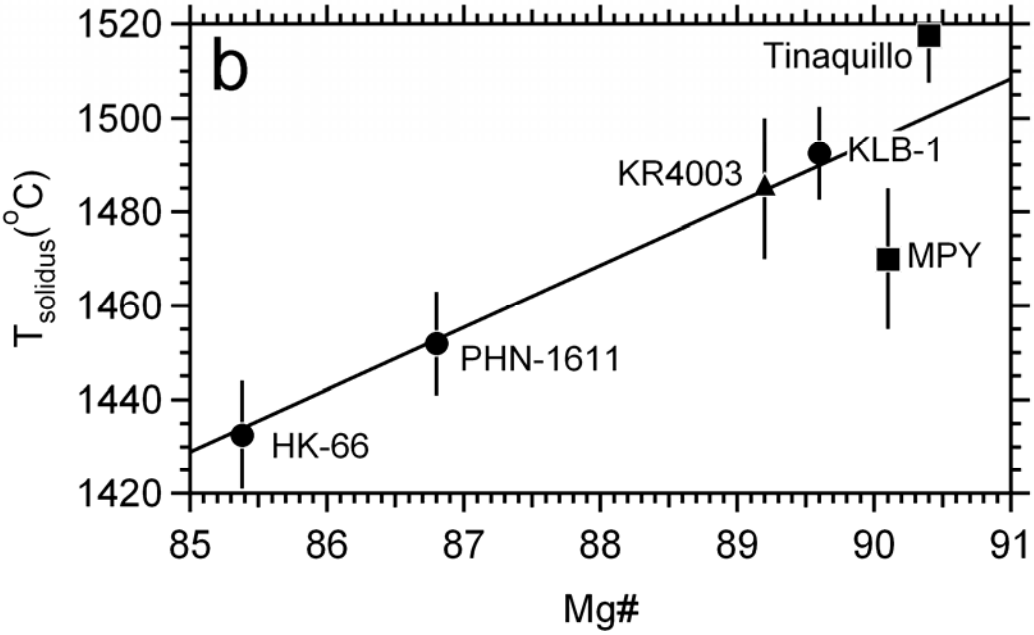

Figure 3.17b.

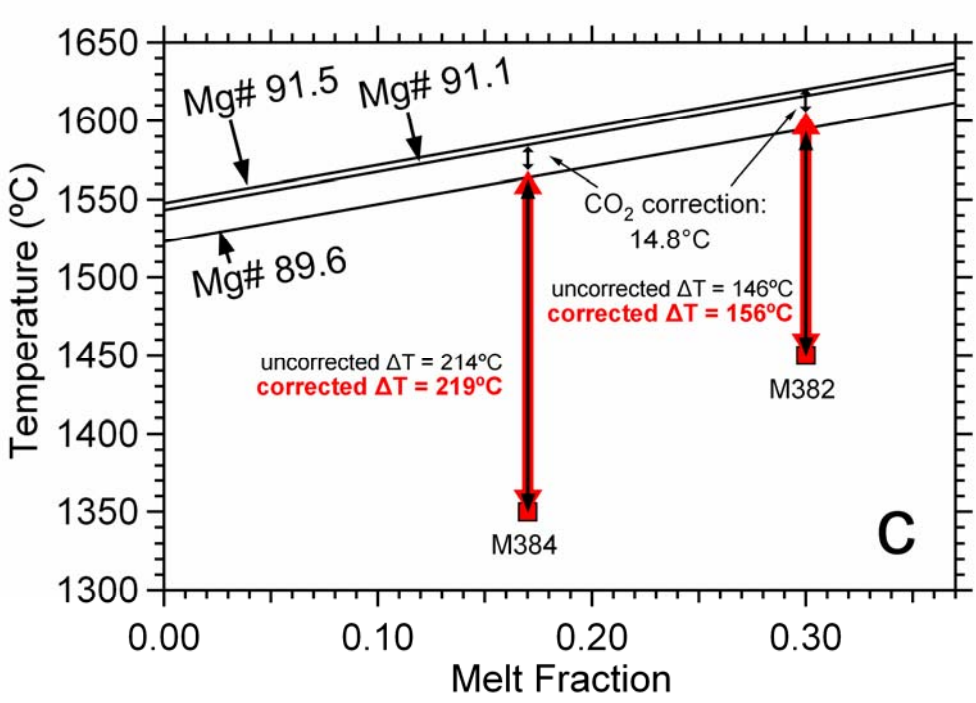

Figure 3.17c.

Figure 3.17. Plots illustrating the methods used to calculate ΔT from the experiments, including corrections for Fe loss and CO_2 infiltration. **(a)** To calculate the relationship between temperature and melt fraction for dry partial melting of fertile garnet lherzolite at 3.5 GPa we interpolate from the 3 and 4 GPa experiments of Walter (1998), which yield linear fits of T(ºC) = 255.2F + 1487 and T(ºC) = 229.8F + 1572, respectively. This, combined with the solidus (1523 °C) taken from Hirschmann (2000) yields T(ºC) = 242.5F + $T_{solidus}$(ºC). **(b)** To correct for experiments with bulk peridotite Mg# deviating from typical fertile lherzolite (89.6; Davis *et al.*, 2009) owing to Fe-loss, we quantify the influence of Mg# on the solidus temperature of nominally anhydrous peridotite at 3 GPa, after Hirschmann (2000), including data for peridotites HK-66 and KLB-1 (Hirose & Kushiro, 1993), PHN-1611 (Kushiro, 1996), Tinaquillo and MPY peridotite (Robinson & Wood, 1998), and KR4003 (Walter, 1998). This results in a correction of 13.3°C/Mg#.

(c) Illustration of Fe-loss and CO_2 gain corrections to ΔT for experiments M382 and M384. Starting with the anhydrous T versus F correlation from Fig. 3.17a, the uncorrected values of ΔT are 146 and 214ºC, as given by the difference in temperature between the temperatures at which the dry melting trend and the actual experiments achieve the observed melt fractions. The dry melting trend is then adjusted to hotter temperatures owing to Fe-loss (determined by mass balance) for M382 and M384, which have bulk Mg#s of 91.5 and 91.1, respectively, resulting in corrections to ΔT relative to fertile peridotite (Mg# = 89.6) of 25 and 20º, respectively. Finally, ΔT is reduced by 15 degrees to account for the solidus-lowering effect of CO_2 infiltration, resulting in corrected values of ΔT of 156 and 219º, respectively.

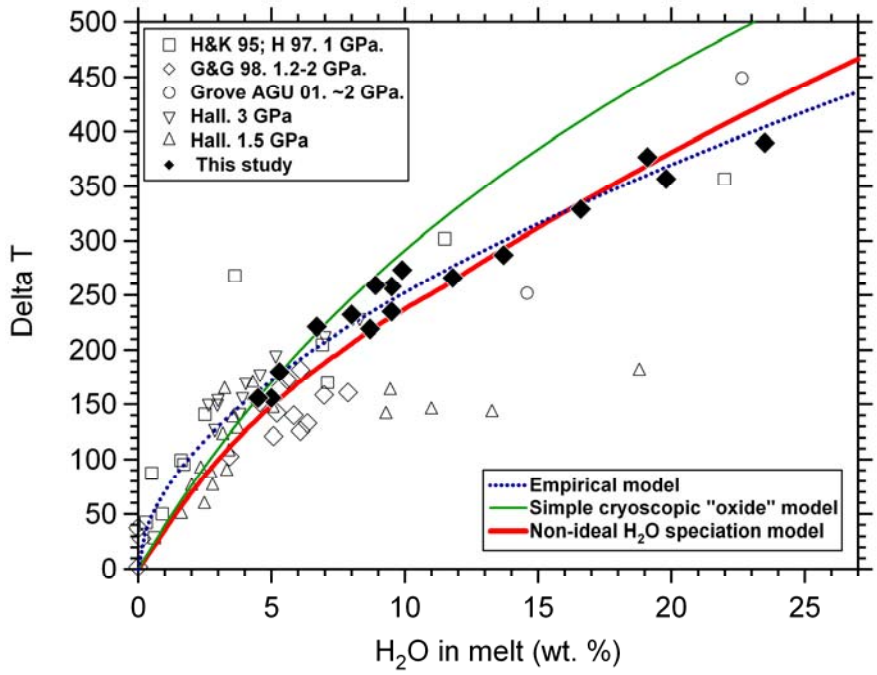

Figure 3.18. Experimental determinations of ΔT as a function of the H_2O content in the melt. Solid symbols represent data from this study. Open symbols are from the studies of Hirose & Kawamoto (1995), Hirose (1997), Gaetani & Grove (1998), Hall (1999), and Grove (2001). Data from this study are in broad agreement with those from previous

studies, but with less scatter. The empirical fit given by Eqn. 10 (Katz *et al*., 2003) uses the following parameters: K=70.9 and γ=0.552. This fit likely overestimates the effect of water on freezing point depression for melt water contents below ~5 wt. %. The simple cryoscopic "oxide" model (Eqn. 11) is that given by Hirschmann *et al.*, (2009). It assumes that all dissolved H_2O in the melt is of the form OH^- and that one mole of silicate in the melt can be calculated based on components with simple oxide stoichiometry. The speciation model (Eqn. 13) assumes that H_2O is present both as H_2O and OH^- species according to a non-ideal mixing model for albite melts (Silver *et al.*, 1990), as recommended for basaltic melts by Dixon *et al.* (1995).

Chapter IV

H_2O storage capacity of olivine and orthopyroxene from 10 to 13 GPa: Consequences for dehydration melting above the transition zone.

The onset of hydrous partial melting above the transition zone is dictated by the H_2O storage capacity of peridotite, which is defined as the maximum concentration that the solid assemblage can store at *P* and *T* without stabilizing a hydrous fluid or melt. H_2O solubilities of minerals in simple systems do not adequately constrain the peridotite water storage capacity because they do not account enhanced hydrous melt stability and reduced H_2O activity facilitated by the additional components of multiply saturated peridotite. In this study we present a new method for determining mineral water storage capacities, and determine olivine and orthopyroxene water storage capacities at conditions above the transition zone. Our method involves performing layered multi-anvil experiments, in which the bottom ~2/3 of the capsule is packed with hydrated KLB-1 oxide analog peridotite with 0.5, 0.75, or 1 wt.% bulk H_2O. The top ~1/3 of the capsule is packed with a monomineralic layer of hydrated Mg# 89.6 olivine with 0.5, 0.75, or 1 wt.% bulk H_2O, which facilitates the growth of ~200 μm olivine crystals from experimental run products, as well as accessory orthopyroxenes up to ~50 μm in size. The presence of small amounts of melt ensures that crystalline phases are H_2O saturated, while still retaining the full peridotite assemblage (melt + ol + pyx + gt). Experiments were carried out at pressures ranging from 10-13 GPa, and at temperatures ranging from 1350-1450ºC. At 12 GPa olivine and orthopyroxene water storage capacities decrease

from ~1800-1100 ppm, and ~1400-1100 ppm, respectively, as temperature increases from 1350 to 1450ºC. At 1450ºC olivine water storage capacity increases linearly with increasing pressure, which is a continued trend from an accompanying study of 5-8 GPa olivine water storage capacity at 1450ºC, and is defined by the following: $C_{H_2O}^{olivine}$ (ppm) = (102**P*(GPa)) – 363. Combination of this trend, along with the estimated $D_{H_2O}^{pyx/olivine}$ from this study (0.77±0.07), $D_{H_2O}^{gt/olivine}$, and mineral modes along an oceanic adiabat allows estimation of peridotite water storage capacity, which ranges from 700-1100 ppm at 410 km depth. This suggests that MORB source upper mantle contains too little bulk H_2O to incite a global melt layer above 410 km, but that OIB source mantle and subducted slabs can incite localized hydrous partial melting above the transition zone.

INTRODUCTION

Studies involving the role of H_2O in nominally anhydrous minerals and its effects on upper mantle properties have evolved significantly since earlier works (Skogby *et al.*, 1989; Rossman & Aines, 1991; Bell & Rossman, 1992, Bai & Kohlstedt, 1992; 1993) provided constraints on hydrogen concentrations incorporated into olivine, pyroxene, and garnet. Structurally bound hydrogen in minerals affects their rheological (Chopra & Paterson, 1984; Mackwell *et al.*, 1985; Mei & Kohlstedt, 2000a&b) and electrical (Karato, 1990, Yoshino *et al.*, 2008, Dai & Karato, 2009) properties, and affects seismological (Wood, 1995, Karato & Jung, 1998) and petrologic behavior (Hirth & Kohlstedt, 1996; Asimow & Langmuir, 2003; Katz *et al.* 2003, Aubaud *et al.* 2004, Hirschmann *et al.*, 2009). In particular the great power of H_2O to lower melting temperatures (Hirth & Kohlstedt, 1996; Asmiow *et al.* 2003; Aubaud *et al.*, 2004, Hirschmann *et al*., 2005) has a significant effect on the locus of partial melting in the

mantle. A crucial parameter that controls the locus of partial melting and limits the influence of water on the properties of solid peridotite is the H_2O storage capacity of peridotite, which is defined as the maximum mass fraction of water that can be retained in solid peridotite at a given temperature and pressure (Hirschmann *et al.*, 2005). Finite fractions of hydrous fluid or partial melt are stable only when the bulk water content of peridotite exceeds the H_2O storage capacity.

At high pressures, the co-existence of a mineral and silicate-H_2O rich fluid is commonly referred to as the H_2O solubility of the mineral. Therefore the difference between water storage capacity and water solubility at these conditions bears a slight explanation. High pressure mineral H_2O storage capacity is only achieved when the silicate-H_2O fluid is in equilibrium with all of the peridotite phases, thus providing an H_2O activity that is appropriate to the upper mantle. At upper mantle storage capacity conditions the H_2O activity at a given P and T is lower than simpler systems that lack all of the solid peridotite phases. Additionally, the melting temperature of peridotite is lower than a simple phase assemblage. Many studies have determined high pressure mineral H_2O solubilities, while high pressure H_2O storage capacities have yet to be thoroughly investigated.

Based on measured mineral water solubilities, it is likely that a significant discontinuity in H_2O storage capacity exists across the 410 km discontinuity, evidenced by the difference in water solubilities between olivine (Kohlstedt *et al.*, 1996; Chen *et al.*, 2002; Smyth *et al.*, 2006, Litasov *et al.*, 2007) and its high pressure polymorph wadsleyite (Takahashi *et al.*, 1987; Gasparik *et al.*, 1993; Inoue *et. al*, 1995; Kohlstedt *et al.*, 1996; Kawamoto *et al.*, 1996; Smyth *et al.*, 1997a&b; Chen *et al.*, 2002; Kohn *et al.*,

2002; Litasov *et al.*, 2003; Jacobsen *et al.*, 2005). As $(Mg,Fe)_2SiO_4$ constitutes 60% of the upper mantle by mass (Walter, 1998; Irifune & Isshiki, 1998) it has a significant influence on the mantles H_2O storage capacity. Olivine water solubilities at high pressures are on the order of thousands of ppm while wadsleyite water solubilities approach weight percent (tens of thousands of ppm) levels. At conditions analogous to those near the transition zone (13-15 GPa, 1400-1600ºC) H_2O partitioning between olivine and wadselyite ($D_{H_2O}^{wd/ol}$), ranges from 2-6 (Chen *et al.*, 2002; Hirschmann *et al.*, 2005; Demouchy *et al.*, 2005; Litasov et al., 2007; Frost & Dolejš, 2007).

This large contrast between olivine and wadsleyite water solubilities may lead to partial melting above the transition zone. Bercovici & Karato (2003) hypothesized that upwelling mantle below the 410 km discontinuity, with a bulk water content that exceeds olivine solubility, will shed its water as it crosses 410 km into shallower depths, and that therefore pervasive hydrous melting could occur above the transition zone. If correct, the transition zone water filter model of Bercovici and Karato (2003) would play a key role in the global H_2O cycle in terms of transport of H_2O between the transition zone and upper mantle. Evaluating this hypothesis requires detailed constraints on H_2O storage capacity of the deep upper mantle.

If H_2O-enriched mantle material is advected through the transition zone into the upper mantle, it will incite partial melting only if its bulk H_2O concentration exceeds the upper mantles storage capacity. If this occurs, partial melting will leave behind residues with bulk H_2O concentrations equal to the upper mantle H_2O storage capacity. This is illustrated in Figure 4.1. As this residue advects it will retain an H_2O concentration equivalent to the H_2O storage capacity of the upper mantle at that particular *P* and *T* (Fig.

4.1). Therefore, estimates of upper mantle bulk water contents provide constraints on the water content in the transition zone. MORB source upper mantle estimates range from 50-200 ppm bulk H_2O (Dixon *et al.*, 1988, Michael 1988; 1995; Danyushevsky *et al.*, 2000; Saal *et al.*, 2002; Simons *et al.*, 2002. Salters & Stracke, 2005; Workman & Hart, 2005) while OIB sources range from 300-1000 ppm bulk H_2O (Jambon & Zimmermann, 1990; Sobolev & Chaussidon, 1996; Dixon *et al.*, 1997; 2002; Jamtveit *et al.*, 2001, Hauri *et al.*, 2002; Simons *et al.*, 2002; Seaman *et al.*, 2004; Aubaud *et al.*, 2005; 2006). Additionally, subducted slabs may contain hundreds to thousands of ppm bulk H_2O (Shieh *et al.*, 1998; Okamoto & Maruyama, 1999; Katayama *et al.*, 2003; 2006). Consequently, the peridotite H_2O storage capacity must be lower than these values in order to incite partial melting at the base of the upper mantle.

Peridotite H_2O storage capacity at transition zone conditions has been estimated using two different techniques, documented in the studies of Hirschmann *et al*. (2005) and Hirschmann *et al*. (2009). In Hirschmann *et al*. (2005), H_2O storage capacity was determined by combining individual mineral H_2O solubilities with their modal abundances along a mantle adiabat. This method results in an estimated peridotite H_2O storage capacity of 4,000-12,000 ppm, which strongly argues against any type hydrous melting above the transition zone. However, mineral H_2O solubilities have higher H_2O activities than H_2O storage capacity, which likely means that the range of values of Hirschmann *et al*. (2005) is an overestimate of peridotite H_2O storage capacity. Hirschmann *et al.* (2009) used a different approach to determine the H_2O storage capacity at the transition zone by combining peridotite freezing point depression (Katz *et al.*, 2003, Tenner *et al*., submitted) with peridotite/melt H_2O partitioning ($D_{H_2O}^{peridotite/melt}$)

(Tenner *et al.*, 2009) (Fig. 1.1, Chapter I). The premise for this determination is that hydrous peridotite solidus depression is a direct function of the amount of dissolved H_2O in the incipient melt, which can be calculated by parameterization (Katz *et al.*, 2003, *Tenner et al.*, submitted). At incipient peridotite melting the H_2O concentration in the solid residual assemblage is its H_2O storage capacity. Therefore, if $D_{H_2O}^{peridotite/melt}$ is also known, peridotite H_2O storage capacity can be calculated. Hirschmann *et al.* (2009) used these relationships to infer a peridotite H_2O storage capacity of 520-540 ppm at 410 km depth. This result argues against a pervasive layer of melt atop the transition zone (Bercovici & Karato, 2003), but does not rule out that localized hydrous melting may be associated with plumes or subduction zones. Although this method provides a more realistic approach to attaining peridotite H_2O storage capacity, it is based on $D_{H_2O}^{peridotite/melt}$ values that are grossly extrapolated (from 5 GPa to 13.7 GPa). Additionally, peridotite freezing point depression data at conditions near the transition zone are scattered and lacking. Therefore, the results of Hirschmann *et al.* (2009) likely have considerable uncertainties.

In this study we provide a new method that is a direct determination of a minerals H_2O storage capacity by experimentally equilibrating the mineral of interest with the full peridotite assemblage and a small amount of melt. These experiments consist of two layers: hydrated peridotite, and a hydrated layer of monomineralic olivine. At *P* and *T* the hydrated monomineralic olivine layer facilitates growth of large crystals, allowing quantification of their H_2O content by low H-background SIMS (Koga *et al.*, 2003; Aubaud *et al.*, 2004; 2008; Hauri *et al.*, 2006; Tenner *et al*., 2009), while the presence of melt in contact with both the monomineralic layer and the peridotite layer ensures

equilibration of H_2O concentrations. In this study we use this method to determine the water storage capacity of olivine and orthopyroxene at the base of the upper mantle.

METHODS

Starting materials and experiments

Starting materials consist of two oxide mixtures, one with the compositons equivalent to hydrous olivine oxide, and the second equivalent to hydrated Kilbourne Hole (KLB-1) fertile spinel peridotite (Takahashi & Kushiro, 1983; Davis *et al*., 2009). Hydrous olivine mixtures were synthesized from reagent-grade MgO, $Mg(OH)_2$, SiO_2, and FeO. Initially, we synthesized a "base" hydrous olivine oxide mix with the composition olivine (Mg# 89.6) + 10% H_2O. This base mix was then diluted with additional MgO, FeO, and SiO_2, to produce separate hydrous olivine batches (also Mg# 89.6) with 0.5, 0.75, and 1 wt. % H_2O, respectively. Synthesis of the hydrous KLB-1 oxide was performed in several steps. First, an anhydrous and Fe-free mix was constructed from reagent-grade oxides and carbonates. After decarbonation at 1000ºC, FeO was added. A glass bead of the anhydrous KLB-1 oxide mix was produced by containerless vitrification (Davis *et al.*, 2009) and the composition was determined by electron microprobe analysis (Table 4.1). This anhydrous peridotite was hydrated by mixing in the "base" hydrous olivine oxide, producing 3 separate batches with 0.5, 0.75, and 1 wt. % bulk H_2O. In each experiment, added hydrous peridotite and olivine powders were matched to have the same bulk H_2O content, so that the H_2O content of the total charge would not be affected by small variations in olivine to peridotite ratio. Starting material compositions are shown in Table 4.1.

Starting materials were packed into 1.6 mm diameter Au capsules in the following method: the bottom ~2/3 of the capsule consists of hydrated KLB-1 oxide and the top ~1/3 of the capsule consists of the hydrated olivine oxide mix (Fig. 4.2). The actual ratios were verified by measuring the length of a drill blank plus the starting material as it was packed into the capsule, as well as measuring the mass of each layer. The monomineralic hydrous olivine layer is crucial for these experiments because it facilitates growth of large crystals required for SIMS analysis (Fig. 4.2). Ends of the capsules were sealed by coning by lathe and then spot welding with a water chilled vice, as this technique has been demonstrated to retain H_2O in capsules in previous studies (Tenner *et al.*, 2009, Tenner *et al.*, submitted). Upon final shaping capsules were approximately 1.7 mm in length.

Experiments were carried out in a Walker-style multi-anvil apparatus, and were performed at pressures of 10-13 GPa, and temperatures of 1350, 1400, and 1450ºC. Experimental run durations were 24 or 48 hours (Table 4.2). A 14–8 assembly was employed, and consisted of octahedra with 14 mm edge lengths and ZrO_2 insulators obtained from the COMPRES Multi-Anvil cell assembly development project. Gaskets consist of pyrophyllite, and MgO spacers were used to position the capsule within the assembly. Temperature was controlled with type D ($W_{97}Re_3/W_{75}Re_{25}$) thermocouple that was positioned directly above the capsule about its axis, evidenced by an easily identifiable dent in all post-experiment capsules. Rolled Re foil was used as the furnace. Pressure was calibrated by the Bi I-II and III-V transitions at 25 ºC (Piermarini & Block, 1975) and by the high-pressure fixed point method defined by coexisting $(Mg,Fe)_2SiO_4$ polymorphs (Frost & Dolejš, 2007) (Fig. 4.3, Table 4.3), and closely match previous

calibrations of the multi-anvil apparatus using the same techniques with a similar assembly (Withers & Hirschmann 2007) (Fig. 4.4). Ideally the use of a stepped $LaCrO_3$ furnace is desirable for the high-pressure multi-anvil assembly because the thermal gradient though capsules of similar size to this study is believed to be within 30º of the nominal run temperature (Withers *et al.*, 2007). However, there is a temporary shortage of usable $LaCrO_3$ furnace material in the experimental community owing to the departure from the market of the chief industrial supplier. Our attempts at using furnaces fashioned from sub-optimum $LaCrO_3$ failed because they would not properly heat to the temperatures of interest. While the use of Re furnaces proved to be reliable, previous studies have documented that they introduce a significant thermal gradient within a capsule, on the order of 50-200ºC/mm (LaTourrette & Holloway, 1994; Lesher *et al.*, 2003). We investigated the thermal gradient through our capsules by bracketing the $(Mg, Fe)_2SiO_4$ polymorphs at the bottom of the fixed point pressure calibration as a function of temperature, using the phase diagrams of Frost & Dolejš (2007) (see caption to Table 4.3 for details). Using this method we predict a thermal gradient of 195 ºC/mm, with temperature increasing downward in the capsule. This large thermal gradient compromised some aspects of our experiments (see Discussion).

Upon quench capsules were ground with a 9 μm diamond lapping film to expose the run products. Then 3μm and 1μm diamond lapping films were used to further expose the run products into a window ~400-600 microns in width (Fig 4.2). During polishing the run products were impregnated with Crystalbond™ 509 (Aremco Products), which is completely dissolvable in acetone.

Electron Microprobe Analysis (EMPA)

Major element concentrations of all phases from run products were determined by wave dispersive spectroscopy with a JEOL JXA8900R electron microprobe. A 15 kV accelerating voltage was used with a 10 nA beam current, and counting times of 10 seconds for peaks and 5 seconds for backgrounds. Standards consisted of San Carlos olivine, enstatite, diopside, Na-bearing omphacite, pyrope, hornblende, chromite, Mn-hortonolite, K-feldspar, and two basaltic glasses, used in various, but consistent combinations to determine the major element compositions of olivine, orthopyroxene, clinopyroxene, garnet, and quenched partial melt from run products. Partial melts are in the form of heterogeneous quench mats, so their equilibrium compositions were determined using the methodology of Tenner *et al.* (submitted), which consists of mapping a grid of analyses (n = 100-300) over the entire quench region, and then filtering the analyses according to their olivine/melt Fe/Mg exchange equilibria:

$$K_D = \frac{[X_{Fe}^{ol}][X_{Mg}^{melt}]}{[X_{Fe}^{melt}][X_{Mg}^{ol}]} \quad (1)$$

Melt analyses with a wide K_D range (0.25-0.40) are used to determine the average melt composition. We use a wide K_D range because of the variations in determinations of K_D in high pressure studies in peridotite-related systems (Takahashi, 1986; Agee & Walker, 1988; Herzberg & Zhang, 1996; Walter, 1998; Mibe *et al.*, 2006, Tenner *et al.*, submitted) presumably owing to variability in capsule type, thermal profiles in assemblies, and fO_2.

Secondary Ion Mass Spectrometry (SIMS)

Quantitative determination of H-storage capacity in olivines and orthopyroxenes from this study were determined by low-H background SIMS (Koga *et al.*, 2003; Hauri *et al.*, 2006, Aubaud *et al.*, 2004; 2008; Withers & Hirschmann 2007; 2008; Tenner *et al.*,

2009; O'Leary *et al.*, 2010). Experimental run products and standards were cleaned with successive baths of acetone and ethyl alcohol to remove Crystalbond™ and any other H-bearing contaminants, and were then baked overnight at 100 ºC in a vacuum drying oven. Samples and standards were then pressed into indium (Fig. 4.5), and the mounts were sputter coated with Au prior to SIMS analysis.

SIMS analyses were performed on the Cameca 6f at Arizona State University. The instrument was baked out for 24 hours prior to use to achieve as low a vacuum as possible. A Cs^+ source was used to generate primary ions, along with a ~10 nA beam current, and an impact energy of 19 KeV. Tuning of the ion source in critical illumination mode produced a uniform beam diameter of ~25 μm. For each measurement the primary ion beam was adjusted with electromagnetic steering plates to achieve co-linearity in x and y, which is necessary due to slight sample tilt or surface topology. With the mass set to ^{16}O the electromagnetic steering plates were adjusted so that the primary ion beam generated secondary ions onto the secondary ion optical axis (Tenner *et al.*, 2009). Tuning of the primary ion beam in this manner is critical for achieving precise measurements. A -9000V potential was applied to the sample to accelerate negative secondary ions away from sputtering site created by primary ion impact. A 100 μm field aperture was placed into the secondary ion path, which allows only those ions from a ~10 μm circular area, centered within the sputtered crater, to pass into the mass spectrometer. Secondary ions with kinetic energies of 0 ± 125 eV (energy bandpass centered and wide open) were allowed into the mass spectrometer, and were counted with an electron multiplier. Sample charging was controlled by use of an electron gun (Slodzian, 1986) that was tuned to match the filament voltage to the sample potential. In this manner,

electrons only reach the sample if it charges up positively through positive primary ion impact and negative secondary ion departure. For each analysis, negative ion intensities were measured for ^{12}C, $^{16}O^{1}H$, ^{18}O, ^{19}F, and ^{30}Si, with counting times of 10, 5, 5, 5, and 2 seconds, respectively. This cycle was repeated 6 times for each analysis. ^{12}C and ^{19}F count rates were used as a rough proxy for determining whether or not an analysis may yield spurious $^{16}O^{1}H$ measurements due to foreign surface material and/or cracks and pits (secondary ion imaging of ^{12}C and ^{19}F on areas of interest also aids in determining the cleanliness of the sample surface).

Hydrous orthopyroxene (Aubaud *et al.*, 2007) and olivine standards (Aubaud *et al.*, 2007, Withers *et al.*, in prep.) have known OH contents that have been determined by Fourier transform infrared spectroscopy (FTIR). Orthopyroxene (Aubaud *et al.*, 2007) and olivine standards (Withers *et al.*, in prep.) are calibrated against $(^{16}O^{1}H/^{30}Si)_{SIMS} \times (SiO_2)_{EMPA}$, and the resulting calibration curves (Fig. 4.6) are used to quantify the hydrogen contents of olivine and orthopyroxene unknowns. The H-background during our SIMS session is estimated by combining the olivine calibration curve with measurements on a dry Fo_{100} blank, and 13 measurements taken over the 5 day analytical session yielded a background of 23 ± 5 ppm.

RESULTS

Experimental textures

Exposed polished surfaces of experimental charges revealed that the hydrous olivine layer produced several large crystals of 50-500 μm in diameter (Fig. 4.2). Orthopyroxene crystals were interspersed throughout the olivine layer, and in 6 of the 10 experiments these were large enough (50-100 μm in diameter) to analyze by SIMS.

Electron backscattered images, as well as line scan analyses by EMPA suggest that the olivines and orthopyroxenes are homogeneous. The hydrous KLB-1 layer produced the assemblage melt+ol+opx+cpx+gt except for 2 experiments, which lacked cpx (Table 4.2). Mineral phases in the KLB-1 layer are typically 10-30 microns in diameter and are homogeneous. Olivines and orthopyroxenes in the monomineralic layer and the KLB-1 layer have no compositional differences. Partial melts form an hourglass-like texture within the KLB-1 layer owing to the thermal profile of the multi-anvil assembly, and in many cases are easily identified as large mats of bladed quench crystals (Fig 4.2). The exposed cross section of the capsule is relatively close to its outer edge, where melts are highly concentrated due to the thermal profile, and facilitates in retaining relatively large regions of quenched melt. Rims of garnet crystals (with interspersed quenched melt) form adjacent to the quenched partial melts, and mark the presence of partial melt in run products where either the melt fraction is low, or the exposed cross section does not favorably expose the melt. In 5 of the 10 experiments the quenched partial melt was sufficiently large and well-preserved to analyze by EMPA.

Phase compositions

The compositions of olivine, orthopyroxene, clinopyroxene, and garnet, and melt are given in tables 4.4 through 4.8, respectively. The Mg# of olivines, orthopyroxenes, and clinopyroxenes show relatively little variability in all experiments, with ranges of 91-93, 93-94.5, and 91-93, respectively. The pyroxenes are quite low in alumina, with orthopyroxenes and clinopyroxenes containing 0.17-0.31, and 0.80-1.20 wt.% Al_2O_3, respectively. Garnets vary in Mg# from 79 to 86 and have a normative majorite component that ranges from 15-24%, based on the calculation of Locock (2008). Melt

compositions (normalized anhydrous) are FeO-rich (12-19 wt.%) and highly refractory, with SiO_2 values ranging from 28-43 wt.% and MgO values ranging form 23-31 wt.%. The melts have low amounts of Al_2O_3 (1-4 wt.%), and CaO/Al_2O_3 ratios range from 4 to 11.

SIMS determinations of water storage capacity of olivine and orthopyroxene

SIMS derived storage capacities of olivine and orthopyroxene are given in Table 4.9. At 12 GPa and constant temperature, variable bulk H_2O in experiments yields some variability in olivine and orthopyroxene storage capacity (Fig. 4.7a&b), however, there is no systematic trend in isobaric, isothermal H_2O storage capacity as a function of bulk H_2O. This result justifies extrapolation to small bulk H_2O contents appropriate for incipient partial melting of peridotite near its storage capacity. Measured olivine and orthopyroxene H_2O storage capacities range from 580-2100 and 550-1600 ppm, respectively. At 1450°C olivines from experiments at 10, 11, 12, and 13 GPa exhibit a general increase in H_2O storage capacity, with 720, 580, 1160, and 830 ppm, respectively (Fig. 4.8). At 12 GPa, olivine H_2O storage capacity decreases from ~1800 to 1100 ppm (Fig. 4.9a), and orthopyroxene H_2O storage capacity decreases from ~1400 to 1100 ppm, as temperature increases from 1350 to 1450 °C (Fig. 4.9b). In the six experiments with coexisting orthopyroxene and olivine, and the water partitioning value, $D_{H_2O}^{opx/olivine}$, has a value of 0.77 ± 0.07 (Table 4.9).

DISCUSSION

Effect of a steep thermal gradient on water storage capacity and mass balance.

In our experiments the attainment of olivine and orthopyroxene water storage capacity is brought about by equilibration of the olivine layer with interconnected

peridotite partial melt. This ensures that the olivine layer is at an H_2O activity that is appropriate with respect to the upper mantle. A problematic issue though, is that the estimated thermal gradient through our capsules (200ºC/mm) could introduce an error in H_2O storage capacity measurements, as variable temperatures affect the H_2O activity of the system due to a shift in the proportion of silicate and H_2O in the fluid phase. However, we do not believe that the thermal gradient has a significant effect on measured storage capacities for a few reasons. First, individual SIMS measurements within a sample exhibit no systematic variability based on their location within the olivine layer (Fig 4.10), and errors of our SIMS measurements are similar to those of Ardia *et al.* (in prep.), who employ assemblies with a smaller thermal gradient. Second, major element compositions of crystalline phases between the olivine and peridotite layers are the same, which argues against severe, thermally driven disequilibrium. Third, while it may be possible that the thermal gradient has an effect on the absolute H_2O storage capacities, no discontinuity exists in the 5-13 GPa pressure trend between our results and those of Ardia *et al.* (in prep.) (Fig. 4.8).

In addition to measuring the H_2O storage capacity of olivine and orthopyroxene, we were able to determine the composition of partial melt (and residual phases) in 5 experiments, which allowed for calculation of mass balance to determine the melt fractions and estimate the water concentrations in the melt (Table 4.8). Combining the H_2O_{melt} concentrations with the measured mineral H_2O storage capacities yields mineral/melt partitioning ($D_{H_2O}^{mineral/melt}$), as $D_{H_2O}^{olivine/melt}$ and $D_{H_2O}^{opx/melt}$ have values of 0.013-0.020 and 0.009-0.0015, respectively (Table 4.9).

However, we suspect that the water concentrations in the melt, inferred by mass balance, are strongly affected by the thermal gradient, as the large melt pools analyzed by EMPA are below the olivine layer in the capsule (Fig. 4.2), where temperatures are hotter. Calculation of freezing point depression as a function of dissolved H_2O in the melt (Katz *et al*., 2003; Hirschmann *et al*., 2009; Tenner *et al.*, submitted) (Fig. 1.1, Chapter I) supports this explanation. Using the nominal experimental temperatures and mass balance-derived melt water concentrations from our experiments we estimate that ~10 wt.% dissolved water in the melt elicits ~650ºC of freezing point depression, which is significantly greater than the prediction based on the 10-20 GPa cryoscopic paramterization of Hirschmann *et al.* (2009) (Fig. 4.11). However, we believe that our melts are likely ~100-300 degrees hotter than the nominal experimental temperatures due to the steep thermal gradient and that, therefore, our calculated freezing point depression is severely overestimated. With respect to mineral/melt H_2O partitioning, the consequence of our melts being hotter is that they are more diluted in H_2O than they would be if they were at the nominal temperatures of experiments. As a result, our calculated $D_{H_2O}^{mineral/melt}$ values more than likely represent maxima.

Comparison of olivine and orthopyroxene water solubility versus water storage capacity

Several high pressure (8-14.5 GPa) water solubility studies of olivine (Bali *et al.*, 2008; Smyth *et al.*, 2006, Litasov *et al.*, 2007; Withers & Hirschmann, 2008) have observed substantial decreases in water solubility as a function of increasing temperature, which is likely due to the fact that the fluid in equilibrium with olivine has a higher proportion of dissolved silicate at higher temperatures, which reduces the H_2O activity in

the melt and coexisting solid assemblage. Additionally, the water storage capacity of the solid assemblage should decrease toward a value of "0" as the temperature approaches the dry solidus (Hirschmann *et al.*, 2005). We observe a similar trend at 12 GPa, as olivine water storage capacity exhibits a decrease from ~1800 to 1100 ppm as temperature increases from 1350-1450ºC (Fig 4.9a). However, when comparing data within the same temperature range, our water storage capacities are lower than the olivine water solubility data of Smyth *et al.* (2006). This difference likely occurs because the H_2O activity required to stabilize peridotite partial melts is lower than the H_2O activity required to stabilize partial melts of pure olivine. As a result, olivine water storage capacity is a factor of ~2 less than olivine water solubility at conditions near the 410 km transition zone (Fig. 4.9a).

Our measured H_2O storage capacities of orthopyroxene also decrease as a function of temperature at 12 GPa, from ~1400-1100 ppm as temperature increases from 1350-1450ºC (Fig 4.9b). Studies of clinoenstatite between 10 and 13 GPa (Yamada *et al*., 2004; Withers *et al.*, 2007) also show decreases in water solubility with increasing temperature. Coincidentally, our 12 GPa orthopyroxene water storage capacities overlap with the 11.6 GPa clinoenstatite H_2O solubility data of Withers *et al.* (2007) (Fig. 4.9b). This could suggest that differences in water activity between peridotite-H_2O and MgO-SiO_2-H_2O systems have a negligible effect on orthopyroxene water storage capacity relative to water solubility. On the other hand, complex peridotite-derived orthopyroxenes may have an increased H_2O storage capacity (relative to clinoenstatite) due to enhanced point defect incorporation of hydrogen, thus causing the observed overlap. For example, Withers *et al.* (2009) demonstrated that water solubility doubles

when decreasing from endmember enstatite to Mg# 80 orthopyroxene at 6 GPa, perhaps due to hydrogen incorporation through defects in the metal sites in the pyroxene structure, in a method similar to that proposed in olivine by Zhao *et al.* (2004). Additionally, pyroxene water solubility/storage capacity may exhibit significant increases with pressure, on the order of a factor of 5 increase from 12 to 13 GPa (Withers & Hirschmann, 2007). Therefore, at 12 GPa our orthopyroxene H_2O storage capacities may approach the H_2O solubility of 11.6 GPa clinoenstatites at comparable temperatures. We note, however, that these explanations are very speculative, and more data are necessary to provide a more detailed comparison between orthopyroxene water solubility and storage capacity.

Peridotite water storage capacity atop the 410 km transition zone

The main goal of this study is to provide constraints on peridotite H_2O storage capacity in order to accurately determine the conditions necessary for hydrous melting at the base of the upper mantle. By combining individual mineral H_2O storage capacities ($C_{H_2O}^{mineral}$) with their modal abundances (X^i) along a high pressure adiabat (Irifune & Isshiki, 1998; Stixrude & Lithgow-Bertelloni, 2005; 2007) we can estimate peridotite H_2O storage capacity ($C_{H_2O}^{peridotite}$):

$$C_{H_2O}^{peridotite} = X^{ol} C_{H_2O}^{ol} + X^{pyx} C_{H_2O}^{pyx} + X^{gt} C_{H_2O}^{gt} \quad (2)$$

For $C_{H_2O}^{ol}$, we use the fit to our water storage capacity data at 1450ºC (Fig. 4.8) as this temperature is appropriate to conditions near the base of the upper mantle. Our temperature and pressure constraints of orthopyroxene H_2O storage capacity do not provide for a 1450ºC pressure trend, but they do provide a tight constraint on

$D_{H_2O}^{orthopyroxene/olivine}$ (0.77± 0.07, n = 6). Therefore, we use $D_{H_2O}^{orthopyroxene/olivine}$ to infer pyroxene H_2O storage capacity, as:

$$D_{H_2O}^{pyx/olivine} = \frac{C_{H_2O}^{pyx}}{C_{H_2O}^{olivine}} \quad (3)$$

which yields:

$$C_{H_2O}^{pyx} = C_{H_2O}^{olivine} D_{H_2O}^{pyx/olivine} \quad (4)$$

We assume that orthopyroxene and clinopyroxene have the same H_2O partitioning, which is likely a fair approximation based on low pressure (1-5 GPa) studies (Aubaud *et al.*, 2004; 2008; Hauri *et al.*, 2006; Tenner *et al*., 2009). The Al_2O_3 concentrations of our orthopyroxenes (0.17-0.31 wt. %) are similar to estimates of near-solidus pyroxene Al_2O_3 concentrations (1 ± 1 wt.%) (Hirschmann *et al*., 2009), meaning that any effect of Al_2O_3 on pyroxene H_2O concentrations (Aubaud *et al.*, 2004; 2008; Hauri *et al.*, 2006; Tenner *et al*., 2009) is likely negligible.

Similar to the method for pyroxene, we use $D_{H_2O}^{garnet/olivine}$ values obtained from the literature to infer $C_{H_2O}^{garnet}$ (Eqns 3&4). We choose to use a wide range of values, as relatively little is known about the storage capacity behavior of garnet at depth. At the low end we use a $D_{H_2O}^{garnet/olivine}$ value of 0 from the study of Withers *et al.* (1998), who found that garnet in the system pyrope + 10 wt.% SiO_2 + 10 wt.% H_2O has ~0 ppm at pressures of 7, 8, and 13 GPa at 1000ºC, perhaps due to an excess silica condition that limits H_2O incorporation by hydrogarnet substitution at high pressures. At the high end, we use the maximum $D_{H_2O}^{garnet/olivine}$ value (1.27) observed from Mookherjee & Karato (2010). This value may be an overestimate by a factor of ~3, as the olivine concentration

is based on FTIR spectroscopy that was calibrated by the methods of Paterson (1982) (which likely underestimates olivine concentration by a factor of ~3).

Combination of $C_{H_2O}^{olivine}$, $D_{H_2O}^{pyx/olivine}$, $D_{H_2O}^{garnet/olivine}$, and the corresponding modal abundances allows for calculation of peridotite water storage capacity above the 410 km transition zone (Eqns 2-4), which is illustrated in Figure 4.12. We predict that $C_{H_2O}^{peridotite}$ increases from 500-650 ppm at 300 km (10 GPa) to 700-1100 ppm at 410 km (13.7 GPa).

Implications for hydrous partial melting at the base of the upper mantle.

An important consideration that the peridotite storage capacity studies of Hirschmann *et al.* (2005; 2009) have pointed out is that water fluxed partial melting cannot occur if the bulk H_2O from rising material in the transition zone does not exceed the peridotite storage capacity at the base of the upper mantle. Based on this criterion, our predicted peridotite water storage capacity of 700-1100 ppm disagrees with the hypothesis of H_2O-enriched transition zone material inciting a global layer of hydrous melt above the transition zone (Bercovici & Karato, 2003). If pervasive melting were occurring, it would hydrate peridotite residues to their storage capacities (i.e. 500-1100 ppm between 300 and 410 km), and MORB source bulk water contents of 50-200 ppm (Dixon *et al.*, 1988, Michael 1988; 1995; Danyushevsky *et al.*, 2000; Saal *et al.*, 2002; Simons *et al.*, 2002. Salters & Stracke, 2005; Workman & Hart, 2005) simply do not reflect this occurrence. However, our predicted H_2O storage capacity does not rule out localized melting in OIB source regions, which have 300-1000 ppm bulk H_2O (Jambon & Zimmermann, 1990; Sobolev & Chaussidon, 1996; Dixon *et al*., 1997; 2002; Jamtveit *et al.*, 2001, Hauri *et al.*, 2002; Simons *et al.*, 2002; Seaman *et al.*, 2004; Aubaud *et al.*, 2005; 2006). Additionally, OIB source adiabats are hotter than oceanic adiabats by

~200ºC (Putirka 2005; 2009), which means that perhaps the peridotite water storage capacity is lower in OIB source mantle than our 1450ºC estimate of 700-1100 ppm, as both olivine and pyroxene water storage capacities have decreasing trends at 12 GPa and 1350-1450ºC (Fig. 4.9a&4.9b).

Several seismic studies (Revenaugh & Sipkin, 1994; van der Meijde *et al.*, 2003; Courtier & Revenaugh, 2007; Jasbinsek *et al.*, 2010) have detected low velocity regions above 410 km which are associated with subducted slabs. These low velocity regions are either inferred to be hydrous melt (i.e. Revenaugh & Sipkin, 1994) or hydrated mantle (i.e. van der Meijde *et al.*, 2003). Our peridotite H_2O storage capacities support both observations. If deep subducted slabs contain a bulk H_2O content that exceeds the peridotite H_2O storage capacity, which may be possible through assemblages consisting of hydrous (Okamoto & Maruyama, 1999; Shieh *et al.*, 1998), and/or nominally anhydrous phases (Katayama *et al.*, 2003; 2006), they will shed their water as the slab is heated by the surrounding mantle (Irifune *et al.*, 1998). This water will then incorporate into transition zone phases, and advection of this transition zone material will incite hydrous partial melting when it crosses into the upper mantle. Hydrous partial melting will then remove water from the residue until it reaches a storage capacity of 700-1100 ppm. Continued advection will incite small amounts of melting, but the residue will still contain a substantial amount of H_2O, as our calculated peridotite H_2O storage capacity is still 500-650 ppm at 300 km depth (Fig. 4.12). Observations of seismic waves from van der Meijde *et al.* (2003) suggest that the 410-km discontinuity beneath the Mediterranean subduction region is thickened by 20-40 km due to hydration of the peridotite phase assemblage. Their estimated range of olivine H_2O concentrations necessary to produce

this observed thickening (500-1000 ppm) is nearly identical to our range of olivine H_2O storage capacities (650-1030 ppm) between 300 and 410 km.

CONCLUSIONS

• We provide a novel method for determining mineral water storage capacities in the form of a layered experiment, where the bottom 2/3 of the capsule consists of hydrated peridotite and the top 1/3 of the capsule consists of a hydrated monomineralic layer. The monomineralic layer facilitates the growth crystals on the order of hundreds of microns in diameter, allowing for quantifying water storage capacities by low-H background SIMS. Interconnectivity of low-degree peridotite melts between the peridotite layer and the monomineralic layer provides and H_2O activity that achieves H_2O storage capacity conditions.

• At 12 GPa, olivine and orthopyroxene water storage capacities decrease (~1800-1100 ppm and ~1400-1100 ppm, respectively) as a function of temperature from 1350 to 1450ºC. Olivine water storage capacity is approximately a factor of 2 less than olivine water solubility at 12 GPa and 1350-1450ºC, which likely occurs because the H_2O activity required to stabilize peridotite partial melts is lower than the H_2O activity required to stabilize partial melts of pure olivine.

• Combination of this study with Ardia *et al.* (in prep.) suggests that olivine water storage capacity increases linearly from 5 to 13 GPa at 1450ºC with the following function: $C_{H_2O}^{olivine}$ (ppm) = (102**P*(GPa)) – 363. Combining this trend with the $D_{H_2O}^{pyx/olivine}$ of this study (0.77±0.07), $D_{H_2O}^{gt/olivine}$, and modal abundances along a ridge adiabat provides an estimated peridotite water storage capacity of 700-1100 ppm at the base of the upper mantle.

• Future studies of garnet and clinopyroxene water storage capacities using this method will provide more robust constraints to peridotite water storage capacity at various *P-T* conditions throughout the mantle. Additionally, this experimental technique may be useful in determining other volatile storage capacities. Other systems (i.e. Martian, basaltic) may also benefit from this experimental technique in determining volatile storage capacities, and their effect on incipient partial melting.

Table 4.1. Starting material compositions.

	Nat. KLB-1[1]	KLB-1-ox.[2]	Base hyd. Ol. Ox.*	**Hyd. KLB-1ox. Batch 1***	**Hyd. KLB-1ox. Batch 2***	**Hyd. KLB-1ox. Batch 3***	**Hyd. Ol. Ox. Batch 1***	**Hyd. Ol. Ox. Batch 2***	**Hyd. Ol. Ox. Batch 3***
SiO_2	44.84	44.92	36.60	44.46	44.20	43.99	40.64	40.54	40.44
TiO_2	0.11	0.16	--	0.13	0.14	0.14	--	--	--
Al_2O_3	3.51	3.92	--	3.52	3.53	3.53	--	--	--
Cr_2O_3	0.32	0.28	--	0.29	0.27	0.25	--	--	--
FeO*	8.20	8.09	8.98	8.18	8.16	8.15	9.97	9.94	9.92
MnO	0.12	0.12	--	0.11	0.11	0.11	--	--	--
MgO	39.52	38.76	44.02	39.36	39.25	39.15	48.89	48.77	48.65
CaO	3.07	3.79	--	3.23	3.33	3.41	--	--	--
Na_2O	0.30	0.25	--	0.27	0.24	0.23	--	--	--
K_2O	0.02	0.03	--	0.02	0.03	0.03	--	--	--
H_2O	0.00	0.00	10.40	0.45	0.75	1.00	0.50	0.75	1.00
Total	100.01	100.32	100	100	100	100	100	100	100
Mg#	89.6	89.5	89.7	89.6	89.5	89.5	89.7	89.7	89.7

[1] Measured value of glass sphere from Davis *et al.* (2009)
[2] Measured value of glass sphere using the methodology of Davis *et al.* (2009)
* Compositions are based on mass of oxides added to the mixture. Hydrous KLB-1 oxide batches consist of KLB-1 oxide and base hydrous olivine oxide, mixed in proportions that produce the reported bulk H_2O contents. Hydrous olivine oxide batches were synthesized by diluting the base hydrous olivine oxide with additional MgO, FeO, and SiO_2, mixed in proportions to produce the reported Mg# and bulk H_2O contents.

Table 4.2. Experimental conditions and run products.

Exp. #	Bulk H_2O (wt.%)	T (°C)	P(GPa)	t(h)	Phase assemblage
M455	1.00	1450	10	24	melt+ol+opx+cpx+gt
M461	0.48	1450	11	24	melt+ol+opx+cpx+gt
M463	0.48	1450	12	24	melt+ol+opx+cpx+gt
M465	0.48	1450*	13	24	melt+ol+opx+gt
M467	0.48	1400	12	24	melt+ol+opx+cpx+gt
M468	0.48	1350	12	24	melt+ol+opx+cpx+gt
M470	0.75	1450	12	24	melt+ol+opx+cpx+gt
M471	0.75	1400	12	24	melt+ol+opx+cpx+gt
M474	1.0	1350	12	24	melt+ol+opx+cpx+gt
M476	1.0	1400	12	48	melt+ol+opx+gt

Table 4.3. Phase compositions determined by EMPA for the fixed point pressure calibration

Chamber	Phase	n	MgO	Al2O3	SiO2	CaO	FeO*	Total	Fe#
Capsule Top*									
A	Ol	12	47.13(0.39)	0.06(0.03)	38.95(0.38)	0.01(0.01)	12.96(0.25)	99.2	0.134
A	Wad	8	41.44(0.33)	0.74(0.06)	38.29(0.21)	0.01(0.01)	19.62(0.30)	100.11	0.21
B	Ol	11	45.67(0.37)	0.05(0.03)	38.91(0.60)	0.02(0.01)	14.69(0.64)	99.34	0.153
B	Wad	10	39.50(0.18)	0.68(0.04)	37.60(0.22)	0.01(0.01)	21.86(0.23)	99.65	0.237
C	Wad	10	36.74(0.15)	0.38(0.03)	36.93(0.25)	0.01(0.02)	25.73(0.28)	99.8	0.282
C	RW	11	29.69(0.22)	0.11(0.03)	35.70(0.24)	0.00(0.01)	34.71(0.25)	100.22	0.396
D	Wad	22	38.12(0.25)	0.43(0.14)	37.10(0.33)	0.00(0.01)	24.15(0.26)	99.81	0.262
Capsule Bottom**									
A	Wad	14	37.01(0.24)	0.67(0.07)	36.65(0.22)	0.02(0.03)	24.92(0.39)	99.28	0.274
B	Wad	12	35.04(0.18)	0.68(0.10)	36.01(0.34)	0.02(0.02)	27.58(0.35)	99.33	0.306
B	RW	12	28.45(0.19)	0.22(0.03)	34.95(0.22)	0.01(0.03)	35.74(0.64)	99.37	0.413
C	Wad	10	35.39(0.21)	0.72(0.01)	36.40(0.28)	0.00(0.03)	27.16(0.49)	99.67	0.301
C	RW	12	28.16(0.17)	0.23(0.04)	34.92(0.26)	0.01(0.03)	36.09(0.75)	99.4	0.418
D	Wad	12	34.76(0.20)	0.51(0.09)	36.39(0.19)	0.02(0.03)	27.65(0.49)	99.33	0.309
D	RW	13	28.16(0.21)	0.27(0.06)	34.87(0.22)	0.01(0.03)	36.96(0.47)	100.27	0.424

Errors are reported as the 1σ standard deviation.

*The phases measured from the top of the capsule determine a fixed point pressure of 13.25 ± 0.07 GPa (Fig. 4.3).

** The phases measured at the bottom of the capsule are used to estimate the thermal gradient in the capsule. Using the estimated pressure (13.25 GPa), the $(Mg,Fe)_2SiO_4$ diagrams of Frost and Dolejš (2007) predict that the iron-rich side of the Wad-RW coexisting phase loop has Fe# values of 0.323, 0.385, and 0.442 at 1200, 1400, and 1600ºC, respectively. These values fit the following 13.25 GPa trend: T(ºC) = (3364(Fe#)) + 110, r^2 = 1. Combining this equation with the ringwoodite Fe# data from the experimental chambers measured at the bottom of the capsule (0.413, 0.418, and 0.424) predicts that the temperature there is 1517 ± 18ºC. As the nominal run temperature was 1400ºC, and the capsule is 0.6 mm in length, this provides a rough estimate of the thermal gradient (195º/mm) through the capsule.

Table 4.4. Composition (in weight percent) of olivine

Exp. #	M455	M461	M463	M465	M467	M468	M470	M471	M474	M476
P (GPa)	10	11	12	13	12	12	12	12	12	12
T (ºC)	1450	1450	1450	1450*	1400	1350	1450	1400	1350	1400
Bulk H_2O (wt. %)	1.00	0.48	0.48	0.48	0.48	0.48	0.75	0.75	1.00	1.00
n	10	14	15	15	15	17	11	12	11	14
SiO_2	41.27(0.25)	40.60(0.20)	41.31(0.25)	40.45(0.59)	40.89(0.26)	40.93(0.20)	41.26(0.21)	41.10(0.17)	40.75(0.24)	40.98(0.29)
TiO_2	-0.02(0.08)	0.03(0.08)	0.00(0.09)	0.03(0.09)	0.07(0.09)	0.00(0.09)	0.05(0.08)	0.02(0.07)	0.02(0.06)	0.00(0.09)
Al_2O_3	0.05(0.03)	0.04(0.03)	0.02(0.02)	0.01(0.02)	0.02(0.01)	0.01(0.02)	0.05(0.02)	0.03(0.02)	0.03(0.02)	0.03(0.03)
Cr_2O_3	0.01(0.07)	0.02(0.05)	0.01(0.06)	-0.01(0.06)	0.03(0.05)	0.00(0.07)	0.03(0.04)	0.02(0.04)	0.04(0.06)	0.04(0.04)
FeO*	6.96(0.13)	8.38(0.16)	8.26(0.15)	8.81(0.23)	8.57(0.16)	8.89(0.22)	7.40(0.10)	7.69(0.08)	8.35(0.14)	7.77(0.12)
MnO	0.07(0.06)	0.06(0.02)	0.05(0.03)	0.06(0.03)	0.05(0.03)	0.04(0.05)	0.04(0.03)	0.05(0.02)	0.06(0.03)	0.05(0.03)
MgO	51.78(0.19)	50.18(0.37)	51.20(0.32)	50.07(0.35)	49.89(0.30)	49.69(0.29)	50.93(0.26)	50.73(0.22)	50.36(0.33)	50.77(0.25)
CaO	0.08(0.02)	0.05(0.02)	0.05(0.02)	0.04(0.03)	0.05(0.02)	0.03(0.02)	0.05(0.02)	0.02(0.02)	0.04(0.03)	0.04(0.03)
Na_2O	0.01(0.01)	0.02(0.03)	0.01(0.02)	0.03(0.02)	0.01(0.02)	0.03(0.02)	0.01(0.02)	0.01(0.01)	0.01(0.02)	0.01(0.02)
K_2O	0.02(0.01)	0.03(0.02)	0.01(0.02)	0.02(0.02)	0.03(0.02)	0.01(0.02)	0.02(0.01)	0.02(0.01)	0.02(0.01)	0.02(0.01)
Total	100.23	99.43	100.92	99.51	99.60	99.64	99.84	99.68	99.67	99.71
Mg#	93.0	91.4	91.7	91.0	91.2	90.9	92.5	92.2	91.5	92.1

Errors (in parentheses) are reported as the 1σ standard deviation.

Table 4.5. Composition (in weight percent) of orthopyroxene

Exp. #	M455	M461	M463	M465	M467	M468	M470	M471	M474	M476
P (GPa)	10	11	12	13	12	12	12	12	12	12
T (ºC)	1450	1450	1450	1450*	1400	1350	1450	1400	1350	1400
Bulk H_2O (wt. %)	1.00	0.48	0.48	0.48	0.48	0.48	0.75	0.75	1.00	1.00
n	11	6	15	15	10	14	12	11	13	13
SiO_2	57.48(0.29)	56.59(0.27)	57.77(0.24)	57.04(0.43)	57.19(0.33)	57.20(0.34)	57.81(0.25)	57.38(0.34)	57.43(0.61)	57.52(0.30)
TiO_2	0.01(0.08)	-0.01(0.08)	-0.04(0.07)	-0.01(0.05)	0.05(0.14)	0.02(0.11)	0.03(0.14)	-0.01(0.09)	-0.01(0.08)	0.00(0.08)
Al_2O_3	0.31(0.03)	0.30(0.03)	0.20(0.02)	0.13(0.02)	0.18(0.02)	0.17(0.03)	0.25(0.03)	0.19(0.02)	0.18(0.03)	0.21(0.04)
Cr_2O_3	0.07(0.06)	0.04(0.04)	0.05(0.06)	0.02(0.05)	0.02(0.03)	0.02(0.05)	0.06(0.08)	0.05(0.05)	0.02(0.07)	0.04(0.04)
FeO*	3.97(0.07)	4.64(0.06)	4.59(0.14)	5.01(0.16)	4.73(0.43)	5.12(0.41)	4.13(0.07)	4.25(0.13)	4.59(0.15)	4.26(0.09)
MnO	0.06(0.04)	0.07(0.02)	0.04(0.04)	0.05(0.03)	0.06(0.03)	0.04(0.04)	0.03(0.05)	0.04(0.03)	0.04(0.04)	0.03(0.03)
MgO	36.89(0.29)	36.84(0.37)	36.79(0.28)	37.07(0.32)	36.70(0.23)	36.58(0.28)	37.23(0.23)	37.20(0.15)	37.26(0.21)	37.10(0.19)
CaO	0.72(0.10)	0.59(0.03)	0.62(0.04)	0.43(0.05)	0.36(0.06)	0.30(0.08)	0.52(0.05)	0.42(0.05)	0.39(0.03)	0.45(0.06)
Na_2O	0.04(0.02)	0.06(0.02)	0.04(0.03)	0.06(0.02)	0.06(0.03)	0.05(0.03)	0.06(0.03)	0.06(0.03)	0.03(0.02)	0.04(0.02)
K_2O	0.02(0.02)	0.02(0.02)	0.03(0.01)	0.03(0.02)	0.02(0.01)	0.02(0.02)	0.02(0.01)	0.02(0.02)	0.01(0.02)	0.01(0.02)
Total	99.57	99.14	100.09	99.81	99.38	99.52	100.13	99.61	99.95	99.66
Mg#	94.3	93.4	93.5	93.0	93.3	92.7	94.1	94.0	93.5	93.9

Errors (in parentheses) are reported as the 1σ standard deviation.

Table 4.6. Composition (in weight percent) of clinopyroxene

Exp. #	M455	M461	M463	M467	M468	M470	M471	M474
P (GPa)	10	11	12	12	12	12	12	12
T (ºC)	1450	1450	1450	1400	1350	1450	1400	1350
Bulk H_2O (wt. %)	1.00	0.48	0.48	0.48	0.48	0.75	0.75	1.00
n	6	10	15	19	22	23	23	10
SiO_2	55.02(0.18)	55.37(0.50)	55.21(0.27)	55.36(0.27)	55.22(0.48)	55.96(0.34)	55.46(0.43)	54.87(0.42)
TiO_2	0.00(0.08)	0.02(0.08)	0.00(0.10)	0.02(0.10)	0.00(0.11)	0.06(0.11)	-0.01(0.09)	0.04(0.09)
Al_2O_3	0.80(0.04)	1.20(0.04)	1.10(0.07)	1.07(0.05)	1.18(0.09)	0.97(0.05)	0.96(0.04)	0.89(0.03)
Cr_2O_3	0.22(0.03)	0.28(0.06)	0.21(0.06)	0.22(0.07)	0.27(0.06)	0.21(0.07)	0.17(0.09)	0.19(0.08)
FeO*	3.05(0.14)	3.98(0.12)	3.30(0.13)	3.13(0.14)	3.12(0.13)	2.83(0.16)	2.74(0.11)	3.01(0.12)
MnO	0.09(0.02)	0.09(0.03)	0.06(0.03)	0.08(0.04)	0.06(0.04)	0.07(0.04)	0.05(0.04)	0.06(0.04)
MgO	22.60(0.20)	22.76(0.23)	20.71(0.36)	20.39(0.45)	19.37(0.27)	21.29(0.26)	20.37(0.34)	20.24(0.23)
CaO	16.47(0.21)	14.92(0.47)	17.81(0.53)	18.26(0.72)	19.59(0.38)	18.51(0.25)	19.41(0.25)	19.64(0.36)
Na_2O	0.58(0.03)	0.94(0.04)	0.56(0.03)	0.93(0.07)	1.05(0.08)	0.79(0.06)	0.83(0.05)	0.80(0.09)
K_2O	0.02(0.02)	0.02(0.02)	0.03(0.01)	0.02(0.02)	0.03(0.01)	0.03(0.02)	0.02(0.02)	0.02(0.03)
Total	98.86	99.58	98.98	99.47	99.88	100.72	100.00	99.77
Mg#	93.0	91.1	91.8	92.1	91.7	93.1	93.0	92.3

Errors (in parentheses) are reported as the 1σ standard deviation.

Table 4.7. Composition (in weight percent) of garnet

Exp. #	M455	M461	M463	M465	M467	M468	M470	M471	M474	M476
P (GPa)	10	11	12	13	12	12	12	12	12	12
T (ºC)	1450	1450	1450	1450*	1400	1350	1450	1400	1350	1400
Bulk H_2O (wt. %)	1.00	0.48	0.48	0.48	0.48	0.48	0.75	0.75	1.00	1.00
n	10	9	13	6	21	19	23	23	10	10
SiO_2	44.30(0.38)	44.65(0.08)	45.76(0.47)	44.96(0.47)	44.71(0.31)	44.86(0.19)	45.83(0.60)	44.61(0.91)	44.66(0.30)	44.34(0.27)
TiO_2	0.11(0.08)	0.16(0.10)	0.21(0.06)	0.35(0.11)	0.23(0.13)	0.21(0.12)	0.27(0.17)	0.27(0.18)	0.26(0.09)	0.19(0.14)
Al_2O_3	18.71(0.18)	17.69(0.27)	16.38(0.23)	14.07(0.25)	17.01(0.24)	16.90(0.15)	16.61(0.44)	16.60(0.62)	16.75(0.40)	17.59(0.19)
Cr_2O_3	1.69(0.16)	1.54(0.14)	1.60(0.14)	1.60(0.19)	1.55(0.15)	1.46(0.01)	1.50(0.25)	1.56(0.28)	1.35(0.11)	1.45(0.09)
FeO*	6.62(0.30)	7.60(0.18)	7.64(0.18)	10.39(0.36)	8.54(0.20)	9.14(0.21)	7.18(0.31)	7.77(0.37)	8.50(0.13)	7.61(0.13)
MnO	0.21(0.03	0.15(0.03)	0.17(0.05)	0.17(0.04)	0.21(0.04)	0.20(0.04)	0.15(0.05)	0.16(0.06)	0.17(0.04)	0.18(0.06)
MgO	22.86(0.35)	23.11(0.16)	23.28(0.42)	22.37(0.14)	21.96(0.28)	21.33(0.20)	22.27(0.80)	21.96(0.65)	21.97(0.20)	22.68(0.35)
CaO	4.68(0.33)	4.21(0.10)	4.80(0.14)	5.59(0.18)	5.36(0.25)	5.56(0.21)	6.48(0.79)	6.17(0.53)	5.62(0.30)	5.28(0.44)
Na_2O	0.04(0.02)	0.10(0.02	0.07(0.03)	0.15(0.02)	0.11(0.03)	0.14(0.03)	0.10(0.03)	0.11(0.03)	0.10(0.03)	0.08(0.03)
K_2O	0.02(0.02)	0.02(0.01)	0.02(0.02)	0.03(0.02)	0.02(0.02)	0.01(0.01)	0.02(0.02)	0.02(0.02)	0.02(0.02)	0.01(0.02)
Total	99.24	99.23	99.92	99.69	99.70	99.79	100.40	99.24	99.39	99.41
Mg#	86.0	84.4	84.5	79.3	82.1	80.6	84.7	83.4	82.2	84.2
% majorite	15	17	24	22	19	24	19	19	19	15

Errors (in parentheses) are reported as the 1σ standard deviation.
Majorite component derived from the garnet endmember calculator of Locock (2008).

Table 4.8. Composition (in weight percent, recalculated anhydrous) of melt.

Exp. #	M463	M465	M468	M474	M476
P (GPa)	12	13	12	12	12
T (ºC)	1450	1450[1]	1350	1350	1400
Bulk H_2O (wt. %)	0.48	0.48	0.48	1.00	1.00
n	25	5	122	46	113
SiO_2	43.31(6.42)	28.11(2.07)	35.55(2.60)	38.48(3.29)	35.41(3.48)
TiO_2	0.34(0.21)	0.96(0.12)	0.78(0.32)	0.62(0.35)	0.75(0.32)
Al_2O_3	1.77(0.31)	4.22(1.15)	1.15(0.20)	1.23(0.81)	1.46(0.31)
Cr_2O_3	0.19(0.08)	0.40(0.16)	0.17(0.07)	0.17(0.11)	0.14(0.08)
FeO*	12.27(3.56)	18.00(0.73)	18.67(2.26)	16.37(2.36)	15.70(2.10)
MnO	0.23(0.09)	0.29(0.07)	0.22(0.06)	0.18(0.05)	0.21(0.10)
MgO	22.96(4.45)	31.28(2.73)	30.41(2.50)	29.08(4.76)	29.86(3.18)
CaO	18.29(3.70)	16.51(1.27)	11.61(2.46)	12.46(4.05)	15.95(6.27)
Na_2O	0.62(0.23)	0.20(0.09)	1.37(0.57)	1.31(0.48)	0.47(0.15)
K_2O	0.02(0.02)	0.03(0.04)	0.06(0.03)	0.10(0.04)	0.05(0.03)
Mg#	76.9	75.6	74.4	76	77.2
Avg. K_D	0.31	0.31	0.29	0.29	0.29
Olivine:KLB-1ox[2]	0.31:0.69	0.29:0.71	0.31:0.69	0.31:0.69	0.31:0.69
F[3]	0.08	0.07	0.04	0.10	0.09
H_2O_{melt} (wt.%)[4]	5.9	6.6	10.2	9.7	10.4

Errors (in parentheses) are reported as the 1σ standard deviation.
[1]Temperature was estimated based on the power required to heat the experiment.
[2] Ratio of starting materials used to estimate the bulk composition used in the mass balance.
[3]*F* values are derived by mass balance. They are to be treated as rough estimates, due to high thermal gradients within the multi-anvil assembly (see discussion for details).
[4] H_2O_{melt} concentrations are estimated by batch melting, using a $D_{H2O}^{residue/melt}$ value of 0.004, based on the high pressure estimate of Hirschmann *et al.* (2009). They are to be treated as rough estimates, due to high thermal gradients within the multi-anvil assembly (see discussion for details).

Table 4.9. H_2O storage capacities of olivine and opx, and partitioning of H_2O between olivine, opx, and melt.

Exp. #	M455	M461	M463	M465	M467	M468	M470	M471	M474	M476
P (GPa)	10	11	12	13	12	12	12	12	12	12
T (ºC)	1450	1450	1450	1450*	1400	1350	1450	1400	1350	1400
Bulk H_2O (wt. %)	1.00	0.48	0.48	0.48	0.48	0.48	0.75	0.75	1.00	1.00
n (ol, opx)	8	8	8	8, 5	8, 3	9, 3	7, 3	5, 2	7, 3	7
Olivine storage cap. (ppm)	720 (80)	580 (90)	1060 60	830 (160)	1340 (70)	2010 (90)	1260 (70)	2100 (80)	1610 (110)	1520 (60)
Opx storage cap. (ppm)				600 (40)	1040 (60)	1580 (60)	1110 (80)	1370 (50)	1250 (60)	
$D_{H2O}^{opx/ol}$				0.73	0.78	0.79	0.88	0.65	0.78	
$D_{H2O}^{ol/melt}$			0.018	0.013		0.020			0.017	0.015
$D_{H2O}^{opx/melt}$				0.009		0.015			0.013	

Errors (in parentheses) are reported as the 1σ standard deviation.
* Temperature estimated from the power required to heat the experiment.

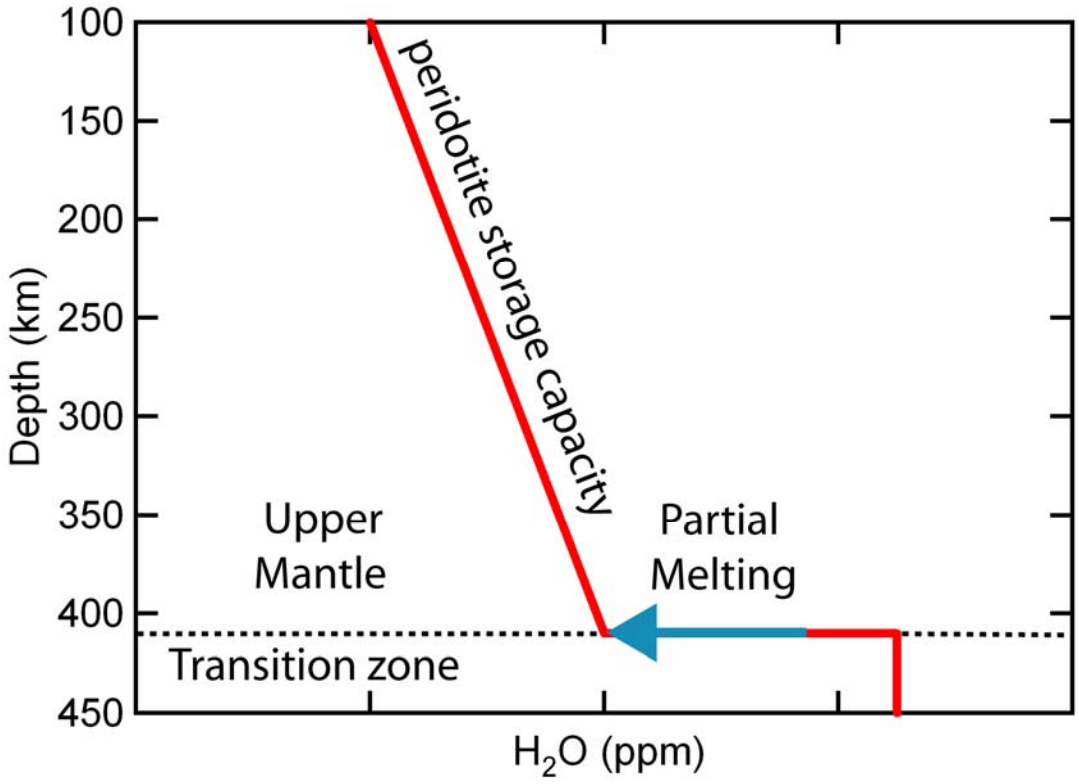

Figure 4.1. Schematic diagram illustrating hydrous partial melting at the 410 km transition zone. In the transition zone, H_2O enriched mantle advects (represented by the vertical red line) and reaches 410 km depth. At this point, its bulk H_2O concentration is greater than the peridotite H_2O storage capacity at the base of the upper mantle. Therefore, hydrous partial melting is incited, which is represented by the blue arrow. Melting will extract H_2O from the residual peridotite until the H_2O storage capacity at the base of the upper mantle is met. If peridotite H_2O storage capacity decreases with depth, as suggested by parameterizations of Hirschmann *et al.* (2005 & 2009), continued upwelling of the mantle will incite small amounts of hydrous melting to incrementally

achieve residual H_2O storage capacity. This process will hydrate the upper mantle to its H_2O storage capacity over a large depth interval.

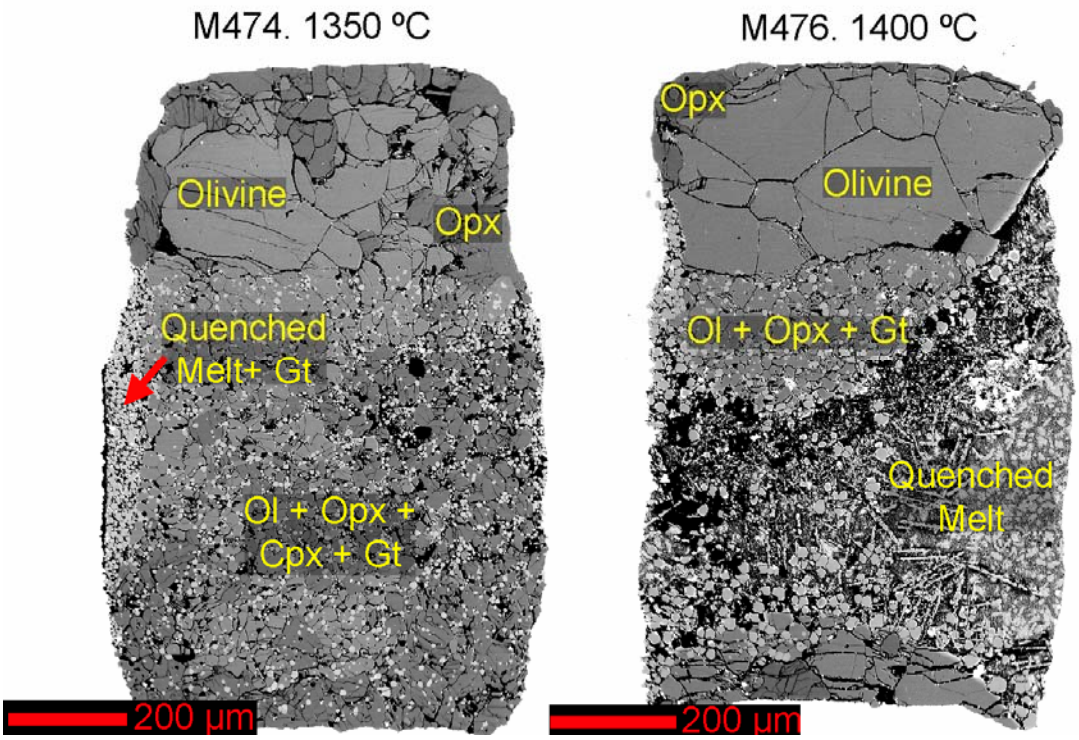

Figure 4.2. Backscattered electron images of experiments M474 and M476 illustrating the hydrated olivine layer (top 1/3 of the capsule), equilibrated with hydrated peridotite (bottom 2/3 of the capsule). The monomineralic olivine layer facilitates growth of several of crystals up to 200 µm in diameter providing several crack and pit-free regions for SIMS analysis. In all experiments orthopyroxenes were also nucleated within the olivine layer. In experiment M474 exposed opx regions were large enough to perform 3 analyses by SIMS, while the opx region in M476 was too small and compromised by pits and cracks to provide for any clean analyses. The hydrous peridotite layer consists of

olivine + orthopyroxene + garnet ± clinopyroxene + melt for experiments of this study. M476 is one of two experiments in the study that lacks cpx. Melt is networked throughout the capsule, but is highly concentrated in easily detectable regions, either as large mats of bladed quench crystals (M476) or concentrated as smaller pools within clusters of garnet crystals (M474).

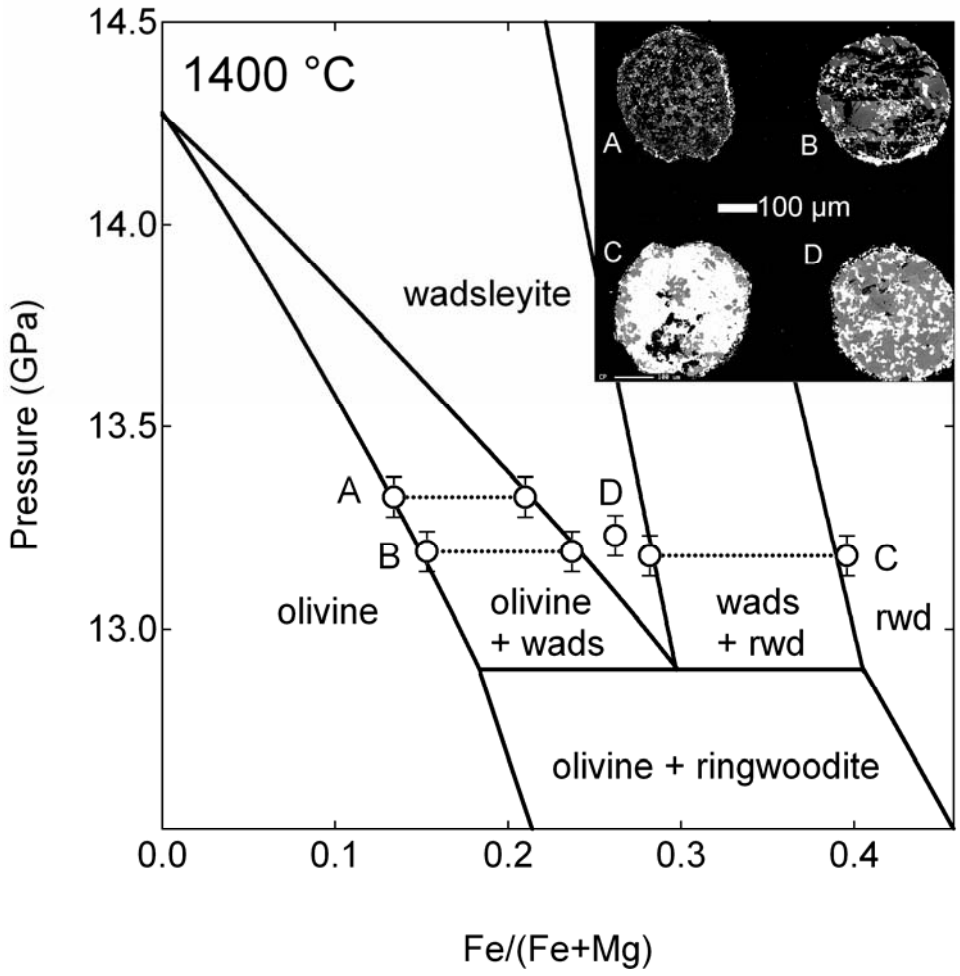

Figure 4.3. $(Mg,Fe)_2SiO_4$ phase diagram, modeled after Frost & Dolejš (2007), with corresponding data from the fixed-point pressure calibration. Data are plotted in terms of Fe# (Fe/(Fe + Mg)) of each of the $(Mg,Fe)_2SiO_4$ polymorphs present in the 4 chambers

of the Al_2O_3 capsule (labeled A-D in the inset backscattered electron image). Chamber D contains only wadsleyite, as the bright phase in the electron backscattered image is magnesiowüstite. Tie lines between data points denote coexisting pairs of polymorphs within their respective chambers. The three coexisting polymorph pairs predict a pressure of 13.25 ± 0.07 GPa, which is similar to the pressure (13.4 GPa) reported by Withers and Hirschmann (2007).

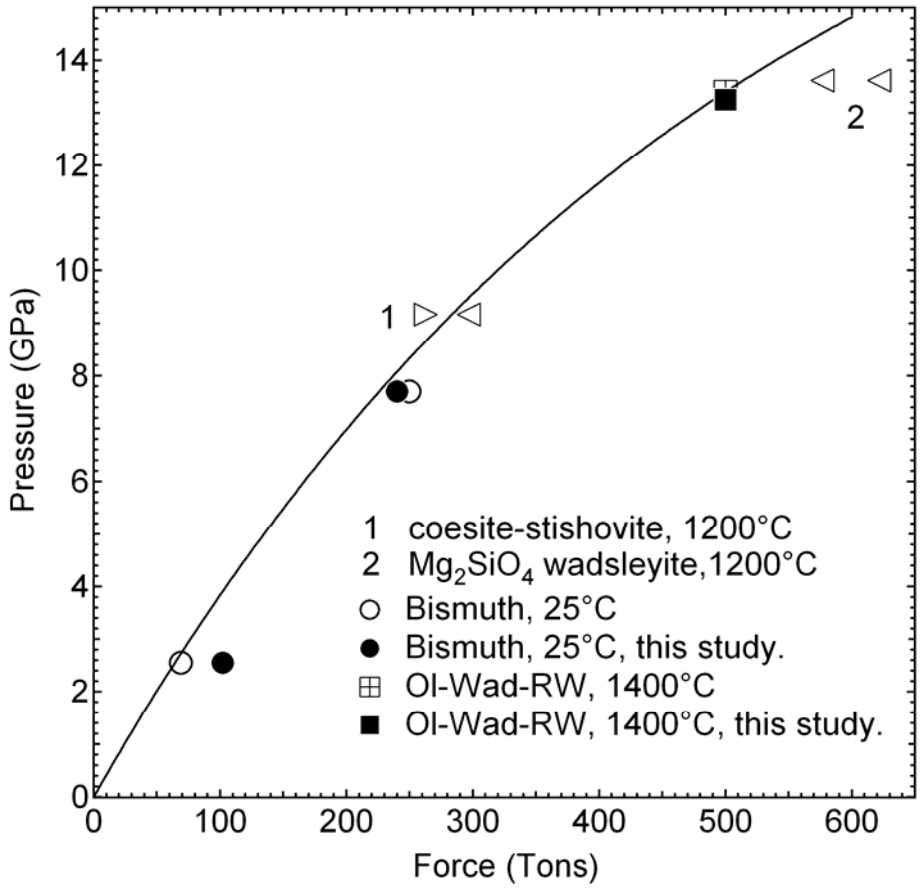

Figure 4.4. 14□8 multi-anvil assembly pressure calibration. Open symbols are from previous calibrations reported in Withers & Hirschmann (2007), along with the fit to the data. New pressure calibrations using Bi I-II and III-V transitions (filled circles)

(Piermarini & Block, 1975) and the $(Mg,Fe)_2SiO_4$ fixed point method (filled square) (Frost & Dolejš, 2003) are within the error range (± 0.5 GPa) of the established calibraition curve reported in Withers & Hirschmann (2007). Therefore, we use this same calibration curve to correlate multi-anvil tonnage to the desired pressures.

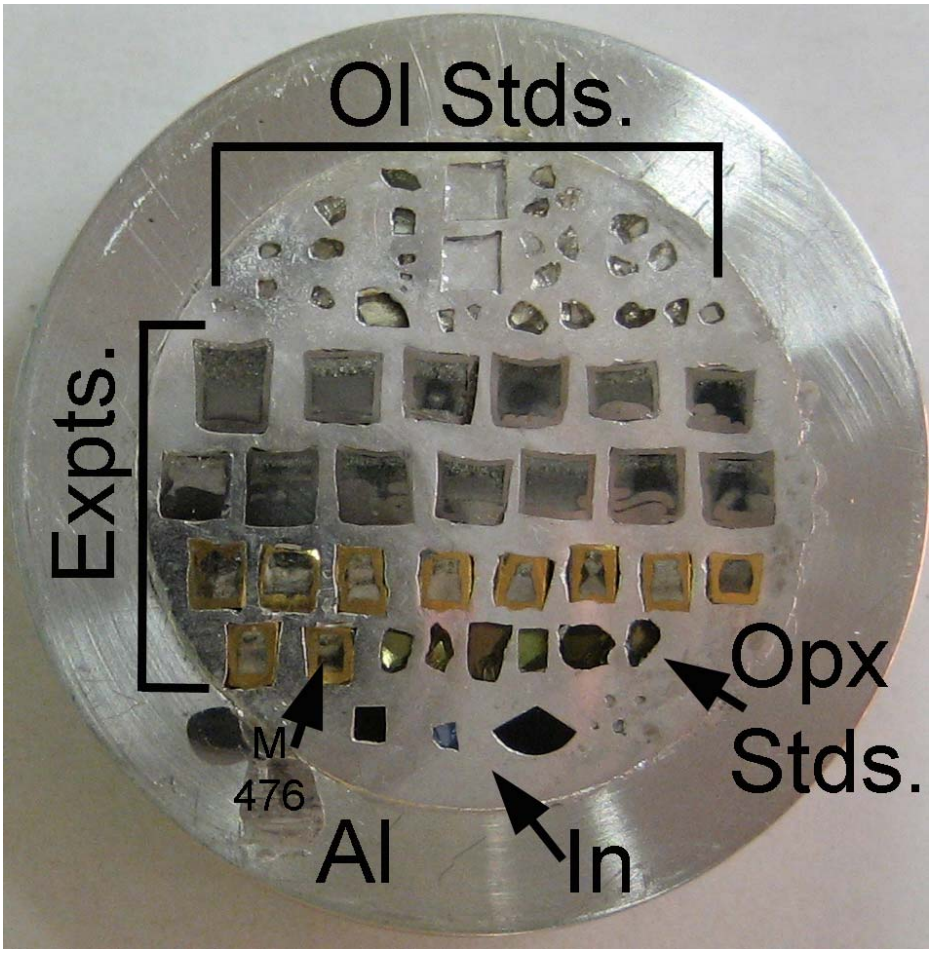

Figure 4.5. Image of the SIMS mount, which contains olivine standards (reported in Withers *et al.* (in prep.)), orthopyroxene standards, and experimental run products. The larger, AuPd sectioned capsules are run products from the 5-8 GPa olivine storage capacity study of Ardia *et al.* (in prep.), while the smaller, exposed gold capsules are run

products from this study. For reference, M476 (Fig. 4.2) is labeled. Standards and samples are pressed into nominally hydrogen-free indium to aid in reducing the background signal. Additionally, placement of standards and samples on one mount negates the need for sample changes that disturb the SIMS vacuum, which again aids in a consistent and low background. The diameter of the mount is 2.54 cm, and additional details of the mount can be found in Aubaud *et al.* (2007).

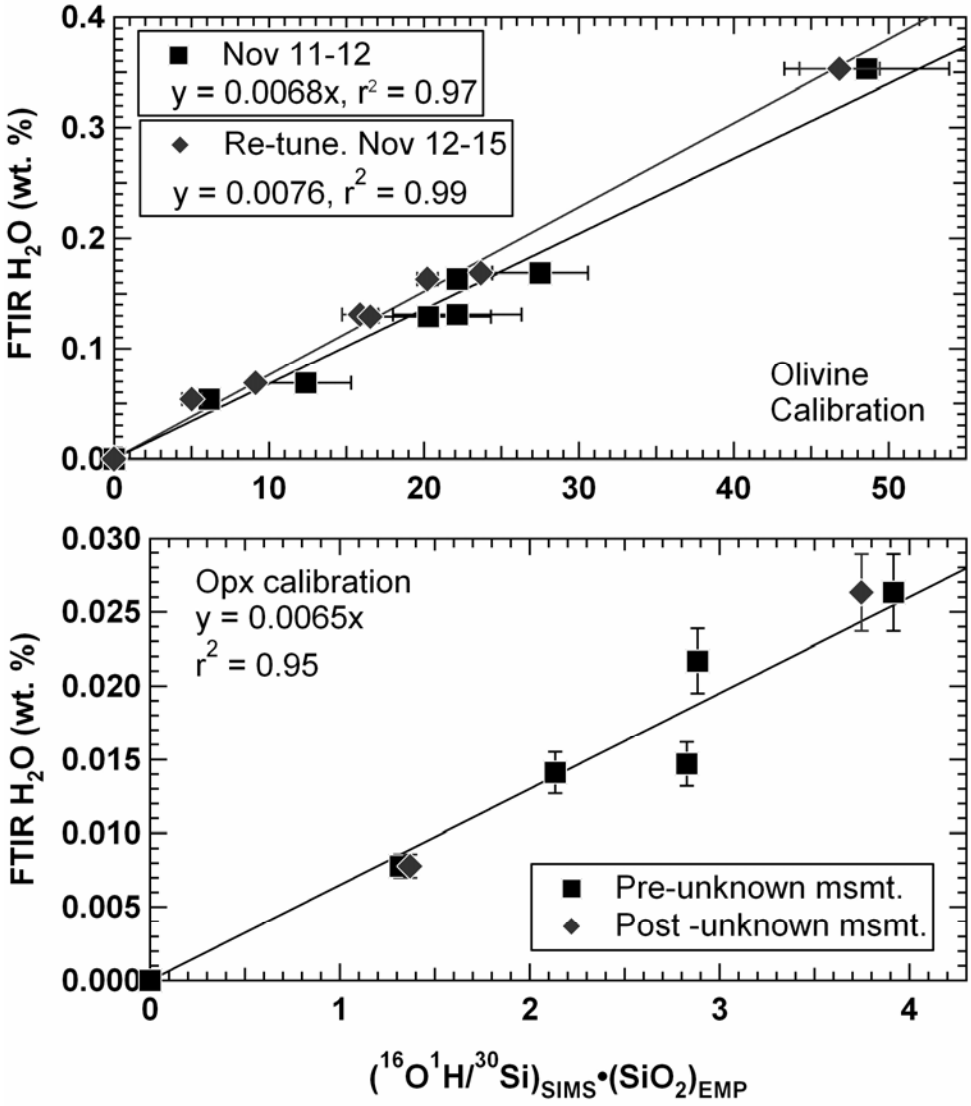

Figure 4.6. Olivine and orthopyroxene SIMS calibration curves. For olivine, horizontal error bars depict the variability in repeated measurements of the same standard over the course of the SIMS session. The initial (Nov. 11-12, 2009) calibration is represented as solid squares. After 2 days of analyses the SIMS was re-tuned and this new condition was stable from Nov. 12-15, but it shifted the calibration slightly (solid diamonds). Analyses of the same unknowns in both time periods show no systematic relative errors when compared to each other. Additional information regarding the olivine standards can be found in Withers *et al.* (in prep.) The orthopyroxene calibration curve was established (solid squares) and immediately following the calibration all of the orthopyroxene unknowns were measured. Following the measurement of unknowns, 2 additional measurements on orthopyroxene standards (solid diamonds) suggest minimal drift. Opx standards consist of Bamble Dry, Damaping, India, Kenya, KBH1, and ROM-273-OG2 (Aubaud *et al.*, 2007).

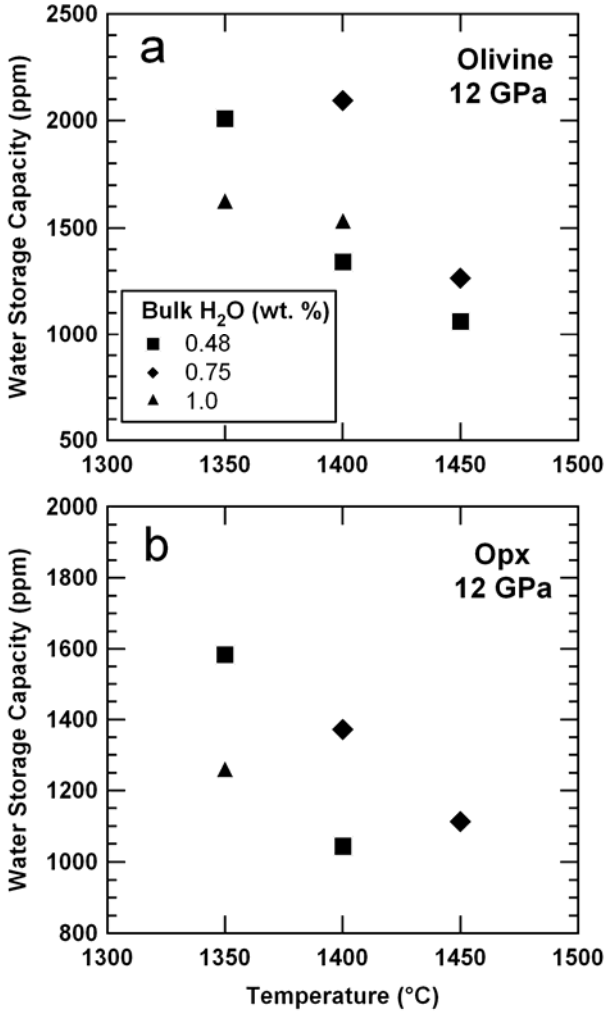

Figure 4.7. Comparison of 12 GPa water storage capacity measurements of olivine and orthopyroxene as a function of temperature and bulk H_2O content. Olivine (**a**) and orthopyroxene (**b**) water storage capacity decrease as a function of increasing temperature, ranging from 1350-1450ºC. The data exhibit some scatter in terms of bulk H_2O content, but do so without a systematic trend in variability at a constant temperature.

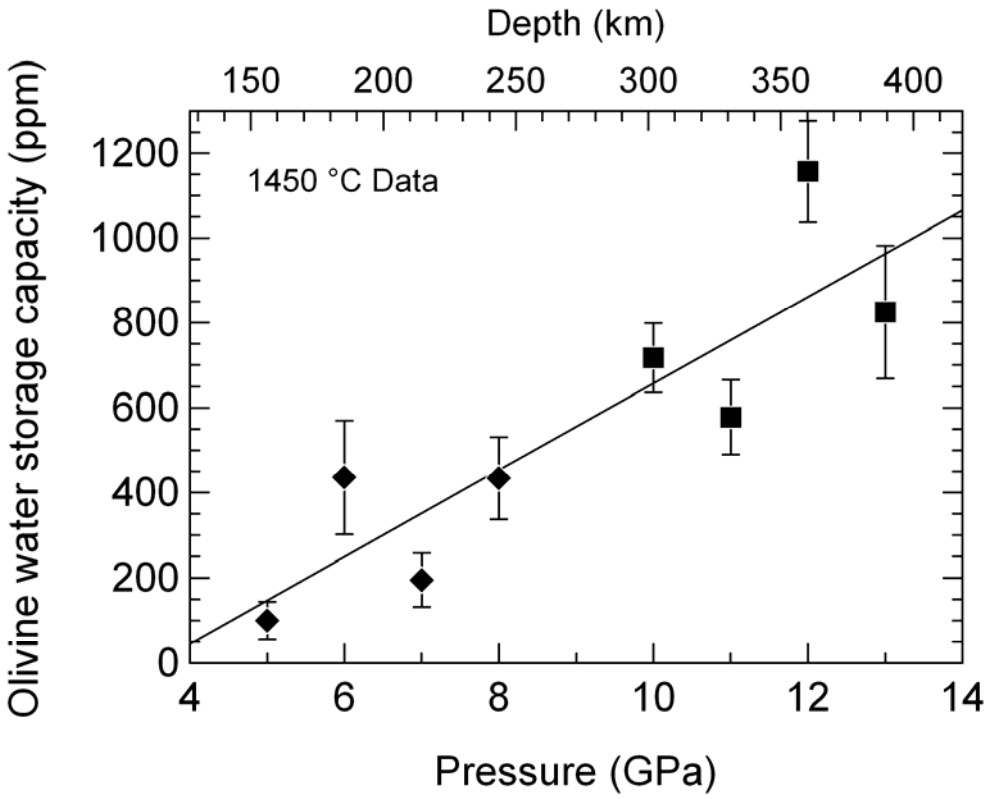

Figure 4.8. 1450ºC olivine water storage capacity as a function of pressure. Solid squares are data from this study, while solid diamonds are from the corresponding study of Ardia *et al.* (in prep.). Error bars are the 1σ standard deviation of repeated measurements on the same sample. Combination of these studies suggests a linear increase in olivine water storage capacity, with the following fit: $C_{H_2O}^{olivine}$ (ppm) = (102**P*(GPa)) – 363 (r^2 = 0.75). This trend suggests that olivine water storage capacity is ~1030 ppm at 410 km depth (13.7 GPa) along a ridge adiabat.

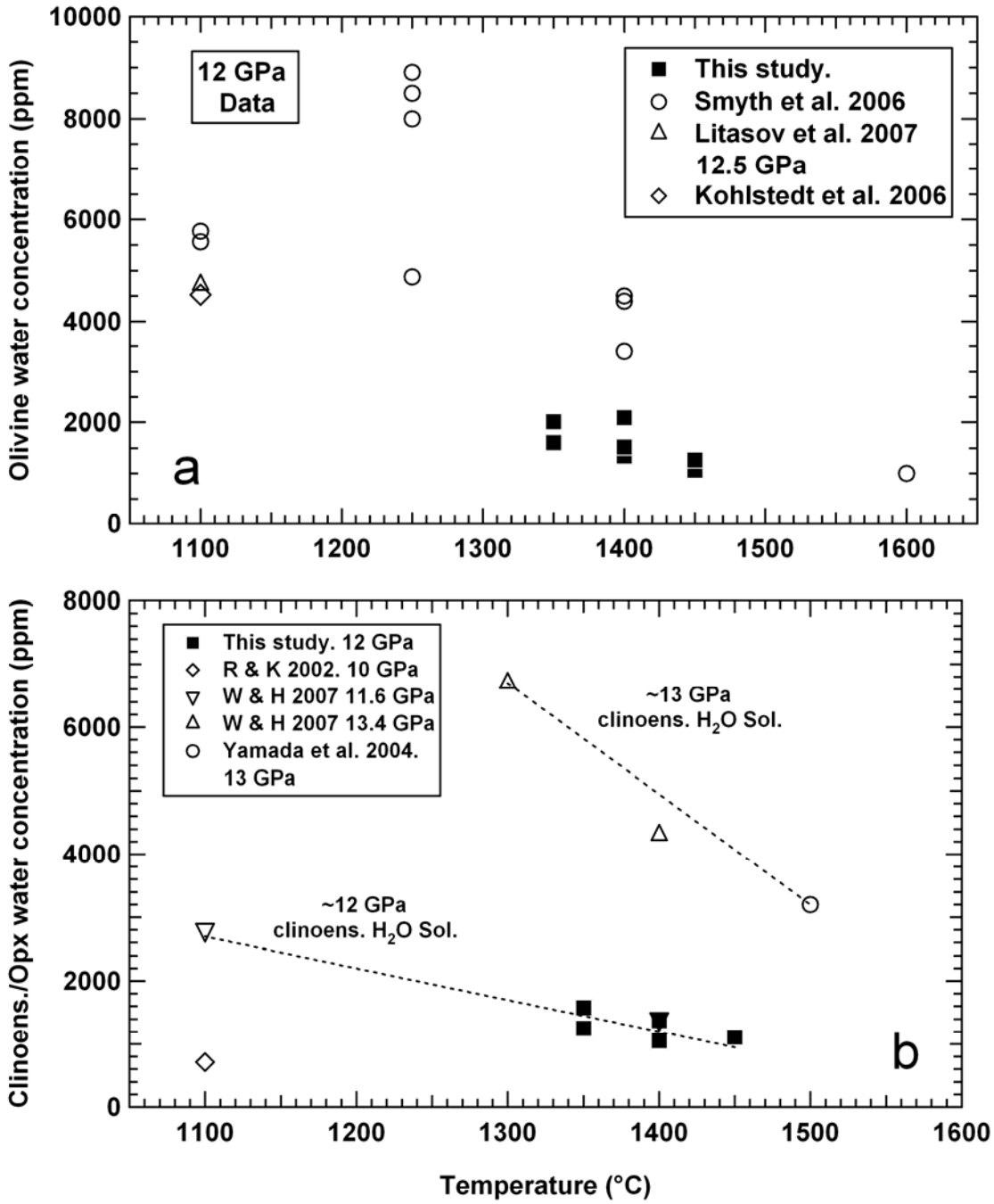

Figure 4.9. Olivine and orthopyroxene water storage capacity (solid squares) versus water solubility (open symbols). **a)** Olivine data at 12 GPa suggests that water storage capacity/solubility decreases from ~1800-1100 ppm as temperature increases from 1350-1450ºC. Comparison of our data to the olivines of Smyth *et al.* (2006) suggests olivine

water storage capacity is approximately a factor of 2 less than olivine water solubility at 1400ºC. The explanation for this difference is that the H_2O activity required to stabilize peridotite partial melts is lower than the H_2O activity required to stabilize partial melts of pure olivine. **b**) Similar to olivine, orthopyroxene water storage capacity decreases from ~1400-1100 ppm as temperature increases from 1350-1450ºC. Our 12 GPa orthopyroxene water storage capacities overlap 11.6 GPa clinoenstatite water solubilities (Withers & Hirschmann, 2007) as a function of temperature. This may suggest that the reduced H_2O activity in the system peridotite-H_2O has a minimal effect on decreasing orthopyroxene water storage capacity relative to solubility. Alternatively, complex peridotite-derived orthopyroxenes may have an increased H_2O storage capacity (relative to clinoenstatite) due to enhanced point defect incorporation of hydrogen, thus causing the observed overlap. The 0.4 GPa difference between our orthopyroxenes (12 GPa) and the 11.6 GPa clinoenstatites of Withers & Hirschmann (2007) may also lead to the overlap, as a 1 GPa increase from 12-13 GPa yields a factor of ~5 increase in clinoenstatite water solubility (Yamada *et al*., 2004; Withers *et al.*, 2007).

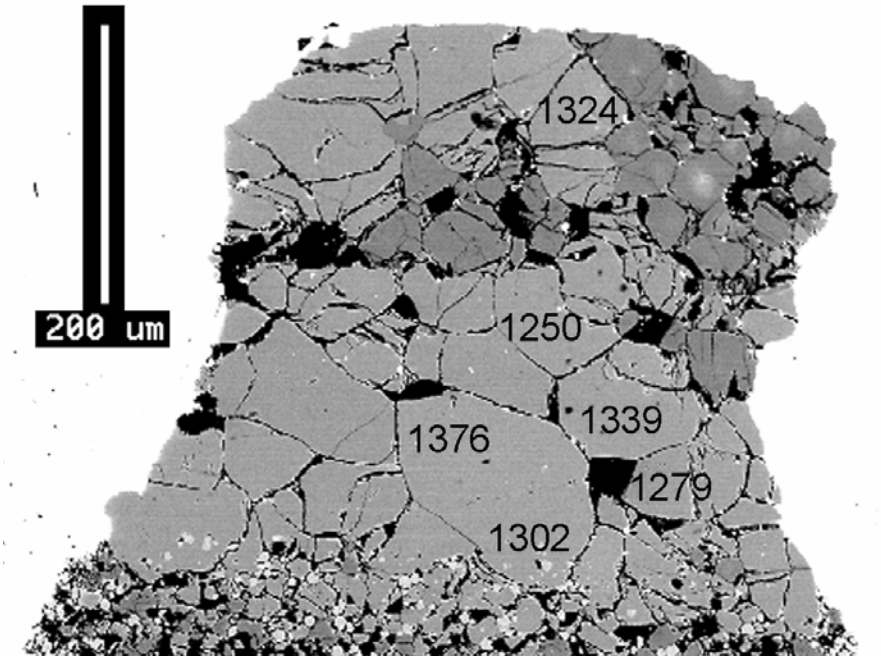

Figure 4.10. Electron backscattered image of the olivine layer of experiment M467. Superimposed are SIMS measurements (in ppm) of olivine H_2O storage capacity, with respect to the location that the measurements were taken. These measurements suggest no systematic trend in H_2O storage capacities due the strong thermal gradient of the multi-anvil assembly.

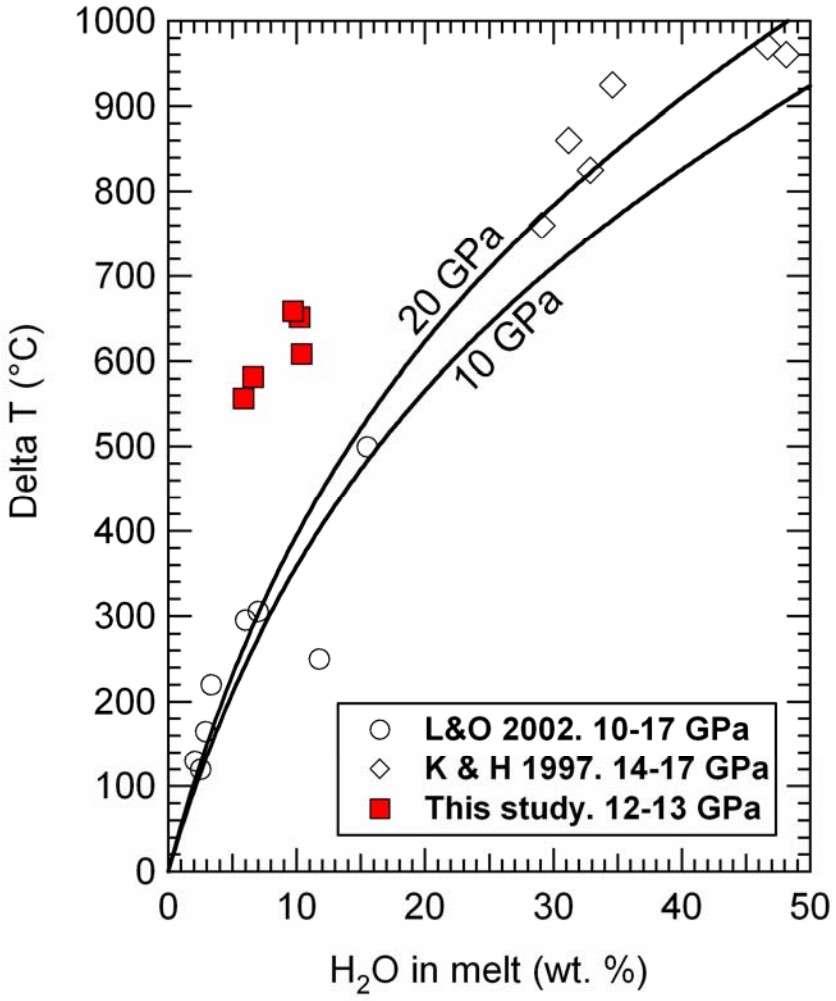

Figure 4.11. Comparison of freezing point depression from high pressure experiments and parameterization. Values of freezing point depression are calculated as ΔT, which is equal to $T_F^{\text{dry}} - T_F^{\text{hydrous}}$, where F is the melt fraction. T_F^{hydrous} is derived from experiments, and T_F^{dry} is calculated using the interpolation method of Hirschmann *et al.* (2009). The 10 and 20 GPa models are cryoscopic calculations of Hirschmann *et al.* (2009). Using the nominal temperatures of experiments for T_F^{hydrous} to calculate ΔT, our study suggests that

H_2O_{melt} provides 200-300ºC greater freezing point depression than the models of Hirschmann *et al.* (2009) or the data of Litasov & Ohtani (2002). We infer that this discrepancy is caused by the extreme thermal gradient through our capsules due to the use of Re furnaces, and that T_F^{hydrous} is likely 100-300º hotter than the nominal temperature of our experiments. K & H 1997: Kawamoto & Holloway (1997).

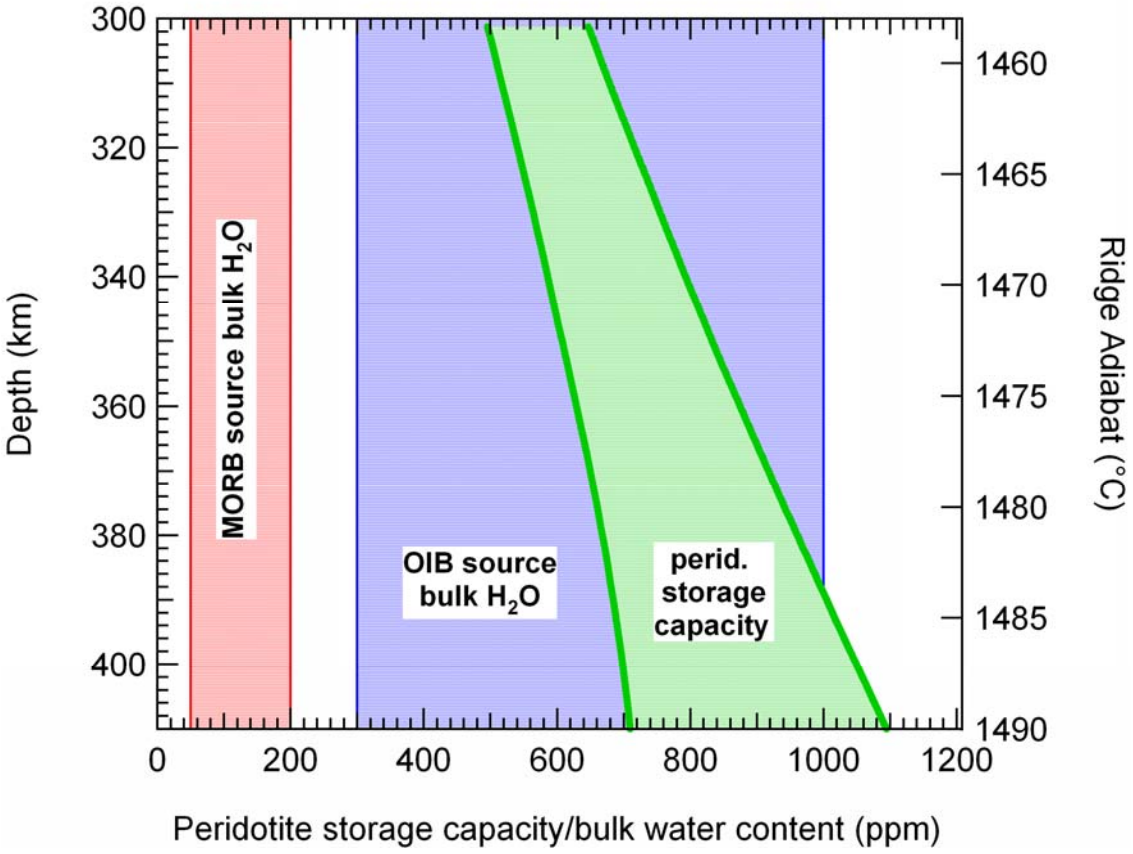

Figure 4.12. Estimated peridotite water storage capacity from 300-410 km depth (10-13.7 GPa). Peridotite water storage capacity values are derived by using the fit to the olivine water storage capacity pressure trend (Fig. 4.8), and then using a $D_{H_2O}^{\text{pyx/olivine}}$ value of 0.77 (from this study) and a $D_{H_2O}^{\text{gt/olivine}}$ range of 0-1.27 (Withers et al., 1998;

Mookherjee and Karato, 2010). Modal abundances are calculated based on the parameterizations of Hirschmann et al. (2009) to the data of Irifune and Isshiki (1998) and Stixrude and Lithgow-Bertelloni (2005, 2007) for proportions of phases along a ridge geotherm. The parameters are as follows: $X^{ol} = 0.6$, $X^{cpx} = 0.000463P^3 + 0.009274P^2 - 0.04597P + 0.1917$, $X^{gt} = 0.000297(P\text{-}3.2)^3 - 0.003128(P\text{-}3.2)^2 + 0.01545(P - 3.2) + 0.135$, where pressure is in GPa, and X^{opx} is taken as the difference from unity of the other modal abundances. If the advecting mantles bulk H_2O content exceeds peridotite storage capacity at the base of the upper mantle (700-1100 ppm) it will incite fluxed melting. Partial melting will extract H_2O from the residue until the storage capacity condition is met at that particular *P-T* condition. As peridotite water storage capacity decreases with depth, continued upwelling will cause the mantle to incrementally exceed the storage capacity, inciting small amounts of dehydration melting. However residues will remain at their H_2O storage capacity (i.e. peridotite at 300 km will have an H_2O concentration of 500-650 ppm). MORB source bulk H_2O contents (shaded red) of 50-200 ppm do not contain enough water to incite a global melt layer above 410 km. However, OIB source regions (300-1000 ppm bulk H_2O) at the wetter end of the spectrum likely incite localized hydrous melting at the transition zone, and it is likely that the hotter adiabat of these regions will further enhance the ability for OIB source mantle to induce fluxed melting, as both olivine and orthopyroxene water storage capacity decrease as a function of temperature (Fig 4.9a&b). Additionally, if subducted slabs retain a bulk water content that exceeds the peridotite storage capacity, they too will incite hydrous partial melting above 410 km, which could explain seismic evidence of

low velocity layers above 410 km associated with ancient subduction zones (Revenaugh and Sipkin, 1994; van der Meijde *et al.*, 2003; Courtier and Revenaugh, 2006; Jasbinsek et al., 2010).

BIBLIOGRAPHY

Adam J. & Green, T. (2003). The influence of pressure, mineral composition and water on trace element partitioning between clinopyroxene, amphibole and basanitic melts. *European Journal of Mineralogy* **15**, 831–841.

Agee, C.B. & Walker, D. (1988). Static compression and olivine flotation in ultrabasic silicate liquid. *Journal of Geophysical Research* **93**, 3437-3449.

Agee, C.B. (2008). Static compression of hydrous silicate melt and the effect of water on planetary differentiation. *Earth and Planetary Science Letters* **265**, 641–654.

Anderson, D.L. (1989). Theory of the Earth. *Blackwell Science Publishing*, Boston, MA, United States (USA).

Ardia, P., Hirschmann, M.M., Tenner, T.J., Withers, A.C. & Hervig, R.L. (in prep.). H_2O storage capacity of olivine at 5-8 GPa and consequences for dehydration partial melting of the upper mantle.

Asimow, P.D. & Langmuir, C.H. (2003). The importance of water to oceanic mantle melting regimes. *Nature* **421**, 815-820.

Asimow, P.D., Dixon, J.E. & Langmuir, C.H. (2004). A hydrous melting and fractionation model for mid-ocean ridge basalts: Application to the Mid-Atlantic Ridge near the Azores. *Geochemistry Geophysics Geosystems* **5**, doi:10.1029/2003GC000568.

Aubaud, C., Hauri, E.H. & Hirschmann, M.M. (2004). Hydrogen partition coefficients between nominally anhydrous minerals and basaltic melts. *Geophysical Research Letters* **31**, doi:10.29/2004GL021341.

Aubaud, C., Pineau, F., Hekinian, R. & Javoy, M. (2005). Degassing of CO_2 and H_2O in submarine lavas from the Society hotspot. *Earth and Planetary Science Letters* **235**, 511-527.

Aubaud, C., Pineau, F., Hekinian, R. & Javoy, M. (2006). Carbon and hydrogen isotope constraints on degassing of CO_2 and H_2O in submarine lavas from the Pitcairn hotspot (South Pacific). *Geophysical Research Letters* **33**, L02308.

Aubaud, C., Withers, A.C., Hirschmann, M.M., Guan, Y., Leshin, L.A., Mackwell, S.J. & Bell, D.R. (2007). Intercalibration of FTIR and SIMS for hydrogen measurements in glasses and nominally anhydrous minerals. *American Mineralogist* **92**, 811–828.

Aubaud, C., Hirschmann, M.M., Withers, A.C. & Hervig, R.L. (2008). Hydrogen partitioning between melt, clinopyroxene, and garnet at 3 GPa in a hydrous MORB with 6 wt.% H_2O. *Contributions to Mineralogy and Petrology* **156**, 607-625.

Bai, Q. & Kohlstedt, D.L. (1992). Substantial hydrogen solubility in olivine and implications for water storage in the mantle. *Nature* **357**, 672-674.

Bai, Q. & Kohlstedt D.L. (1993). Effects of chemical environment on the solubility and incorporation mechanism for hydrogen in olivine. *Physics and Chemistry of Minerals* **19**, 460-471.

Baker, M. B. & Stolper, E.M. (1994). Determining the composition of high-pressure mantle melts using diamond aggregates. *Geochimica et Cosmochimica Acta* **58**, 2811–2827.

Baker, M.B., Hirschmann, M.M., Ghiorso, M.S. & Stolper, E.M. (1995). Compositions of near-solidus peridotite melts from experiments and thermodynamic calculations. *Nature* **375**, 308–311.

Bali, E., Bolfan-Casanova, N. & Koga, K.T. (2008). Pressure and temperature dependence of H solubility in forsterite: An implication to water activity in the Earth interior. *Earth and Planetary Science Letters* **268**, 354-363.

Bell, D.R. & Rossman, G.R. (1992). Water in Earth's mantle: The role of nominally anhydrous minerals. *Science* **255**, 1391-1397.

Bell, D.R., Ihinger, P.D. & Rossman, G.R. (1995). Quantitative analysis of trace OH in garnet and pyroxenes. *American Mineralogist* **80**, 465–474.

Bell, D.R., Rossman, G.R., Maldener, J., Endisch, D. & Rauch, F. (2003). Hydroxide in olivine: a quantitative determination of the absolute amount and calibration of the IR spectrum. *Journal of Geophysical Research* **108**, doi:10.29/2001JB000679.

Bell, D.R., Rossman, G.R. & Moore, R.O. (2004). Abundance and partitioning of OH in a high-pressure magmatic system: megacrysts from the Monastery kimberlite, South Africa. *Journal of Petrology* **45**, 1539–1564.

Bercovici, D. & Karato, S.-I. (2003). Whole-mantle convection and the transition-zone water filter. *Nature* **425**, 39-43.

Bolfan-Casanova, N., Keppler, H. & Rubie, D.C. (2000). Water partitioning between nominally anhydrous minerals in the MgO-SiO_2-H_2O system up to 24 GPa:

implications for the distribution of water in the Earth's mantle. *Earth and Planetary Science Letters* **182**, 209-221.

Bultitude, R.J. & Green D.H. (1967-1968). Experimental study at high pressures on the origin of olivine nephelinite and olivine melilitite nephelinite magmas. *Earth and Planetary Science Letters* **3**, 325-337.

Canil, C. (1992). Orthopyroxene stability along the peridotite solidus and the origin of cratonic lithosphere beneath southern Africa. *Earth and Planetary Science Letters* **111**, 83–95.

Carr, M.J. & Rose, W.I. (1984). CENTAM: A data base of Central American volcanic rocks. *Journal of Volcanology and Geothermal Research* **33**, 239-240.

Chen, J. (2002). Effect of water on olivine-wadsleyite phase boundary in the (Mg, $Fe)_2SiO_4$ system. *Geophysical Research Letters* **29**, doi:10.1029/2001GL014429.

Chopra, P.N. & Paterson, M.S. (1984). The role of water in the deformation of dunite. *Journal of Geophysical Research* **89**, 7861–7876.

Clement, S.W.J. & Compston, W. (1990). SIMS at high sensitivity and high mass resolution. In: Benninghoven, A. (Ed.), *Secondary ion mass spectrometry, SIMS VII.* J. Wiley & Sons, Chichester.

Courtier, A.M. & Revenaugh, J. (2007). Deep upper-mantle melting beneath the Tasman and Coral Seas detected with multiple *ScS* reverberations. *Earth and Planetary Science Letters* **259**, 66-76.

Dai, L. & Karato, S.-I. (2009). Electrical conductivity of orthopyroxene: Implications for the water content of the asthenosphere. *Proceedings of the Japan Academy, Series B* **85**, 466-475.

Danyushevsky, L.V., Eggins, S.M., Falloon, T.J. & Christie, D.M. (2000). H_2O Abundance in Depleted to Moderately Enriched Mid-ocean Ridge magmas; part I: Incompatible Behaviour, Implications for Mantle Storage, and Origin of Regional Variations. *Journal of Petrology* **41**, 1329–1364.

Dasgupta, R., Hirschmann, M.M. & Withers, A.C. (2004). Deep global cycling of carbon constrained by the solidus of anhydrous, carbonated eclogite under upper mantle conditions. *Earth and Planetary Science Letters* **227**, 73-85.

Dasgupta, R., Hirschmann, M.M. & Smith, N.D. (2007). Water follows carbon: CO_2 incites deep silicate melting and dehydration beneath mid-ocean ridges. *Geology* **35**, 135-138.

Dasgupta, R., Hirschmann, M.M. & Smith, N.D. (2007). Partial Melting Experiments of Peridotite + CO_2 at 3 GPa and Genesis of Alkalic Ocean Island Basalts. *Journal of Petrology* **48**, 2093-2124.

Davis, F.A., Tangeman, J.A., Tenner, T.J. & Hirschmann, M.M. (2009). The composition of KLB-1 peridotite. *American Mineralogist* **94**, 176-180.

Demouchy, S., Deloule, E., Frost, D.J. & Keppler, H. (2005). Pressure and temperature-dependence of water solubility in Fe-free wadsleyite. *American Mineralogist* **90**, 1084-1091.

Dixon, J.E., Stolper, E.M. & Delaney, J.R. (1988). Infrared spectroscopic measurements of CO_2 and H_2O in Juan de Fuca Ridge basaltic glasses. *Earth and Planetary Science Letters* **90**, 87-104.

Dixon, J.E., Clague, D.A., Wallace, P. & Poreda, R. (1997). Volatiles in Alkalic Basalts from the North Arch Volcanic Field, Hawaii: Extensive Degassing of Deep Submarine-erupted Alkalic Series Lavas. *Journal of Petrology* **38**, 911–939.

Dixon, J.E., Leist, L., Langmuir, C. & Schilling, J.-G. (2002). Recycled dehydrated lithosphere observed in plume-influenced mid-ocean-ridge basalt. *Nature* **420**, 385–389.

Falloon, T.J. & Danyushevsky L.V. (2000). Melting of Refractory Mantle at 1.5, 2 and 2.5 GPa under Anhydrous and H_2O undersaturated Conditions: Implications for the Petrogenesis of High-Ca Boninites and the Influence of Subduction Components on Mantle Melting. *Journal of Petrology* **41**, 257-283.

Falloon, T.J., Danyushevsky, L.V. & Green, D.H. (2001). Peridotite Melting at 1 GPa: Reversal Experiments on Partial Melt Compositions Produced by Peridotite-Basalt Sandwich Experiments. *Journal of Petrology* **42**, 2363–2390.

Fine, G. & Stolper E. (1986). Dissolved carbon dioxide in basaltic glasses: concentrations and speciation. *Earth and Planetary Science Letters* **76**, 263-278.

Frost, D.J. & Dolejš D. (2007). Experimental determination of the effect of H_2O on the 410-km seismic discontinuity. *Earth and Planetary Science Letters* **256**, 182-195.

Gaboardi, M. & Humayun, M. (2009) Elemental fractionation during LA-ICP-MS analysis of silicate glasses: implications for matrix-independent standardization. *Journal of Analytical Atomic Spectrom*etry **24**, 1188-1197.

Gaetani, G.A. & Grove T.L. (1998). The influence of water on melting of mantle peridotite. *Contributions to Mineralogy and Petrology* **131**, 323-346.

Gasparik, T. (1993). The role of volatiles in the transition zone. *Journal of Geophysical Research* **98**, 4287-4299.

Grant, K.J., Kohn, S.C. & Brooker, R.A. (2007). The partitioning of water between olivine, orthopyroxene and melt synthesized in the system albite–forsterite–H_2O. *Earth and Planetary Science Letters* **260**, 227–241.

Green, D.H. & Ringwood, A.E. (1970). Mineralogy of peridotitic compositions under upper mantle conditions. *Physics of the Earth and Planetary Interiors* **3**, 359-371.

Green, D.H. (1973a). Conditions of melting of basanite magma from garnet peridotite. *Earth and Planetary Science Letters* **17**, 456-465.

Green D.H. (1973b). Experimental melting studies on a model upper mantle composition at high pressure under water-saturated and water-undersaturated conditions. *Earth and Planetary Science Letters* **19**, 37-53.

Green T.H., Blundy, J.D., Adam, J. & Yaxley, G.M. (2000). SIMS determination of trace element partition coefficients between garnet, clinopyroxene and hydrous basaltic liquids at 2–7.5 GPa and 1080–1200 ºC. *Lithos* **53**, 165–187.

Grove, T.L., Parman, S.W. & Dann, J.C. (1999). Conditions of magma generation for Archean komatiites from the Barberton Mountainland, South Africa. In: Fei, Y., Bertka, C.M. & Mysen, B.O. (ed.) *Mantle Petrology: Field Observations and High Pressure Experimentation: A tribute to Francis R. (Joe) Boyd. The Geochemical Society, Special Publication* **6**, 155-167.

Grove, T.L. (2001). Vapor-Saturated Melting of Fertile Peridotite Revisited: A new Experimental Approach and Re-evaluation of the Hydrous Peridotite Solidus. *American Geophysical Union, Fall Meeting.* Abstract #T31F-05.

Grove, T.L., Elkins-Tanton, L.T., Parman, S.W., Chatterjee, N., Müntener, O. & Gaetani, G.A. (2003). Fractional crystallization and mantle-melting controls on calc-alkaline differentiation trends. *Contributions to Mineralogy and Petrology* **145**, 515-533.

Grove, T.L., Chatterjee, N., Parman, S.W. & Médard, E. (2006). The influence of H_2O on mantle wedge melting. *Earth and Planetary Science Letters* **249**, 74-89.

Hacker, B.R. (2008). H_2O subduction beyond arcs. *Geochemistry Geophysics Geosystems* **9**, doi:10.1029/2007GC001707.

Hall, L. (1999). The effect of water on mantle melting. Ph.D. thesis, University of Bristol. Microform DX239155.

Hall, L.J., Brodie, J., Wood, B.J. & Carroll, M.R. (2004). Iron and water losses from hydrous basalts contained in $Au_{80}Pd_{20}$ capsules at high pressure and temperature. *Mineralogical Magazine* **68**, 75-81.

Hauri, E.H. (2002). SIMS analysis of volatiles in silicate glasses 2. isotopes and abundances in Hawaiian melt inclusions. *Chemical Geology* **183**, 115–141.

Hauri, E.H., Gaetani, G.A. & Green T.H. (2006). Partitioning of water during melting of the Earth's upper mantle at H_2O-undersaturated conditions. *Earth and Planetary Science Letters* **248**, 715-734.

Herzberg, C.T. & Zhang, J. (1996). Melting experiments on anhydrous peridotite KLB-1: compositions of magmas in the upper mantle and transition zone. *Journal of Geophysical Research* **101**, 8271-8295.

Hess, P.C. (1995). Thermodynamic mixing properties and the structure of silicate melts. *Reviews in Mineralogy and Geochemistry* **32**, 147-189.

Hirose, K. & Kushiro, I. (1993). Partial melting of dry peridotites at high pressures: Determination of compositions of melts segregated from peridotite using aggregates of diamond. *Earth and Planetary Science Letters* **114**, 477-489.

Hirose, K. & Kawamoto, T. (1995). Hydrous partial melting of lherzolite at 1 GPa: The effect of H_2O on the genesis of basaltic magmas. *Earth and Planetary Science Letters* **133**, 463-473.

Hirose, K. (1997). Melting experiments on lherzolite KLB-1 under hydrous conditions and generation of high-magnesian andesitic melts. *Geology* **25**, 42-44.

Hirschmann, M.M., Baker, M.B. & Stolper, E.M. (1998). The Effect of Alkalis on the Silica Content of Mantle-Derived Melts. *Geochimica et Cosmochimica Acta* **62**, 883-902.

Hirschmann, M.M., Asimow, P.D., Ghiorso, M.S. & Stolper, E.M. (1999). Calculation of Peridotite Partial Melting from Thermodynamic Models of Minerals and Melts. III. Controls on Isobaric Melt Production and the Effect of Water on Melt Production. *Journal of Petrology* **40**, 831-851.

Hirschmann, M.M. (2000). Mantle solidus: Experimental constraints and the effects of peridotite composition. *Geochemistry, Geophysics, Geosystems* **1**, Paper number 2000GC000070.

Hirschmann, M.M., Aubaud, C. & Withers, A.C. (2005). Storage capacity of H_2O in nominally anhydrous minerals in the upper mantle. *Earth and Planetary Science Letters* **236**, 167-181.

Hirschmann, M.M. (2006). Water, melting, and the deep earth H_2O cycle. *Annual Review of Earth and Planetary Sciences* **34**, 629-653.

Hirschmann, M.M., Withers, A.C. & Aubaud, C. (2006). Petrologic structure of a hydrous 410 km discontinuity. In: Jacobsen, S.D. & van der Lee, S. (ed.) *Earth's Deep Water Cycle, Geophysical Monograph Series.* AGU, Washington D.C. **168**, 277-287.

Hirschmann, M.M., Tenner, T.J., Aubaud, C.A. & Withers, A.C. (2009). Dehydration melting of nominally anhydrous mantle: The primacy of partitioning. *Physics of the Earth and Planetary Interiors* **176**, 54-68.

Hirschmann, M.M. (2010). Partial melt in the low velocity zone. *Physics of the Earth and Planetary Interiors* **179**, 60-71.

Hirth, G. & Kohlstedt D.L. (1996). Water in the oceanic upper mantle: implications for rheology, melt extraction and the evolution of the lithosphere. *Earth and Planetary Science Letters* **144**, 93-108.

Huang, X., Xu, Y. & Karato, S–I. (2005). Water content in the transition zone from electrical conductivity of wadsleyite and ringwoodite. *Nature* **434**, 746–749.

Humayun, M., Simon, S. B. & Grossman L. (2007) Tungsten and hafnium distribution in calcium-aluminum inclusions (CAIs) from Allende and Efremovka. *Geochimica et Cosmochimica Acta*, **71**, 4609-4627.

Humayun, M., Davis, F.A. & Hirschmann M.M. (submitted). Major element analysis of natural silicates by laser ablation ICP-MS. *Journal of Analytical Atomic Spectrometry*.

Inoue, T., Yurimoto, H. & Kudoh, Y. (1995). Hydrous modifies spinel, $Mg_{1.75}SiH_{0.5}O_4$: a new water reservoir in the mantle transition region. *Geophysical Research Letters* **22**, 117-120.

Irifune, T. & Ringwood, A.E. (1993). Phase transformations in subducted oceanic crust and buoyancy relationships at depths of 600-800 km in the mantle. *Earth and Planetary Science Letters* **117**, 101-110.

Irifune, T. & Isshiki, M. (1998). Iron partitioning in a pyrolite mantle and the nature of the 410-km discontinuity. *Nature* **392**, 702-705.

Irifune, T., Kubo, N., Isshiki, M. & Yamasaki, Y. (1998). Phase transformations in serpentine and transportation of water into the lower mantle. *Geophysical Research Letters* **25**, 203-206.

Ito, G., Lin, J. & Graham, D. (2003). Observational and theoretical studies of the dynamics of mantle plume-mid-ocean-ridge interaction. *Reviews of Geophysics* **41,** doi:10.1029/2002RG000117.

Jacobsen, S.D., Demouchy, S., Frost, D.J., Ballaran, T.B. & Kung, J. (2005). A systematic study of OH in hydrous wadsleyite from polarized FTIR spectroscopy and single-crystal X-ray diffraction: oxygen sites for hydrogen storage in Earth's interior. *American Mineralogist* **90**, 61-70.

Jamtveit, B., Brooker, R., Brooks, K., Larsen, L.M. & Pedersen, T. (2001). The water content of olivines from the North Atlantic Volcanic Province. *Earth and Planetary Science Letters* **186**, 401–415.

Jambon, A. & Zimmermann, J.-L. (1990). Water in the oceanic basalts: evidence for dehydration of recycled crust. *Earth and Planetary Science Letters* **101**, 323-331.

Jaques, A.L. & Green D.H. (1980) Anhydrous melting of peridotite at 0-15 kbar pressure and the genesis of tholeiitic basalts. *Contributions to Mineralogy and Petrology* **73**, 287-310.

Jasbinsek, J.J. (2010). Characterizing the 410 km discontinuity low-velocity layer beneath the LA RISTRA array in the North American Southwest. *Geochemistry Geophysics Geosystems* **11**, Q03008.

Jochum, K. P., B. Stoll, K. Herwig, M. Willbold, A. W. Hofmann, M. Amini, S. Aarburg, W. Abouchami, E. Hellebrand, B. Mocek, I. Raczek, A. Stracke, O. Alard, C. Bouman, S. Becker, M. Ducking, H. Bratz, R. Klemd, D. de Bruin, D. Canil, D. Cornell, C. J. de Hoog, C. Dalpe, L. Danyushevsky, A. Eisenhauer, W. R. Premo, W. D. D. Sun, M. Tiepolo, R. Vannucci, T. Vennemann, D. Wayne & J. D. Woodhead, (2006) MPI-DING reference glasses for in situ microanalysis: New reference values for elemental concentrations and isotope ratios. *Geochemistry Geophysics Geosystems* **7**, 1-44.

Karato, S. (1990). The role of hydrogen in the electrical conductivity of the upper mantle. *Science* **347**, 272–273.

Karato, S–I. & Jung, H. (1998). Water, partial melting and the origin of the seismic low velocity and high attenuation zone in the upper mantle. *Earth and Planetary Science Letters* **157**, 193–207.

Katayama, I. & Nakashima, S. (2003). Hydroxyl in clinopyroxene from the deep subducted crust: Evidence for H_2O transport into the mantle. *American Mineralogist* **88**, 229–234.

Katayama, I., Nakashima, S. & Yurimoto, H. (2006). Water content in natural eclogite and implication for water transport into the deep upper mantle. *Lithos* **86**, 245-259.

Katz, R.F., Spiegelman, M. & Langmuir, C.H. (2003). A new parameterization of hydrous mantle melting. *Geochemistry Geophysics Geosystems* **4**, doi:10.1029/2002GC00043.

Kawakatsu, H., Kumar, P., Takei, Y., Shinohara, M., Kanazawa, T., Araki, E. & Suyehiro, K. (2009). Seismic evidence for sharp lithosphere-asthenosphere boundaries of oceanic plates. *Science* **324**, 499-502.

Kawamoto, T. & Hirose, K. (1994). Au-Pd sample containers for melting experiments on iron and water bearing systems. *European Journal of Mineralogy* **6**, 381-385.

Kawamoto, T. & Holloway, J.R. (1997). Melting temperature and partial melt chemistry of H_2O-saturated mantle peridotite to 11 Gigapascals. *Science* **276**, 240-243.

Kawamoto, T. (2004). Hydrous phase stability and partial melt chemistry in H_2O-saturated KLB-1 peridotite up to the uppermost lower mantle conditions. *Physics of the Earth and Planetary Interiors* **143**, 387-395.

Kawamoto, T. (2006). Hydrous phases and water transport in the subducting slab. *Reviews in Mineralogy and Geochemistry* **62**, 273-289.

Koga, K., Hauri, E., Hirschmann, M. & Bell, D. (2003). Hydrogen concentration analyses using SIMS and FTIR: Comparison and calibration for nominally anhydrous minerals. *Geochemistry Geophysics Geosystems* **4**, doi:10.1029/2002GC000378.

Kohlstedt, D.L., Keppler, H. & Rubie, D.C. (1996). Solubility of water in the α, β, and γ phases of $(Mg, Fe)_2SiO_4$. *Contributions to Mineralogy and Petrology* **123**, 345-357.

Kohn, S.C., Booker, R.A., Frost, D.J., Slesinger, A.E. & Wood B.J. (2002). Ordering of hydroxyl defects in hydrous wadsleyite (β-Mg_2SiO_4). *American Mineralogist* **87**, 293-301.

Kohn, S.C., Roome, B.M., Smith, M.E. & Howes, A.P. (2005). Testing a potential mantle geohygrometer; the effect of dissolved water on the intracrystalline partitioning Al in orthopyroxene. *Earth and Planetary Science Letters* **238**, 342–350.

Kojitani, H. & Akaogi, M. (1997). Melting enthalpies of mantle peridotite: calorimetric determinations in the system CaO-MgO-Al_2O_3-SiO_2 and application to magma generation. *Earth and Planetary Science Letters* **153**, 209-222.

Kröger, F.A. & Vink, H.J. (1956). Relations between the concentration of imperfections in crystalline solids. In: Seitz, F, Turnball, D (eds). *Solid State Physics, 3.* Academic Press, New York, pp 367–435.

Kushiro, I., Syono, Y. & Akimoto, S.-I. (1968). Melting of a peridotite nodule at high pressures and high water pressures. *Journal of Geophysical Research* **73**, 6023-6029.

Kushiro, I. (1972). Effect of water on the composition of magmas formed at high pressures. *Journal of Petrology* **13**, 311-334.

Kushiro, I., Shimizu, N. & Nakamura, Y. (1972). Compositions of coexisting liquid and solid phases formed upon melting of natural garnet and spinel lherzolites at high pressures: a preliminary report. *Earth and Planetary Sciences*, **14**, 19-25.

Kushiro, I. (1975). On the nature of silicate melt and its significance in magma genesis: regularities in the shift of the liquidus boundaries involving olivine, pyroxene, and silica minerals. *American Journal of Science* **275**, 411-431.

Kushiro, I. (1996). Partial melting of a fertile mantle peridotite at high pressure and experimental study using aggregates of diamond. In: Basu, A. & Hart, S. (ed.) *Earth Processes: Reading the Isotopic Clock, Geophysical Monograph Series* AGU, Washington D.C. **95**, 109-122.

Lambert, I.B. & Wyllie, P.J. (1968). Stability of hornblende and a model for the low velocity zone. *Nature* **219**, 1240-1241.

LaTourette, T. & Holloway, J.R. (1994). Oxygen fugacity of the diamond + C-O fluid assemblage and CO_2 fugacity at 8 GPa. *Earth and Planetary Science Letters* **128**, 439-451.

Le Bas, M.J. (1989). Nephelinitic and basanitic Rocks. *Journal of Petrology* **30**, 1299-1312.

Le Bas, M.J. (2000). IUGS reclassification of the high-Mg and picritic volcanic rocks. *Journal of Petrology* **41**, 1467-1470.

Lesher, C.E., Pickering-Witter, J., Baxter, G. & Walter, M. (2003). Melting of garnet peridotite: Effects of capsules and thermocouples, and implications for high-pressure mantle solidus. *American Mineralogist* **88**, 1181-1189.

Litasov, K. & Ohtani, E. (2002). Phase relations and melt compositions in CMAS-pyrolite-H_2O system up to 25 GPa. *Physics of the Earth and Planetary Interiors* **134**, 105-127.

Litasov, K. & Ohtani, E. (2003). Stability of various hydrous phases in CMAS pyrolite-H_2O system up to 25 GPa. *Physics and Chemistry of Minerals* **30**, 147-156.

Litasov, K.D., Ohtani, E., Kagi, H., Jacobsen, S.D. & Ghosh, S. (2007). Temperature dependence and mechanism of hydrogen incorporation in olivine at 12.5-14.0 GPa. *Geophysical Research Letters* **34**, doi:10.1029/2007GL030737.

Locock, A.J. (2008). An excel spreadsheet to recast analyses of garnet into end-member components, and a synopsis of the crystal chemistry of natural silicate garnets. *Computers & Geosciences* **34**, 1769-1780.

Longhi, J. (2002). Some phase equilibrium systematics of lherzolite melting: I. *Geochemistry Geophysics Geosystems* **3**, doi: 10.29/2001GC000204.

Lu, R. & Keppler, H. (1997). Water solubility in pyrope to 100 kbar. *Contributions to Mineralogy and Petrology* **129**, 35-42.

Mackwell, S.J., Kohlstedt, D.L. & Paterson, M.S. (1985). The role of water in the deformation of olivine single crystals. *Journal of Geophysical Research* **90**, 11319-11333.

McGuire, A.V., Francis, C.A. & Darby Dyar, M. (1992). Mineral standards for electron microprobe analysis of oxygen. *American Mineralogist* **77**, 1087–1091.

Medard, E. & Grove, T.L. (2008). The effect of H_2O on the olivine liquidus of basaltic melts: experiments and thermodynamic models. *Contributions to Mineralogy and Petrology* **155**, 417–432.

Mei, S. & Kohlstedt, D.L. (2000a). Influence of water on plastic deformation of olivine aggregates 1. Diffusion creep regime. *Journal of Geophysical Research* **105**, 21457-21469.

Mei, S. & Kohlstedt, D.L. (2000b). Influence of water on plastic deformation of olivine aggregates 2. Dislocation creep regime. *Journal of Geophysical Research* **105**, 21471-21481.

Mibe, K., Fujii, T., Yasuda, A. & Ono, S. (2006). Mg-Fe partitioning between olivine and ultramafic melts at high pressures. *Geochimica et Cosmochimica Acta* **70**, 757-766.

Michael, P.J. (1988). The concentration, behavior and storage of H_2O in the suboceanic mantle: Implications for mantle metasomatism. *Geochimica et Cosmochimica Acta* **52**, 555–566.

Michael, P.J. (1995). Regionally distinctive sources of depleted MORB: Evidence from trace elements and H_2O. *Earth and Planetary Science Letters* **131**, 301–320.

Mierdel, K., Keppler, H., Smyth, J.R. & Langenhorst, F. (2007). Water solubility in aluminous orthopyroxene and the origin of Earth's Asthenosphere. *Science* **315**, 364-368/

Mookherjee, M. & Karato, S.-I. (2010). Solubility of water in pyrope-rich garnet at high pressures and temperature. *Geophysical Research Letters* **37**, doi:10.1029/2009GL041289.

Mysen, B.O. & Boettcher, A.L. (1975). Melting of Hydrous Mantle I. Phase relations of natural peridotite at high pressures and temperatures with controlled activities of water, carbon dioxide, and hydrogen. *Journal of Petrology* **16**, 520-548.

Nichols, A.R.L., Carroll, M.R. & Höskuldsson, Á. (2002). Is the Iceland hot spot also wet? Evidence from the water contents of undegassed submarine and subglacial pillow basalts. *Earth and Planetary Science Letters* **202**, 77–87.

Nisbet, E.G., Cheadle, M.J., Arndt, N.T. & Bickle, M.J. (1993). Constraining the potential temperature of the Archaean mantle: A review of the evidence from komatiites. *Lithos* **30**, 291-307.

O'Leary, J.A., Gaetani, G.A. & Hauri, E.H. (submitted). The effect of tetrahedral Al^{3+} on the partitioning of water between clinopyroxene and silicate melt. *Earth and Planetary Science Letters.*

Ohlhorst, S., Behrens, H. & Holtz, F. (2001). Compositional dependence of molar absorptivities of near-infrared OH- and H_2O bands in rhyolitic to basaltic glasses. *Chemical Geology* **174**, 5-20.

Okamoto, K. & Maruyama S. (1999). The high-pressure synthesis of lawsonite in the MORB + H_2O system. *American Mineralogist* **84**, 362-373.

Paterson, M.S. (1982). The determination of hydroxyl by infrared absorption in quartz, silicate glasses and similar materials. *Bulletin de Mineralogie* **105**, 20–29.

Perkins III, D. Holland T.J.B. & Newton, R.C. (1981). The Al_2O_3 contents of enstatite in equilibrium with garnet in the system MgO-Al_2O_3-SiO_2 at 15-40 kbar and 900º-1600º C. *Contributions to Mineralogy and Petrology* **78**, 99-109.

Piermarini, G.J. & Block, S. (1975). Ultrahigh pressure diamond-anvil cell and several semiconductor phase transition pressures in relation to fixed point pressure scale. *Review of Scientific Instruments* **46**, 973-979.

Putirka, K.D. (2005). Mantle potential temperatures at Hawaii, Iceland, and the mid-ocean ridge system, as inferred from olivine phenocrysts: Evidence for thermally driven mantle plumes. *Geochemistry, Geophysics, Geosystems* **6**, Q05L08.

Putirka, K.D. (2009). Excess temperatures at ocean islands: Implications for mantle layering and convection. *Geology* **36**, 283-286.

Rauch, M. & Keppler, H. (2002). Water solubility in orthopyroxene. *Contributions to Mineralogy and Petrology* **143**, 525–536.

Revenaugh, J. & Sipkin, S.A. (1994). Seismic evidence for silicate melt atop the 410-km mantle discontinuity. *Nature* **369**, 474-476.

Ringwood, A.E. (1994). Role of the transition zone and 660 km discontinuity in mantle dynamics. *Physics of the Earth and Planetary Interiors* **86**, 5-24.

Robinson, J.A.C., Wood, B.J. & Blundy, J.D. (1998). The beginning of melting of fertile and depleted peridotite at 1.5 GPa. *Earth and Planetary Science Letters* **155**, 97-111.

Rossman, G.R. & Aines, R.D. (1991). The hydrous components in garnets: Grossular-hydrogrossular. *American Mineralogist* **76**, 1153-1164.

Saal, A.E., Hauri, E.H., Langmuir, C.H. & Perfit, M.R. (2002). Vapour undersaturation in primitive mid-ocean-ridge basalt and the volatile content of Earth's upper mantle. *Science* **419**, 451–455.

Salters, V.J.M. and Stracke J.-G. (2005). Composition of the depleted mantle. *Geochemistry Geophysics Geosystems* **5**, Q05004.

Schiano, P., Eiler, J.M., Hutcheon, I.D. & Stolper, E.M. (2000). Primitive CaO-rich, silica-undersaturated melts in island arcs: Evidence for the involvement of clinopyroxene-rich lithologies in the petrogenesis of arc magmas. *Geochemistry Geophysics Geosystems* **1**, Paper number 1999GC000032.

Schmidt, M.W., Green, D.H. & Hibberson, W.O. (2004). Ultra-calcic magmas generated from Ca-depleted mantle: an experimental study on the origin of ankaramites. *Journal of Petrology* **45**, 531-554.

Seaman, C., Sherman, S.B., Garcia, M.O., Baker, M.B., Balta, B. & Stolper, E. (2004). Volatiles in glasses from the HSDP2 drill core. *Geochemistry Geophysics Geosystems* **5**, doi: 10.1029/2003GC000596.

Shaw, D.M. (1970). Trace element fractionation during anatexis. *Geochimica et Cosmochimica Acta* **34**, 237-243.

Shieh, S.R., Mao, H., Hemley, R.J. & Chung Ming, L. (1998). Decomposition of phase D in the lower mantle and the fate of dense hydrous silicates in subducting slabs. *Earth and Planetary Science Letters* **159**, 13-23.

Silver, L., & Stolper, E. (1985). A thermodynamic model for hydrous silicate melts. *Journal of Geology* **93**, 161-177.

Silver, L.A., Ihinger, P.D., & Stolper, E. (1990). The influence of bulk composition on the speciation of water in silicate glasses. *Contributions to Mineralogy and Petrology* **104**, 142-162.

Simons, K., Dixon, J., Schilling, J.-G., Kingsley, R. & Poreda, R. (2002). Volatiles in basaltic glasses from the Easter-Salas y Gomez Seamount Chain and Easter Microplate: Implications for geochemical cycling of volatile elements. *Geochemistry Geophysics Geosystems* **3**, doi: 10.1029/2001GC000173.

Sisson, T.W. & Bronto, S. (1998). Evidence for pressure-release melting beneath magmatic arcs from basalts at Galunggung, Indonesia. *Nature* **391**, 883-886.

Skogby, H. & Rossman, G.R. (1989). OH^- in pyroxene: An experimental study of incorporation mechanisms and stability. *American Mineralogist* **74**, 1059-1069.

Slodzian, G., Chaintreau, H. & Dennebouy, R. (1986). Self-regulated potential at insulating surfaces in the presence of a strong electrostatic extraction field. *Microbeam Analysis*, **78**.

Smyth, J.R., Bell, D.R. & Rossman, G.R., 1991. Incorporation of hydroxyl in upper-mantle pyroxenes. *Nature* **351**, 732–735.

Smyth, J.R., Kawamoto, T., Jacobsen, S.D., Swope, R.J., Hervig, R.L. & Holloway, J.R. (1997). Crystal structure of monoclinic hydrous wadsleyite β-$(Mg, Fe)_2SiO_4$. *American Mineralogist* **82**, 270-275.

Smyth, J.R. & Kawamoto, T. (1997). Wadsleyite II, A new high pressure hydrous phase in the peridotite-H_2O system. *Earth and Planetary Science Letters* **146**, E9-E16.

Sobolev, A. & Chaussidon, M. (1996). H_2O concentrations in primary melts from supra-subduction zones and mid-ocean ridges: implications for H_2O storage and recycling in the mantle. *Earth and Planetary Science Letters* **137**, 45-55.

Stalder, R. & Skogby, H. (2002). Hydrogen incorporation in enstatite. *European Journal of Mineralogy* **14**, 1139–1144.

Stixrude, L. & Lithgow-Bertelloni, C. (2005). Mineralogy and elasticity of the oceanic upper mantle: Origin of the low velocity zone. *Journal of Geophysical Research* **110**, doi:10.1020/2004JB002965.

Stixrude, L. & Lithgow-Bertelloni, C. (2007). Influence of phase transformations on lateral heterogeneity and dynamics in Earth's mantle. *Earth and Planetary Science Letters* **263**, 45-55.

Stolper, E. (1980). A phase diagram for mid-ocean ridge basalts: Preliminary results and implications for petrogenesis. *Contributions to Mineralogy and Petrology* **74**, 13-27.

Stolper, E. (1989). Temperature dependence of the speciation of water in rhyolitic melts and glasses. *American Mineralogist* **74**, 1247-1257.

Stolper, E. & Newman S. (1994). The role of water in the petrogenesis of Mariana trough magmas. *Earth and Planetary Science Letters* **121**, 293-325.

Takahashi, E. & Kushiro, I. (1983). Melting of dry peridotite at high pressures and basalt magma genesis. *American Mineralogist* **68**, 859–879.

Takahashi, E. (1986). Melting of a dry peridotite KLB-1 up to 14 GPa: implications on the origin of peridotitic upper mantle. *Journal of Geophysical Research* **91**, 9367-9382.

Tenner, T.J., Hirschmann, M.M., Withers, A.C. & Hervig, R.L. (2009). Hydrogen partitioning between nominally anhydrous upper mantle minerals and melt between 3 and 5 GPa and implications to hydrous peridotite partial melting. *Chemical Geology* **262**, 42-56.

Tenner, T.J., Hirschmann, M.M. & Humayun, M. (submitted). The effect of H_2O on partial melting of garnet peridotite at 3.5 GPa. *Journal of Petrology.*

Toplis, M.J. (2005). The thermodynamics of iron and magnesium partitioning between olivine and liquid: criteria for assessing and predicting equilibrium in natural and experimental systems. *Contributions to Mineralogy and Petrology* **149**, 22-39.

Ulmer, P. (1989). The dependence of the Fe^{2+}-Mg cation-partitioning between olivine and basaltic liquid on pressure, temperature and composition. *Contributions to Mineralogy and Petrology* **101**, 261-273.

van der Meijde, M., Marone, F., Giardini, D. & van der Lee, S. (2003). Seismic evidence for water deep in Earth's upper mantle. *Science*, **300**, 1556-1558.

Wallace, P.J., Frey, F.A., Weis, D. & Coffin, M.F. (2002). Origin and Evolution of the Kerguelen Plateau, Broken Ridge and Kerguelen Archipelago: Editorial. *Journal of Petrology* **47**, 1105-1108.

Wallace, P.J. (2005). Volatiles in subduction zone magmas: concentrations and fluxes based on melt inclusion and volcanic gas data. *Journal of Volcanology and Geothermal Research* **140**, 217-240.

Walter, M.J. (1998). Melting of garnet peridotite and the origin of komatiite and depleted lithosphere. *Journal of Petrology* **39**, 29-60.

Wang, Z., Hiraga, T. & Kohlstedt, D.L. (2004). Effect of H^+ on Fe–Mg interdiffusion in olivine, $(Fe, Mg)_2SiO_4$. *Applied Physics Letters* **85**, doi:10.1063/1.1769593.

Withers, A.C. & Behrens, H. (1999). Temperature-induced changes in the NIR spectra of hydrous albitic and rhyolitic glasses between 300 and 100K. *Physics and Chemistry of Minerals* **27**, 119–132.

Withers, A.C. & Hirschmann, M.M. (2007). H_2O storage capacity of $MgSiO_3$ clinoenstatite at 8-13 GPa, 1100-1400ºC. *Contributions to Mineralogy and Petrology*, **154**, 663-674.

Withers, A.C. & Hirschmann, M.M. (2008). Influence of temperature, composition, silica activity and oxygen fugacity on the H_2O storage capacity of olivine at 8 GPa. *Contributions to Mineralogy and Petrology* **156**, 595-605.

Withers, A.C., Hirschmann, M.M. & Tenner T.J. (2009). The effect of Fe on OH^- content of olivine: Implications for extraction of H_2O from the Martian mantle. *40th Lunar and Planetary Science Conference*, abstract 1490.

Withers, A.C., Hirschmann, M.M., Tenner T.J. (in prep.) Intercalibration of FTIR and SIMS for hydrogen measurements in olivine.

Wood, B.J. (1995). The effect of H_2O on the 410 km seismic discontinuity. *Science* **268**, 74-76.

Workman, R.K. & Hart, S.R (2005). Major and trace element composition of the depleted MORB mantle (DMM). *Earth and Planetary Science Letters* **231**, 53-72.

Wyllie, P.J. (1979). Magmas and volatile components. *American Mineralogist* **64**, 469–500.

Xu, Y., Poe, B.T., Shankland, T.J. & Rubie, D.C. (1998). Electrical Conductivity of Olivine, Wadsleyite, and Ringwoodite Under Upper-Mantle Conditions. *Science* **280**, 1415–1418.

Yamada, A., Inoue, T., & Irifune, T. (2004). Melting of enstatite from 13 to 18 GPa under hydrous conditions. *Physics of the Earth and Planetary Interiors* **147**, 45-56.

Yang, Y., Forsyth, D.W. & Weeraratne, D.S. (2007). Seismic attenuation near the East Pacific Rise and the origin of the low-velocity zone. *Earth and Planetary Science Letters* **258**, 260-268.

Yoshino, T., Manthilake, G., Matsuzaki, T. & Katsura, T. (2008). Dry mantle transition zone inferred from the conductivity of wadsleyite and ringwoodite. *Nature* **451**, 223–372.

Zhao, Y.-H., Ginsberg, S.B. & Kohlstedt, D.L. (2004). Solubility of hydrogen in olivine: dependence of temperature and iron content. *Contributions to Mineralogy and Petrology* **147**, 155-161.